Title

Theory of Multiscale and Multicomponent Transport and Thermodynamics in Water-Filled Phase-Separated Cation-Exchange Membranes

Author

Crothers, Andrew Robert

Publication Date

2020

Peer reviewed|Thesis/dissertation

Theory of Multiscale and Multicomponent Transport and Thermodynamics in Water-Filled Phase-Separated Cation-Exchange Membranes

By

Andrew R. Crothers

A dissertation submitted in partial satisfaction of the

requirements for the degree of

Doctor of Philosophy

in

Chemical Engineering

in the

Graduate Division

of the

University of California, Berkeley

Committee in charge:

Professor Clayton J. Radke, Co-Chair
Dr. Adam Z. Weber, Co-Chair
Professor David B. Graves
Professor Mark Asta

Summer 2020

Theory of Multiscale and Multicomponent Transport and Thermodynamics in Water-Filled Phase-Separated Cation-Exchange Membranes

Andrew R. Crothers

Abstract

Theory of Multiscale and Multicomponent Transport and Thermodynamics in Water-Filled Phase-Separated Cation-Exchange Membranes

by

Andrew R. Crothers

Doctor of Philosophy in Chemical Engineering

University of California, Berkeley

Professor Clayton J. Radke, Co-Chair
Dr. Adam Z. Weber, Co-Chair

Phase-separated water-swollen cation-exchange membranes are an important component in numerous energy-conversion devices. These materials make possible more established technologies such as low-temperature fuel cells, water electrolyzers, and the chlor-alkali process. Solvent-swollen membranes also play a key role in burgeoning energy-storage devices, such as redox-flow batteries (RFB), as well as processes geared towards electrifying the chemical industry, such as artificial photosynthesis and electrochemical ammonia production. The membrane is central to these technologies.

To understand the role that these membranes play in energy-conversion devices, this work initially considers a RFB as a case study. This dissertation examines the effect that membrane properties, such as conductivity and ion permeability, have on cell performance and efficiency. There is typically a tradeoff between membranes with high conductivity and low ion permeability. Given specific operational constraints, we quantitatively map when this tradeoff should be made. Thermodynamic and transport properties of the membrane fundamentally influence process performance. These water-swollen membranes contain concentrated electrolyte solutions, often with multiple ionic species. The multicomponent and concentrated nature of these materials invalidates classic theoretical treatments of the material that invoke ideal dilute-solution approximations. To promote improved material design and process optimization, this dissertation develops mathematical models of the concentrated-solution thermodynamic and transport phenomena in these membranes.

Perfluorinated sulfonic-acid (PFSA) ionomers (e.g., Nafion® developed by DuPont de Nemours, Inc.) is the quintessential phase-separated, solvent-swollen, cation-exchange membrane material. PFSAs consist of a hydrophobic polytetrafluoroethylene (PTFE) backbone with side chains terminating in hydrophilic sulfonate groups. The sulfonate groups are negatively charged and balanced by positively charged aqueous protons or other cations. In aqueous solutions or humid vapor, water absorbs into the membrane, hydrating the sulfonate groups. The hydrophilicity difference between the polymer backbone and hydrated ions drives nanophase separation and the formation of a bicontinuous structure

with sulfonate groups imbedded at the hydrophobic/hydrophilic domain interface. The hydrophilic phase forms a network of connected aqueous water-filled channels that facilitate transport of ions and solvent across the membrane. The transport and thermodynamic phenomena occur across multiple length scales. Molecular interactions dictate the microscale behavior of species in the channels. The hydrophilic-phase network introduces mesoscale effects. Macroscopic membrane properties are a function of both the microscale and mesoscale.

To first quantify the important molecular interactions and the role of the microscale on membrane properties, this dissertation develops a microcontinuum mathematical model of a representative water-filled channel. Negatively charged sulfonate groups are immobilized at the channel walls and mobile cations are distributed across the channel. The model calculates the potential of mean force and distribution functions of the cations. The model considers solvation energy, electrostatic interactions, image charges, finite-size effects, and dispersion forces. Bulk-electrolyte cation mobility is modified by electrohydrodynamic and confinement effects. Model predictions show that the portion of mobile cations is governed by a competition between solvation energy that promotes cation dissociation from the sulfonate groups and electrostatic interactions that induce ion-pair formation. The hydrophilic-phase tortuosity upscales the microscale transport model, specifying macroscopic conductivity. Tortuosity is fit to data using one adjustable parameter. Membrane conductivity is governed by the tortuosity of the hydrophilic channels and the microscale interactions inside the channels. These contributions vary with water content and membrane chemistry.

Having identified the key microscale phenomena, this work develops molecular thermodynamic and transport models for the multicomponent membrane system. The thermodynamic model proposes a free energy that includes excess contributions proposed in the microcontinuum model (electrostatic interactions and solvation effects) as well as ion-pair formation, swelling forces, and confinement along with semi-empirical non-electrostatic specific-ion interactions,. Bulk-electrolyte solution properties parameterize most of the free-energy contributions. The thermodynamic model calculates ion and water partitioning into the membrane from dilute and concentrated aqueous solutions and water uptake from water vapor. The model calculations compare favorably to experimental measurements.

Having established a thermodynamic framework, this work develops a multicomponent concentrated-solution model of transport that fully calculates macroscopic ion and solvent-transport properties of the membrane. The model uses a Stefan-Maxwell formalism describing frictional interactions between species. Bulk-electrolyte solution properties specify ion/ion and ion/solvent friction coefficients inside the water-filled channels. A classic electrokinetic treatment determines ion/membrane and solvent/membrane friction coefficients. Channel tortuosity upscales the microscale friction coefficients. The model predicts macroscopic conductivity, water permanence, ion-transference numbers, and electro-osmotic coefficients that agree with experiments of membranes in dilute and concentrated aqueous electrolyte solutions.

As a case study, this dissertation uses the multicomponent thermodynamic and transport models to understand the performance of membranes in a vanadium RFB. The model reveals that concentration gradients of various species each drive transport of other species. This coupling is both thermodynamic in nature – with concentration gradients inducing chemical potential gradients in other species – and frictional – with molecular interactions among species influencing the transport of one another. This new model provides structure-function-performance relationships for RFB membranes and rationalizes how RFB performance results from the collective interactions between all of the species present.

The proposed transport models invoke a ubiquitous assumption from literature that tortuosity of water-filled channels uniformly upscales microscale transport properties. This dissertation examines the usefulness of this approach using network simulations and theory. The models explore the role of the mesoscale on water, proton, and electrokinetic transport properties in PFSA membranes. Network simulations account for the size distribution of channels throughout the membrane to calculate macroscopic properties. An experimentally consistent 3D Voronoi network tessellation characterizes the topology of the membrane hydrophilic phase. Experimental water, proton, and electrokinetic transport properties validate model calculations. We show that the network does not uniformly upscale microscale transport properties. The simulations predict dissimilar tortuosities arising for water, proton, and electrokinetic transport coefficients. The pathways that water travels across the membrane are different than those taken by protons due to their intrinsic microscale interactions within a hydrophilic channel combined with a wide distribution of channel sizes. The distribution of transport properties across the network induces local electrokinetic gradients that couple water and proton transport. As a result, the macroscopic proton transport coefficient is a function of the microscale water and electrokinetic transport properties. This work provides a holistic approach to connect experiments and theory of microscale to macroscale properties.

The fundamental analysis of transport and thermodynamic phenomena provided here informs design of improved solvent-filled ion-exchange membranes. Moreover, this work provides engineering models that facilitate optimization of energy-conversion devices.

To my parents.

You taught me math, insisting it would have real-world applications

I'm still waiting for one

Contents

List of Figures

List of Tables

Acknowledgments

Thanks to the United States government and the American taxpayers, I was allowed me to perform this research. In particular, this work was funded by the United States National Science Foundation Graduate Research Fellowship Program, Department of Energy's Advanced Research Projects Agency–Energy and Fuel Cell Technologies Office, and the Department of Defense. I hope to be able to repay the favor someday.

I thank my advisers Prof. Clay Radke and Dr. Adam Weber for all the time and support. Without their involvement in my PhD, I would have graduated two years sooner. Despite my pleas, they demanded high quality work that never sacrificed rigor or sophistication in exchange for my sanity. At the beginning of my PhD, Clay told me, "you are not going to invent the next great fuel cell during graduate school, but you are going to think deeply." Clay was right. I did not invent the next great fuel cell. To me, Adam and Clay are extraordinary researchers, teachers, and friends. Adam and Clay mentored me professionally and personally and they ceaselessly advocated for me. In exchange, I helped them move swim spas or bookshelves around their houses. I could not have asked for better PhD advisers.

I also thank two mentors, Dr. Ahmet Kusoglu and Prof. John Prausnitz. During late nights and weekends in the office, Ahmet lead countless discussions on polymers and the wider world. He shaped my understanding of PFSA membranes and was instrumental in all this work. Ahmet gave the inspiration for the graphics and figures in this dissertation (if he did not make them directly). It was also a great privilege to work with Prof. Prausnitz on an independent project during my PhD on molecular thermodynamics of mixed-solvent electrolytes. (Unfortunately, this project did not fit into this dissertation). During our project, Prof. Prausnitz provided me with keen insights about thermodynamics and life. I am sorry I could not devote more time to working with him.

I thank the UC Berkeley Chemical and Biomolecular Engineering Department. The professors, students, and administrators are extraordinary. I enjoyed learning from everyone and having open and engaging discussions about science at ChemE Keg, colloquiums, and practice preliminary and qualifying exams. In particular, I thank the PhD cohort of 2014 for study nights and nights out. I thank Carlet Altamirano for repeatedly saving me from bureaucratic nightmares. In particular among the professors, I thank Professors Nitash Balsara, Kranthi Mandadapu, and Bryan McCloskey for useful discussions on transport phenomena, polymer physics, and electrochemistry. I thank my committee members David Graves and Mark Asta for reading and providing feedback on this dissertation. Outside of Berkeley, Robert Darling instigated much of this work and counseled me throughout it.

I thank members of the Energy Conversion group and Radke lab past and present, specifically, the graduate students: Grace Anderson, Claire Arthurs, Sarah Berlinger, Ashley Bird, Justin Bui, Anamika Chowdhury, Peter Dudenas, Tom Dursch, Victoria Ehlinger, Julie Fornaciari, David Liu, Johnny Petrovick, Oyin Romiluyi, Meron Tesfaye, and Philomena Weng, the post-doctoral researchers and staff scientists: Mike Gerhardt, Priyamvada, Lalit Pant, Jessica Luo, Iryna Zenyuk, Rohini Bala Chandran, Jiangjin Liu, Nemanja Danilovic, Doug Kushner, and Huai-Suen Shiau, and the visiting academics: Shouwen Shi, Franz Spingler, Tobias Schuler, and Marc Secanell, and the undergraduate students I mentored: Timothy Quah, Charles Li, and Ryan Lee. It has been an honor to work with all of these brilliant and dedicated scientists. We had great times in lab, at happy hours, socials, and retreats. Sorry I got us lost on so many hikes.

Among these people, this dissertation is particularly indebted to Lalit, Priyam, Iryna, Philomena, Anamika, and Rohini for their insights and help with mathematical modeling and discussions on what electrical potential really is. Doug kept my mathematical fantasies grounded by harsh experimental reality and Shouwen worked hard to collect some of the data in this dissertation. I thank Meron and Franz for trips and superb and honest conversations. Pete is an exceptional scientist and I could not have asked for a better partner in crime for a PhD. We almost figured out all there is to know about Nafion. Undoubtedly we will gain acclaim for discovering the torsional oscillations in fluoropolymer backbone motion.

Most of the matrix math in this dissertation comes from Joey Author, who explained it to me between our philosophical musings over beers at Jupiter or hikes at Point Reyes. Vincent was kind enough to remain my friend throughout graduate school despite me giving him hypothermia and snoring throughout our time together as undergraduate roommates. Along with Sarah and Pete, the rest of the Alligator house, Matt, Constance, Parry, Tammy, Kyle, and Julie made returning home after failed simulations less disheartening and they have been a great crew to shelter-in-place with during the COVID-19 pandemic.

My parents, Mike and Sharon, and siblings, Christina and Will, instilled in me the work ethic, creativity, and character required for this dissertation. Our dinner table arguments during my childhood taught me more about the scientific method than any class has since. My parents also taught me calculus, which has been occasionally useful. I thank Rebecca Pinals for accepting my email invitation to a bike ride (i.e. a date, although she had no idea of my intentions). During the PhD, Rebecca made me and the days brighter. She unconditionally championed and challenged me throughout. I am excited for all the adventures of our future.

1 Introduction

1.1 Electrochemical Energy-Conversion Devices

Unabated fossil-fuel use generates greenhouse-gas emissions.[1] Reducing these emissions is imperative if humanity is to avoid the worst extents of climate change.[1] Eliminating fossil-fuel use is challenging because it involves in many different sectors of the economy from electrical-power production to transportation to chemical processing.[1] Renewable-energy electricity plants (e.g., solar and wind farms) have lower greenhouse-gas emissions, providing a sustainable alterative to fossil-fuel-based electricity.[1] Due to intense research and development efforts, the cost of renewable-electricity production has sharply declined in the past decade and is economically competitive with fossil-fuel-based electricity in an increasing number of cases.[1-2] Using cheap, sustainable electricity to replace fossil fuels in other sectors of the economy, such as the chemical and transportation industries, is a promising route to reducing global greenhouse-gas emissions.[2-7]

One avenue to use electrical energy is to convert it into chemical energy.[3-7] The chemical energy can be stored for later use (such as charging and then discharging redox-flow batteries or splitting water to hydrogen that is later used in fuel cells). Inputting chemical energy can convert low-value chemicals to higher value products (such as making carbon dioxide into formate and methanol).[2-7] These approaches typically require electrochemical energy-conversion devices.[3-7] Even with inexpensive electricity prices, current electrochemical energy-conversion technology is not economically feasible outside a few industries.[3-7] However, improving device efficiency and performance while decreasing costs can allow this technology compete with chemical energy that currently comes from fossil fuels.[3-7]

Electrochemical-conversion cells contain an anode, a cathode, and an electrolyte separating these electrodes.[8-10] The anode oxidizes reactants (removes electrons from molecules) and the cathode reduces reactants (adds electrons to molecules).[8-10] Electrons pass through an external circuit from the anode to the cathode (i.e. an electronic current) as they are prevented from traversing the separator.[8, 10] Depending on the type of reaction, the external circuit either introduces power into the systems, converting electrical into chemical energy, or removes power from the cell, converting chemical into electrical energy.[8, 10] The electrolyte allows only ions to pass between the anode and cathode via an ionic current, which is equal to the electronic current passing through the external circuit.[8, 10] The electrolyte prevent electrons from bypassing the external circuit and shorting the cell and moving directly between electrodes.[8, 10] For electrochemical cells that contain gas, liquid, or soluble reactants, the electrolyte also prevents reactants from opposing electrodes mixing and reacting.[8-10] An ideal electrolyte has high ionic conductivity, negligible electronic conductivity, and does not allow undesirable transport of species between electrodes.[8-11]

Solvent-filled phase-separated ion-exchange membranes are an important class of electrolytes.[12] These membrane are used in hydrogen electrolysis, hydrogen fuel cells, chloralkali process, and carbon-dioxide reduction, among other technologies.[12] These membranes are macroscopic solids that minimize mixing of reactant species. They are imbued with solvent that increases their ionic conductivity.[12]

Phase-separated ion-exchange membranes operate in a wide range of environmental conditions that include varying temperatures and levels of humidification.[12] In addition to the solvent, multiple ionic and non-ionic chemical species can exist in the membrane.[12] Membrane functionalities change dramatically in different environmental conditions and in the presence of different species.[12] Although the membrane absorbs numerous solvents, water is most often the solvent in energy-conversion devices.[12]

Prediction of the properties of the membrane under these different conditions and understanding their physical bases enables improved design and operation of electrochemical cells.[9] To this end, mathematical models underscore quantitative design and analysis.[9] Physics-based models that use molecular descriptions are particularly valuable because they link an observed phenomenon directly its microscale origin.[9, 13] As a result, the model makes valid predictions in any situation as long as the molecular nature of the system has not changed.[13] These conditions can be challenging to access experimentally.[13]

In this dissertation, theory and simulations model mass-transport and thermodynamic phenomena of solvent-filled ion-exchange membranes. The proposed models calculate membrane performance and link it to molecular-scale phenomena. The remainder of this chapter briefly summarizes the nature of solvent-filled phase-separated ion-exchange membranes, details the scope of the dissertation, and summarizes how this dissertation builds on prior work in the field. Solvent-swollen phase-separated ion-exchange membrane appear in a wide range of applications beyond energy conversion including water purification, drug delivery, and dialysis.[14-17] Although these applications are not the motivating technology for this work, the analyses herein are still applicable to their design and optimization.

1.2 Summary of Solvent-Filled Phase-Separated Ion-Exchange Membranes

Solvent-swollen phase-separated ion-exchange membranes consist of crosslinked, charged polymers that absorb solvent.[12, 18-19] The polymer phase separates into nanoscale solvophilic solvent-filled domains and solvophobic domains.[*] The solvophilic domains (or channels) connect to one another to form a sample-spanning network that facilitates transport of mobile ions and solvent across the membrane.[12, 18] When water is the solvent, mobile ions primarily exist in the hydrophilic domains where they have relatively high mobility.[12, 18] Hydrophobic polymer domains provide the membrane with structural integrity and durability.[12, 18] The size of each type of domain is on the order of single nanometers.[12, 18]

Typically these materials are often cation-exchange membranes (CEM), in which case the polymer contains negatively charged groups charge balanced by dissolved atomic or small-molecule cations.[20] In many energy-conversion devices, the counter cation is a proton.[20] Alternatively, the polymer can be an anion-exchange membrane (AEM), which contains positive fixed charges with negatively charged counter anions.[21] AEMs can offer various material advantages to energy-conversion devices.[21] However, CEMs are a more mature technology, exhibiting higher conductivity and superior durability than AEMs, with numerous commercially available chemistries.[12, 21] This dissertation focuses on CEM chemistries because they are better

[*] These domains are generally solvophilic and solvophobic, respectively, but as water is the usual solvent, they are denoted as hydrophilic and hydrophobic throughout this work.

characterized and literature provides numerous datasets for model validation. But the modeling methodology and approach can readily be applicable to AEMs.

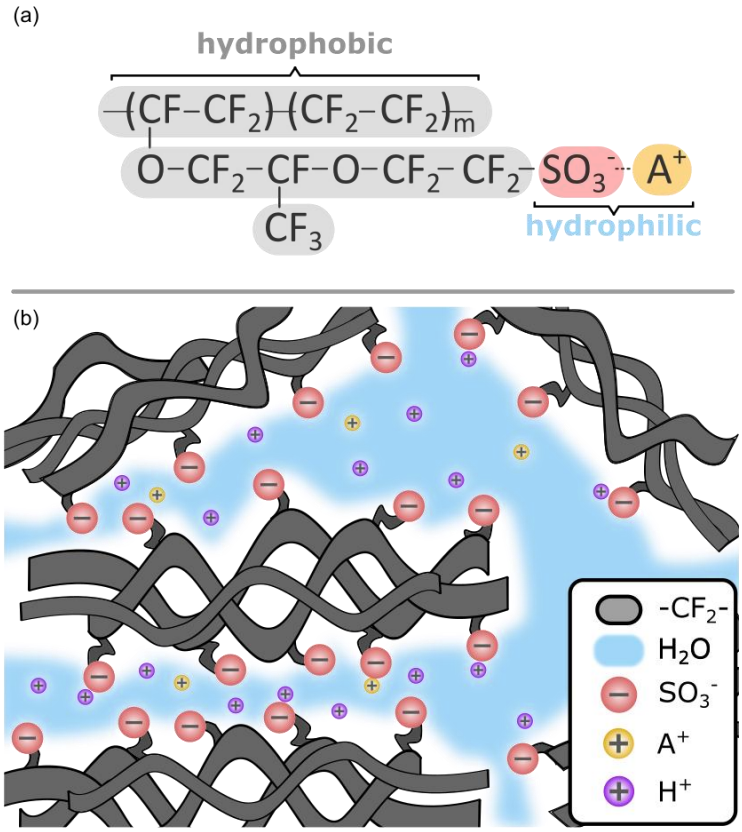

Figure 1-1. (a) Molecular formula of the Nafion PFSA and (b) a cartoon of the microstructure of a hydrated PFSA membrane. A^+ denotes a generic cation.

Perfluorosulfonic acid (PFSA) polymer is the quintessential solvent-swollen phase-separated CEM.[12] PFSAs contain polytetrafluoroethylene (PTFE, brand name is Teflon) backbone side chains terminating with a sulfonate group, as Figure 1-1a illustrates.[12] The PTFE backbone is hydrophobic, semi-crystalline, and forms bundles that constitute hydrophobic domains.[12] Polymer sulfonate groups are hydrophilic and promote water absorption into the membrane.[12] The sulfonate groups line the interface between the hydrophilic and hydrophobic domains, as Figure 1-1b pictures.[12] The most well-known PFSA commercial membrane is Nafion developed by DuPont.[12]

Polymer chemistry and processing history differentiate types of PFSA membranes.[12] Equivalent weight (EW, g-polymer per mole of sulfonate group) characterizes the ratio of hydrophobic to hydrophilic constituents (i.e., side-chain spacing). PFSA membranes typically have EWs between 725 and 1500 g/mol.[12] Different producers of PFSA membranes create different sidechain lengths ranging from a short-sidechain chemistry, Aquivion (from Solvay Specialty that contains two CF_2 spacer groups on the sidechain), a medium-length sidechain from 3M (that contains four CF_2 spacer groups on the sidechain), and the long sidechain of Nafion (that contains three CF_2 spacers and a perfluoroether group). Membranes undergo different processing history.[12] Manufacturers extrude or directly cast membranes from solution.[12] Membranes are also frequently pretreated

before use through annealing or heating in aqueous solutions.[12] The chemistry of the PFSA and its processing history affect its transport, mechanical, and thermodynamic properties.[12]

PFSAs are semi-crystalline and exist in a quasi-equilibrium state.[12] They are never truly in equilibrium with their surrounding environment as their properties vary indefinitely with time.[12] Quasi-equilibrium properties are relevant for device operation and, therefore, researchers measuring properties account for the timescale over which the properties are applicable.[12] Important membrane properties include those that are thermodynamic (e.g., water uptake from humid air and aqueous solutions and ion partitioning from electrolytes), transport (e.g., ion mobility, conductivity, and water diffusion), mechanical (e.g., modulus and viscoelasticity), and structural (e.g., hydrophilic domain sizes and shape), among others.[12]

Water uptake is particularly important because all other properties are strong functions of it. Water activity (i.e. relative humidity in humid vapor) of the surrounding environment dictates water uptake and, in turn, most other properties.[12] Membrane water content is often quantified as the moles of water per mole of sulfonate group, denoted by λ.[12] In Nafion membranes, λ ranges from 0 to ~23, corresponding to a water volume fraction of 0 and ~0.44, respectively.[12]

Mathematical models of solvent-filled membrane are valuable tools because they predict membrane properties at different electrochemical cell environmental conditions (e.g., relative humidity) that can be time consuming or impossible to measure experimentally.[9, 12-13, 22] These mathematical descriptions can be engineering models that are semi-empirical and allow highly accurate interpolation or limited extrapolation of membrane properties under different operating conditions.[22] These models help cell designers optimize performance at these different conditions. Alternatively, mathematical models can be entirely based on physical first principles with little or no empiricism.[22] These first-principle models are often more complex or less accurate than engineering models. But these models are important because they specify the underlying principles governing membrane properties that inform the design of polymers with desirable characteristics.[9, 12-13, 22]

There are two aspects of solvent-filled phase-separated membranes that give rise to complex physics that are not trivially modeled using existing engineering or first-principles theories. First, as Figure 1-1b shows, the connected nanophase-separated domains of these materials creates a multiscale system.[12, 18, 23-24] Intermolecular interactions at the microscale dictate transport and thermodynamic behavior of species within the solvent-filled channels.[12, 18, 25-26] These channels form a connected mesoscale transport network that mediates movement across the membrane.[12, 18, 25-26] Macroscopically observable properties are the cumulative effect of interactions across the microscale and mesoscale.[12, 27] As such, an undesirable membrane characteristic can originate at any of these length scales.[12, 27] The strategy to eliminate these unwanted characteristics depends on which length scale is important.[27] For example, an undesirable characteristic that arises from molecular interactions within membrane channels can only be addressed by altering microscale properties through, for example, changing the chemical nature of the membrane.[28] In contrast, a deleterious behavior arising at the mesoscale should be ameliorated by altering the nature of the hydrophilic-domain network.[29]

The second challenge of modeling water-filled phase-separated membranes is that the electrolyte inside the hydrophilic domains is highly concentrated (> 2.4 mol L^{-1}).[12, 23-24] Many widely-used transport and thermodynamic models of solutions assume that the aqueous phase is ideally dilute.[9, 30] As this assumption is not valid, the widely-used ideal dilute models must be modified to account

for the additional interactions present in concentrated solutions.[9] In dilute solutions, binary interactions only between solutes and the solvent are sufficient to describe behavior. In concentrated systems, interactions between solutes must also be considered.[9] Consequently, the number of pairwise potentials between species scales as $N(N-1)/2$, where N is the number of species including the membrane.[9] Each pairwise potential gives rise to a transport property and a thermodynamic-model parameter that quantifies these interactions.[9] In energy-conversion devices, there are frequently multiple ionic species and, consequently, numerous transport properties and thermodynamic-model parameters.[31-33] In this dissertation, the proposed thermodynamic and mass-transport models account for the multiscale and concentrated nature of solvent-filled phase-separated membranes.

1.3 Scope of Dissertation

This dissertation contains six chapters (in addition to this introduction) modeling transport and thermodynamic phenomena of solvent-filled phase-separated ion-exchange membranes. Each chapter uses the insights of previous ones and provides a progressively more sophisticated understanding of the system.

Chapter 2 is a case study for how, at a systems level, properties of water-filled phase-separated ion-exchange membranes influence performance of redox-flow batteries.[11, 34] Redox-flow batteries (RFBs) are electrochemical devices that are promising energy-storage technologies.[35] RFB performance and efficiency depend upon the properties of the membrane.[11, 34] Chapter 2 is an extended motivation for the rest of the dissertation. It illustrates why and how the community needs mass-transport and thermodynamic models of these membrane to optimize device performance.

Chapter 3 proposes a microcontinuum transport model of a hydrophilic domain of a PFSA membrane. This model identifies relevant molecular interactions in the channels, such as the role of cation solvation and electrostatic interactions between sulfonate groups and mobile cations. The proposed theory calculates how cations are distributed throughout water-filled channels, showing agreement with molecular-dynamics simulations. To compare the model to experiment, inclusion of the tortuosity of the hydrophilic transport network upscales the calculated microscale conductivity. Chapter 3 elucidates the important molecular interactions in PFSA membranes and quantifies the relative impact of microscale and mesoscale phenomena on macroscopic properties.

Chapter 4 proposes a multicomponent molecular thermodynamic model of water and ion uptake in phase-separated cation-exchange membranes. Informed by the detailed microscale analysis from Chapter 3, Chapter 4 develops a free-energy function that accounts for electrostatic and non-electrostatic specific interactions between ions, solvation effects, confinement, and membrane swelling. The model calculates ion and water partitioning into PFSA membranes from dilute and concentrated electrolyte solutions and membrane water uptake from surrounding water vapor.

Using the thermodynamic analysis in Chapter 4, Chapter 5 proposes a multicomponent molecular transport model. Stefan-Maxwell-Onsager concentrated-solution theory[36] provides the model framework. The microscale insights from Chapter 3 guide the functional forms of the frictional interactions between species. The model calculates the conductivity, water transport coefficient, transference numbers, and electro-osmotic coefficient of membranes equilibrated with dilute and concentrated electrolyte solutions. These properties agree with measurements.

Motivated by Chapter 2, Chapter 6 combines the transport and thermodynamics models from Chapters 4 and 5 to calculate membrane performance of a vanadium RFB. The analysis informs experimental analysis of membranes and RFB operation strategies. By spanning the analysis from molecular transport and thermodynamic theories to device performance, Chapter 6 proposes structure-function-performance relationships for RFB membranes.

Finally, Chapter 7 examines the fundamental nature of tortuosity and the role of different length scales on macroscopic PFSA membrane properties. In Chapters 3 and 5, an adjusted tortuosity scales microscopic properties to calculate macroscopic transport coefficients. This treatment is widespread and is useful,[37] but Chapter 7 shows that tortuosity is different for different mass-transport phenomena. The closing chapter of this thesis demonstrates that macroscopic properties emerge out of mesoscale-mediated microscale interactions.

1.4 Previous Literature

This dissertation relies extensively on experiments, models, theories, and simulations of previous researchers. The relevant contributions from literature are discussed within each chapter. Here, we provide a brief summary of the key literature and how this work fits within the broader community. Figure 1-2 shows a cluster network analysis of the literature cited within Chapters 3-6 created using the VOSviewer software package.[38] Each node is a paper cited in this thesis and a line between nodes denotes one paper citing another. The number of links from a node (i.e., the number of times a paper cites or is cited by one of the other papers in the network) specifies its size and is a measure of how frequently it is cited within this literature. The nodes are clustered and colored according to how much they cite one another using an algorithm based on modularity clustering technique and a LogLin layout.[38-39] In essence, the clusters corresponds to the different communities in literature from which this thesis draws.

On the right side of the Figure 1-2 there are two clusters that are closely linked containing publications on fundamental research of PFSA membranes. This community strongly influenced Chapter 3 (shown as the large sphere labeled Crothers 2017). Three literature reviews that are particularly important to this community are those of Kusoglu and Weber,[12] Mauritz and Moore,[19] and Kreuer et al.[18] Molecular-dynamics simulations from Voth and Coworkers[40-41] and Devanthan et. al.[42-43] and experimental characterization by Berrod et al.[44] strongly influenced Chapter 3's description of molecular interactions in PFSAs. Chapter 3 closely builds on microcontinuum models from Pintuaro and Coworkers,[14, 45-46] Berg and Benjaminsen,[47] Eikerling et al.[48], Bazant et al.,[49] and Paddison and Coworkers.[50-51] Chapter 3 draws on work in the surface-science community from Karraker and Radke[52] to model interactions of ions at interfaces. Experimental analysis from Kusoglu et al.[53-57] and Kreuer et al.[58-59] provide the physical descriptions on which the model in Chapter 3 builds upon.

At the top of Figure 1-2, there is a cluster containing Chapter 4 (the node labeled Crothers 2020c) and studies on non-PFSA membranes systems. Chapter 4 draws on the fundamental PFSA literature (shown by is location close to right-side cluster), but incorporates thermodynamic analysis from the broader polyelectrolyte, hydrogels, and ionomer community. This includes thermodynamic models from Radke and Coworkers,[17, 60-61] Manning,[62] Kamcev et al.[16, 63-64], and Freger[65], among others. The macroscopic thermodynamic formulation in Chapter 4 follows the

methods of Guggenheim[30] and, for electrolytes, Newman.[9] The specific molecular thermodynamic formulations draw upon work by Prausnitz and Coworkers.[13, 66]

At the bottom of Figure 1-2, there is a cluster containing Chapter 5 (the node labeled Crothers 2020a) encompassing various transport-phenomena literature. To validate model predictions, Chapter 5 uses the extensive characterization of PFSA transport properties by Okada et al.[67-71] The formulation of the model follows a tradition coming from Pintuaro and Bennion,[72] Delacourt at al.,[32] Monroe et al.[73-75], Weber and Coworkers,[23-24, 33, 76-77] and Newman and Coworkers.[78-79]The work uses a concentrated-solution-theory framework articulated generally by Curtiss et al.[36, 80] and for electrolyte in particular by Newman and Thomas-Alyea.[9] Work from Krishna et al.,[81] Lightfoot et al.,[82-83] Wesselingh et al.,[84] and Chapman[85] inform the functional form for concentrated-solution-theory transport coefficients of electrolytes and species inside a membrane.

On the left side of Figure 1-2 there is a cluster of literature on RFBs that contains Chapter 6 (node labeled Crothers 2020b). This chapter draws upon membrane modeling by Darling et al.[11, 34, 86-87] and cell modeling by Knehr et al.[88-90], among many others. Experimental membrane characterization by Zawodzinski and Coworkers[91-94], Sing et al.[95], and Gandomi et al.[96] informs the scientific questions in Chapter 6.

Chapter 7 (citations from this Chapter are not included in Figure 1-2) uses paradigms from the porous-media field as summarized by Dullien.[37] Recent theory on electrokinetic coupling in porous media proposed by Mani et al.[97-98] was developed concurrently to this work.[99] Multicomponent effective medium theories in Chapter 7 were based on work from Bonilla et al,[100] following from the pioneering work by Kirkpatrick.[101]

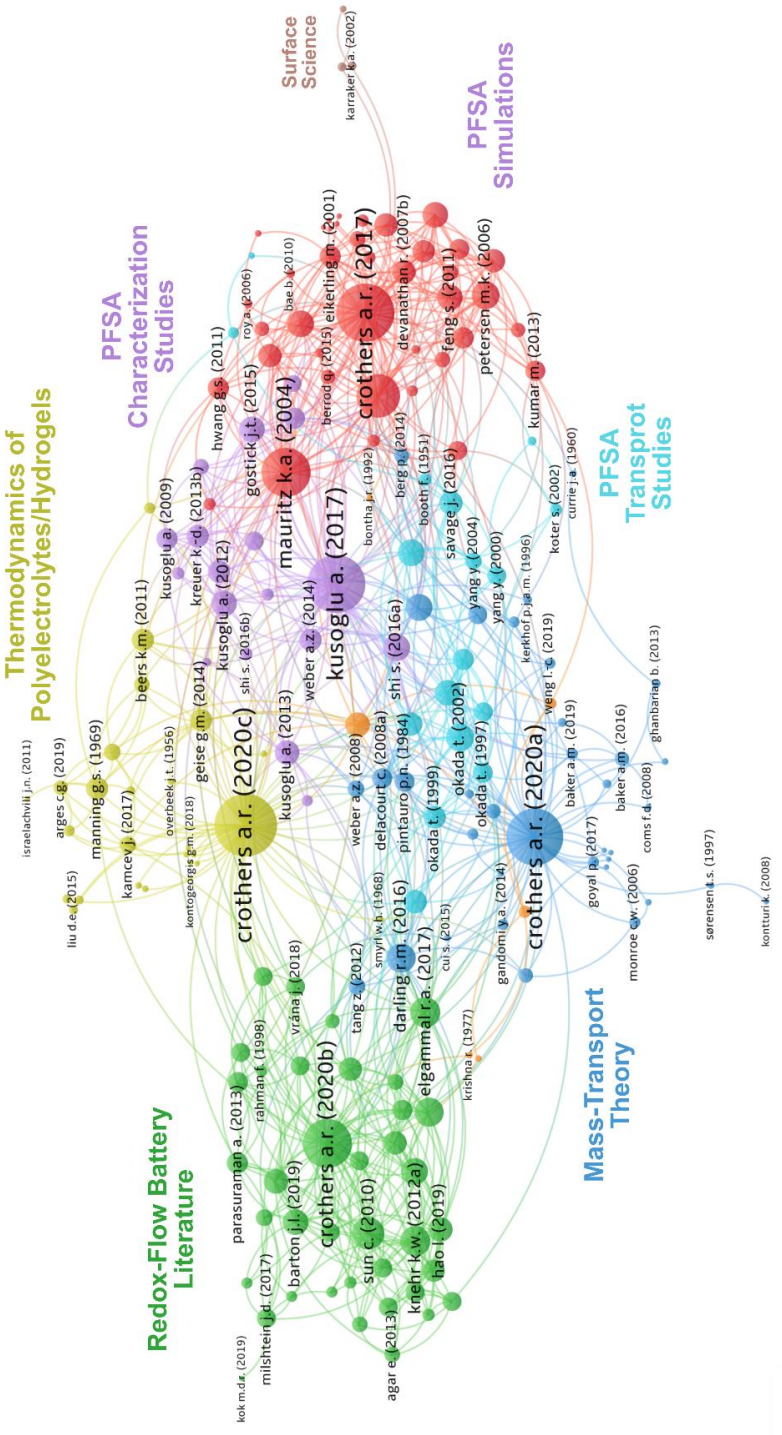

Figure 1-2. Cluster diagram of cited literature in this dissertation using VOSviewer.[38] Nodes (circles) denote papers cited with a line connecting the nodes if one paper cites the other. The size of the node is set by the number of connections it has. The nodes are arranged so that papers citing one another are clustered.

2 Transport Phenomena in Flow Battery Ion-conducting Membranes

2.1 Chapter Abstract

Selectively tuning ion transport through redox-flow-battery separators is a promising approach towards increasing cell capacity, power density, and, ultimately, economic feasibility. However, this process is complex with numerous forces and coupled molecular interactions driving and impacting transport under different operating regimes. A fundamental description of ion transport in flow-battery separators can guide development of new separators by identifying the nature of ion selectivity under given conditions. In this paper, we highlight different contributing factors of transport phenomena, explore how these factors influence cell performance, and the performance tradeoffs inherent in membrane design.[†]

2.2 Introduction

Transport through redox-flow-battery (RFB) separators is at the heart of various underlying issues affecting the long-term viability of RFB technology, especially under heavy duty cycles.[11, 34] This transport is intimately related to durability and performance issues ranging from capacity fade due to crossover of redox active species to low power density due to the high ionic resistance of the ion-conducting membrane.[35, 102-103] Current commercial ion-exchange membranes are optimized for fuel cells rather than RFBs, emphasizing the need for understanding transport under these disparate conditions.[12] In contrast to fuel cells, RFBs contain numerous ionic species that transport through the membrane, as shown in Figure 2-3. Therefore, approaches to improve cell and separator membrane performances are directed at improving ion selectivity, which is the ratio of favored species conductivity to undesirable species flux (*e.g.* H^+:VO^{2+} for a vanadium RFB). Improving membrane selectivity will reduce crossover, which is required to achieve the required multi-year operational longevity of RFB stacks, without introducing additional ionic resistance or complex rebalancing schemes that increase stack size and capital costs.[35, 87, 102-103] However, these two objectives are often interrelated, where decreased ionic resistance is generally followed by increased crossover of the redox active species and vice versa, creating a challenge for membrane development.

This paper briefly summarizes the complex phenomena of multi-ion transport through RFB separators and identifies key properties. We then show the practicality of using this fundamental analysis by linking separator transport properties to cell performance. The review concludes by exploring the property space accessible to current separator architectures and possible avenues to improvement.

[†] Published as Kushner, D. I. (equal contribution); Crothers, A. R. (equal contribution); Kusoglu, A.; Weber, A. Z., Transport phenomena in flow battery ion-conducting membranes. *Current Opinion in Electrochemistry* **2020,** *21*, 132-139.

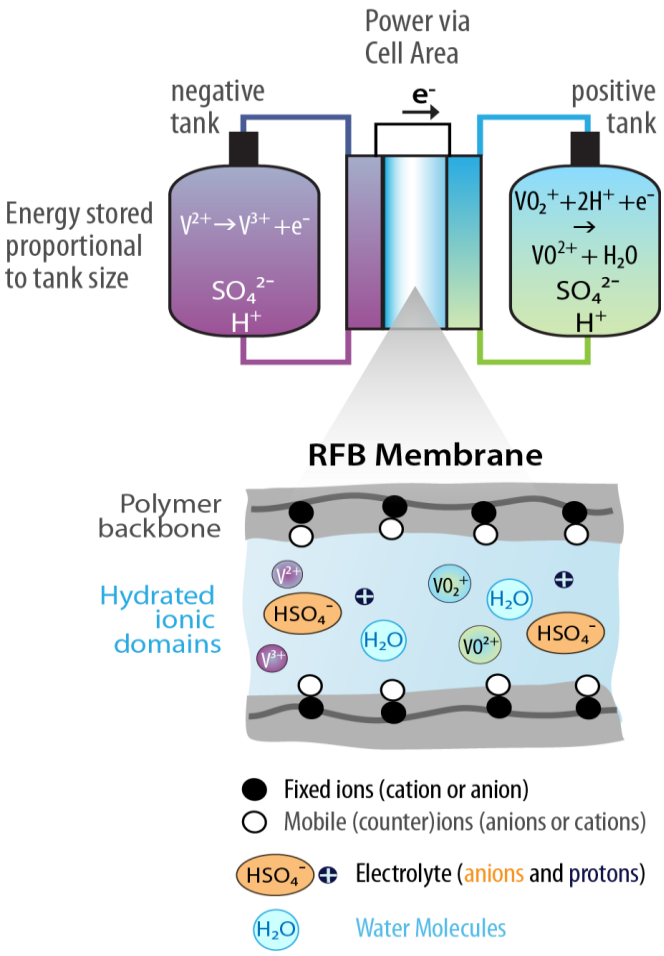

Figure 2-3. Schema of a vanadium redox flow battery with magnification into a generic membrane separator showing the multiple ions present in the membrane (note that the surface species can be charged or not, thereby explaining the lack of explicit electroneutrality in the schema).

2.3 Modes and Driving Forces for Transport

Ion transport through RFB membranes is driven by diffusion, convection, and migration.[86] The diffusive flux is characterized by the membrane permeability at zero current.[86] Migration occurs under an applied current that drives active ions in a particular direction, which flow in opposing or allied directions of diffusive flux.[86] Furthermore, because RFB electrolytes comprise of concentrated electrolytes (>1 M), numerous interactions involving the movement of any single ionic species depends on the concentration gradients of all other species present.[104] Mathematically, the flux of species i across the membrane (in 1-D, coordinate x) is[9, 31, 72, 104]

$$N_i = \frac{t_i}{z_i F} i + L_i^{\Pi} \frac{\partial \Pi}{\partial x} - L_i^{p} \frac{\partial p}{\partial x} - D_{ii} \frac{\partial c_{s/i}}{\partial x} - \sum_{s/j \neq 0, s/i} D_{ij} \frac{\partial c_{s/j}}{\partial x} \qquad 2\text{-}1$$

where Chapter 6 outlines the derivation of this equation. On the right side, the first term is due to migration where t_i is the transference number and z_i is the charge number of species i, F is Faraday's constant, and i is current density. The second term is due to flux from an osmotic pressure gradient where Π is the osmotic pressure and L_i^{Π} is the osmotic transport coefficient of i; the sign on this term is positive because water moves up its osmotic pressure gradient, convecting species i along with it. The third term is due to pressure gradients ($\partial p/\partial x$) driving flux of i proportional to the hydraulic pressure transport coefficient L_i^p. The fourth term is due to diffusion of i down the concentration gradient of its constituent neutral salt s/i ($\partial c_{s/i}/\partial x$) and proportional to the diffusion coefficient D_{ii}. The fifth term is due to cross-species diffusion in which the concentration gradients of salt species s/j ($\partial c_{s/j}/\partial x$) influence the flux of species i proportional to the diffusion coefficient D_{ij}; the sum is taken over salts. The osmotic pressure is proportional to the sum of species concentrations, $\Pi = \phi RT\sum \nu_i c_{s/i}$, where ϕ is the molar osmotic coefficient, R is the gas constant, T is absolute temperature, and $c_{s/i}$ is the concentration of a salt containing i that dissociates into ν_i ions.[30] The molar osmotic coefficient accounts for thermodynamic nonidealities of water.[30] The diffusion coefficients account for both how concentration gradients change the system free energy and the frictional interactions between species as they diffuse. Transport coefficients are defined with the membrane velocity as the frame of reference. The concentrations in Equation 2-1 can be defined as the external solution concentration (i.e. D_{ij} is a permeability), concentrations of i in the membrane defined on an interstitial basis (i.e. moles divided by water volume fraction) or superficial basis (i.e. moles divided by total membrane volume); any of these definitions is valid, although the accompanying transport coefficients take on different values depending on the definition of c_i. Figure 2-4a summarizes different modes of transport that are represented in Equation 2-1.

The second and fifth terms on the right side are rarely incorporated in RFB models and experimental analysis because they are negligible in dilute systems, from which the theories were adapted.[9, 86, 105-106] However, experiments in RFB-relevant conditions demonstrate that measured permeability depends on the nature of the concentration gradients species are diffusing against and the osmotic pressure gradients across the membrane.[91] This suggests that the cross-species diffusion and osmotic pressure-driven flow are relevant phenomena in RFBs. As a consequence, analysis that neglects the cross-species diffusion coefficients will be incomplete under different conditions.[9]

To illustrate why accounting for multiple driving forces may be important, Figure 2-4b shows the difference in concentration (i.e. driving force), or, in the case of water, $-\sum \nu_i c_i$, across the membrane of a typical vanadium-flow battery as a function of state of charge (SOC). During the cell discharge cycle from 100% to 0% SOC, the species ratio changes as $VO_2(SO_4)_{1/2}$ reduces to $VOSO_4$ and VSO_4 oxidizes to $V(SO_4)_{3/2}$, commonly referred to as V(V) or VO_2^+, V(IV) or VO^{2+}, V(II) or V^{2+}, and V(III) or V^{3+}, respectively. Concentration gradients then change, altering the driving forces in Equation 2-1. We assume the total sulfate ion concentration in each electrode is constant across SOC. Osmotic pressure drives species transport preferentially to the positive electrode and sulfuric-acid concentration gradient drives species to the negative electrode. Across multiple cycles and with electrolyte rebalancing, these gradients will change as will the corresponding fluxes. Accounting for the magnitude of cross-species diffusion and osmotic-driven flux is therefore essential to understanding cell performance and lifetime.

These driving forces are further complicated by their coupled nature. For example, water solvates dissociated ions, leading to multiple water molecules within the hydration shell of each ion. Ion diffusion due to concentration gradients transport water molecules across the membrane, leading to large electrolyte volume changes.[107] On-the-other-hand, osmotic pressure gradients find balance by driving water molecules across the membrane.[107] Osmotic pressure and water concentration imbalances in the cell are a large driving force and must also be accounted for when measuring species crossover. Although these multiple driving forces can be detrimental, engineering of RFB cells can take advantage of these additional transport couplings. For example, by balancing the osmotic pressure, gradients can be mitigated or beneficially imposed by using balancing salts,[87] draw solutes,[108] or countered by imposing hydraulic pressure gradients.[89-90, 109] However, these strategies may induce other complexities in the experiments if not properly accounted.

In addition to diffusion, Figure 2-4c shows the species flux, represented as a charge capacity loss, across a Nafion membrane separator with changing current for a vanadium flow battery using a simulated case by solving Equation 2-1 for $VOSO_4$ (V(IV)).[11, 86] Transport due to hydraulic pressure gradients are neglected in this analysis because of the relatively small pressure drop across the separator (~ 10 kPa).[109] The final term in Equation 2-1 has not been measured experimentally and, lacking a reasonable value, is neglected in this analysis. In the low-current-density regime, the flux is diffusion controlled due to the concentration and osmotic pressure gradient across the membrane. As the current density approaches 500 mA cm^{-2}, when the direction of current and diffusion are aligned, contributions from diffusion and migration to the flux are approximately equal, marking the point at which migration becomes the dominant crossover contribution.

As Figure 2-4c shows, knowing the values of transport coefficients in Equation 2-1 is essential for elucidating the magnitude of active species crossover and developing mitigation strategies. Unfortunately, diffusion coefficients D_{ij} and D_{ii} are challenging to measure.[12] If any osmotic or other concentration gradients are present in ex-situ measurements of ion permeability, the calculated diffusion coefficient will be a convolution of multiple D_{ij}'s, resulting in measurements that describe system-level properties rather than purely membrane properties.[91] Careful experimental design with systematic variations of the concentration gradients across the separator can isolate D_{ij}'s. Additionally, the thermodynamic nonidealities (*e.g.* the osmotic coefficient, ϕ) is unknown for many RFB systems. Quantifying these nonidealities is essential to predict the crossover of active species under different SOCs.

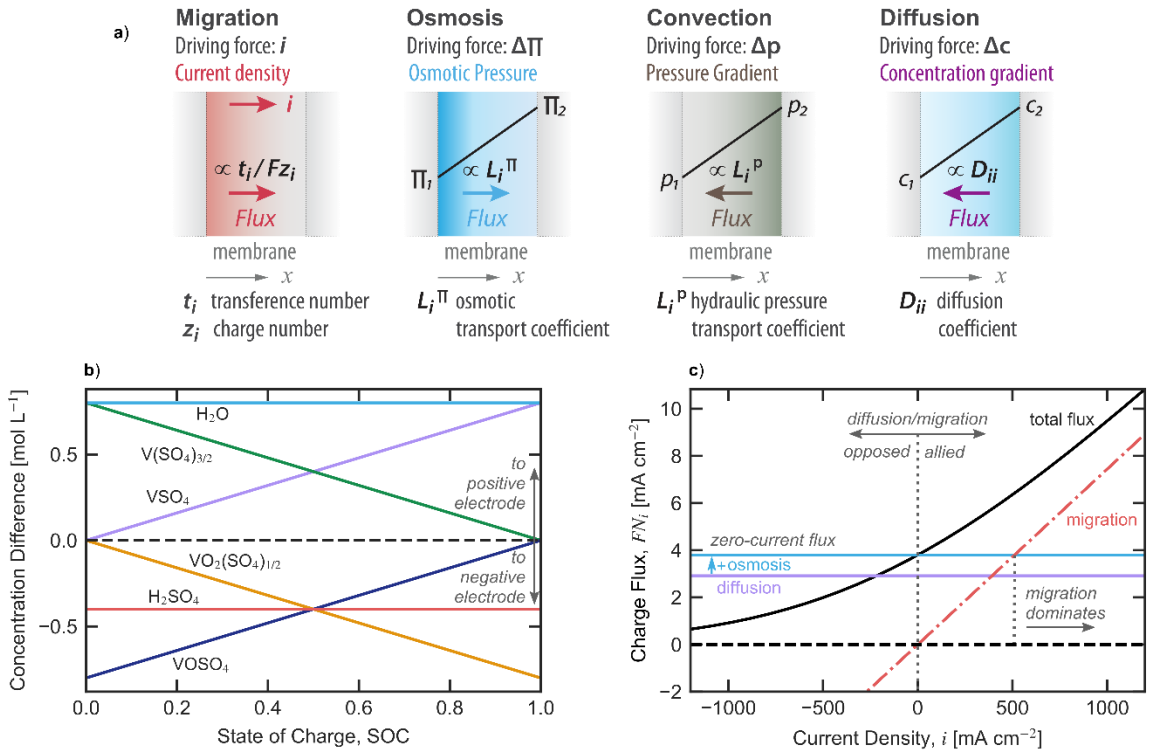

Figure 2-4. (a) Different contributing driving forces associated with the crossover of redox active species in RFBs. (b) Dynamic changes in concentration gradient driving forces as a function of state of charge for a vanadium redox flow battery and (c) the influence of current density on the charge flux of VO^{2+} (denoted IV) predicted from the solution to Equation 2-1 (where $t_{IV} = 0.015$, $D_{IV,IV} = 1.2$ x10^{-10} m^2 s^{-1}, $L_{IV}^{\Pi}\partial\Pi/\partial x$ = 1.6 x10^{-4} mol m^{-2} s^{-1}, $c_{IV}(x = 0)$ = 0.12 mol L^{-1}).

2.4 Coupled Membrane Conductivity/Crossover Tradeoffs

The flux described in Equation 2-1 directly impacts RFB performance. The overall performance of a cell can be described using energy efficiency and discharge power density, which are dependent on transport within the cell. Darling, et al. have established many of the relationships that are used for cell-level modeling through a series of publications.[11, 86, 110] The combination of Coulombic efficiency, ε_C, and voltaic efficiency, ε_V, which are related to the crossover, or total charge loss, of active species during cycling and the energy lost due to overpotential, respectively, describe the overall round-trip energy efficiency, ε_E ($=\varepsilon_C\varepsilon_V$). [11, 86]

The Coulombic efficiency can be approximated by[11, 86]

$$\varepsilon_C \approx \frac{i_d - i_x}{i_d + \tau i_x} \qquad 2\text{-}2$$

where i_d, i_x, and τ are the discharge current density, crossover current density, and charge/discharge time ratio, respectively. The crossover current density is related to the flux of all active species in the system and how the positive and negative electrode species react with each other (i.e. self-discharge reactions). For example, for a VRFB at the negative electrode, $i_x = F(2|N_V| + |N_{IV}| +$

$|N_{II}|$) where N_i is the flux of V(V), V(IV), and V(II) across the membrane.[11, 86] V(III) is omitted as it does not contribute to i_x. The coefficients accompanying the fluxes account for the stoichiometry of self-discharge reactions between active species.[11, 86] i_x links the fundamental description of flux in Equation 2-1 and the involved transport couplings to cell efficiency. At low current densities, i_x is only a function of species diffusion (denoted i_x^0) whereas high current densities, migration dominates giving, for VRFB $i_\mathrm{x} = t_\mathrm{x} i = (2t_\mathrm{V}/z_\mathrm{V} + t_\mathrm{IV}/z_\mathrm{IV} + t_\mathrm{II}/z_\mathrm{II})i$, where t_x is the crossover transference number. When migration dominates, ε_C is independent of current density and governed by activity-species transference numbers. Because i_x^0 is related to ion permeability, it is inversely related to membrane thickness, l_mem, whereas at high current densities, i_x is independent of l_mem. i_x^0 depends on separator transport coefficients (*e.g.* D_{ii}, L_i^Π, *etc.*) and the concentration and hydraulic gradients across the membrane.

The voltaic efficiency can be approximated by

$$\varepsilon_\mathrm{V} \approx \frac{U - i_\mathrm{d} R_\mathrm{cell}}{U + i_\mathrm{d} R_\mathrm{cell}} \qquad 2\text{-}3$$

where R_cell and U are the cell resistance and open-circuit potential, respectively. The numerator in Equation 2-3 is smaller than the denominator because the cell voltage is higher on charge than discharge due to various overpotentials.

Darling et al. measured the efficiencies for a N212 separator membrane, shown in Figure 2-5a with model (Equations 2-2 and 2-3) fits of the efficiency.[11, 86] The diffusional crossover is the greater contributor to the ε_C (*i.e.* $i_\mathrm{x} = i_\mathrm{x}^0$), which rises with increasing current density. As the current density approaches 200 mA cm^{-2}, the migration flux becomes the controlling contribution to ε_C (*i.e.* $i_\mathrm{x} = t_\mathrm{x} i$) and lessens the improvement with increasing current density. The switch between governing mechanisms of ε_C occurs when more redox-active species are transported between electrode by migration than by the flux without current (i.e. $i t_\mathrm{x} > i_\mathrm{x}^0$). A limiting case of ε_V is calculated using the resistance of only the cell hardware and with the membrane excluded, which follows Ohm's law.

Along with efficiency, the amount of power that can be deployed by the cell on discharge dictates its profitability. The area-specific discharge power density, Ψ_d, is the product of the cell potential and current density,

$$\Psi_\mathrm{d} = i_\mathrm{d}(U - i_\mathrm{d} R_\mathrm{cell}). \qquad 2\text{-}4$$

Figure 2-5b maps out the influence of crossover current density and cell resistance, which are primarily membrane properties, on the discharge power density with an energy efficiency of 80%. Cells operating at 80% energy efficiency with increasing resistance must use separator membranes with lower crossover current in order to maintain the high discharge power densities. As the crossover current falls below 1 mA cm^{-2}, the power density losses sensitivity to changing crossover current at a constant cell resistance.

The relationship between crossover current and membrane resistance can be further correlated by determining the number of cycles before 20% capacity loss has been incurred, which was a target metric for the previously funded IONICS project from ARPA-E.[111] Historically, membrane

thickness has been used to combat the crossover of active species, leading to higher resistance with increased cycle capability.[112] To maintain an energy efficiency of 80%, increases in cell resistance require crossover current reductions as shown in Figure 2-5b. This is largely due to the fact that the reduction in voltage efficiency requires higher Coulombic efficiency. Two cases of electrolyte treatment are used when determining the number of cycles to 20% capacity loss (i) electrolyte can be rebalanced (*i.e.* nondestructive) and (ii) redox species is unrecoverable (*i.e.* destructive) after crossover. Rebalancing leads to an order of magnitude increase in cycle number before 20% capacity fade is achieved.

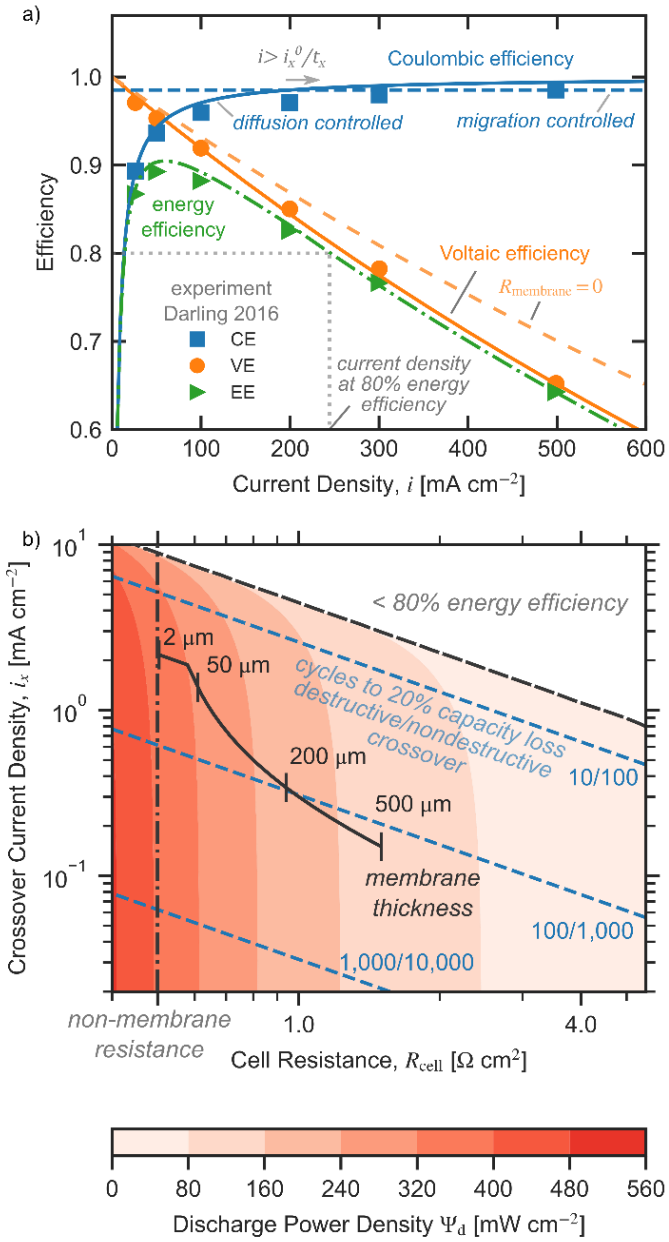

Figure 2-5. (a) Vanadium redox flow battery efficiency map. (b) Heat map of the peak power density regime at which the energy efficiency is 80% with changing crossover current and cell resistance. The black dashed line shows the crossover current density above which the RFB cannot achieve 80% energy efficiency. The vertical dash-dotted line is the non-membrane cell resistances, $R_{non-mem}$. The solid black line represents the transport properties of a N212 membrane ($i_x l_{mem} =$ 0.75 mA m^{-1}, $t_x = 0.0074$, $\kappa = 5$ S m^{-1})[11] with a simulated thickness of 2, 50, 200, and 500 µm in a vanadium redox flow battery system. The blue dashed lines represents the crossover current density and cell resistance at which the number of cycles represent the point of 20% capacity loss. (For these calculations, $U = 1.41$ V, $R_{non-mem} = 0.5$ Ω cm^2).

2.5 Tuning Membrane Selectivity Pathways

The cell resistance and crossover current can be tuned by changing κ and D_{ij}, L_i^{Π}, and other transport properties (see Equation 2-1). Polymeric membranes can be separated into the following classes (i) ion-exchange membranes (cation- = CEM, anion- = AEM) that rely on fixed charges for transport and (ii) porous membranes doped with electrolyte for facilitating transport. Similarly, these classes often favor either conductivity or crossover but this trade-off between the two properties that must be taken into account, as discussed earlier. Figure 2-6 summarizes reported data for polymeric membranes based on perfluorosulfonic acid (PFSA, a common CEM), polybenzimidazole (PBI, a common porous membrane), and other AEM and CEM hydrocarbon chemistries for vanadium RFBs. The normalized crossover current density as calculated using the Coulombic efficiency values using Equation 2-2, whereas the resistance is measured using an ex-situ or in-situ technique resulting in the scatter in the data for the same material.

Interestingly, while these polymer systems are quite diverse, the data sets occupy a region that aligns with a boundary of selectivity. The dotted line scales selectivity on the basis of the ratio of dilute-solution theory crossover current to conductivity

$$\frac{i_{\mathrm{x}} l_{\mathrm{M}}}{\kappa} = \frac{RT4c_{\mathrm{IV}}D_{\mathrm{IV}}}{F c_{\mathrm{H}} D_{\mathrm{H}}} \qquad 2\text{-}5$$

where c_{IV} is the concentration of vanadium IV at the positive electrode, D_{IV} is the vanadium diffusivity in solution (= 2 x 10^{-10} m^2 s^{-1}), c_{H} is the concentration of protons in the membrane (the ratio $c_{\mathrm{IV}}/c_{\mathrm{H}}$ = 0.024), and D_{H} is the diffusivity of protons in solution (= 9.3 x 10^{-9} m^2 s^{-1}). The success of this simple scaling relationship suggests that transport through these membranes relies on similar transport mechanisms, as shown in the Figure 2-6 cartoon. Because these membranes contain electrolyte within their structure or free-volume, the trend of transport through their conductive pathways follow a similar trend as their selectivity predicted by solution diffusion coefficients and a constant ratio of vanadium to proton uptake in the membrane

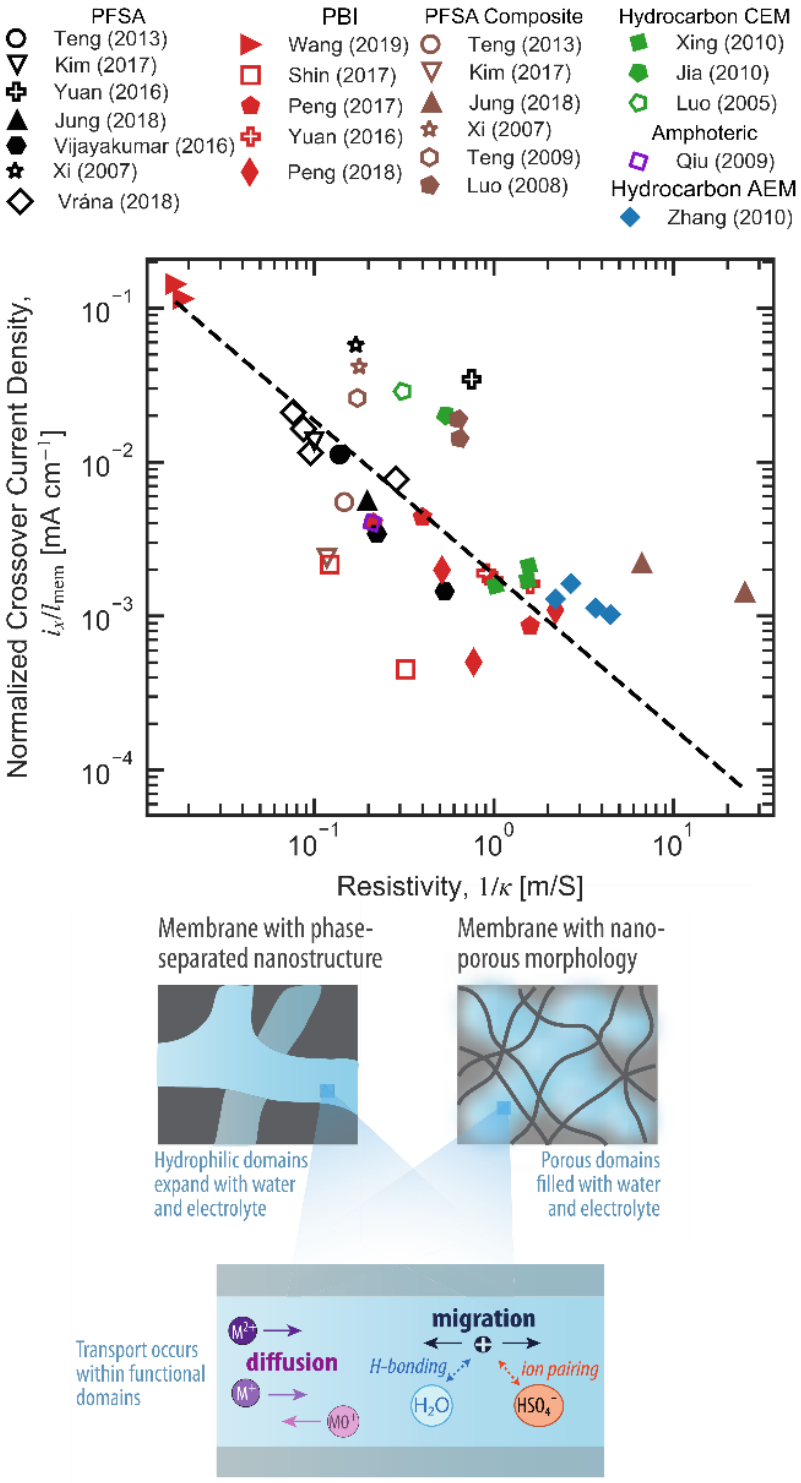

Figure 2-6. Membrane thickness-normalized crossover current for PFSA[113-119], PFSA-composite[113-115, 120], PBI[116, 121-124], and AEM[125] and CEM[126-130] hydrocarbon -based membranes used for vanadium redox flow batteries.

There are several active approaches for driving the selectivity of membranes towards more favorable regions (*i.e.* low crossover current and resistance). One approach is to change the transport coefficient or uptake of ions in the membrane. In particular, by making redox species that are much larger, such as organic species like quinones[131] and even larger redox active polymers[132]. Another approach involves controlling the membrane pore size to closely match the size of the redox species in order to take advantage of size exclusion, an area in which polymers of intrinsic porosity have started to successfully tune with pore sizes approaching 0.5 nm.[133-134] Inclusion of a fixed charge also promotes Donnan exclusion where repulsion of unwanted species occurs. For membranes like PFSAs that have relatively large channels filled with water, the electrolyte overcomes Donnan exclusion at electrolyte concentrations as low as 0.01 M.[135]

Beyond targeting membrane transport properties, new strategies can take advantage of the numerous driving forces for transport to mitigate crossover of active species. Crossover can be reduced by varying osmotic pressure gradients or introducing a spectator species to diffuse against the redox-active molecular. Further, targeted electrolyte rebalancing may reduce unfavorable osmotic pressure gradients and asymmetric charge/discharge cycles can beneficially align diffusion and migration. Transport is at the crux of both approaches and requires fundamental understanding of how new membranes and redox species respond in these environments to propel flow batteries as a technology.

2.6 Concluding Remarks

Understanding transport through the polymeric separators in mature and burgeoning redox-flow-battery technologies is essential for predicting and tuning system performance. Addressing the coupled nature of transport will be important going forward for membranes to push beyond the observed selectivity envelope. Membranes operating at high current density are more susceptible to migration fluxes, minimizing the effect of a diffusive flux, which emphasizes the need for more crossover studies at current rather than zero current. With this in mind, membranes with low resistance and low migration are required going forward. Lastly, while this paper used published data related to vanadium redox-flow batteries for insight, ion-transport correlations are adaptable to flow batteries as a technology and are essential as redox species and membranes continue being developed. In particular, one needs to understand and note these coupled phenomena in testing, validating, and designing materials, cells, and diagnostics.

3 Impact of Nano- and Mesoscales on Macroscopic Cation Conductivity in Perfluorinated-Sulfonic-Acid Membranes

3.1 Chapter Abstract

A mean-field local-density theory is outlined for ion transport in perfluorinated-sulfonic-acid (PFSA) membranes. A theory of molecular-level interactions predict nanodomain and macroscale conductivity. The effects of solvation, dielectric saturation, dispersion forces, image charge, finite size, and confinement are included in a physically consistent 3D-model domain geometry. Probability-distribution profiles of aqueous cation concentration at the domain-scale are in agreement with atomistic simulations using no explicit fitting parameters. Measured conductivities of lithium-, sodium-, and proton-form membranes with equivalent weights of 1100, 1000, and 825 g/mol(SO3) validate the macroscale predictions using a single-value mesoscopic fitting parameter. Cation electrostatic interactions with pendant sulfonate groups are the largest source of migration resistance at the domain-scale. Tortuosity of ionically conductive domains is the largest source of migration resistance at the macroscale. Our proposed transport model is consistent across multiple lengthscales. We provide a compelling methodology to guide material design and optimize performance in energy-conversion applications of PFSA membranes.[‡]

3.2 Introduction

Ion transport in cation-exchange membranes is fundamentally linked to the performance of a variety of burgeoning clean-energy technologies such as polymer-electrolyte fuel cells (PEFC).[136] A prototypical PEFC membrane consists of a phase-separated polymer with interconnected conductive, nanoscale, aqueous domains embedded in a nonconductive matrix that provides structural integrity and durability.[12, 18-19] Interactions between appended charged polymer groups and aqueous counterions cause ion-transport behavior in the aqueous domains to differ from that in bulk aqueous solution.[12, 18] To understand how molecular interactions among polymer, water, and ions at the nanoscale mediate transport at the macroscale, we formulate a multiscale mechanistic model for ion transport in fuel-cell membranes.

Perfluorinated-sulfonic-acid (PFSA) copolymers are the prototypical PEFC membrane material. PFSAs consist of a fluorocarbon backbone with perfluoroether sidechains that terminate in negatively charged sulfonate groups.[19] The sulfonate anion is charge compensated by an aqueous cation, such as a proton. Unfavorable interactions between the hydrophilic sulfonate moiety and the hydrophobic backbone cause the polymer to phase separate into solid polymer bundles and an interconnected network of ionically conductive, hydrophilic domains or "pores."[12, 18-19, 137]

Because the ionic conductivity of PFSA membranes increases drastically with water content, PEFC membranes typically operate under humidified conditions.[136] A wet environment leads to water absorption into the hydrophilic domains of the membrane with the subsequent water content

[‡] Published as Crothers, A. R.; Radke, C. J.; Weber, A. Z., Impact of Nano- and Mesoscales on Macroscopic Cation Conductivity in Perfluorinated-Sulfonic-Acid Membranes. *J. Phys. Chem. C* **2017,** *121* (51), 28262-28274.

described as the molar ratio of water per sulfonate site, λ (mole H_2O/mole SO_3^-).[12] Because the sulfonate anions are immobilized by covalent bonds to the polymer matrix, electrolyte conduction through the membrane is accomplished by movement of aqueous cations.[18]

The amount of absorbed water controls the degree to which the cation and the sulfonate group dissociate.[18, 28] Figure 3-1a depicts a completely dry PFSA domain in which the sulfonate group and cation form an ionically bound ion pair.[18, 28, 138] The proton exists as a hydronium cation since desorption of the constituent water molecule occurs only at extreme temperatures (>200 °C).[12] Figure 3-1b depicts water solvating the bound ions. At low water contents, there is not enough water to separate the ions; they remain as bound contact pairs.[18, 28, 138] Ions forming salt complexes or contact pairs are immobile and do not facilitate conduction.[138] Figure 3-1c depicts water completely solvating the ions at higher water contents allowing complete ion dissociation.[18, 28, 138]

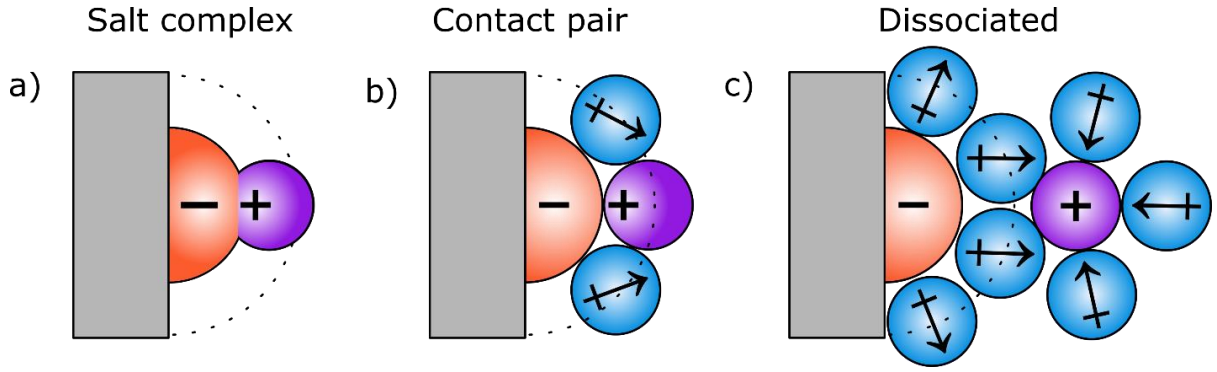

Figure 3-1. Depiction of the cation center of charge (+) and water dipole (↛) distributions around a pendant sulfonate group (–). Solid lines denote the hard-sphere radius. Dotted lines denote the first solvation shell of the sulfonate group. Grey region denote PFSA polymer. a) In completely dry conditions, the sulfonate ions and cations are tightly bound as salt complex. b) In low-water conditions, ions form contact pairs. c) In high-water conditions some of the ion pairs dissociate.

Water content increases conductivity because hydration dissociates ion pairs,[18, 27, 76, 139-144] increases the hydrophilic volume fraction of the polymer, [145-147] and decreases the tortuosity between domains. [48, 76, 147-150] Conversely, increasing water content otherwise decreases conductivity because the concentration of free aqueous cations is lower.[47, 146-147] Quantifying the relative contributions of these factors is challenging because they are all coupled to water content.[18, 44, 146] Research observations are often attributed to any one of these factors without considering the others.[18, 44, 147] The modeling approach herein elucidates these factors and their specific effects on measurable macroscale properties.

Molecular-dynamics (MD) and *ab-initio* simulations provide invaluable understanding of intermolecular interactions among polymer, solvent, and ions in the nanodomains, but often do not describe transport processes.[27, 42-43, 140, 142, 151-155] Conversely, microcontinuum models provide crucial insights into transport processes in the nanodomains, but current models have selective applicability to PEFC systems because they do not examine varying hydration[14, 156] or exclude relevant nanoscale interactions, such as solvation energies.[47, 139, 157-160] Both approaches often

focus on nanoscale properties without connection to macroscopic observables.[12] Our model is grounded in physical descriptions provided by microcontinuum theories and atomistic simulations but goes beyond previous work by giving a consistent mechanistic description within the nanodomains and at the mesoscale as a function of hydration.

To elucidate how molecular-level interactions among solvent, ions, and polymer matrix affect macroscopic properties, a quantitative model is developed for domain-scale physics of cation conduction in PFSA membranes. The approach includes molecular-scale interactions including finite-size, confinement, ion solvation, dielectric saturation, image charge, and dispersion forces. The proposed micro/macro-scale model is validated against both atomistic simulations[42, 152] and experimentally measured ion conductivity.[161] To ensure physical veracity, realistic geometric parameters are adopted from direct imaging of the PFSA membrane pore structure. The presence of mobile coins and multiple couterions is not considered, but the conductivity of fully ion-exchanged sodium and lithium-form membranes[54] are studied in addition to proton transport.

3.3 Theory

3.3.1 Physical Model

In PFSAs, the hydrophobic phase surrounds hydrophilic domains consisting of immobilized sulfonate groups, counterions, and absorbed water.[19] In the fully hydrated state ($\lambda \approx 20$), the hydrophilic domains are locally flat, ribbon-like channels with an average (mean) thickness of 0.85 nm and a width of 2.5 nm.[58, 137, 162]

Assuming a realistic physical representation of the aqueous nanodomains is imperative to provide a useful mathematical model. Figure 3-2 provides this representation. Solvent regions are completely phase separated from the polymer backbone and sidechains to form lamellar channels with appended ionized sulfonate groups. Hydrophilic sulfur and oxygen atoms of the sulfonate groups are coarse grained as hemispheres. Because neighboring sulfonate groups need not be attached to the same PFSA chain, the amount of backbone between sidechains does not dictate the spacing between sulfonates along the channel. Rather, the anion groups are uniformly distributed along the walls of the channel such that the distance between groups is maximal; electrostatic repulsion between sulfonate groups is minimized. Consequently, water swells the domain isotropically. This representation reduces the hydrophilic lamellar channel into repeating periodic cubic unit cells of dimension l.

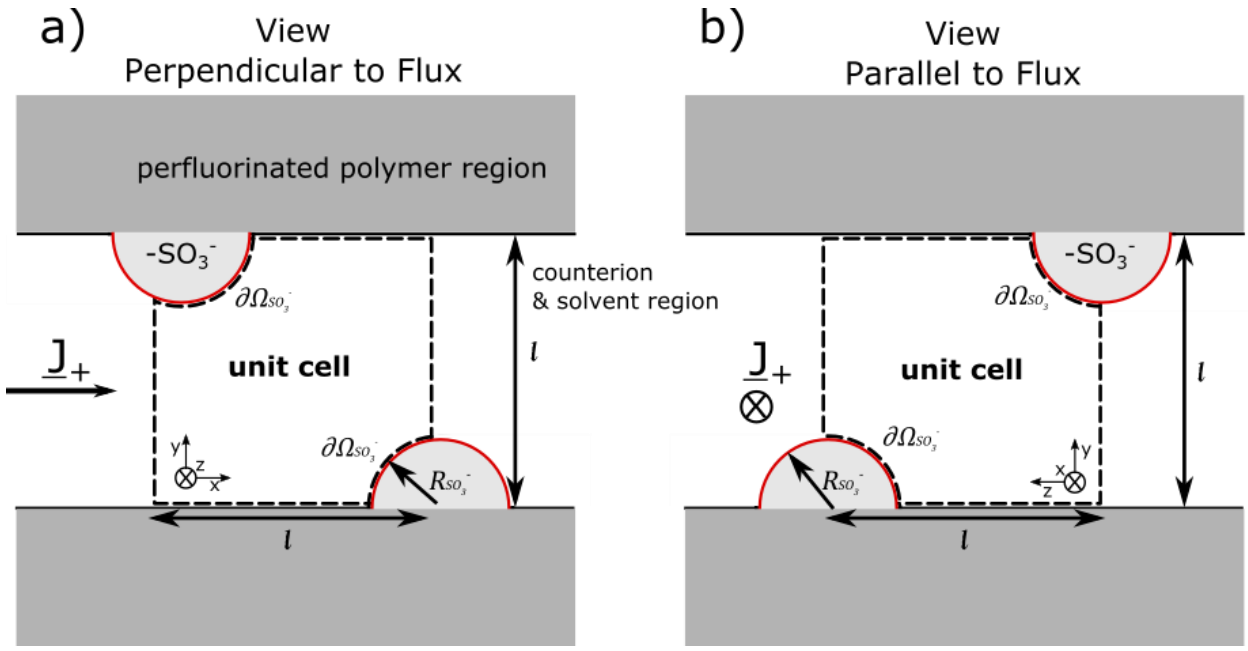

Figure 3-2. Schematic of the unit cell from (a) direction perpendicular to the direction of flow, i.e. x-y surface of unit cell, and from (b) direction parallel to the direction of cation flux, i.e. y-z surface. $\partial\Omega_{SO_3^-}$ denotes the surface of protruding sulfonate groups. See text for details of notation.

The volume of the aqueous-domain unit cell consists of a single cation of unhydrated radius R_+, λ water molecules each of volume V_w, and four quarters of a sulfonate group with radius $R_{SO_3^-}$ each at alternating corners of the cube. The λ water molecules include free waters and those solvating the ions. The unit cell is bounded by an insulating polymer ceiling and floor (i.e. in the y-direction) and mirrored periodic unit cells on each side (i.e. in the x- and z- directions). Channel thickness of the unit cell with λ = 20 [H_2O/SO_3] is 0.86 nm, close to that experimentally measured.[137, 162]

Water molecules and cations are internal to the system; sulfonate moieties and polymer matrix are external. The membrane is in equilibrium with external water vapor at the overall boundary of the membrane and does not exchange ions with the environment. The chemical potential of water is constant throughout the membrane. Cations are idealized as spheres; hydrated protons exist as hydronium ions.

3.3.2 Mathematical Model

3.3.2.1 Transport

Transport of cations along the channels is driven by an applied electrostatic potential difference $-\Delta\Phi$ in the *x*-direction. No net current flows in the *y*- and *z*-directions. The cross-section average current density $\langle i \rangle$ across a unit cell of the channel is proportional to the average applied electric field[9]

$$\langle i \rangle = \langle \kappa \rangle \left(-\frac{\Delta \Phi}{l} \right) \quad 3\text{-}1$$

where $\langle \kappa \rangle$ is the integrated conductivity of the unit cell. The average current density is obtained by averaging of the local current density $\underline{i}$ over a surface of the unit cell normal to the direction of transport. Because the sulfonate anion is immobile, the local current density is due only to the cation flux $\underline{J}_+$[9]

$$\underline{i} = -z_+ e \underline{J}_+ \quad 3\text{-}2$$

where z_+ is the valence of the cation, e is elementary charge, and underbars denote vectors. At constant pressure and temperature and negligible convection, the local flux $\underline{J}_+$of cations in the hydrophilic channels is driven by a gradient in the cation electrochemical potential $\tilde{\mu}_+$[36, 82]

$$\underline{J}_+(\underline{r}) = -\underline{\underline{u}}(\underline{r}) \cdot \rho_+(\underline{r}) \nabla \tilde{\mu}_+(\underline{r}) \quad 3\text{-}3$$

where $\underline{r}$ is the position vector inside the pore, ρ_+ is the local molecular concentration (i.e. time averaged probability density) of the cation, and $\underline{\underline{u}}$ is the anisotropic, diagonal cation mobility tensor. $\underline{\underline{u}}$ deviates from the scalar mobility in bulk solution, u_+^∞, due to hydrodynamic-drag tensor against the domain walls, $\underline{\underline{\beta}}$,[163-165] and increased viscosity of the liquid phase, η, around sulfonate groups due to dielectric friction (i.e. resistance of dipole rotation in an electrostatic field)[166] so that

$$\underline{\underline{u}}(\underline{r}) = u_+^\infty \underline{\underline{\beta}}(\underline{r}) \frac{\eta^\infty}{\eta(\underline{r})} \quad 3\text{-}4$$

where η^∞ is the viscosity of the pure solvent. Appendix 3-A discusses calculation of $\underline{\underline{\beta}}$. Einstein's law in the ideal dilute-solution limit (i.e. $\rho_+ \to 0$) relates cation mobility in bulk aqueous solution to conductivity, κ_+^∞ [167]

$$u_+^\infty = \frac{\kappa_+^\infty N_A}{e^2 z_+^2 \rho_+^\infty} \quad 3\text{-}5$$

where $\kappa_+^\infty / \rho_+^\infty$ is the molar cation conductivity at infinite dilution and N_A is Avogadro's number. Values of u_+^∞ for studied cations are in Table 3-1. Proton mobility given by Equation 3-5 includes both vehicular and Grotthus (i.e. proton hopping) contributions because proton conductivity at infinite dilution occurs by both mechnisms.[18]

Table 3-1. Cation parameters used in the study.

	H^+*	Li^+	Na^+
R_+ [Å]**	1.00	0.780	1.02
ΔG^∞ [kJ mol^{-1}]†	–432	-510	-411
ΔG^{sat} [kJ mol^{-1}]‡	-304	-387	-296
u_+^∞[s kg^{-1}] x 10^{-11} §	22.6	2.50	3.24
α [1E-24 cm^3] $^{/\!/}$	0.98	0.029	0.179
I [eV] $^{/\!/}$	12.62	5.391	5.139

* All properties based on a hydronium ion except u_+^∞, which is the dilute solution proton mobility.
** taken from Refs [45], [168] and [169]. † for liquid water $\varepsilon_b = 78$ at 298 K taken from Refs [170], [171], and [169].
‡ for liquid water calculated using Equation 23 in Ref [156], using the parameters listed in this.
§ for liquid water at 298 K taken from Ref [172].
$^{/\!/}$ taken from Refs [173] and [174].

At steady state, the divergence of the local flux is zero

$$-\nabla \cdot \underline{J}_+(\underline{r}) = 0 \qquad 3\text{-}6$$

Boundary conditions for Equation 3-6 are zero flux at the polymer floor and ceiling of the unit cell ($y = 0, l$), at the interface with the sulfonate groups, $\partial\Omega_{SO_3}$, and, because of symmetry, at the boundary of the neighboring cells that are parallel to the direction of transport ($z = 0, l$)

$$\nabla\tilde{\mu}_+(\underline{r}) = 0, \qquad \forall \underline{r} \in \partial\Omega_{SO_3^-}, y, z = 0, l \qquad 3\text{-}7$$

Boundary conditions at the upstream ($x = 0$) and downstream ($x = l$) boundaries are Dirichlet conditions of a fixed potential drop

$$\tilde{\mu}_+(\underline{r}) = \tilde{\mu}_+^{us}, \qquad \forall \underline{r} \in x = 0 \qquad 3\text{-}8$$
$$\tilde{\mu}_+(\underline{r}) = \tilde{\mu}_+^{us} - e\Delta\Phi\,, \qquad \forall \underline{r} \in x = l$$

where $\tilde{\mu}_+^{us}$ is a reference upstream electrochemical potential. $\Delta\Phi$ is set to an applied potential of 10^{-8} V (equivalent to an electric field of 116 V m^{-1} for a unit cell with $\lambda = 20$), which is small enough to ensure linearity of the flux with respect to the applied potential but large enough for numerical precision.

3.3.2.2 Thermodynamics

Numerous molecular interactions in the PFSA aqueous domains dictate the distribution of the cation throughout the channel, including electrostatic interactions between the sulfonate and cation, solvation forces, dispersion and image-charge forces at the interface between the solvent and hydrophobic polymer walls and thermal entropy. Interactions are expressed through the electrochemical potential of the cation, $\tilde{\mu}_+$,

$$\tilde{\mu}_+(\underline{r}) = \tilde{\mu}_+^0 + k_B T \ln \rho_+(\underline{r}) + z_+ e\Phi(\underline{r}) + \mu_{\text{fs}}(\underline{r}) + \mu_{\text{solv}}(\underline{r}) + \mu_{\text{dsp}}(\underline{r}) + \mu_{\text{img}}(\underline{r}) \quad 3\text{-}9$$

where $\tilde{\mu}_+^0$ is the reference electrochemical potential of the cation, k_{B} is the Boltzmann constant, T is absolute temperature, Φ is ionic potential, and μ_{fs}, μ_{solv}, μ_{dsp}, and μ_{img} are the excess chemical potentials (i.e. excess free energies) due to ion finite-size, solvation, dispersion, and image charge, respectively. The first two terms in Equation 3-9 describe ideal-solution behavior, whereas the third term characterizes electrostatics. The final four terms account for ion non-idealities. Each term, except the reference chemical potential, is a function of position inside the pore.

μ_{fs} accounts for the entropy loss by excluding water from regions with high ion concentrations. It is expressed with the widely used local-density Bickermann equation[49, 175]

$$\mu_{\text{fs}}(\underline{r}) = -k_{\text{B}} T \ln\left(1 - \frac{4}{3}\pi a^3 \rho_+(\underline{r})\right) \quad 3\text{-}10$$

where a is a finite-size parameter. Equation 3-10 is valid for lattice systems in which the solvent and ion have equal radii. When the ion and solvent are of different size, the choice of a is unclear. The results are relatively insensitive to the choice of a, and here a is set equal to the radius of a water molecule.

Cation-solvation excess chemical potential, μ_{solv}, accounts for the change in solvent potential energy due to dipoles orienting around the cation. Relative permittivity, ε, gauges the amount that dipoles can orient around a cation. Permittivity is extremely heterogeneous across a PFSA membrane nanodomain. Water solvating the sulfonate groups is dielectrically saturated ($\varepsilon = 1.8$) but water separated from the ions has a permittivity of bulk water ($\varepsilon = 78.3$).[139, 156] Relative permittivity of the polymer backbone is 2.1.[176] The dependence of solvent permittivity on $\underline{r}$ is discussed in the next section. Solvation excess chemical potential at $\underline{r}$ is equal to the work to discharge a cation in a reference dielectric plus the work of charging the cation in a dielectric at $\underline{r}$[169]

$$\mu_{solv} = \int_V dV \int_0^D \frac{D}{\varepsilon \varepsilon_0} - \frac{D}{\varepsilon^\infty \varepsilon_0} dD \quad 3\text{-}11$$

where V is volume, D is the displacement field of the cation ($D = z_+ e / 4\pi r_+^2$), ε_0 is vacuum permittivity, and ε^∞ is the relative permittivity of bulk water, which is the reference dielectric. For a medium in which the permittivity varies slowly over space, the integral with respect to the displacement field was accurately approximated by Bontha and Pintauro as[156]

$$\mu_{\text{solv}}(\underline{r}) = -\int_0^{2\pi} d\theta \int_0^{\pi} d\psi \int_{R_+}^{\infty} dr_+(\underline{r}) \frac{A}{r_+^2(\underline{r})} \left(\frac{1}{\varepsilon(\underline{r})} - \frac{1}{\varepsilon^\infty}\right) \quad 3\text{-}12$$

where θ and ψ are spherical angular coordinates, r_+ is the distance to the center of the cation, R_+ is the radius of the cation, and A is a constant. The value of A is determined by interpolating between the solvation free energy in bulk solution, ΔG^∞, and the solvation free energy in a dielectrically saturated solution, ΔG^{sat},

$$A = \frac{R_+}{4\pi}\left(\frac{\Delta G^{\mathrm{sat}} - \Delta G^{\infty}}{\frac{1}{\varepsilon^{\mathrm{sat}}} - \frac{1}{\varepsilon^{\infty}}}\right) \tag{3-13}$$

where $\varepsilon^{\mathrm{sat}}$ is the relative permittivity of a dielectrically saturated solvent. Values of ΔG^{∞} and ΔG^{sat} for different cations are in Table 3-1. The forms of Equations 3-12 and 3-13 are the same as those given by Bontha and Pintauro[156] except that we explicitly integrate over the volume rather than assume permittivity varies slowly over space. Equation 3-12 reduces to the solvation excess chemical potential given by Bontha and Pintauro[156] in the limit of $\nabla\varepsilon = 0$. To avoid simultaneously solving Equations 3-3, 3-6, 3-9, and 3-12, which is a set of coupled integral-differential equations, we approximate μ_{solv} as the linear superposition of the solvation excess chemical potentials due to interactions with the PTFE floor and ceiling of the unit cell, which is only a function of the distance to the boundaries, d_y, and interactions with the sulfonate group, which is only a function of distance to the groups, $d_{SO_3^-}$ as discussed in

Appendix 3-B.

Solvation free energies account for polarization of permanent dipoles whereas van der Waals forces account for induced oscillating polarization of atoms. The dispersion force on a cation is the difference in van der Waals forces acting on a cation from water and from the PTFE polymer walls. The excess chemical potential accounting for dispersion forces, μ_{dsp}, is thus[52]

$$\mu_{\mathrm{dsp}}(\underline{r}) = \frac{B}{y^3} + \frac{B}{(1-y)^3} \tag{3-14}$$

where

$$B = \frac{\pi\alpha_+ I_+}{4}\left(\frac{\rho_{\mathrm{w}}\alpha_{\mathrm{w}} I_{\mathrm{w}}}{I_+ + I_{\mathrm{w}}} - \frac{\rho_{\mathrm{T}}\alpha_{\mathrm{T}} I_{\mathrm{T}}}{I_+ + I_{\mathrm{T}}}\right) \tag{3-15}$$

and α, $I$and $\bar{\rho}$ are the diamagnetic polarizability, first ionization potential, and molecular density. Subscripts $+$, w, and T denote the cation, water, and PTFE, respectively. Values of α and I for studied cations are in Table 3-1. Equation 3-14 superimposes dispersion forces arising from the unit-cell floor and ceiling (first and second terms, respectively).

μ_{img} accounts for electrostatic interactions felt by an ion near the interface between two media with different dielectric constants. For the case of an aqueous ion adjacent to a water/PTFE interface, the method of image charges and Coulomb's law gives μ_{img} as[177]

$$\mu_{\mathrm{img}}(\underline{r}) = \left(\frac{\varepsilon^{\infty} - \varepsilon_{\mathrm{T}}}{\varepsilon^{\infty} + \varepsilon_{\mathrm{T}}}\right)\frac{e^2 z_+^2}{16\pi\varepsilon^{\infty}\varepsilon_0}\left(\frac{1}{y} + \frac{1}{l-y}\right) \tag{3-16}$$

Figure 3-3 shows the excess chemical potential of solvation, dispersion, and image charges as a function distance from a wall (or sulfonate group for $\mu_{\mathrm{solv}}^{SO_3^-}$). Solvation forces are the dominant excess free energy. Beyond 0.6 nm from the walls, all excess chemical potentials are relatively small.

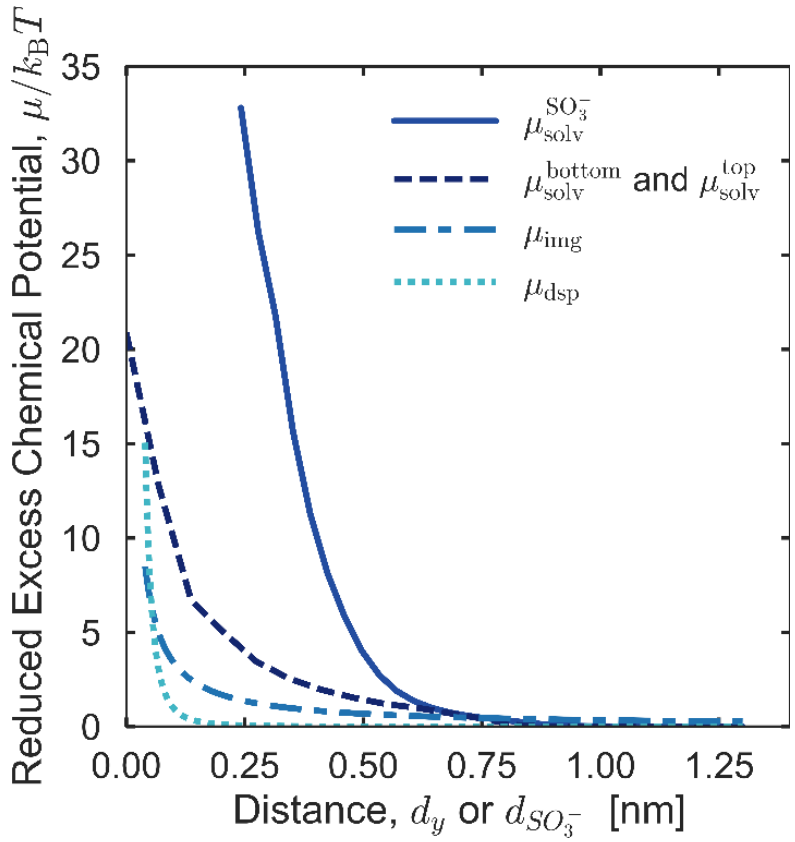

Figure 3-3. Excess hydronium chemical potentials $\mu_{\text{solv}}^{\text{bottom}}$ and $\mu_{\text{solv}}^{\text{top}}$ (dashed line), μ_{dsp} (dotted line), and μ_{img} (dash-dotted line) as a function of distance from the polymer wall and $\mu_{\text{solv}}^{\text{SO}_3^-}$ (solid line) as a function of distance from a sulfonate group.

3.3.2.3 Ionic Potential

Poisson's equation is necessary to close the above system of equations

$$\nabla \cdot \varepsilon(\underline{r})\nabla\Phi(\underline{r}) = -\frac{e}{\varepsilon_0} z_+ \rho_+(\underline{r}) \qquad 3\text{-}17$$

The strong electric field due to the charged sulfonate groups[178] and disruption of the hydrogen-bond network of water due to wall proximity[179] creates variations in ε across the unit-cell domain. Booth's equation describes how the relative permittivity saturates with increased electric field[178, 180]

$$\varepsilon(\underline{r}) = n^2 + \frac{3\left(\varepsilon^{\text{con}}(\underline{r}) - n^2\right)}{\gamma|\nabla\Phi(\underline{r})|}\left[\frac{1}{\tanh[\gamma|\nabla\Phi(\underline{r})|]} - \frac{1}{\gamma|\nabla\Phi(\underline{r})|}\right] \qquad 3\text{-}18$$

where

$$\gamma = \left(\frac{5p}{2k_B T}\right)(n^2 + 2),$$

n is the bulk refractive index of water, p is the water dipole moment, and $\varepsilon^{\mathrm{con}}$ is the relative water permittivity before an electric field is applied. $\varepsilon^{\mathrm{con}}$ is reduced from bulk-water permittivity because the polymer walls disrupt the hydrogen-bonding network of water that causes the high permittivity of bulk water.[179] Water coordinates with neighboring water molecules forming a cluster of radius $R^{\infty}_{\mathrm{cluster}}$.[181] At a phase boundary, water coordination is disrupted reducing the cluster radius to R_{cluster}.[181] Decreased cluster size reduces permittivity.[181] Lamm et al.[179] show that at 298 K the effect of water confinement on relative permittivity is well approximated as

$$\varepsilon^{\mathrm{con}}(\underline{r}) = 17.5\left(1 + 1.7f(\underline{r})^{\frac{1}{6}} + 0.5f(\underline{r})^{\frac{1}{3}} + f(\underline{r}) + 0.24f(\underline{r})^{\frac{1}{2}}\right) + 0.8 \qquad 3\text{-}19$$

where $f = (R_{\mathrm{cluster}}/R^{\infty}_{\mathrm{cluster}})^{\frac{1}{3}}$. Appendix 3-B details calculation of f.

Boundary conditions for Equation 3-17 are

$$\underline{n} \cdot \varepsilon_0 \varepsilon(\underline{r}) \nabla\Phi(\underline{r}) = \begin{cases} 0, & y, z = 0, l \\ \sigma_-, & \underline{r} \in \partial\Omega_{SO_3^-} \\ -\underline{n} \cdot \varepsilon_0 \varepsilon(\underline{r}) \nabla\Phi(\underline{r})\big|_{x=0}, & x = l \end{cases} \qquad 3\text{-}20$$

and

$$\Phi(\bar{r}) = \Phi(\bar{r})|_{x=0} - \Delta\Phi, \qquad x = l \qquad 3\text{-}21$$

where $\underline{n}$ is the unit normal vector to the boundary and σ_- is the charge density on the sulfonate group assuming that the negative charge distributes uniformly on the surface of the representative hemisphere, $\sigma_- = e/(2\pi R_{SO_3^-})$. The first boundary condition specifies zero current through the insulating polymer and perpendicular to the channel. The second condition is Gauss's law accounting for the charge of the sulfonate groups. Third and fourth boundary conditions impose periodicity of the unit cells. Because neighboring unit cells are the mirror images of each other, the boundary conditions are similarly mirrored at the boundaries (e.g. the lower-right corner of the downstream boundary in Figure 3-2a maps to the upper-left corner of the upstream boundary). Figure 3-12 in Chapter 3 Supporting Information (SI-3) displays boundary conditions.

3.3.3 Numerical Method

Equations 3-6, 3-9, and 3-17 were solved simultaneously using COMSOL Multiphysics 5.1 (COMSOL, Inc., Palo Alto, CA) on the 3-D geometry portrayed in Figure 3-2. The mesh consisted of tetrahedrals with triangular elements at the boundaries. 30,153 to 23,893 domain elements were used with 2,680 to 2,558 boundary elements; the number of elements increased with increasing water content. Resulting 173,996 to 138,148 degrees of freedom for the coupled physics were solved using the MUMPS general solver using Newton-Raphson iteration to resolve nonlinearities. Convergence was achieved for a relative tolerance of $1\text{x}10^{-8}$.

3.4 Results and Discussion

3.4.1 Nanoscale Physics

3.4.1.1 Aqueous Domain Free Energies

The negatively charged sulfonic acid groups impose strong electrostatic fields throughout the unit cell. Figure 3-4 and Figure 3-13 in SI-3 show 2D intensity maps on the x-y surface of the unit cell to illustrate the impact of the resulting field. Figure 3-13a shows the electrostatic field leads to a sharp decline in ionic potential near the sulfonate groups. Figure 3-4a shows that near the sulfonate groups the electrostatic field combined with wall confinement disrupts the bonding structure of water resulting in a lower relative permittivity than that of bulk water (i.e. ~78). The strong electric field orients the water surrounding the sulfonate groups causing dielectric saturation of the water that is solvating the sulfonates. Conversely, water near the center of the channel exhibits bulk-like permittivity.

Figure 3-4b shows the cation concentration, ρ_+ (normalized by the average cation concentration in the unit cell, $\rho_+^0 = 1/V_{\mathrm{tot}}$, where V_{tot} is the unit-cell volume). Figure 3-5 shows the cation concentration between two adjacent sulfonate groups at $\lambda = 9$ (solid line) and $\lambda = 4$ (dot-dashed line). Cations are distributed throughout the channel with the highest concentrations near the surface of the sulfonate groups and near the midpoints between groups. By plotting the electrostatic and solvation free energies (dashed and dotted lines for $\lambda = 9$ and 4, respectively), Figure 3-5 shows that the distribution of cations in the channel is due to competition between electrostatic and solvation forces resulting in a balance of free energies, consistent with the work of Pintauro and coworkers.[156] Electrostatic free energy is most favorable when aqueous cations are close to the negatively charged sulfonate groups. Conversely, solvation free energy is most favorable when aqueous cations are outside the solvation shell of the sulfonate groups. The strong electrostatic fields of the sulfonate group cause cations within the solvation shell of the sulfonates to dehydrate partially. At low water contents, there is insufficient water to hydrate the cations fully, which decreases the solvation energy at the center of the channel, and results in the dominance of electrostatic interactions. Figure 3-14 in SI-3 shows that as water content decreases, the free energy balances from solvation to electrostatic and increases the fraction of cations associated with sulfonate groups. The predicted fraction of cations associated with sulfonate groups shows excellent agreement with atomistic simulations.[42-43, 152]

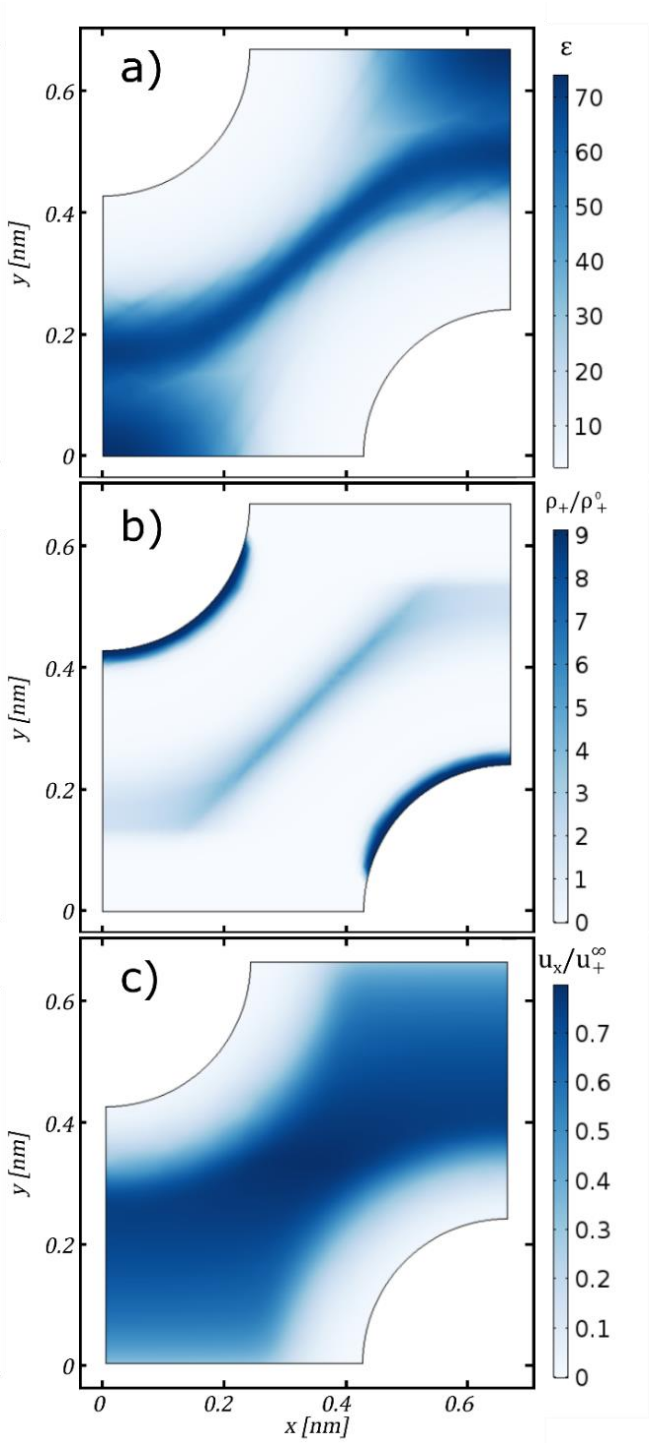

Figure 3-4. 2D intensity map of the x-y surface of the unit cell for protonated membrane at λ = 9 [H_2O/SO_3] of (a) water relative permittivity, ε, (b) hydronium probability density normalized by the average unit cell probability density, ρ_+/ρ_+^0, and (c) the x-component of hydronium mobility, reported as u_x/u_+^∞, colored from white (light) to blue (dark) to represent low to high values.

Figure 3-6 shows that the radial distribution function (RDF) of the cation with respect to the center of the sulfonate group displays three peaks, also consistent with molecular dynamics simulations.[152] SI-3 gives details of the RDF calculation. The first peak, located at 2.4 Å, is caused by partially desolvated cations that form contact-ion pairs with the sulfonate groups (Inset a). The second peak located near 4-6 Å is caused by solvated cations that separate from the sulfonate groups and reside near the center of the channel (Inset b). The third peak, near 5.5-9 Å, arises from cations that form ion pairs with opposing sulfonate groups (Inset c).

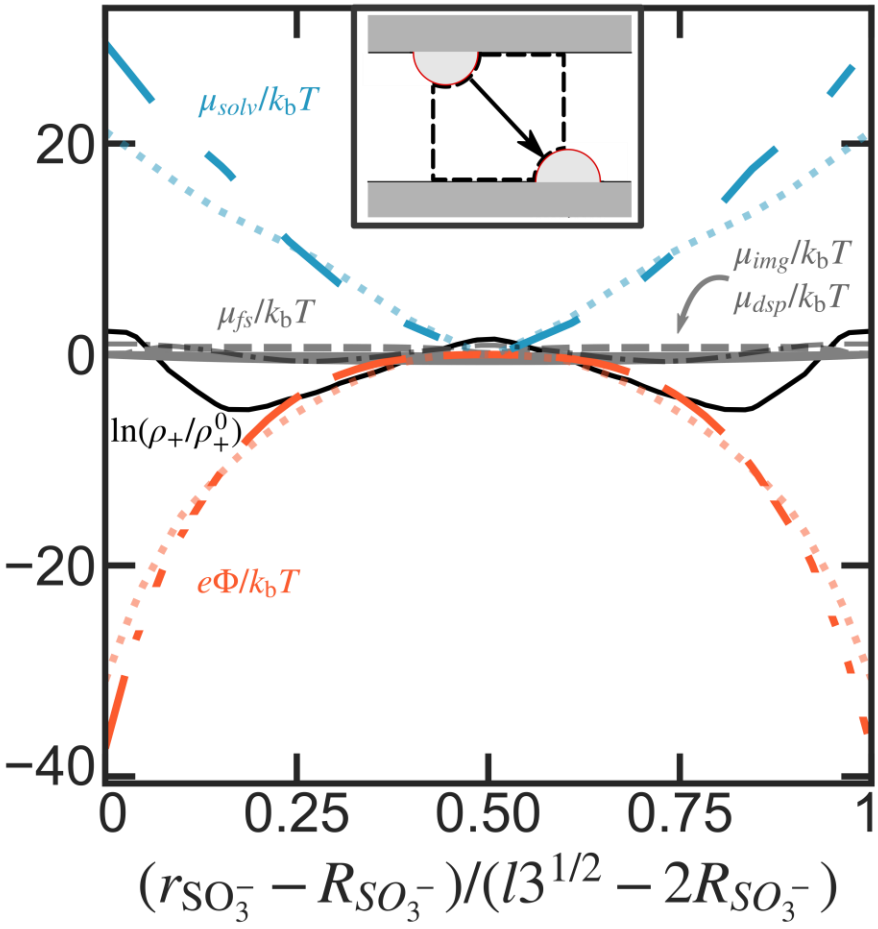

Figure 3-5. $\ln(\rho_+/\rho_+^0)$ (denoted solid and dot-dashed lines), $e\Phi/k_bT$ (denoted dashed and dotted lines), and μ/k_bT (denoted solid lines for image charge, dispersion and finite size effects and dashed and dotted lines for solvation) terms evaluated on a diagonal between two opposing sulfonate groups across the bottom of the unit cell at $\lambda = 9$ and 4 [H2O/SO3], respectively, for a protonated membrane. The distance is normalized between 0 and 1. The insert is a simplification of Figure 3-2a with an arrow indicating the diagonal between the opposing sulfonate groups. μ_{ex} terms are referenced to the midpoint between the opposing sulfonate groups.

Positions of the second and third peaks of the RDF in Figure 3-6 shift depending on membrane water content. As water content decreases from $\lambda = 15$ (solid line) to $\lambda = 9$ (dashed line) and $\lambda =$

4 (dotted line), the unit cell shrinks; the distance between sulfonate groups decreases. The distance between a sulfonate group and cation contact pairs of opposing sulfonate groups decreases; the third RDF peak shifts inward. Similarly, as water content decreases, the distance between a sulfonate group and the center of the channel decreases causing the second RDF peak to shift inward. The radial distribution function specifies cation distribution to the furthest extent of the cubic unit cell (i.e. $3^{1/2}l$).

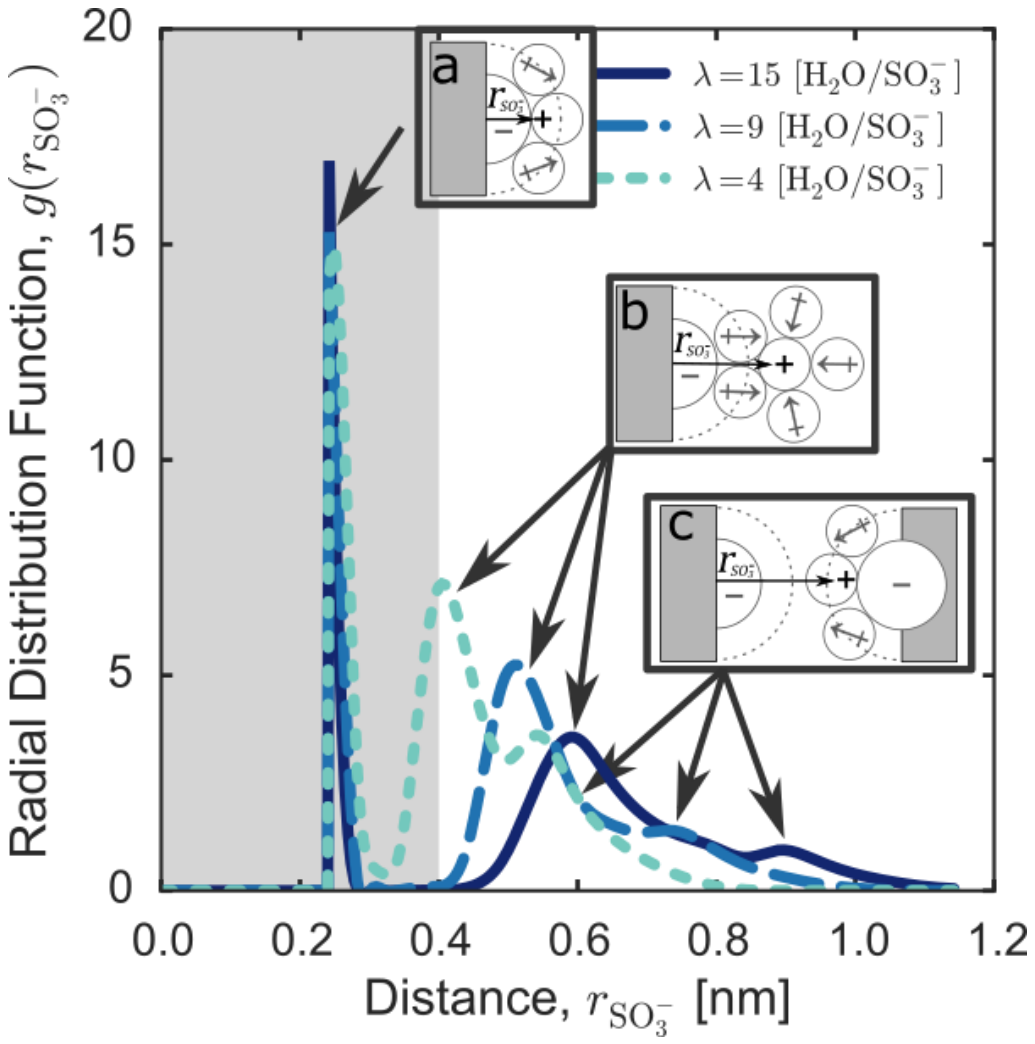

Figure 3-6. Hydronium RDF with respect to the center of a sulfonate group at water content of λ = 4 (dotted line), 9 (dashed line), and 15 [H_2O/SO_3] (solid line) for an 1100 EW membrane. The region shaded dark grey locates the first solvation shell of sulfonate. Schematic inserts depict the water dipole structure (↛) around the aqueous cation center of charge (+) with respect to a sulfonate group (–) for each peak in the RDF; solid lines denote the hard-sphere radius of the species, dotted lines denote the first solvation shell of the sulfonate group. Arrows indicate the distance $r_{SO_3^-}$. Grey region denotes the polymer. Only water dipoles solvating the cation are shown.

3.4.1.2 Aqueous Domain Transport

The strong electrostatic fields around the negatively charged sulfonate groups increases water viscosity due to dielectric friction, as Figure 3-13b in SI-3 shows. Viscosified water corresponds to water molecules that solvate the sulfonate groups. Conversely, water near the center of the channel is more bulk-like. This is qualitatively consistent with prior work of Yang and Pintauro[14, 46], but they attributed increased solvent viscosity directly to ion concentration effects. Figure 3-4c illustrates that increased water viscosity combined with increased hydrodynamic drag near the walls significantly reduces aqueous cation mobility throughout the channel. Decreased mobility near the walls causes the local conductivity to be maximum near center of the channel, as Figure 3-13c in SI-3 shows. Cation conductivity is facilitated by solvated cations transporting along the center of the channel.

Figure 3-7 shows unit-cell conductivity as a function of water content. Ideal-solution conductivity at the average concentration of the unit cell, κ_+^∞ (dotted line), decreases with increasing water content because water dilutes the number of charge carriers. Dielectric friction caused by the electric field emanating from the sulfonate groups reduces conductivity (dashed line, calculated using Equation 3-3 with $\underline{\underline{u}} = \underline{\underline{I}} u_+^\infty \eta/\eta^\infty$ where $\underline{\underline{I}}$ is the identity tensor). There is a maximum in the dielectric friction-corrected cation conductivity at $\lambda = 4$ because below this water content increasing water content decreases the fraction of immobile, bound cations, which increases conductivity. Above this water content, dilution effects dominate and conductivity decreases with increasing water content. Average domain conductivity, $\langle\kappa\rangle$, includes the resistance from the hydrodynamic drag on the cations due to confinement (solid line, calculated using Equation 3-3 with $\underline{\underline{u}}$ given by Equation 3-4). Nanoscale factors reduce conductivity from the ideal-solution limit the most at low water contents. The resulting domain conductivity changes relatively little with water content (~26% difference between the smallest and largest values of $\langle\kappa\rangle$ versus ~520% difference for κ_+^∞). Figure 3-15 shows that although nanoscale resistance depends on water content, it is relatively insensitive to how the domains swell (anisotropic vs. isotropic swelling).

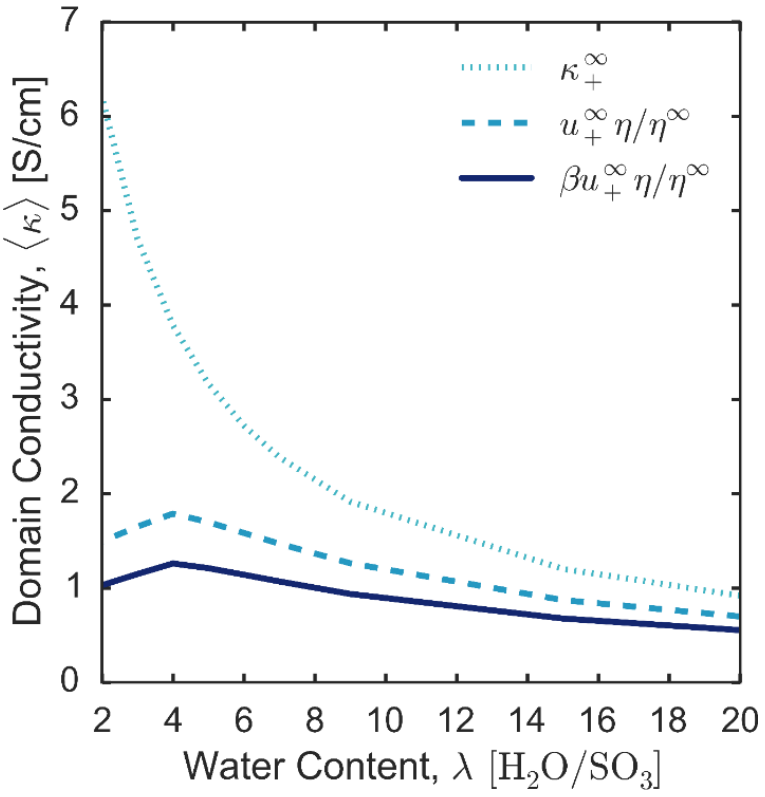

Figure 3-7. Average hydronium conductivity in a domain, $\langle\kappa\rangle$, as function of water content, λ, calculated from κ_+^∞ at the average unit-cell concentration (dotted line), from Equation 3-3 with $u = u_+^\infty \eta/\eta^\infty$ (dashed line), and from Equation 3-3 with $u = \beta_\parallel u_+^\infty \eta/\eta^\infty$ (solid line).See Appendix 3-A for calculation of $\beta_\parallel$.

3.4.1.3 Impact of Side-Chain Size

The molecular composition of the PFSA sidechain (e.g. the number of fluorocarbon or fluoroether groups) influences the partial charge on molecular groups neighboring sulfonates[29] and, consequently, the overall membrane conductivity.[12, 182] Charge delocalization decreases the fraction of cations associated with the sulfonate groups and increases membrane conductivity.[29, 154, 182-183] Charge delocalization is modeled qualitatively by increasing the size of charged hemisphere, $R_{SO_3^-}$, to account for the increase of the effective size of the negatively charged moiety which include the sulfonate group and some amount of polymer sidechain over which the negative charge is delocalized. Figure 3-8 reports average domain hydronium conductivity (solid line) and the fraction of hydronium ions associated with sulfonate groups (dashed line) at $\lambda = 9$ as a function of $R_{SO_3^-}$. Delocalization of the negative sulfonate-group charge (with increasing $R_{SO_3^-}$) decreases the fraction of cations associated with sulfonate groups. Charge delocalization lessens the electrostatic free-energy benefit of cation/sulfonate group contact pairs, which increases the number of solvated cations. Decreasing the fraction of cations associated with sulfonate groups causes conductivity to increase up to a point where most of the cations are completely dissociated. Additional delocalization of the negative charge causes the conductivity to decrease slightly because the sidechains create physical obstacles to transport.

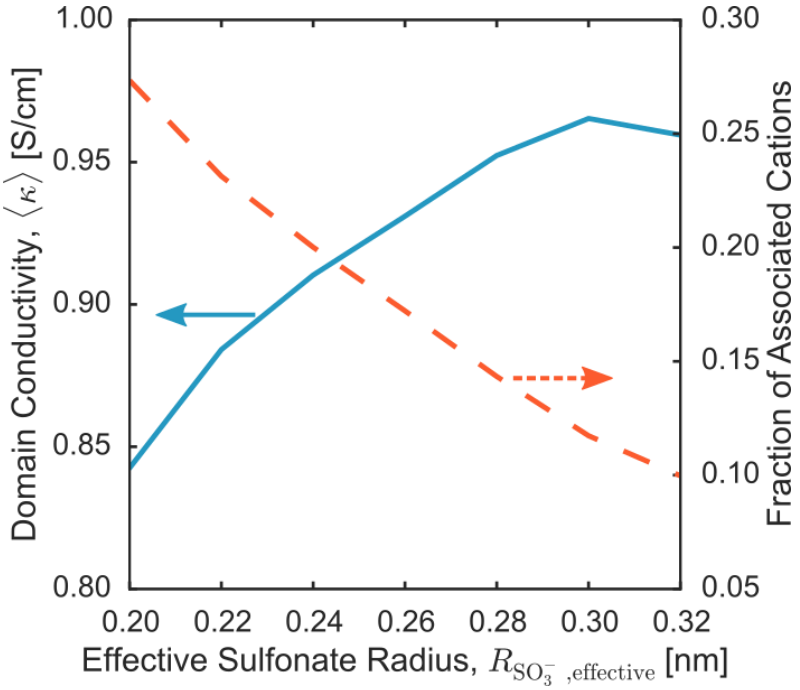

Figure 3-8. Hydronium conductivity (solid line, left axis) and fraction of cations within the radius of association (4 Å) of sulfonate groups (dashed line, right axis) at $\lambda = 9$ [H_2O/SO_3] as a function of the size of the negatively charged side-chain moiety.

3.4.2 Macroscale Physics

The unit-cell model for PFSA membranes captures the essence of known behavior at the nanoscale.[12] We now extend the aqueous-domain results to predict macroscopic transport properties in PFSAs. Modeling macroscopic properties is challenging because the aqueous-domain model only accounts for phenomena at the nanoscale. It does not account for transport across a network of connected domains. A bundle-of-tubes model describes transport through the medium. The effective macroscopic conductivity κ^{eff} is[184]

$$\kappa^{\text{eff}} = \frac{\varphi}{\tau^2}\langle\kappa\rangle \qquad 3\text{-}22$$

where κ^{eff} is the effective macroscopic conductivity of the membrane, τ is the tortuosity of the network, and φ is membrane hydrophilic volume fraction, which is taken as the combined volume fraction of water and sulfonate groups

$$\varphi = \frac{V_w\lambda + \frac{4}{3\pi R_{SO_3^-}^3}}{V_w\lambda + \frac{EW}{N_A\hat{\rho}_{\text{poly}}}} \qquad 3\text{-}23$$

where $\hat{\rho}_{\text{poly}}$ is the mass density of dry polymer (~ 2 g/cm^3)[185] and EW is the equivalent weight of the membrane (g polymer/mole of sulfonate groups).

Varying the cation type of the membrane ("cation form") and polymer chemistry changes τ and $\langle\kappa\rangle$ in Equation 3-22 independently. For example, for the same membrane chemistry and water content, tortuosity is assumed independent of cation type. Specifying $\langle\kappa\rangle$ with the nanoscale model and fitting φ/τ^2 to conductivity of one cation-form membrane predicts resistance of other cation-forms. Figure 3-9a shows experimental (symbols) and predicted (lines) membrane conductivity, κ^{eff}, for sodium and proton membranes with φ/τ^2 fit using conductivity of lithium membrane at the same water content. Agreement is good. Proton-form membranes have the highest conductivity because hydronium cations readily dissociate from the sulfonate group and have the largest mobility. Conductivity of lithium- and sodium-form membranes are similar; sodium ions have a higher bulk mobility than lithium ions but are hindered in the domains because they are more likely to form ion pairs with sulfonate groups.

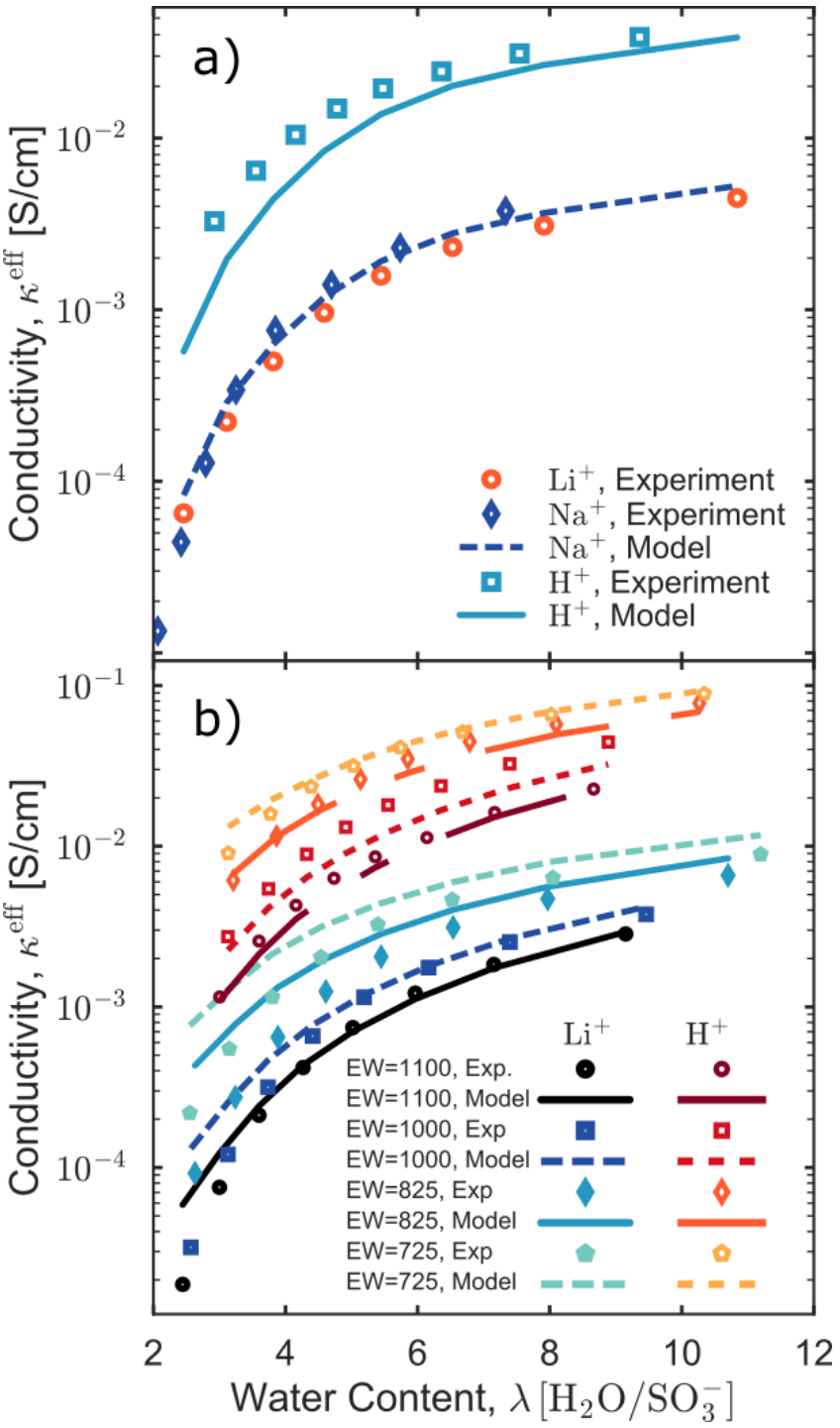

Figure 3-9. Experimental (symbols) and predicted (lines) conductivity of (a) Nafion membrane (1100 g/mol SO_3 EW) conductivity for lithium- (circles), sodium- (diamonds), and proton-form (squares) membranes and (b) 3M membrane with EWs of 1100 (circles), 1000 (squares), and 825 (diamonds), and 725 g/mol SO_3 (pentagons) in lithium- (blue) and proton-form (red) as a function of water content. Lines are model predictions (Equation 3-22).

Additionally, conductivity of different membrane chemistries further validates the model. We assume that network tortuosity is solely a function of the hydrophilic-phase volume fraction and distribution (i.e. $\tau(\varphi)$) and that aqueous domain-scale conductivity is entirely a function of the local water content, cation form, and pore geometry (i.e. $\langle\kappa\rangle(\lambda)$). The effect of network tortuosity and aqueous domain-scale conductivity is separated by changing the amount of hydrophobic backbone in the polymer per sulfonate group (i.e. EW) and by measuring the conductivity of the membranes at different water contents. To account for how tortuosity varies with hydrophilic volume fraction we use the empirical expression[186]

$$\tau = e^{\frac{k}{2}\left(\frac{1}{\phi}-1\right)} \qquad 3\text{-}24$$

where k is a fitting parameter. Substitution of Equation 3-24 into Equation 3-22 specifies the effective macroscopic conductivity at a given water content and membrane chemistry. k is 0.93, which was fit so membrane conductivity from Equations 3-22 and 3-24 matched measured conductivity of a lithium-form membrane at 90% relative humidity (i.e. at $\lambda = 9$). k was taken constant for all EW membranes in lithium- and proton-form. Figure 3-9b shows that predicted membrane conductivity from Equation 3-22 (lines) agrees well with measured conductivity (symbols) for both lithium and proton membranes as a function of water content across a range of equivalent weights. The membrane conductivity increases with decreasing EW at the same water content because the hydrophilic volume fraction increases, thereby lowering network tortuosity.

Discrepancy between theory and experiment shown in Figure 3-9b results from the breakdown in the assumption that tortuosity is exclusively a function of water content. Hydrophilic domain morphology (i.e. locally flat domains or inverted micelles) and related domain connectivity depend slightly on water content and cation form rather than solely on water volume fraction.[12, 44] Furthermore, any domain coalescence or related significant structural changes are not considered

Because Equation 3-22 explicitly relates transport parameters at the nanoscale ($\langle\kappa\rangle$) and mesoscale (ϕ and τ) to macroscale conductivity, the influence of each length scale is deconvoluted. The ideal-solution proton conductivity, κ_+^∞, at the average concentration of the unit cell, is the upper limit (as defined by Equation 3-5). Figure 3-10 shows the calculated ideal-solution conductivity as a function of water content (dotted line). κ_+^∞ decreases with hydration because water dilutes the proton charge carriers. The dashed line in Figure 3-10 is the proton domain-scale conductivity, $\langle\kappa\rangle$, which is equivalent to the solid line in Figure 3-6. The difference between the dotted and dashed lines represents the conduction losses due to cation interactions with the polymer matrix and sulfonate side groups. $\langle\kappa\rangle$ is relatively constant with water content because the effect of charge carrier concentration is countered by proton/polymer interactions at lower water content that reduce conductivity. Guided by Equation 3-22, including the resistances imparted by ϕ (dot-dashed line) and τ (solid line) further reduces the conductivity. The solid line is the measured macroscopic conductivity of an 1100 EW 3M PFSA proton-form membrane, as shown in Figure 3-9b. Designing polymers that mitigate these interactions may offer an avenue to improve macroscopic conductivity (e.g., delocalization of sidechain charge). However, domain-scale interactions are not the only factors controlling macroscopic conductivity. Network tortuosity and the volume fraction of the conductive phase also dramatically impact conductivity. The importance of the network-level effects of tortuosity and conductive-phase volume fraction explains the success of efforts to increase conductivity by decreasing the hydrophobic volume fraction of the

polymer[187] (e.g., lower EW) and reducing the tortuosity.[188-189] Chapter 7 explores the nature of network tortuosity and the validity of Equation 3-22.

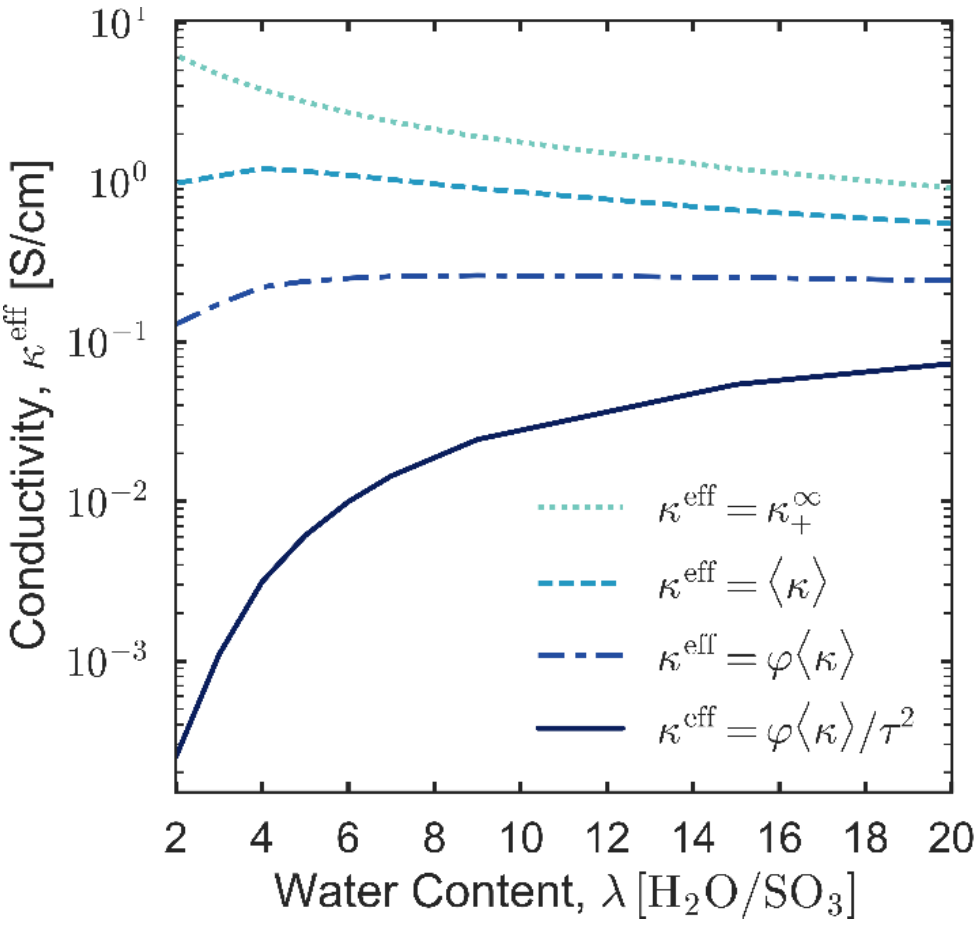

Figure 3-10. Proton-form membrane conductivity as a function of water content at the conductive ideal solution limit at the concentration of the unit cell, κ_{+}^{∞}(dotted line), with the model conductivity from Equation 3-22, $\langle\kappa\rangle$ (dot-dashed line), with the model conductivity from Equation 3-22 and accounting for the hydrophilic volume fraction, $\varphi\langle\kappa\rangle$ (dashed line), and with the model conductivity and accounting for the hydrophilic volume fraction and network tortuosity, $\varphi\langle\kappa\rangle/\tau^{2}$ (solid line).

3.5 Conclusions

A mean-field, local-density model of ion transport and distribution inside hydrophilic aqueous domains of PFSA membranes was developed and validated. The model adopts an experimentally consistent 3D geometry and accounts for solvation, electrostatic, image charge, dispersion, and finite-size free energies in addition to dielectric friction and wall confinement. The simple macroscale model up-scales the nanoscale model to predict macroscopic conductivity by accounting for the volume fraction and tortuosity of the conductive domains.

Membrane conductivity is facilitated by the movement of solvated cations inside PFSA hydrophilic domains. The fraction of solvated cations is governed by a competition between

electrostatic attraction between the cation and negatively charged polymer sulfonate moieties and cation solvation energy. The balance between these two free energies can be varied, for example, by changing sidechain chemistry to delocalize the negative charge on the sidechains, which decreases the fraction of cations binding to the sulfonate groups and increases conductivity.

Aqueous microscale conductivity is relatively constant with water content due to the competition of charge-carrier concentration, which increases conductivity with decreasing water content, and cation solvation, which increases conductivity with increasing water content. Macroscale conductivity increases with increased water content because membrane transport is strongly affected by the tortuosity of the network, which decreases with increasing water content. Addressing transport limitations at both the nano- and network-scales offer avenues to improve membrane performance. Conversely, focus on optimizing and exploring transport at a single lengthscale without regard for the other may not be fruitful. The model developed here provides a framework to understand the root causes of ion-transport resistances in ion-conductive polymers.

3.6 Notation

Roman

A	slope of solvation energy with respect to the inverse of the dielectric constant, J mol^{-1}
a	finite size parameter, m
B	constant used in Equation 3-14
D	displacement field, C m^{-2}
d	distance, m
e	elementary charge, 1.602x10^{-19} C
EW	equivalent weight of polymer, g/mol (SO_3)
f	fraction of sphere remaining after being intersected by a wall and/or sulfonate groups
ΔG	change in energy due to solvation with a reference to solvation in a vacuum, J mol^{-1}
g	radial distribution function
I	first ionization potential
$\underline{\underline{I}}$	identity matrix
i	ionic current density, A m^{-2}
J	diffusive flux, mol m^{-2} s^{-1}
l	length of the unit cell, m
k	fitting parameter in Equation 3-24
k_B	Boltzmann Constant, 1.381x10^{-23} m^2 kg s^{-2} K^{-1}
n	refractive index of water at 298 K, 1.330
$\underline{n}$	unit normal vector
N_A	Avogadro number, 6.022x10^{23} molecules mol^{-1}
p	dipole moment of water, 6.17x10^{-30} C m
R	radius, m
r	distance to point, m
$\underline{r}$	position vector, m
T	absolute temperature, K
u	mobility, s kg^{-1}

V	molecular volume
z	valance

Greek

α	diamagnetic polarizability
β	hydrodynamic mobility correction
γ	constant used in Equation 3-18
ε	relative permittivity
ε_0	vacuum permittivity, 8.854×10^{-12} F m^{-1}
κ	conductivity, S cm^{-1}
η	viscosity of water, cP
λ	water content, mole H_2O (mole SO_3)$^{-1}$
$\tilde{\mu}$	electrochemical potential, J molecule^{-1}
ρ	molecular concentration
$\bar{\rho}$	molecular density
$\hat{\rho}_{poly}$	polymer mass density, 2 g m^{-3} [185]
σ_{-}	surface charge density, C m^{-2}
τ	square-root of tortuosity
τ_d	Debye dielectric relaxation time for water, 0.82×10^{-11} s from Ref [190]
$\Delta\Phi$	applied ionic potential, 1×10^{-8} V
Φ	ionic potential, V
φ	hydrophilic phase volume fraction
$\langle \ldots \rangle$	domain average

Subscripts

$+$	cation
$\parallel$	parallel to direction of diffusion
$\perp$	perpendicular to direction of diffusion
cluster	cluster of water molecules over which short range interactions are important ($R^{\infty}_{\text{cluster}} = 5.91 \times 10^{-10}$ m from Ref [179])
dsp	dispersion
fs	finite size
img	image charge
S	cation type
SO_3^-	sulfonate group
solv	solvation
T	PTFE ($\alpha_T = 1.97 \times 10^{-24}$ cm^3, $I_T = 13.2$ eV, from Ref [191], $\rho_T = 0.0440$ mol cm^{-3} from Ref [173], $\varepsilon_T = 2.0$ from Ref [176])
tot	accounting for all the unit cell
w	water ($V_w = 2.993 \times 10^{-29}$ m^3 molecule^{-1}, $\alpha_w = 1.45 \times 10^{-24}$ cm^3, $I_w = 12.62$ eV, $\rho_w = 0.0554$ mol cm^{-3} $R_w = 1.38$ Å from Ref [173])
x	x-component of vector
y	with respect to top or bottom of unit cell

Superscripts

0	reference

∞	in solution at infinite dilution (η_∞= 0.8903 cP from Ref [190], ε_∞ = 78.3[156])
bottom	bottom of the unit cell
con	parameter including confinement but not electrostatic effects
eff	effective macroscopic property for the membrane
hf	high frequency ($\varepsilon^{\mathrm{hf}}$= 5.2 from Ref [190])
sat	saturated
SO_3^-	sulfonate group
top	top of the unit cell
us	upstream side of the unit cell

*The distance of closest approach between the sulfonate group and water molecule, $R_{SO_3^-} + R_{H_2O}$, is the location of the first peak of the water radial distribution function (RDF) with respect to sulfur.[43] $R_{SO_3^-}$ is specified by subtracting the hard sphere radius of water.

3.7 Appendix 3-A

The Stokes-Einstein equation predicts that ion mobility varies inversely with solvent viscosity, which provides the basis for the $\eta^\infty/\eta(\underline{r})$ correction to mobility in Equation 3-4. Yang and Pintauro corrected the solvent viscosity based on increased ion concentration.[14, 46] We account for increased water viscosity due to dielectric friction of the sulfonate groups, consistent with nonequilibrium statistical-mechanics calculations.[14, 46, 139] Hubbard determined that the increase in η due to the slower relaxation of dipoles in an electric field to be[166]

$$\eta(\underline{r}) = \eta^\infty \left[1 + \frac{\tau_d}{16\pi\eta^\infty}\left(\varepsilon^\infty - \varepsilon^{\mathrm{hf}}\right)|\nabla\Phi|^2\right] \qquad 3\text{-}25$$

where τ_d is the Debye dielectric relaxation time, and ε^∞ and $\varepsilon^{\mathrm{hf}}$ are the unperturbed and high-frequency dielectric constants of the solvent, respectively.

Because the fraction of bulk mobility due to hydrodynamic drag parallel to a wall, $\beta_\parallel$, and perpendicular to wall, $\beta_\perp$, are different $\underline{\underline{\beta}}$ is an anisotropic, diagonal tensor

$$\underline{\underline{\beta}}(\underline{r}) = \begin{bmatrix} \beta_\parallel & 0 & 0 \\ 0 & \beta_\perp & 0 \\ 0 & 0 & \beta_\parallel \end{bmatrix} \qquad 3\text{-}26$$

$\beta_\perp$ has an exact solution effectively estimated as[163]

$$\beta_\perp \approx \frac{6\left(\frac{d_y}{R_+}\right)^2 + 2\left(\frac{d_y}{R_+}\right)}{6\left(\frac{d_y}{R_+}\right)^2 + 9\left(\frac{d_y}{R_+}\right) + 2} \qquad 3\text{-}27$$

where d_y is the scalar distance from the center of the cation to the nearest wall (i.e. $y' = y$ or $= l - y$). $\beta_\parallel$ is estimated as[165]

$$\beta_{\parallel} \approx 1 - \frac{9}{16}\frac{R_+}{R_+ + d_y} + \frac{1}{8}\left(\frac{R_+}{R_+ + d_y}\right)^3 - \frac{45}{256}\left(\frac{R_+}{R_+ + d_y}\right)^4 - \frac{1}{16}\left(\frac{R_+}{R_+ + d_y}\right)^5 \quad 3\text{-}28$$

3.8 Appendix 3-B

To avoid simultaneously solving Equations 3-3, 3-6, 3-9, and 3-12, which is a set of coupled integral-differential equations, we approximate μ_{solv} as the linear superposition of the solvation excess chemical potentials due to solvation interactions with the PTFE floor and ceiling of the unit cell, $\mu_{\text{solv}}^{\text{top}}$ and $\mu_{\text{solv}}^{\text{bottom}}$, respectively, and with the nearest sulfonate group, $\mu_{\text{solv}}^{\text{SO}_3^-}$,

$$\mu_{\text{solv}}(\underline{r}) \approx \mu_{\text{solv}}^{\text{top}}(\underline{r}) + \mu_{\text{solv}}^{\text{bottom}}(\underline{r}) + \mu_{\text{solv}}^{\text{SO}_3^-}(\underline{r}) \quad 3\text{-}29$$

$\mu_{\text{solv}}^{\text{top}}$ and $\mu_{\text{solv}}^{\text{bottom}}$ are solutions to Equations 3-12 and 3-13 for a system with an aqueous cation a distance d_y from a semi-infinite polymer wall ($d_y = y$ and $l - y$ in $\mu_{\text{solv}}^{\text{top}}$ and $\mu_{\text{solv}}^{\text{bottom}}$, respectively) with a relative permittivity of PTFE, ε_{T}, as shown in Figure 3-11a. Because of confinement, ε is slightly lower than ε^{∞} close to the walls. $\mu_{\text{solv}}^{\text{top}}$ and $\mu_{\text{solv}}^{\text{bottom}}$ are each functions only of y and $l - y$, respectively. $\mu_{\text{solv}}^{\text{SO}_3^-}$ is the solution to Equations 3-12 and 3-13 for a second system with a single negatively charged sulfonate group and an aqueous cation a distance $d_{\text{SO}_3^-}$ from the sulfonate, as shown in Figure 3-11b. The sulfonate group with the charge uniformly distributed on the surface of the hemisphere causes a displacement field

$$D = e/2\pi r_{\text{SO}_3^-}^2 \quad 3\text{-}30$$

for $y > 0$ where $r_{\text{SO}_3^-}$ is the distance to the center of the sulfonate group. The displacement field causes the solvent to saturate dielectrically around the appended sulfonate ion, as discussed in the next section. To avoid double counting the effect of the polymer wall in μ_{solv} by both $\mu_{\text{solv}}^{\text{top}}$ or $\mu_{\text{solv}}^{\text{bottom}}$ and $\mu_{\text{solv}}^{\text{SO}_3^-}$, the relative permittivity of the wall (i.e. $y < 0$) is ε^{∞} in the evaluation of $\mu_{\text{solv}}^{\text{SO}_3^-}$, which is a function only of $d_{\text{SO}_3^-}$. Equation 3-29 makes μ_{solv} a function only of $d_{\text{SO}_3^-}$ and y. In the evaluation of $\mu_{\text{solv}}^{\text{top}}$, $\mu_{\text{solv}}^{\text{bottom}}$, and $\mu_{\text{solv}}^{\text{SO}_3^-}$, Equation 3-12 was computed using midpoint integration in 3D with 8x10^6 grid points spaced approximately 3 pm apart extending 0.6 nm from the cation in the x- and z-directions and 0.6 nm in the $+y$-direction for values of y from 0 to 1.2 nm in increments of 0.1 nm with linear interpolation used for intermediate values of y.

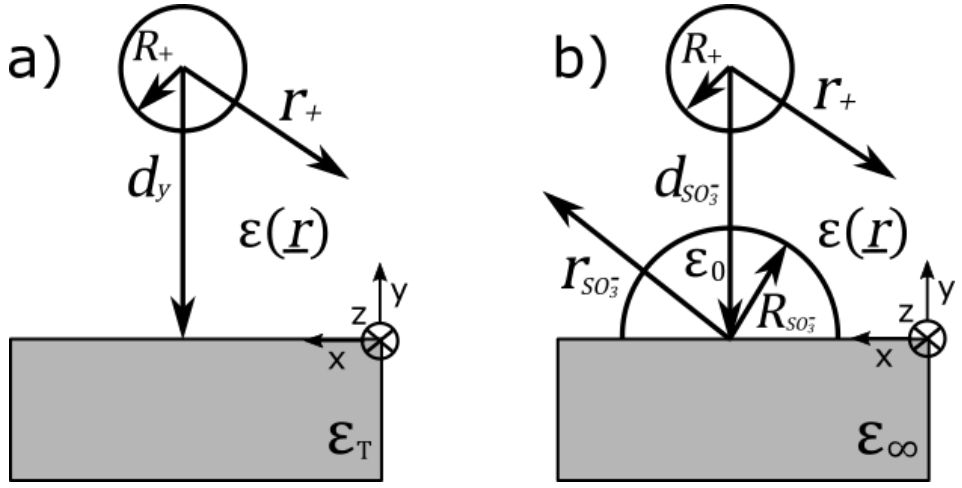

Figure 3-11. Representation of systems used to calculate the pairwise excess chemical potentials. (a) $\mu_{\text{solv}}^{\text{wall}}$ and (b) $\mu_{\text{solv}}^{\text{SO}_3^-}$ where the circle and semicircle represent the cation and sulfonate, and the shaded region represents polymer walls. Arrows indicate distances.

3.9 Appendix 3-C

From simple geometric arguments, the fraction f_j of a sphere of radius R_i remaining after being intersected by each j sulfonate groups or wall a distance d_j from the surface of the sphere is

$$f(\underline{r}) = 1 - \sum_{j}^{\text{all SO}_3^-} \frac{\left(R_i - d_j(\underline{r})\right)^2 \left(3R_i - d_j(\underline{r})\right)}{4R_i^3} \qquad 3\text{-}31$$

for all $d_j \leq R_i$.

3.10 Chapter 3 Supporting Information

3.10.1 Boundary Conditions

Boundary conditions for the unit cells, as discussed in the main text, are shown graphically in Figure 3-12

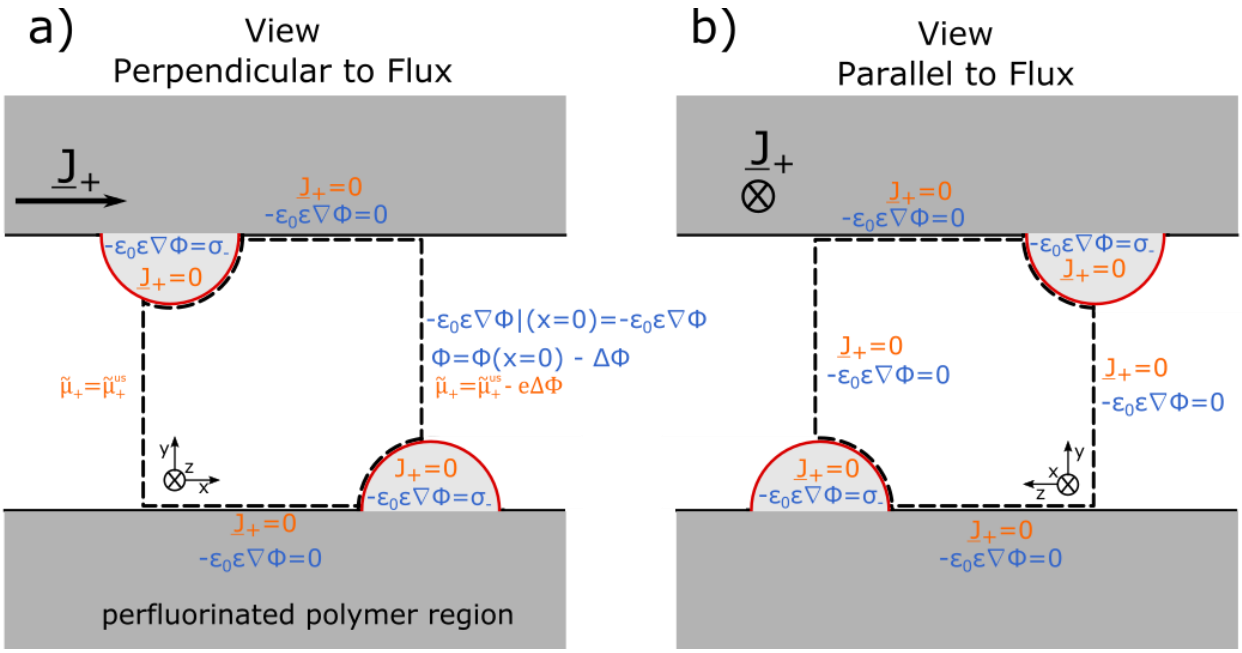

Figure 3-12. Graphical display of boundary conditions of pore-model.

3.10.2 Radial Distribution Function

The radial distribution function (RDF) of cation R^+ with respect to the center of the sulfonate group is

$$g_{SO_3^- - R^+}\left(r_{SO_3^-}\right) = \frac{\iint_S \rho_+(r) r_{SO_3^-}{}^2 d\theta d\phi}{\iint_S \frac{N_A}{\left(V_w\lambda + \frac{EW}{\hat{\rho}_{poly}}\right)} r_{SO_3^-}^2 d\theta d\phi} \qquad 3\text{-}32$$

where EW is the equivalent weight of the membrane (g polymer/mole of sulfonate groups) and $\hat{\rho}_{poly}$ is the mass density of the dry polymer (~ 2 g/cm^3 [185]). The numerator in Equation 3-32 is the number density of cations on a spherical surface a distance $r_{SO_3^-}$ from the sulfur atom; the denominator is the number density on the same surface when cations are uniformly distributed. The RDF was evaluated at intervals of $r_{SO_3^-}$ of 0.2 Å from 0 to 3.42 Å and then increments of 0.5 Å up to 11.42 Å. Lines in Figure 3-6 are drawn using a smooth spline approximation of the points with degree 3.

3.10.3 Nanoscale Ionic Potential, Viscosity, and Conductivity

Figure 3-13 shows electrostatic potential (a), viscosity (b) and nanoscale conductivity (c) for $\lambda = 9$. Local conductivity, κ_x, is defined as $\kappa_x \equiv -i_x l/\Delta\Phi$ where i_x is the x-component of current.

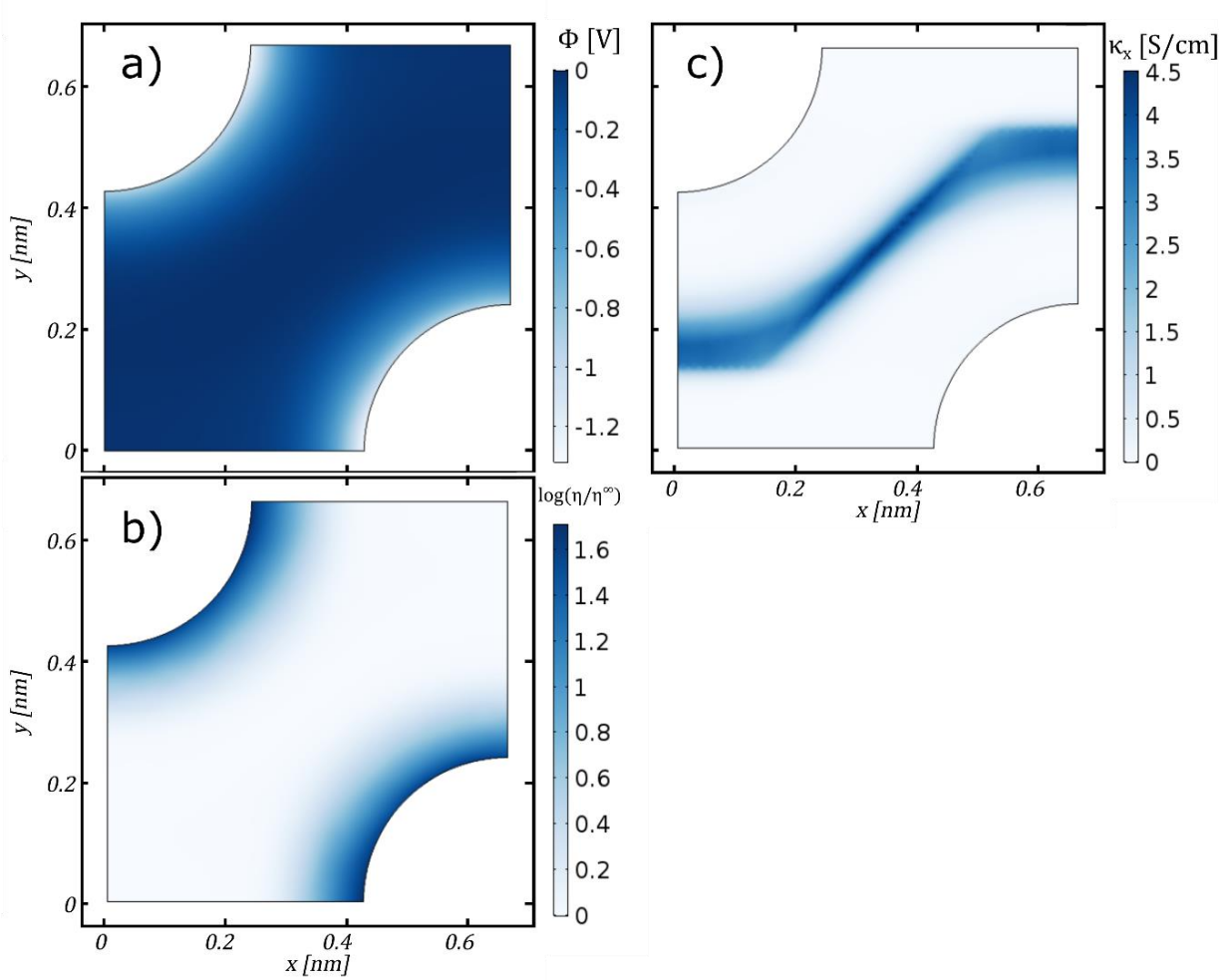

Figure 3-13. intensity map on the x-y surface of the unit cell for protonated membrane at $\lambda = 9$ [H_2O/SO_3] of (a) ionic potential, Φ, (b) viscosity, reported as $log(\eta/\eta^{\infty})$, and (c) local domain conductivity in the x-direction, κ_x, colored from white (light) to blue (dark) represent low to high values.

3.10.4 Validation with Atomistic Simulations

To compare our results with atomistic simulations[42-43, 152] a cutoff is made at $r_{SO_3^-} = 4$ Å, corresponding to the first solvation shell of the sulfonate group (shaded region in Figure 3-6), consistent with atomistic simulations.[42-43, 152] Aqueous cations that lie within this cutoff distance of any sulfonate group are considered associated with the sulfonate ion. Figure 3-14 illustrates that the fraction of hydronium ions associated with a sulfonate group decreases with increasing water content. As water content increases, more water is available to solvate the cations allowing them to move away from the sulfonate groups. Comparison of our calculations (solid line) to atomistic simulations (symbols)[42-43, 152] show excellent agreement using no fitting constants.

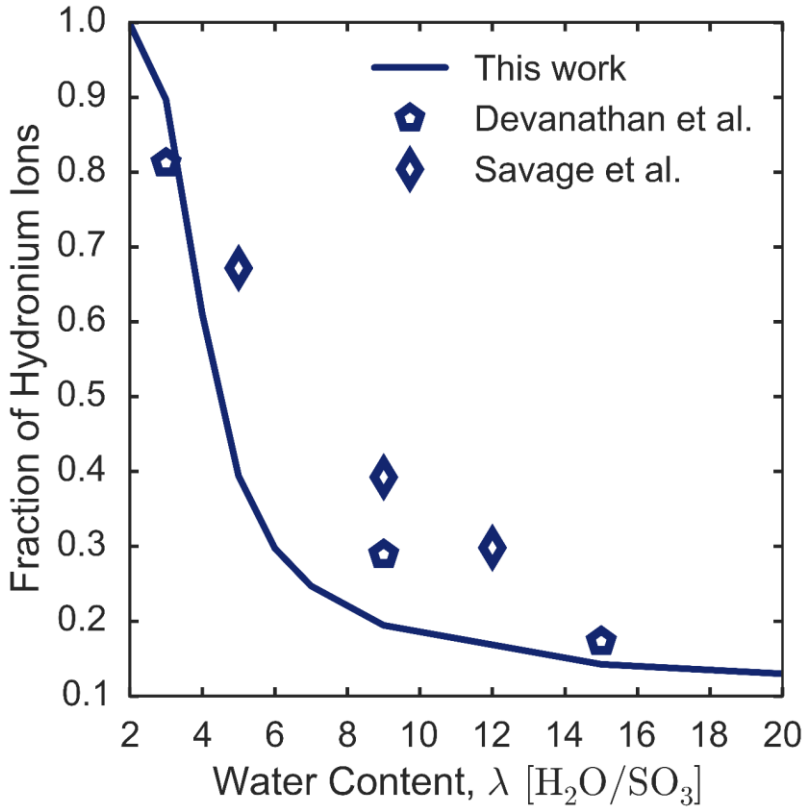

Figure 3-14. Fraction of hydronium cations associated with at least one sulfonate as defined in the text for this work (solid line) and from atomistic simulations (pentagons[42], diamonds[152]) as a function of water content.

3.10.5 Anisotropic Swelling

Our model is relatively insensitive to the size of the channels. Therefore, deviations from this assumption cause only small errors. Figure 3-15 shows the domain conductivity for channels that swell isotropically (solid line) and anisotropically (dashed line) as a function of water content. The insert in the lower left corner shows channel height for the two cases. The degree of anisotropic swelling is postulated based on small angle X-ray scattering experiments.[56] The insert in the upper right corner shows an intensity map of cation probability distribution normalized by the average cation concentration at $\lambda = 15$ in the anisotropic case. The anisotropic-swelled channel has slightly lower conductivity at higher water content because some cations are trapped in a bridging position between neighboring sulfonate groups, as noted in the insert.

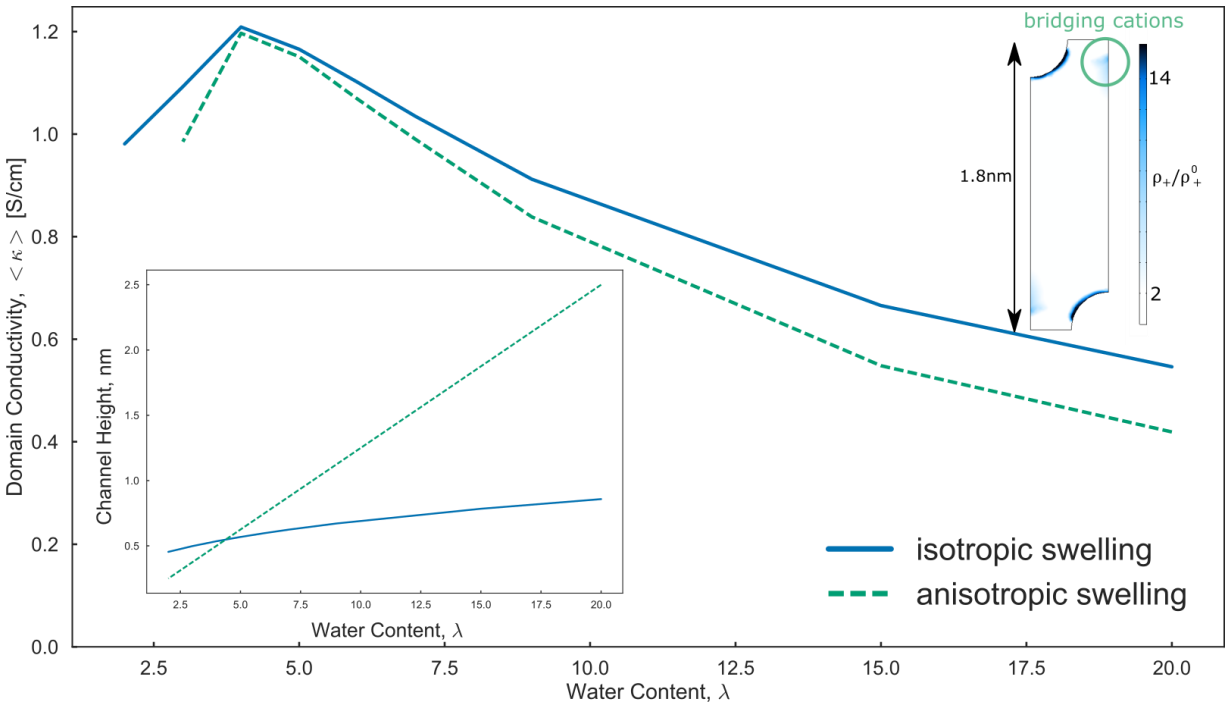

Figure 3-15. Average hydronium conductivity in a domain, $\langle\kappa\rangle$, as function of water content, λ, for isotropic (solid line) and anisotropic (dashed line) swelling. The bottom left insert shows channel height for isotropic (solid line) and anisotropic (dashed line) as a function of water content. The top right insert shows a 2D intensity map of hydronium probability density normalized by the average unit cell probability density, ρ_+/ρ_+^0, on the x-y surface of the anisotropic ally swelled unit cell at $\lambda = 15$ colored from white (light) to blue (dark) represent low to high values.

4 Theory of Multicomponent Phenomena in Cation-Exchange Membranes, I: Thermodynamic Model and Validation

4.1 Chapter Abstract

We present and validate a mathematical model for multicomponent thermodynamic activity in phase-separated cation-exchange membranes (*e.g.*, perfluorinated sulfonic-acid ionomers). The model consists of an expression for the free energy of the membrane and of the surrounding electrolyte solution. A modified Stokes-Robinson ionic solvation framework treats the solution-like non-idealities resulting from hydration, electrostatics, ion association, and physical interactions in bulk solution and in ionomer hydrophilic domains. Inside the membrane, a mechanics-based composite approach accounts for the swelling of the hydrophobic matrix. Treating the membrane microstructure as a disordered system of domains calculates steric exclusion of ions. Electroneutrality guarantees that the charge of mobile ions in the membrane is equal to the charge on polymer groups. Osmotic coefficients for electrolytes from literature parameterize solution-like interactions while mechanical and X-ray scattering characterization gives most membrane-specific parameters. Model predictions compare favorably to measured membrane thermodynamics (*i.e.*, water and ion uptake) in dilute and concentrated binary and ternary salt electrolytes and in water vapor. Interactions between ions in the membrane are similar to those present in bulk electrolytes. Our results reveal that water and ion uptake is dictated by a balance between solution-like energetics and membrane swelling.[§]

4.2 Introduction

Aqueous cation-exchange polymers are an important class of membrane-electrolytes because the imbibed solvent imbues the material with high conductivity while maintaining mechanical stability.[12, 192-193] Both of these attributes are essential for membrane electrolytes in numerous energy-storage and conversion devices.[11-12, 32, 86, 136, 192-194] However, the favorable ion-transport properties of these membranes pose a challenge when multiple ions are present.[11, 86-87] Specifically, there is tradeoff between increasing the absorption and transport of certain species that are desirable, such as current-carrying ions, while limiting movement of contaminants, additives, or redox-active species that decrease device performance.[11, 16]

Electrolyte membranes and hydrogels in energy-storage and conversion devices typically contain fixed ionic groups that are charge balanced by mobile cations to realize high ionic conductivity.[12] The prototypical ion-conducting membranes are perfluorinated sulfonic-acid (PFSA) ionomers, which contain negatively charge sulfonate groups and protons or other cationic counter ions.[12] These membranes absorb water and ions from the surrounding solution.[12] Intense research efforts have yielded compelling approaches for modeling transport and thermodynamics

[§] Published as Crothers, A. R.; darling, R. M.; Kusoglu, A.; Radke, C. J.; Weber, A. Z., Theory of Multicomponent Phenomena in Cation-Exchange Membranes: Part I. Thermodynamic Model and Validation. *J. Electrochem. Soc.* **2020,** *167* (1), 013547.

in these membranes,[14-15, 32-33, 63-64, 72, 195-199] yet these systems are still poorly understood due to their chemical complexity and corresponding nanostructural heterogeneity.[96]

One source of complexity is the extensive thermodynamic coupling between species.[33, 72, 92, 196] Specifically, the presence, concentration, and properties of one species affect the behavior of all other components.[91-92] The specific and electrostatic interactions of ions with the membrane, solvent, and other ions cause preferential partitioning of some species from the solution over others.[17, 60-61, 156, 200] Furthermore, electroneutrality dictates that charge density everywhere is zero, creating a Donnan potential that induces uptake of ions of opposite charge to the fixed groups on the polymer.[17, 60-61, 133, 193] Further complicating matters, the presence and concentration of species change speciation via shifting acid and ion-pairing equilibria of active species.[194]

Consequently, concentration and speciation of components inside the membrane differ drastically from that in the external solution.[92, 200] Because ion and solvent uptake and species identity impact transport properties, permeability and conductivity depend on the concentration of species in the external solution.[32, 68, 91, 201] Accordingly, experimental characterization of the mobility of species inside separators requires both transport and thermodynamic measurements.[67-68] Moreover, ion partitioning, water uptake, conductivity, and other transport properties in the membrane vary drastically when measured in different liquid electrolytes or after different membrane pretreatments.[87, 94] Membrane properties that are measured in one electrolyte environment do not set the behavior in another.[57, 94] However, mathematical models of molecular thermodynamics can address this challenge by predicting chemical activity across a range of conditions.[13]

The influence of species partitioning on transport properties suggests that tuning thermodynamic properties may improve device performance.[11, 15-16] Numerous membrane characteristics, including chemical structure, water content, and pretreatments, alter membrane performance.[87, 93, 118-119] Microscopic thermodynamic theories provide insights into how characteristics of the membrane influence its properties and inform strategies for improving device performance. Chapter 3 proposes a highly resolved microscale model. In this chapter, we use the insights from Chapter 3 to develop a more tractable thermodynamic model for multicomponent thermodynamics.

This chapter is the first of a three-chapter series that uses mathematical modeling to understand phase-separated cation exchange membranes that contain absorbed solvent and multiple ions. Here in Part I (Chapter 4), we develop and validate a semi-empirical microscopic thermodynamic description of the system. Part II (Chapter 5)[31] develops and validates a microscale concentrated-solution description of multi-ion and solvent transport in these membranes. As a case study, Part III (Chapter 6) [104] simulates transport in an all-vanadium redox flow-battery separator and elucidates the underlying structure/property/function relationship for membranes in these systems and proposes improved design targets.

The outline of the papers is as follows. The theory section presents a molecular thermodynamic model that calculates ion and water uptake as a function of external solution concentration and separator structure. The model relies on semi-empirical parameters that are mostly available from measurements of bulk solution aqueous electrolytes. We discuss parameter choice and summarize numerical implementation of the model. In the results and discussion section, the model is validated against literature data. The theory reveals how the uptake of species is coupled and quantifies the relative importance of the involved molecular interactions.

4.3 Theory

Although numerous water-filled ion-conducting membrane architectures exist,[11, 15] here we focus on the perfluorinated sulfonic-acid (PFSA) chemistry because of its extensive characterization and widespread use.[12] PFSA ionomers nanophase separate into hydrophilic, water-filled, ion-conducting domains and hydrophobic, structural domains.[12] This section first defines the equilibrium conditions dictating ion and solvent uptake in the membrane. A semi-empirical microscopic model of the system provides a free-energy expression and accompanying electrochemical potentials for each species. We also address how to account for species association.

4.3.1 Equilibrium between Phases

Chemical equilibrium dictates ion and solvent partitioning between the external solution phase α and the membrane phase β follows[30]

$$\mu_i^\alpha = \mu_i^\beta \tag{4-1}$$

where μ_i^δ is the (electro)chemical potential of species i in phase δ ($= \alpha$ or β); water is defined as species 0. The chemical potential of neutral species i is defined as the derivative of the free energy of $G^\delta$with respect to n_i, the moles of species i,[9]

$$\mu_i^\delta = \left(\frac{\partial G^\delta}{\partial n_i^\delta}\right)_{T,p,n_{j\neq i}} \tag{4-2}$$

where T and p are the temperature and pressure, respectively. We use Equation 4-2 to calculate the chemical potentials of charged species. The resulting chemical potentials always appear in neutral pairings to ensure that they are independent of the electrical state of the phase[9] (see Species Chemical Potential). Chemical potential, and subsequent predictions of species partitioning, require a well-defined free-energy expression.

4.3.2 Free Energy

We define a hypothetical reference state (denoted with superscript θ) as the pure liquid solvent, hypothetical ionic species that do not interact with each other (*i.e.* ideal solution at unit mole fraction) and fully dissociated, and the unswollen polymer membrane (M). The change in free energy from the reference, G^θ, consists of ideal mixing between ions and solvent, ΔG^{id}, ion solvation, ΔG^{slv}, electrostatic interactions between ions, ΔG^{els}, short-range and non-electrostatic specific physical interaction between ions, ΔG^{phy}, swelling the polymer, ΔG^{swe}, and steric interactions between the ions and polymer, ΔG^{stc}. With the usual assumption of superposition of free energy processes,[13] the free energy of the membrane phase is

$$G^\beta - G^\theta = \Delta G^{\mathrm{id},\beta} + \Delta G^{\mathrm{slv},\beta} + \Delta G^{\mathrm{els},\beta} + \Delta G^{\mathrm{phy},\beta} + \Delta G^{\mathrm{swe},\beta} + \Delta G^{\mathrm{stc},\beta}. \tag{4-3}$$

For the external solution, the final two terms are excluded since the polymer is absent

$$G^\alpha - G^\theta = \Delta G^{\mathrm{id},\alpha} + \Delta G^{\mathrm{slv},\alpha} + \Delta G^{\mathrm{els},\alpha} + \Delta G^{\mathrm{phy},\alpha} \tag{4-4}$$

where the two superscripts denote contribution and phase. The types of interactions in Equations 4-3 and 4-4 are similar to the interactions proposed in Chapter 3 (Equation 3-9). However,

Equation 4-3 and 4-4 are not as sophisticated as the microscale interactions in Chapter 3. Equation 4-3 and 4-4 are therefore more empirical and less computationally expensive than those in Chapter 3. The expressions here in Chapter 4 are engineering models that treat the phenomena at the appropriate level of required without adding excessive complexity based on poorly understood molecular-scale physics.

The first change from the reference state free energy comes from ideal mixing of the ions and solvent [9, 13]

$$\frac{\Delta G^{\mathrm{id}}}{RT} = \sum_i n_i \ln x_i \qquad 4\text{-}5$$

where R is the gas constant and x_i is the mole fraction of species i ($= n_i / \sum_i n_i$). The tethered polymer charged groups are in the hydrophilic domain and partially mix with the absorbed electrolyte solution.[40] We idealize the polymer ionic groups with moles n_{M} as free ions in the hydrophilic domains that contribute to the free energy accordingly. n_{M} is equal to the mass of the polymer divided by its equivalent weight (EW, equal to g-polymer per mole of ionic group).[12] Unlike many models for polymer membranes (*i.e.* Flory-Huggins theory[202]), the model neglects mixing between the uncharged volume fraction of the membrane ϕ_{M} and the solution in the hydrophilic domains because the strong segregation of phases means they are not freely interspersed.[12]

The terms on the right of Equations 4-3 and 4-4 except ΔG^{id} are the "excess" free energy, G^{ex}.[13] For any species i, the excess chemical potential, $(\partial G^{\mathrm{ex}}/\partial n_i)_{n_{j\neq i},T,p}$, is normalized to approach zero ($\rightarrow 0$) as the moles of all species j except the solvent (*i.e.* $j \neq 0$) approaches zero (*i.e.* $n_j \rightarrow 0$) and the membrane is fully relaxed. The excess free energy in most bulk aqueous electrolyte solutions is known.[172] Literature provides numerous theories for these terms in G^{α} [13] and a few expressions for membrane specific terms, $\Delta G^{\mathrm{stc},\beta}$ and $\Delta G^{\mathrm{els},\beta}$.[12, 60, 133, 203] Despite over 100 years of intense research effort, all accurate and tractable thermodynamic theories for concentrated electrolytes (>1 mol L^{-1}) require semi-empirical adjustable parameters.[204]

Here, we choose expressions for the excess free energy that are consistent with the physical description of the membrane, are relatively simple to implement numerically, require few membrane-specific adjustable parameters, and are predictive for bulk single and mixed-salt electrolyte solution thermodynamics or mechanical measurements of the membrane. Because the ion molality inside the membrane can exceed 20 mol kg^{-1},[12] these expressions must also be valid at extremely high electrolyte concentrations. The parameters, while semi-empirical, are physically grounded. By modeling the thermodynamic nonidealities in the membrane hydrophilic domains with expressions for solution-like excess energies, we assume that molecular interactions in the pores are not drastically altered in the confined environment. This assumption is justified by the relatively short range of solvation, specific, and electrostatic interactions, at the high ionic strengths found in the hydrophilic domains of the membrane (*i.e.* the range of molecular interactions is less than the size of the hydrophilic domains).[205]

Solvation energy accounts for the entropy decrease due to free solvent molecules binding to unsolvated ions and limiting the configurations that can be accessed[66, 206]

$$\frac{\Delta G^{\mathrm{slv}}}{RT} = n_0 \ln \alpha_0 + \sum_{i\neq 0} n_i \ln \frac{\alpha_i}{\alpha_i^{\infty}} \qquad 4\text{-}6$$

where α_0 and α_i are the ratios of free solvent and unbound ions, respectively, after solvation to before solvation. α_i^{∞} is the fraction of unsolvated ions i at infinite dilution; the form of the last term in Equation 4-6 ensures that excess chemical potential is normalized so that $\left(\partial \Delta G^{\mathrm{slv}}/\partial n_i\right)_{n_{j\neq i},T,p} \to 0$ as $n_{i\neq 0}/n_0 \to 0$. Chapter 4 Supporting Information (SI-4) discusses expressions for these variables as derived by Stokes and Robinson,[206] Schonert,[207-208] and Zerres and Prausnitz[66] in terms of the solvent/ion i binding constant k_i and the total number of solvent molecules in ion i's solvation shell, $\mathcal{N}_i$.

Upon charging, the ions interact through long-range electrostatic forces. Debye-Hückel theory characterizes these interactions.[9, 208] Accordingly, a solution with ionic strength, I ($= \frac{\rho_0}{2n_0 M_0}\sum_{i\neq 0} z_i^2 n_i$), has an electrostatic free energy

$$\frac{\Delta G^{\mathrm{els}}}{RT} = -\frac{4}{3} ARTI^{\frac{3}{2}}\, n_0 \frac{M_0 \tau\left(aBI^{\frac{1}{2}}\right)}{\rho_0} - n_0 M_0 m_{\mathrm{M}} z_{\mathrm{M}} \frac{2A}{bB} \ln\left(a_{\mathrm{M}} BI^{\frac{1}{2}}\right) \qquad 4\text{-}7$$

where A is the Debye-Huckel limiting slope (= 1.177 $\mathrm{L}^{1/2}$ $\mathrm{mol}^{-1/2}$ for water at 298 K), B is the Debye-Huckel solvent parameter (= 3.291 $\mathrm{L}^{1/2}$ $\mathrm{mol}^{-1/2}$ nm^{-1} for water at 298 K), M_0 is the molecular weight of the solvent (= 18 g mol^{-1}), ρ_0 is the density of the solvent (= 0.997 g cm^{-3}), τ is a function ($\tau(x) = 3/x^3(\ln(1+x) - x + x^2/2)$), a is the average distance of closest approach between ions (i.e. average diameter), b is the spacing between charged groups in the membrane, and z_i is the charge number of species i. The first term accounts for electrostatic interactions between mobile ions and the second term accounts for electrostatic interactions between mobile ions and the ions of the membrane.[9, 209] The second term is zero in the external solution phase. This expression follows from a statistical-mechanical derivation given in Refs [62, 209] that we modify by accounting for the radius of the ions.[9]

Equations 4-6 and 4-7 are parameterized based only on the properties of the individual ions in the electrolyte (*i.e.* k_i and a_i) and are independent of which pairs of cations and anions are present. At higher electrolyte concentrations, specific interactions between cation and anion pairs lead to additional short-range interactions (following Ref [66], we describe this as a physical contribution). Zerres and Prausnitz[66] combined Equations 4-6 and 4-7 with a semi-empirical term for the specific physical interactions outlined by Scatchard[210] where the interactions are proportional to the concentrations of the ions[9]

$$\frac{\Delta G^{\mathrm{phy}}}{RT} = n_0 M_0 \sum_{i\neq 0}\sum_{j\neq 0} \beta_{i,j} m_i m_j \qquad 4\text{-}8$$

where $\beta_{i,j}$ is the specific interaction parameter between i and j and is symmetric (*i.e.* $\beta_{i,j} = \beta_{j,i}$). Because of the rarity of interactions between like-charged ions, $\beta_{i,j} = 0$ for $z_i z_j > 0$.[9] For favorable short-range interactions between species, $\beta_{i,j} < 0$, whereas unfavorable interactions give $\beta_{i,j} > 0$.

Hydrophilic domains must swell to make space for the ions and solvent to enter the membrane.[202] Numerous research gives expressions for the excess Helmholtz free energy of an elastically swelling polymer membrane in terms of the integral of the microscopic swelling pressure, p^{swe}, generally given in the form[56, 65, 202, 211]

$$\frac{\Delta G^{\mathrm{swe}}}{n_{\mathrm{M}}\bar{V}_{\mathrm{M}}} \approx \int_{1}^{\phi_{\mathrm{M}}} \frac{p^{\mathrm{swe}}}{\phi_{\mathrm{M}}^{2}} d\phi_{\mathrm{M}} \tag{4-9}$$

where we approximate the excess Helmholtz energy (on the right side) as equal to the excess Gibbs energy (on the left side) due system incompressibility. The free energy ΔG^{swe} on the left side is normalized by the dry polymer volume, $n_{\mathrm{M}}\bar{V}_{\mathrm{M}}$, where $\bar{V}_{\mathrm{M}}$ is the partial molar volume of polymer per ionic group (= EW/ρ_{M}), ϕ_{M} is the volume fraction of the polymer membrane, and ρ_{M} is the density of the dry membrane (= 2.1 g cm^{-3}). Because there is much less volume of ions than membrane or solvent, we neglect the ion volume fraction for calculations of ϕ_{M} ($\approx n_{\mathrm{M}}\bar{V}_{\mathrm{M}}/(n_{\mathrm{M}}\bar{V}_{\mathrm{M}} + n_0\bar{V}_0)$) and set the partial molar volume to the pure species molar volume. p^{swe} arises from the microscopic deformation of the polymer membrane due to solvent absorption and is unrelated to the thermodynamic pressure p. Specific to phase-separated polymers, we use the expression from Kusoglu *et al.* [65] for the elastic swelling pressure generated due to deformation of the hydrophobic polymer matrix when solvent enters the hydrophilic domains

$$p^{\mathrm{swe}} = E_{\mathrm{b}}^{0}\left(1 - \frac{\frac{d}{2} - R_{\mathrm{domain}}}{\frac{d^{0}}{2} - R_{\mathrm{domain}}^{0}}\right) \tag{4-10}$$

where E_{b}^{0} is Young's modulus of the dry polymer, R_{domain} is the size of hydrophilic domains and d is the spacing between hydrophilic domains and superscript 0 denotes the dry membrane property. R_{domain}^{0} is the size of the domains in the dry state that includes the volume of charged polymer groups and counter ions. SI-4 discusses the specific expressions for the domain size and spacing dependence on membrane volume fraction, *i.e.* $R_{\mathrm{domain}}(\phi_{\mathrm{M}})$ and $d(\phi_{\mathrm{M}})$.

The size of the hydrophilic domains also dictates the steric confinement of the ions inside them (*e.g.* excluded volume that is inaccessible to the ions). The free energy of these steric interactions for an ion i of diameter a_i due to confinement induced entropy loss in the membrane is idealized as a system of randomly oriented walls with an average spacing of $d - d^{0}$ [203]

$$\frac{\Delta G^{\mathrm{stc}}}{RT} = \sum_{i\neq 0,\mathrm{M}} n_i \frac{a_i}{(d - d^{0})} \tag{4-11}$$

where d the same as in Equation 4-10.

4.3.3 Species Chemical Potential

Equation 4-2 defines the chemical potentials of all species. Because the Gibbs energies given in Equations 4-3 and 4-4 are expressed as the sum of different contributions, chemical potential contributions similarly superimpose

$$\mu_i^{\beta} - \mu_i^{\theta} = \mu_i^{\mathrm{id},\beta} + \mu_i^{\mathrm{slv},\beta} + \mu_i^{\mathrm{els},\beta} + \mu_i^{\mathrm{phy},\beta} + \mu_i^{\mathrm{swe},\beta} + \mu_i^{\mathrm{stc},\beta} \tag{4-12}$$

$$\mu_i^{\alpha} - \mu_i^{\theta} = \mu_i^{\mathrm{id},\alpha} + \mu_i^{\mathrm{slv},\alpha} + \mu_i^{\mathrm{els},\alpha} + \mu_i^{\mathrm{phy},\alpha}$$

where the chemical potential of component i satisfies Equation 4-2 and the superscripts correspond to the respective free-energy terms and phase. Table 1 gives expressions for each term. We neglect changes in partial molar volume, which are small.[212]

Although not explicitly shown, the electrochemical potential of charged species depends on the chemical contributions outlined in Equation 4-12 as well as on the electrical state of the phase. To incorporate this latter dependence while ensuring that the chemical contributions to electrochemical potential are thermodynamically accessible,[9] Smyrl and Newman use a reference ion to define a so-called quasi-electrostatic potential, Φ (see [9], pg. 95).[213] A useful reference for PFSAs with water is the proton because it exists in both the external solution and inside the membrane. Accordingly, Φ is defined as

$$z_{\mathrm{H}^+} F \Phi \equiv \mu_{\mathrm{H}^+} - \mu_{\mathrm{H}^+}^{\mathrm{id}} \qquad 4\text{-}13$$

where F is Faraday's constant, z_i is the charge number of i, and the subscript H^+ denotes protons. We define the electrochemical potential of other species such that the reference and excess chemical potentials (*i.e.* all the terms on the right sides of Equations 4-12 except μ_i^{id}) are well-defined and independent of electrical state,

$$\mu_i = \mu_i^{\theta} - \frac{z_i}{z_{\mathrm{H}^+}} \mu_{\mathrm{H}^+}^{\theta} + \mu_i^{\mathrm{id}} + \mu_i^{\mathrm{ex}} - \frac{z_i}{z_{\mathrm{H}^+}} \mu_{\mathrm{H}^+}^{\mathrm{ex}} + z_i F \Phi. \qquad 4\text{-}14$$

At equilibrium, Φ is referenced to the electrostatic potential in the solution (*i.e.* $\Phi^{\alpha} = 0$). We can now use Equation 4-2 to calculate the excess chemical potential of charged species because the excess chemical potential terms in Equation 4-14 appear only in neutral combinations of species guaranteeing that they are independent of electrical state.[9] Electroneutrality in each phase δ is a constraint on (*i.e.* specifies) the quasi-electrostatic potential,

$$\sum_i m_i^{\delta} z_i = 0. \qquad 4\text{-}15$$

Electroneutrality in cation-exchange membranes requires absorption of fewer anions than cations. Many researchers describe this phenomenon as the result of an electrostatic potential difference between the solution and the membrane (*i.e.* Donnan potential)[214]. As an alternative to using a quasi-electrostatic potential to quantify the electric state of the material, one may instead define the potential as proportional to the electrochemical potential of one of the species (*e.g.* set it to the potential of a hydrogen reference electrode).[9] The choice between these two definitions does not affect the calculated ion and water uptake.[9]

Substituting Equation 4-14 for an electroneutral sum of two species (*i.e.* $\mu_i - \frac{z_i}{z_j}\mu_j$) into Equation 4-1 characterizes the tendency of i and j to sorb into the membrane, which the factor Γ_{ij} quantifies[63-64, 198-199]

$$\frac{x_i^{\beta}\left(x_j^{\beta}\right)^{-\frac{z_i}{z_j}}}{x_i^{\alpha}\left(x_j^{\alpha}\right)^{-\frac{z_i}{z_j}}} = \exp\left(\frac{\left(\mu_i^{\mathrm{ex},\alpha} - \mu_i^{\mathrm{ex},\beta}\right) - \frac{z_i}{z_j}\left(\mu_j^{\mathrm{ex},\alpha} - \mu_j^{\mathrm{ex},\beta}\right)}{RT}\right) = \Gamma_{ij} \quad \text{4-16}$$

where Γ_{ij} is independent of the electrostatic potential for $i, j \neq \mathrm{M}$. For a neutral species i, z_i is zero and we drop the second subscript j for convenience. Because μ_i^{ex} is the sum of different free-energy contributions, Γ_{ij} is the product of these contributions. If i and j are two oppositely charged ions (such as the anion and cation of a salt) and $\Gamma_{ij} = 1$, the oppositely charged pairs i and j partition into the membrane according to ideal Donnan equilibrium. $\Gamma_{ij} > 1$ indicates that i and j favorably partition into the membrane while if partitioning is unfavorable $\Gamma_{ij} < 1$.

Table 4-1 Summary of equations for the chemical potential terms.

Contribution	Term	Expression
Ideal mixing	μ_i^{id}	$RT \ln x_i$
Solvation	$\mu_{i\neq 0}^{\mathrm{slv}}$	$RT \ln\left(\frac{\alpha_i}{\alpha_{i,\infty}}\right)$
	μ_0^{slv}	$RT \ln(\alpha_0)$
Charging	$\mu_{i\neq 0}^{\mathrm{els}}$	$-ARTz_i^2 I^{\frac{1}{2}}\left[\frac{1}{1+BaI^{\frac{1}{2}}}+\frac{m_{\mathrm{M}}z_{\mathrm{M}}^2}{2bBI}\right]$
	μ_0^{els}	$ART\left(\frac{2}{3}I^{\frac{3}{2}}\sigma\left(BaI^{\frac{1}{2}}\right)\frac{M_0}{\rho_0}+\frac{M_0 m_{\mathrm{M}}z_{\mathrm{M}}^2}{bB}\right)$
Physical	$\mu_{i\neq 0}^{\mathrm{phy}}$	$2RT\sum_{i\neq 0}\beta_{i,j}m_j$
	μ_0^{phy}	$-M_0 RT\sum_{i\neq 0}\sum_{j\neq 0}\beta_{i,j}m_i m_j$
Swelling	$\mu_{i\neq 0,\mathrm{M}}^{\mathrm{swe}}$	0
	μ_0^{swe}	$\bar{V}_0 E_{\mathrm{b}}^0\left[1-\frac{\frac{d(\phi_{\mathrm{M}})}{2}-R_{\mathrm{domain}}(\phi_{\mathrm{M}})}{\frac{d^0}{2}-R_{\mathrm{domain}}^0}\right]$
Steric	$\mu_{i\neq 0,\mathrm{M}}^{\mathrm{stc}}$	$\frac{RTa_i}{(d-d_0)}$
	$\mu_{i=0}^{\mathrm{stc}}$	0
where $\tau'(x)=\frac{d\tau}{dx}=\frac{3}{x^4}\left\{-3\ln(1+x)+2x-\frac{x^2}{2}+\frac{x}{1+x}\right\}$ $\sigma(x)=\frac{3}{x^3}\left\{(1+x)-2\ln(1+x)-\frac{1}{1+x}\right\}$		

4.3.4 Speciation

The microscale description of the system's free energy, Equations 4-5) to 4-11), are based on the physical properties of all distinct species present, which include solvent, free ions, ion pairs, or undissociated acids. Therefore, the model requires specification of component speciation (we will

call this the "Molecular Construct")—for example, treating sulfuric acid as protons, sulfates, and bisulfates (see Ref [9], pg. 119). Conversely, experiments typically report concentrations of fully dissociated species (we will call this the "Experimental Construct")—for example, treating sulfuric acid as only protons and sulfate ions. Both treatments are thermodynamically consistent.[9] The Molecular Construct introduces an additional variable, $f_{i,j}$: the moles of species i in the Experimental Construct, n_i^{exp}, that partially associates into n_j^{mol} moles of species j in the Model Construct

$$f_{i,j} = -\frac{n_j^{\mathrm{mol}} s_i}{n_i^{\mathrm{exp}} s_j} \tag{4-17}$$

where superscript exp and mol denote the construct and s_i and s_j are the stoichiometric coefficients of the association reaction of species i in species j, respectively. Note that $\sum_j f_{i,j} = 1$. Chemical equilibrium of these reactions specified $f_{i,j}$[30]

$$s_j \mu_j = -\sum_i s_i \mu_i \tag{4-18}$$

where the sum is over species i that associate to form j. The superscript is not applied to the electrochemical potential because it is independent of the chosen construct. For the case $j = i$, $\mu_i = \mu_j$ and $f_{i,i} = n_i^{\mathrm{mol}}/n_i^{\mathrm{exp}}$. The thermodynamic equilibrium constant for the association reaction to form j is $K_j^{\mathrm{eq}} = \exp\left(-\frac{\sum_i s_i \mu_i^\theta + s_j \mu_j^\theta}{RT}\right)$. This speciation equilibrium constant is defined in terms of the species chemical potential at the hypothetical reference state of unit mole fraction and ideal solution (*i.e.* $x_i^\theta = 1$ and $\mu_i^{\mathrm{ex}} = 0$) and is dimensionless; the more-commonly reported equilibrium constant, $K_j^{\mathrm{eq}\prime}$, is defined in terms of species chemical potential at the reference state of an ideal solution at unit molarity (*i.e.* $c_i^\theta = 1$ and $\mu_i^{\mathrm{ex}} = 0$). These two constants are related by $K_j^{\mathrm{eq}\prime} \approx K_j^{\mathrm{eq}} \left(c_0^0/c^\theta\right)^{s_j + \sum_i s_i}$ where c_0^0 is the solvent concentration for an electrolyte with an infinitely dilute salt concentration.[9, 13] At infinite salt dilution, $f_{i,j} \to 0$ for $i \neq j$ and $f_{i,i} \to 1$.[9]

To calculate the contributions to the chemical potential throughout this paper (such as in Table 4-1), we use composition variables in the Molecular Construct, n_i^{mol}, x_i^{mol}, and m_i^{mol}; the superscript mol is not explicitly written throughout for simplicity. If one chooses to write the ideal chemical potential in the Experimental Construct (*i.e.* $\mu_i^{\mathrm{id}} = RT \ln x_i^{\mathrm{exp}}$, as we do in Part III, Chapter 6, of this series[104]) rather than the Molecular Construct (*i.e.* $\mu_i^{\mathrm{id}} = RT \ln x_i^{\mathrm{mol}}$), the term $RT \ln x_i^{\mathrm{mol}}/x_i^{\mathrm{exp}}$ is added to μ_i^{ex}. The calculated chemical potential μ_i is independent of the chosen construct. When presenting results, we convert concentrations to the Experimental Construct for consistency with measurements unless otherwise stated.

4.3.5 Numerical Implementation

Equations 4-1 and 4-18 with those in Table 4-1 are a nonlinear, coupled algebraic system. At a given solution species composition in the Experimental Construct, we calculate the solvent and solute uptake in the membrane as follows: We determine the chemical potential of species in the external solution using Equation 4-12 with expressions from Table 4-1. Equations 4-13 and 4-14 specify the electrochemical potential of each species in solution. A modified Levenberg-

Marquardt[215] algorithm finds $f_{i,j}$ in Equation 4-17 for all species in the external solution that satisfies the root of the equilibrium speciation equations (Equation 4-18 for each speciation reaction). To determine the excess chemical potential of solvation, a modified Powell hybrid algorithm[216] concurrently solves for α_0 that is the root to Equation 4-19 in SI-4 for the solvation expression. The initial guess is a negligible fraction of free solvent.

A modified Levenberg-Marquardt [215] algorithm finds the polymer volume fraction, $\phi_{\mathrm{M}}^{\beta}$, solute molality, $m_{i\neq\mathrm{M}}^{\beta}$, and quasi-electrostatic potential, Φ^{β}, inside the membrane that satisfies electroneutrality (Equation 4-15) and equality of the electrochemical potential of unassociated species between phases (Equation 4-1). Alternatively, Equations 4-15 and 4-16 also specify partitioning, but without requiring calculation of Φ. Because Equation 4-18 makes electrochemical potential of associating ions and their products dependent, using Equation 4-1 on ion-pairs is redundant. Equations 4-12 and 4-14 determine the electrochemical potential of species inside the membrane. All root-finding algorithms are implemented in SciPy 0.18.1 package Python 3.6 with a relative tolerance of 1.49 x 10^{-8}. The NumPy packaged performed array operations.

4.4 Parameters

Operating parameters for this study are ambient temperature (298 K) and pressure (101 kPa). All the electrolytes in this study are aqueous (*i.e.* water is the solvent). We study the Nafion PFSA chemistry because data are widely available.[12, 67-69, 92-93, 217] We use data from Nafion N117, N115, N212, and N211 where the N11x sequence is extruded and the series N21x is cast from a dispersion. Designation x denotes thickness in units of mils. All membranes have an equivalent chemical formula.[12] In addition to different processing methods, the membranes undergo various pretreatments (*e.g.* boiling) that can alter their properties, such as membrane modulus.[53, 56] Variations in water and ion uptake between membranes may be predicted if mechanical properties of the membrane are available. Lacking this information and to ensure that the results are representative of Nafion across treatment history, we use datasets from multiple studies and for membranes from different series at the same environmental conditions. We also note the range of experimental values found in literature whenever possible

Table 4-2 lists the physical properties of the individual ions, the ion pairs, and the membrane that parameterize the model. These parameters have varying levels of empiricism. Certain properties are not fit (R_{domain}, d, and K_j^{eq}) because they are specified by independent measurements or theories that contain no adjustable properties. Based on molecular dynamics simulations and small-angle X-ray measurements, b is 0.47 nm.[218] Due to structural rearrangements of PFSAs, E_{b}^{0} for membranes equilibrated in a solution is lower than membranes in vapor (so-called Schröder's paradox).[56, 211, 219-220] SI-4 details compilation of the values of these parameters from literature.

Table 4-2. The value and approach to model parameters

Parameters	Value		Notes
Individual Ions			
	cations	*anions*	
ion diameter, $a_{i\neq \mathrm{M}}$	$0.3 + 0.18z_i$ [nm]	0.3 [nm]	physical arguments
ion/solvent biding k_i	various, see SI-4	0.0	Fit to bulk-solution data
ion solvation number $\mathcal{N}_i$	$5z_i$	0.0	physical arguments
Ion Pairs			
equilibrium constant K_j^{eq}	various, see SI-4		from literature, various methods
cation/anion interaction parameter $\beta_{i\neq M, j\neq M}$	various, see SI-4		fit to bulk-solution data
cation/membrane interaction parameter $\beta_{i,M}$	various, see Table 4-3		fit to membrane uptake data
Membrane			
dry membrane modulus E_{b}^0	136 (liquid)/ 320 (vapor) [MPa], see SI-4		mechanical measurement and theory
radius of hydrophilic domain R_{domain}	see SI-4		geometric arguments
spacing between domains d	see SI-4		small-angle x-ray scattering measurements
Spacing between charged groups, b	0.47 nm		Molecular dynamics simulations and small-angle X-ray scattering measurements

Other properties are adjusted to fit measured bulk aqueous electrolyte water activity (a_i, k_i, $\mathcal{N}_i$, $\beta_{i\neq \mathrm{M}, j\neq \mathrm{M}}$, the anion/cation interaction parameter). Because there are many parameters to fit uniquely, physical arguments and previous research suggest simplifications. For instance, the weak solvation of anions supports that their k_i's and $\mathcal{N}_i$'s are zero.[66] Further, we follow previous

electrolyte models by setting a_i for $i \neq$ M to a fixed value for each ion charge number because ion radii generally scales accordingly.[9] Ample research demonstrates that these simplifications, although somewhat ad hoc, provide accurate predictions of thermodynamic activity of binary and mixed electrolytes.[9, 66, 208] As SI-4 details, the remaining k_i's and $\beta_{i\neq \mathrm{M}, j\neq \mathrm{M}}$'s are fit to the measured osmotic coefficients of 28 salts consisting of pairings of 10 cations and 5 anions across a large range of concentrations (*e.g.* up to 15 mol kg^{-1} for LiBr).[172, 221]

The only parameters adjusted to fit membrane specific data are E_{b}^{0} the modulus of the polymer backbone in liquid water, and $\beta_{i,\mathrm{M}}$, the cation/membrane interaction parameter. The modulus of the membrane in liquid water is challenging to measure due to a highly non-linear shear response.[222] The backbone modulus is estimated to be between 131 to 181 MPa.[222] By fitting water and ion uptake measurements in liquid water, we set E_{b}^{0} to 136, which is within the measured range. Table 4-3 gives values for $\beta_{i,\mathrm{M}}$ that were fit to water and ion membrane uptake measurements, which are presented in the Results and Discussion section. The physical interactions between H^+, Li^+, Na^+, or K^+ and the membrane have a similar value as these cations have with trifluoromethanesulfonic anions, $CF_3SO_3^-$ ($TFMS^-$), which is a simple fluorosulfonate anion structurally similar to the sulfonate group in PFSAs.[221] We did not find thermodynamic activity of other TFMS salt solutions in the literature.

Table 4-3. Values of membrane-cation specific fitting parameters in the model

Cation	$\boldsymbol{\beta_{i,\mathrm{M}}}$ [kg mol^{-1}]	$\boldsymbol{\beta_{i,\mathrm{TFMS}^-}}$ [kg mol^{-1}]
H^+-M^-	0.133	0.148
Li^+-M^-	0.141	0.128
Na^+-M^-	0.085	0.0576
K^+-M^-	0.000	-0.0293
Cs^+-M^-	-0.08	
Cu^{2+}-M^-	0.55	
Ca^{2+}-M^-	0.28	
Ni^{2+}-M^-	0.4	
Fe^{3+}-M^-	0.85	
VO^{2+}-M^-	0.008	
VO_2^+-M^-	0.25	

Vanadium ions are relevant in flow-battery applications, which is the focus of Part III (Chapter 6)[104], but measurements for thermodynamic activity of vanadium electrolyte solutions are

scarce.[223] Consequently, values of k_i and $\beta_{i,j\neq \mathrm{M}}$ for vanadium ions in their various oxidation states are set equal to cations that have the same charge (see SI-4).

4.5 Results and Discussion

4.5.1 Ion- and Water-Uptake Isotherms in a Single Electrolyte and Water Vapor

Figure 4-1 shows measured (symbols) and calculated membrane water (a) and anion (c) uptake at as a function of external sulfuric acid concentration[93, 217] (circles) for various Nafion types (N117, N212, and N211) and hydrobromic acid (diamonds[224] and triangles[225]). For both water and ion uptake, agreement between the model and experiment is good up to ~8 molal in the external electrolyte. Note the overlap of HBr and H_2SO_4 data points at low concentrations. Despite the very different nature of the HBr (a 1-1 salt) and H_2SO_4 (a 2-1 salt if fully dissociated), water and ion uptake are similar at the same electrolyte concentration This similarity is in part due to the high concentration of H^+ in the membrane that ensures that the sulfate in the membrane is almost entirely in the bisulfate (HSO_4^-) form. Consequently, the HBr and H_2SO_4 both behave as univalent acids.

As the external acid concentration increases, the membrane water content decreases because the difference between solution osmotic pressure ($-(\mu_0^{\mathrm{id},\alpha}+\mu_0^{\mathrm{els},\alpha}+\mu_0^{\mathrm{slv},\alpha}+\mu_0^{\mathrm{phy},\alpha})/\bar{V}_0$) and the membrane osmotic pressure ($-(\mu_0^{\mathrm{id},\beta}+\mu_0^{\mathrm{els},\beta}+\mu_0^{\mathrm{slv},\beta}+\mu_0^{\mathrm{phy},\beta}+\mu_0^{\mathrm{stc},\beta})/\bar{V}_0$) decreases. This leads to water content decreasing as the balance between osmotic, which keeps water in the membrane, and swelling pressures (μ_0^{swe}), which pushes water out of the membrane, shifts in favor of the latter. Using the HBr solution as an example, Figure 4-1b shows that the effect of thermodynamic non-idealities on solvent uptake are small but unfavorable. Solution-like interactions ($\Gamma_0^{\mathrm{sol}}=\Gamma_0^{\mathrm{els}}\Gamma_0^{\mathrm{slv}}\Gamma_0^{\mathrm{phy}}$) of the highly concentrated solution in the membrane are favorable for water uptake, but the reduced entropy of the ions in the membrane due to steric interactions (Γ_0^{stc}) make water uptake less favorable. These two effects partially balance over a range of concentrations. Membrane swelling (Γ_0^{swe}) is always unfavorable for water uptake.

Increasing the external acid concentration drives acid into the membrane as the external concentration is greater than that in the membrane. Figure 4-1d shows the nonidealities associated with hydrobromic acid uptake, Γ_{HBr}, and the contributions from solution-like interactions, $\Gamma_{\mathrm{HBr}}^{\mathrm{sol}}=\Gamma_{\mathrm{HBr}}^{\mathrm{els}}\Gamma_{\mathrm{HBr}}^{\mathrm{slv}}\Gamma_{\mathrm{HBr}}^{\mathrm{phy}}$, and steric effects, $\Gamma_{\mathrm{HBr}}^{\mathrm{stc}}$. There is no swelling contribution to ion chemical potential. Acid partitioning into the membrane is greater than expected for an ideal solution at low external acid concentrations. The enhanced uptake is due to favorable electrostatic interactions (*i.e.* negative excess free energy) that increase with ion concentration (see Equation 4-7). Holding all else constant, ions move to a phase with more electrostatic interactions (*i.e.* to higher ionic strength). Since the membrane has a higher ionic strength than the external solution, the favorable electrostatic interactions ($\ln\Gamma_{\mathrm{HBr}}^{\mathrm{els}}$ = 3.0) compensate for the unfavorable effects of solvation ($\ln\Gamma_{\mathrm{HBr}}^{\mathrm{slv}}$ = -0.5) and specific interactions ($\ln\Gamma_{\mathrm{HBr}}^{\mathrm{phy}}$ = -1.6) in the concentrated electrolyte solution of the membrane.

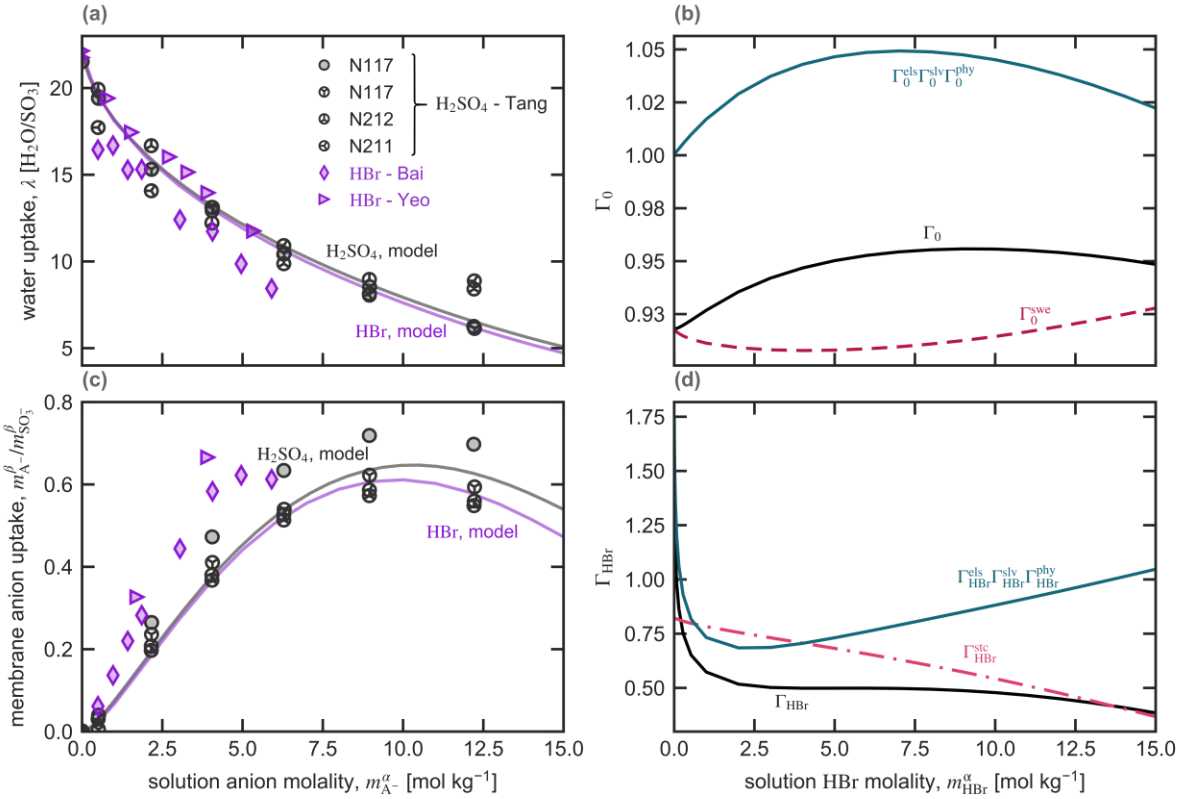

Figure 4-1. Membrane water (a) and anion (c) uptake calculated (solid lines) and measured (symbols) at varying external H_2SO_4 concentration measured by Tang *et al.*[93, 217](circles) for various Nafion types (N117, N212, N211) and HBr concentration measured by Bai[224] (diamonds) and Yeo[225] (triangles), and calculated. (b) shows contributions to the total water Γ_0 in the HBr system from solution-like $\Gamma_0^{sol} = \Gamma_0^{els}\Gamma_0^{slv}\Gamma_0^{phy}$, steric Γ_0^{stc}, and swelling Γ_0^{swe} nonidealities. (d) shows contributions to the total hydrobromic acid Γ_{HBr} from solution-like $\Gamma_{HBr}^{sol} = \Gamma_{HBr}^{els}\Gamma_{HBr}^{slv}\Gamma_{HBr}^{phy}$ and steric Γ_{HBr}^{stc} nonidealities.

At higher external acid concentrations, electrostatic interactions in the membrane are similar to those in the external solution, and the energetic benefit of acid partitioning into the membrane is smaller. Moreover, as water dehydrates the membrane, the pores shrink (see SI-4), and the ions are more sterically hindered. Thus, at high external electrolyte concentrations, anions are excluded more from the membrane than predicted for an ideal solution. However, in the dehydrated membrane, the average hydrophilic domain remains larger than the diameter of the ions and steric hindrance does not fully exclude co-ions.

Figure 4-1 shows that electrolytes with the same cation but different anions partition into PFSA membranes similarly. To explore how the cation impacts electrolyte partitioning, Figure 4-2 shows measured (symbols) and calculated (solid lines) membrane water (a) and anion (b) uptake as a function of external concentration of NaCl[226] (squares) and HBr (diamonds[224] and triangles[225]). The scales in Figure 4-1 and Figure 4-2 are not the same. At low salt concentrations, fractionally changing electrolyte concentrations does not change water content in the membrane. For

concentrations above ~1 molal, the water content decreases with increasing electrolyte concentration in both NaCl and HBr solutions as the membrane absorbs ions and dehydrates due to the high osmotic pressure of the surrounding solution.

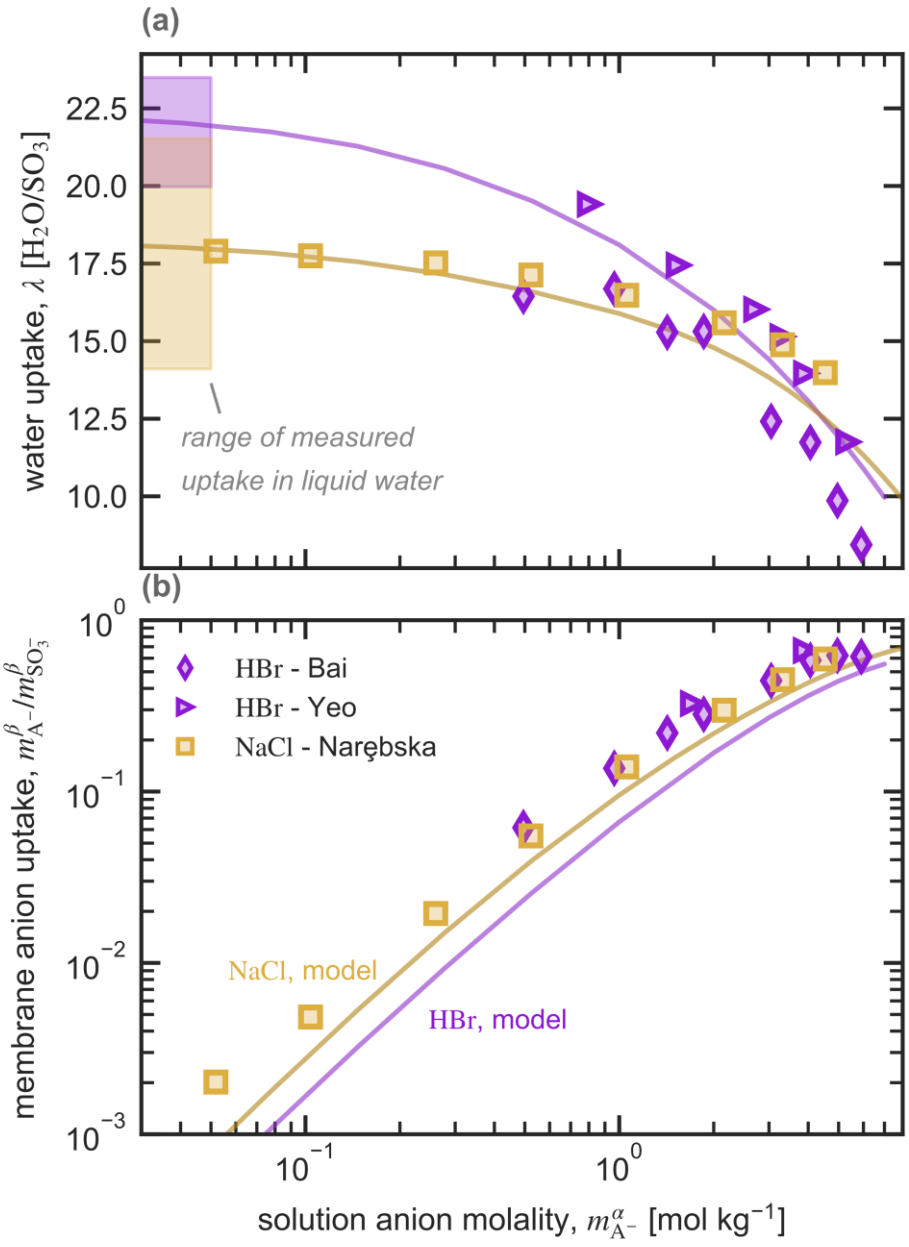

Figure 4-2. Measured (symbols) and calculated (solid lines) membrane water (a) and anion (b) uptake in varying external solution concentrations of NaCl measured by Narębska *et al.*[226] (squares) and HBr measured by Bai[224] (diamonds) and Yeo[225] (triangles). Shaded region denotes the range of values from literature of N117 solvent uptake in liquid water in H- (purple) and Na-form (yellow) membranes.[12]

At low electrolyte concentrations, membranes in NaCl solutions have a lower water content and higher anion uptake than in HBr at the same electrolyte concentration. In the limit of a membrane in pure water, the H-form of the membrane has higher water uptake than the Na-form in pure water; Figure 4-1 shows with the shaded purple and yellow regions, respectively, that provide the range of literature-reported water uptake in these membranes.[12] Compared to Na^+, H^+ has stronger solvation ($k_{H^+} > k_{Na^+}$, provided in SI-4) and unfavorable physical interaction with the sulfonate group on the membrane ($\beta_{Na^+,M^-} < \beta_{H^+,M^-}$, as Table 4-3 shows). Consequently, water uptake and dilution of the H^+-SO_3^- pairs is more favorable than dilution of Na^+-SO_3^- pairs. Similarly, uptake of Na^+ is more favorable than of H^+.

At high concentrations, this effect eliminated with equal or higher water uptake in NaCl than in HBr solutions. Compared to Na^+, the unfavorable interactions between H^+ and its co-ion ($\beta_{Na^+,Cl^-} < \beta_{H^+,Br^-}$, as SI-4 shows) shifts the osmotic pressure balance in favor of the external electrolyte and drives water from the membrane into the solution to dilute H^+-Br^- pairs.

The data shown in Figure 4-1 and Figure 4-2 are used to determine the parameters β_{H^+,M^-} and β_{Na^+,M^-}, respectively, and E_b^0. These values are the best-eye fit to the data. The fitted values of the specific interactions between cations and the membrane, β_{i,M^-}, are very similar to the fitted interactions between alkali cations and $CF_3SO_3^-$ in solution, $\beta_{i,TFMS^-}$. The similarity of β_{i,M^-} and $\beta_{i,TFMS^-}$ suggests that short-range specific interactions between cations and the membrane sulfonate groups are comparable to the interactions between cations and simple sulfonate anions in solution. Consequently, this approach explains the observed water and ions uptake behavior over a range of concentrations by accounting for solution-like interactions in the membrane. Confined pore geometry or long-range electrostatic ion condensation, as other researchers have proposed, can potentially predict β_{i,M^-} without fitting to experiments.[63, 135, 198, 227-228]

Figure 4-3 shows that the model effectively calculates (lines) measured (symbols) water uptake of N212 membranes in proton- (diamonds) and sodium-form (squares) in water vapor. Membrane water uptake at 100% relative humidity and salt-free liquid water is different despite a water activity of unity in both systems. This difference is termed Schröder's paradox and has been extensively studied.[12, 59, 229-230] Here, we attribute the decreased water uptake in water vapor to structural rearrangement of the hydrophilic domains upon exposure to water vapor leading to different backbone polymer moduli E_b^0, (see SI-4 for details).[222] No additional fitting parameters are used to calculate membrane water uptake in water vapor; agreement between theory and experiment is good. The model's successful thermodynamic predictions of membranes vapor and liquid environments further supports the proposed form of the Gibbs energy in Equations 4-3 and 4-4.

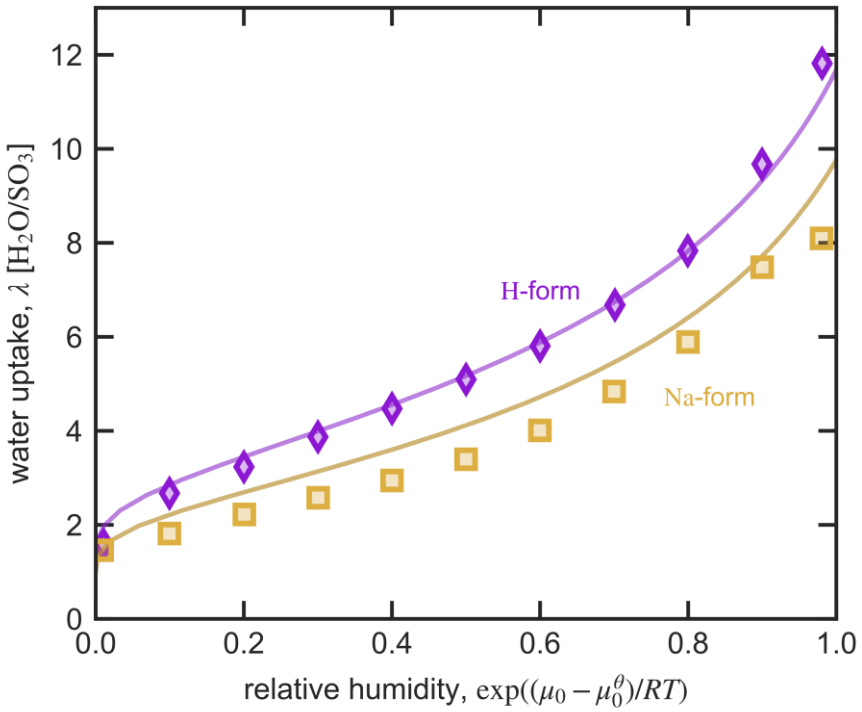

Figure 4-3. Measured (symbols) and calculated (solid lines) N212 membrane water uptake in water vapor as a function of relative humidity for membranes in proton-form (diamonds) and sodium-form (squares) measured by Shi *et al.*[54]

4.5.2 Ion Partitioning in Dilute, Mixed Electrolytes

We explore ion specificity of the model through partitioning of cations from a dilute mixed electrolytes. Focusing on membranes in dilute electrolyte makes anion uptake negligible because of Donnan exclusion. Okada et al. measured water content and cation partitioning in varying compositions of mixed electrolytes of $i\mathrm{Cl}_{z_A}$ and HCl (or LiCl) where i is Li^+, Na^+, K^+, Cs^+, Ni^{2+}, Cu^{2+}, and Fe^{3+}.[67-69, 71] The external solutions were at 0.06 mol kg^{-1} total ion (chloride, proton, and cation i) concentration.[69] The fraction of protons (or lithium ions) in the solution is quantified as the fraction of chloride anions in the solution charge balanced by protons $m^{\alpha}_{\mathrm{H}^+}/m^{\alpha}_{\mathrm{Cl}^-}$ and in the membrane as the fraction of sulfonate groups balanced by protons $m^{\beta}_{\mathrm{H}^+}/m^{\beta}_{\mathrm{M}^-}$(where the subscript H^+ is replaced by Li^+ for membranes exchanged from lithium-form).

Figure 4-4 shows that as the measured[68] (symbols) and predicted (lines) proton fraction in the membrane, $m^{\beta}_{\mathrm{H}^+}/m^{\beta}_{\mathrm{M}^-}$, as a function of the proton fraction of the surrounding mixed proton-alkali electrolyte, $m^{\alpha}_{\mathrm{H}^+}/m^{\alpha}_{\mathrm{Cl}^-}$ (a) and water content, λ, as a function of $m^{\beta}_{\mathrm{H}^+}/m^{\beta}_{\mathrm{M}^-}$ (c). The values of $\beta_{\mathrm{Li}^+,\mathrm{M}^-}$, $\beta_{\mathrm{K}^+,\mathrm{M}^-}$, $\beta_{\mathrm{Cs}^+,\mathrm{M}^-}$ are best-eye fit to the water uptake and ion partitioning in Figure 4-4; we use the values of $\beta_{\mathrm{H}^+,\mathrm{M}^-}$ and $\beta_{\mathrm{Na}^+,\mathrm{M}^-}$ obtained from ion and water uptake isotherms (Figure 4-1 and Figure 4-2) without additional fitting. Agreement is good particularly considering the experimental scatter reported in literature, which Figure 4-4 notes for completely exchanged alkali-form membranes with a shaded region.[12] Figure 4-9 shows that the model is externally valid by

predicting water and ion uptake of membrane in mixed lithium-alkali electrolytes at the same conditions (see SI-4).

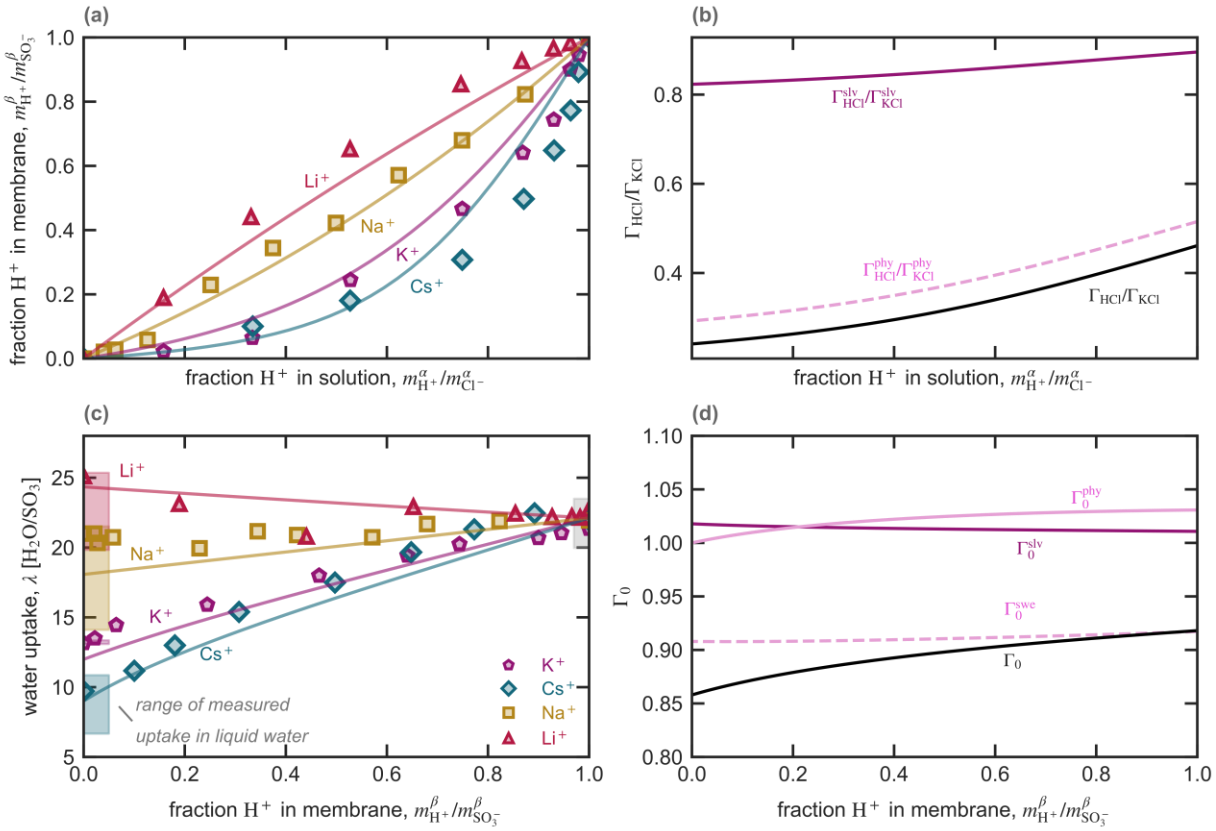

Figure 4-4. Measured[68] (symbols) and calculated (solid lines) membrane proton fraction in the membrane $m^{\beta}_{H^+}/m^{\beta}_{M^-}$ as a function of external solution proton fraction $m^{\alpha}_{H^+}/m^{\alpha}_{Cl^-}$ (a) and water content in the membrane, λ, as a function of proton fraction in the membrane $m^{\beta}_{H^+}/m^{\beta}_{M^-}$ (c) in a mixed aqueous electrolyte of hydrochloric acid and lithium (up triangles), sodium (squares), potassium (pentagons), and cesium (tilted squares) chloride. The external solutions were at 0.06 mol kg-1 total ion concentration.[68] Shaded regions denote the range of published water uptakes of membranes in liquid water of fully ion-exchanged membranes from Ref [12]. (b) shows contributions to the total the ratio $\Gamma_{HCl}/\Gamma_{KCl}$ from solvation $\Gamma^{slv}_{HCl}/\Gamma^{slv}_{KCl}$ and physical $\Gamma^{phy}_{HCl}/\Gamma^{phy}_{KCl}$ nonidealities. (d) shows contributions to the total water Γ_0 from solvation Γ^{slv}_0, physical Γ^{stc}_0, and swelling Γ^{swe}_0 nonidealities.

As the alkali cation fraction in solution increases, the fraction of alkali cations in the membrane increases. If alkali cation i and protons equally partition into the membrane ($\Gamma_{HCl}/\Gamma_{iCl} = 1$), then $m^{\beta}_{H^+}/m^{\beta}_{M^-}$ is a straight line between 0 and 1 for $m^{\alpha}_{H^+}/m^{\alpha}_{Cl^-} = 0$ and 1. Ideal partitioning nearly occurs for Na^+-H^+ exchange. For $\Gamma_{HCl}/\Gamma_{iCl} > 1$, the alkali cations prefer to be in the solution more than do protons; ion exchange shows positive deviation from equal partitioning (*i.e.* curved upward

in Figure 4-4a, as is the case for Li^+-H^+ exchange) whereas for $\Gamma_{HCl}/\Gamma_{iCl} < 1$, the alkali cations prefer to be in the membrane more than protons, and ion-exchange curve shows negative deviation (*i.e.* curved downwards in Figure 4-4a, as is the case for K^+-H^+ and Cs^+-H^+ exchange). Figure 4-4a shows that $\Gamma_{LiCl} < \Gamma_{HCl} \approx \Gamma_{NaCl} < \Gamma_{KCl} < \Gamma_{CsCl}$. This trend follows a Hofmeister series.[231]

To understand why univalent cations follow this trend, we study K^+-uptake more closely as an example; Figure 4-4b plots $\Gamma_{HCl}/\Gamma_{KCl}$ with the contributions of nonideality from solvation, $\Gamma_{HCl}^{slv}/\Gamma_{KCl}^{slv}$, and from physical interactions between the membrane and alkali cations and protons, $\Gamma_{HCl}^{phy}/\Gamma_{KCl}^{phy}$, as a function of $m_{H^+}^{\alpha}/m_{Cl^-}^{\alpha}$. $\Gamma_{HCl}/\Gamma_{KCl}$ is less than unity because K^+ is less solvated than H^+ and can therefore exist in the concentrated solution of the membrane without requiring a full solvation shell (*i.e.* $\Gamma_{HCl}^{slv}/\Gamma_{KCl}^{slv} < 1$). K^+ has more favorable physical interactions with the sulfonate group (*i.e.* $\beta_{K^+,M^-} < \beta_{H^+,M^-}$ so that $\Gamma_{HCl}^{phy}/\Gamma_{KCl}^{phy} < 1$). Because we use the same cation radii for all univalent ions, steric and electrostatic interactions are essentially identical for H^+ and K^+ (*i.e.* $\Gamma_{HCl}^{stc}/\Gamma_{KCl}^{stc} \approx \Gamma_{HCl}^{els}/\Gamma_{KCl}^{els} \approx 1$). Consequently, specific, physical interactions between the cations and sulfate groups primarily dictate uptake preference of ion exchange.

Figure 4-4c shows that the trend of membrane ion exchange preference is also exhibited in water uptake. The water content of membranes exchanged with cations follow the order $Li^+ > H^+ \approx Na^+ > K^+ > Cs^+$. Using H^+-K^+ exchange as an example, Figure 4-4b plots Γ_0 and the contribution to water uptake from solvation Γ_0^{slv}, cation-sulfonate physical interactions Γ_0^{phy}, and swelling Γ_0^{swe}. The decrease in water content as the membrane exchanges from H-form to K-form is due to the more favorable interactions of K^+ with the sulfonate compared to H^+. The more favorable interactions of K^+ with the sulfonate groups means that there is a smaller driving force for water to dilute the K^+-SO_3^+ pairs. Γ_0^{swe} and Γ_0^{slv} change slightly with ion exchange from H-form to K-form. But these changes are not directly due to ion exchange, but indirectly related to higher cation concentration and decreased swelling of the membrane because of lower water content in K-form membranes. Based on this analysis, stronger favorable interactions between cations and sulfonate groups reduce water uptake.

Figure 4-5 shows calculated (lines) and measured[69] (symbols) proton fraction in the membrane, $m_{H^+}^{\beta}/m_{M^-}^{\beta}$, as a function of the proton fraction of the surrounding mixed electrolyte, $m_{H^+}^{\alpha}/m_{Cl^-}^{\alpha}$ (a) and water content, λ, as a function of $m_{H^+}^{\beta}/m_{M^-}^{\beta}$ (c), for mixed chloride electrolytes with protons and multivalent cation Ni^{2+}, Ca^{2+}, Cu^{2+}, and Fe^{3+}. We fit β_{Ni^{2+},M^-}, β_{Ca^{2+},M^-}, β_{Cu^{2+},M^-}, and β_{Fe^{3+},M^-} to the measured water uptake and ion partitioning in Figure 4-5 by eye.

As the proton content of the external solution decreases, the proton content in the membrane sharply decreases. This is consistent with ideal-solution Donnan theory that shows that multivalent ions i preferentially partition into the membrane over univalent ions j according to Equation 4-16 with $\Gamma_{ji} = 1$.[198] Figure 4-5a shows that despite very different bulk solution properties, multivalent ions display nearly identical thermodynamic behavior in the membrane.

The model slightly over predicts exchange into the membrane of divalent ions and has larger errors for trivalent ions. If experimental artifacts from incomplete exchange are negligible, then these results demonstrate that upon accounting for solution-like interactions, the membrane does not uptake trivalent ions as much as expected. In addition to ideal-solution Donnan theory, the principle cause of the preferential partitioning of multivalent cations into the membrane is the

strong electrostatic interactions between the cations and multiple sulfonate groups. However, the extent of these electrostatic interactions in the membrane is overestimated by the model since sulfonate groups are treated as a line-charge rather than as imbeded at the interface of a phase-separated structure that cannot freely interact with the trivalent iron cation. This omission may explain the relatively high values of β_{i,M^-} for multivalent ion i given in Table 4-3.

Figure 4-5b shows that the model very accurately predicts water uptake in these membranes as a function of fractional proton exchange $m^{\beta}_{\mathrm{H}^+}/m^{\beta}_{\mathrm{M}^-}$. Consequently, this approach of incorporating solution-like interactions of multivalent electrolyte solutions in the membrane is sufficient to calculate water uptake into the membranes at dilute conditions. As with monovalent cations, the β_{i,M^-} and k_i values determine the water uptake in the membranes.

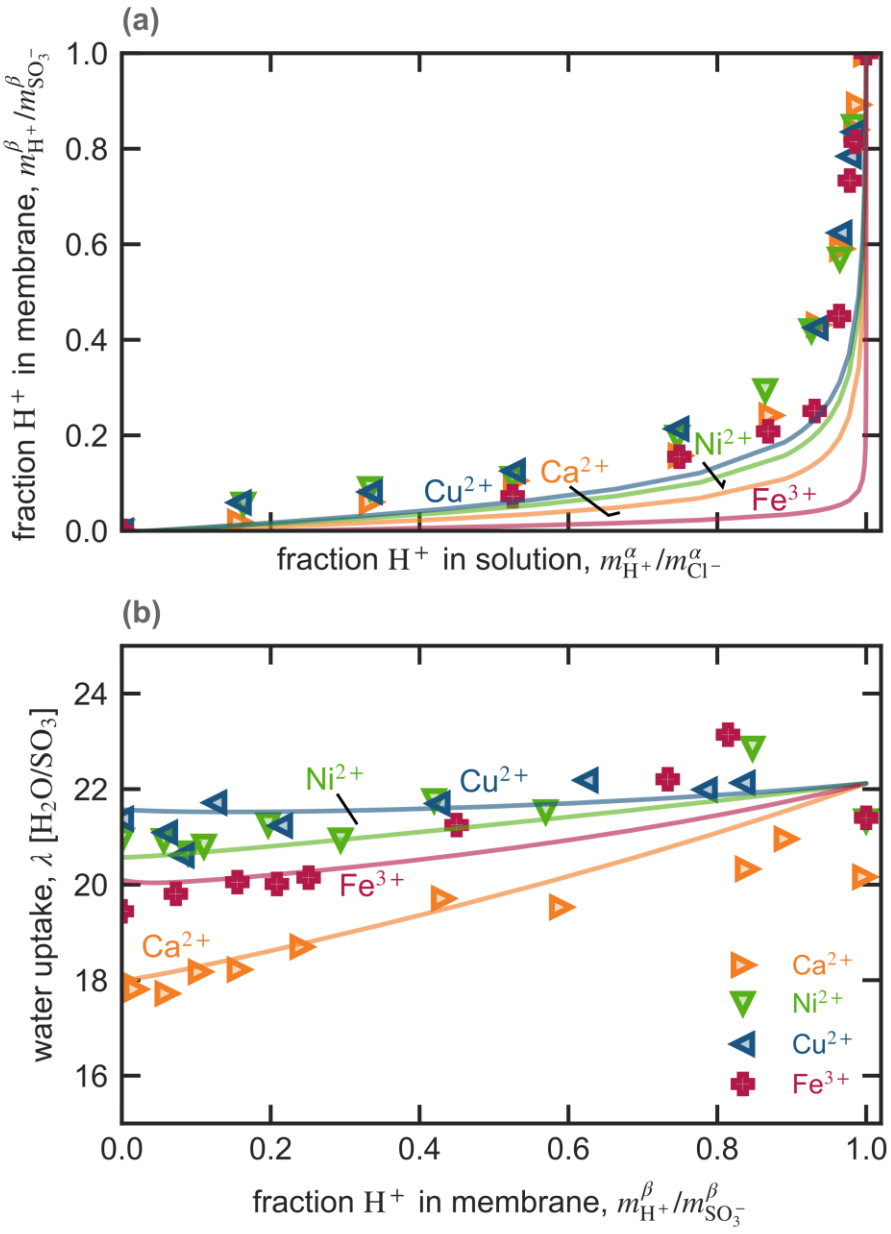

Figure 4-5. Measured (symbols)[69] and calculated (solid lines) membrane proton fraction in the membrane $m^{\beta}_{H^+}/m^{\beta}_{M^-}$ as a function of external solution proton fraction $m^{\alpha}_{H^+}/m^{\alpha}_{Cl^-}$ (a) and water content in the membrane, λ, as a function of proton fraction in the membrane $m^{\beta}_{H^+}/m^{\beta}_{M^-}$ (c) in a mixed aqueous electrolyte of hydrochloric acid and calcium (right triangles), nickel (down triangle), copper (left triangle), and iron (crosses) chloride. The external solutions were at 0.06 mol kg^{-1} total ion concentration.[69, 71]

4.5.3 Ion- and Water-Uptake Isotherms in Mixed Electrolytes

We now consider ion uptake from ternary electrolytes that are relevant in vanadium redox-flow-batteries. Figure 4-6 shows vanadium ion partitioning in a mixed sulfuric-acid electrolyte by plotting measured[92] (symbols) and predicted (lines) uptake of vanadium IV (VO^{2+}) and V (VO_2^+) (a) and total sulfate (dashed lines, right axis) and water uptake (solid lines, left axis) (b) as a function of total external vanadium concentration. The total sulfate molarity is 5 mol L^{-1}, which we convert to molality using a density of sulfuric acid solution of 1.3 g cm^{-3} given by Ref [94]. We fit $\beta_{V(IV)^{2+},M^-}$ and $\beta_{V(V)^+,M^-}$ to reduce error between the measured and calculated vanadium ion uptake in Figure 4-6a (see Table 4-3). As the vanadium concentration in the external solution increases, the membrane absorbs more vanadium. V(V) absorbs less into the membrane because of its lower charge. The water content of the membrane remains constant as the vanadium concentration increases whereas the total sulfate concentration decreases slightly. The model simultaneously calculates these three properties accurately.

In concentrated electrolytes, ion association is an important phenomenon. First, protons and sulfate associate to form bisulfate, as previously discussed. The dotted line in Figure 4-6a shows that HSO_4^- further associates with VO^{2+} leading to $HSO_4^- - VO^{2+}$ ion pairs.[232] Changing concentrations of various species shifts this equilibrium and couples the thermodynamic behaviors of the different species.

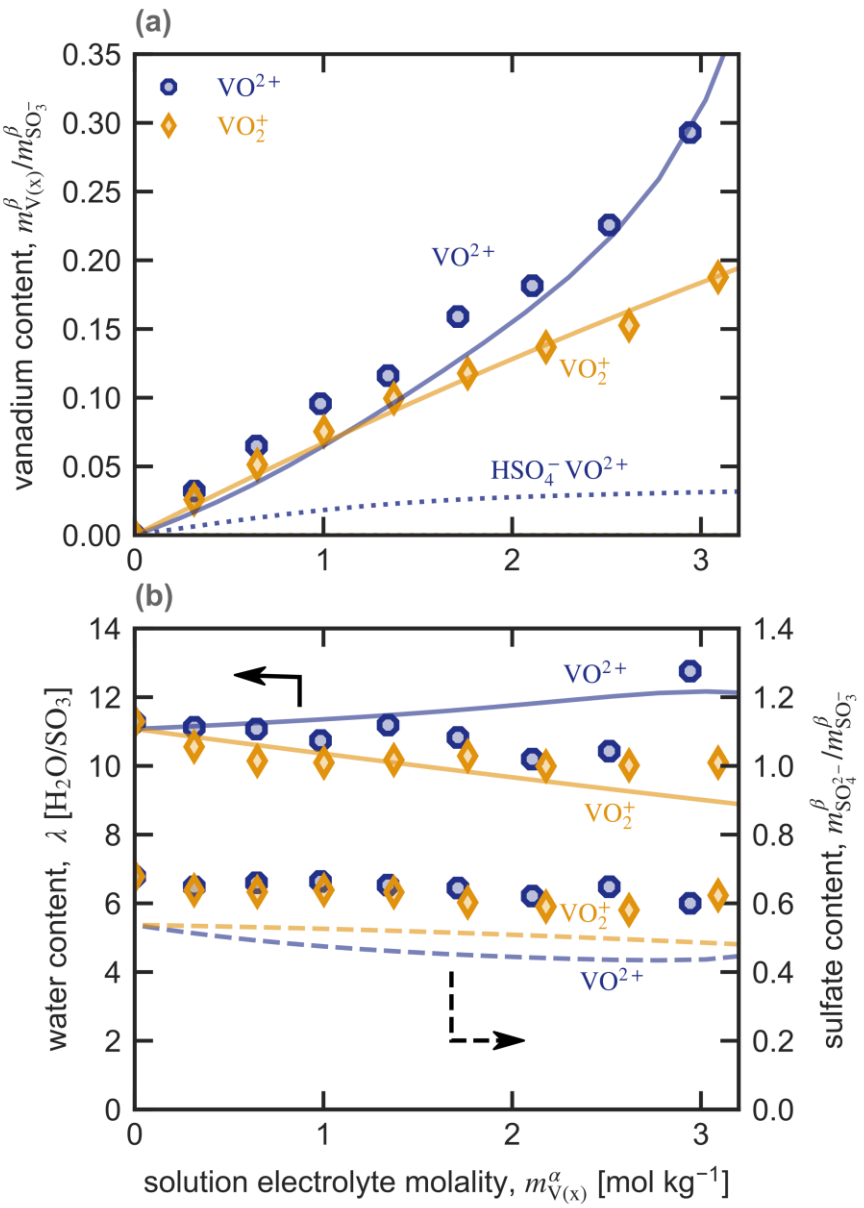

Figure 4-6. Measured[92] (symbols) and calculated (solid lines) membrane vanadium content $m^{\beta}_{V(x)}/m^{\beta}_{M^-}$ of V(IV) (octagons) and V(V) (diamonds) (a), water content λ (b, left axis) and total sulfate content $m^{\beta}_{SO_4^{2-}}/m^{\beta}_{M^-}$ (b, right axis) as a function external vanadium concentration in sulfuric acid with a total sulfate concentration of 5 mol L^{-1}. Dotted line in (a) is the content of V(IV)-bisulfate ion pairs $m^{\beta}_{HSO_4V(x)}{}^{mod}/m^{\beta}_{M^-}$.

4.6 Summary

This work develops a mathematical model for multicomponent thermodynamic activity of both water and ions in phase-separated cation-exchange membranes. Microscale theory predicts how

the free energy of the system changes with electrolyte concentration and membrane water content. The free energy accounts for the thermodynamic behavior of water and ions as they exhibit in bulk electrolyte solutions. We include swelling and steric interactions with the polymer into these expressions to account for the membrane.

The proposed model shows that a balance between solution-like interactions and polymer swelling dictates water uptake of membranes in concentrated electrolytes. The molecular properties of the aqueous cation are particularly important to describe water and ion uptake. Favorable interactions between cations and polymer sulfonate group increase their uptake and reduce water uptake.

The molecular-thermodynamic attributes of the ions in bulk electrolyte solution describe their thermodynamic properties in membranes. The model relies on one membrane-specific adjustable parameter and one membrane-cation specific adjustable parameter. The model quantitatively agrees with experiments over a wide range of electrolyte concentrations and compositions.

4.7 Nomenclature

Roman

$\bar{V}_i$	Partial molar volume of species i, m^3 mol^{-1}
E_b^0	Modulus of the polymer backbone, Pa
EW	Equivalent weight of polymer, $g_{polymer} mol_{SO_3^-}^{-1}$
K_j^{eq}	Equilibrium constant to form associated species j
M_i	Molar mass of species i, g mol^{-1}
N_A	Avogadro's constant, 6.0221 x 10^{23} mol^{-1}
$\mathcal{N}_i$	Total solvation number of ion i
R_{domain}	Domain radius, nm
a_i	Diameter limiting electrostatic interactions of species i, nm
c_i	Molar concentration of species i, mol dm^{-3}
$f_{i,j}$	Dissociation fraction of species i into species j
k_i	Water binding constant to species i
m_i	Molality of species i, mol $kg^{-1}_{solvent}$
n_i	Moles of species i, moles
p^{swe}	Elastic pressure, Pa
x_i	Mole fraction of species i
z_i	Charge number of species i
A	Debye-Hückel limiting slope in water, 1.1777 $mol^{1/2}$ $L^{-1/2}$
B	Debye-Hückel parameter in water, 3.291 $L^{1/2}$ $mol^{-1/2}$ nm^{-1}
F	Faraday's constant, 96,487 C mol^{-1}
G	Free energy, J
I	Ionic strength, mol m^{-3}
R	Universal gas constant, 8.3145 J mole K^{-1}
T	Temperature, 298 K
V	Volume, m^3
a	Average distance of closest approach between ions, nm
b	Spacing between charged groups of the polymer, nm
d	Spacing between hydrophilic domains

m	Scaling constant
p	Pressure, Pa
s_i	Stoichiometric coefficient of species i

Greek

α_i	Ratio of free species i before and after solvation
$\beta_{i,j}$	Specific interaction parameter between i and j, kg mol^{-1}
ϕ_i	Volume fraction of species i
Γ	Absorption non-ideality parameter
Φ	Quasi-electrostatic potential, V
λ	Membrane water content, $\mathrm{mol}_{\mathrm{water}}\,\mathrm{mol}_{\mathrm{SO_3^-}}^{-1}$
μ	Chemical potential, J mol^{-1}
ρ	Density, kg m^{-3}
σ	Debye-Hückel function 2
τ	Debye-Hückel function 1

Subscript

0	Solvent (*i.e.* water)
domain	Hydrophilic domain
M	Membrane
i	Species i

Superscript

∞	Infinite dilution
mol	Molecular Construct
exp	Experimental Construct
θ	Reference
els	Electrostatic contribution
swe	Swelling contribution
ex	Excess contribution
id	Ideal mixing contribution
phy	Physical contribution
slv	Solvation contribution
stc	Steric contribution
α	Solution phase
β	Membrane phase
δ	Phase
0	Dry membrane

4.8 Chapter 4 Supporting Information

4.8.1 Fraction of Solvated Species

Stokes and Robison[206] showed (and later clarified by Schonert,[207-208] and Zerres and Prausnitz[66]) that for stepwise solvation of undissolved ion M^z with valance z by s solvent S molecules to give solvated ion M_i^z(i.e. $M^z + sS \rightarrow M_i^z$), α_0 and α_i is

$$\alpha_0 \equiv \frac{x_{0,\mathrm{slv}}}{x_0} = \frac{\left[\frac{n_0 - \sum_{i\neq 0}\bar{h}_i n_i}{n_0 + \sum_{i\neq 0} n_i\left(1-\bar{h}_i\right)}\right]}{\left[\frac{n_0}{n_0 + \sum_{i\neq 0} n_i}\right]} = \frac{1 - \sum_{i\neq 0}\bar{h}_i \frac{n_i}{n_0}}{x_0 + \sum_{i\neq 0} x_i\left(1-\bar{h}_i\right)} \qquad 4\text{-}19$$

$$\alpha_i \equiv \frac{x_{i,\mathrm{slv}}}{x_i} = \frac{1}{x_0(1+k_i\alpha_0 x_0)^{\mathcal{N}_i}\left(1 + \sum_{j\neq 0}\frac{n_j}{n_0}\left(1-\bar{h}_j\right)\right)}$$

$$\alpha_i^{\infty} = \frac{1}{(1+k_i)^{\mathcal{N}_i}}$$

$$\bar{h}_i = \frac{\mathcal{N}_i k_i \alpha_0 x_0}{1 + k_i \alpha_0 x_0}$$

where $\bar{h}_i$ and $\mathcal{N}_i$ are, respectively, the average solvation number and total number of solvent binding sites of ion i and k_i is its binding constant (= $\exp\frac{-\Delta H_i^{\mathrm{slv}}}{RT}$). Schönert [207] showed that, without losing model fit, $\mathcal{N}_i$ is $4z_i$ for anions and $5z_i$ for cations. Equation 4-4 uses a simplified model of solvation in which each solvent molecule binds to an independent site on the ion that each have a constant molar enthalpy $\Delta H_i^{\mathrm{slv}}$.

4.8.2 Domain Swelling

Geometric arguments give total hydrophilic domain size, R_{domain}, and the central, solvent filled domain radius, R_{solution}

$$R_{\mathrm{domain}} = \frac{d}{2}\phi_{\mathrm{domain}}^{1/n} \qquad 4\text{-}20$$

$$R_{\mathrm{solution}} = \frac{d}{2}\phi_{\mathrm{solution}}^{1/n} \qquad 4\text{-}21$$

where the volume fraction of domains, ϕ_{domain}, is the sum hydrophilic polymer and solution volume fraction ($= \phi^0_{\text{domain}} + 1 - \phi_{\text{M}}$). ϕ_{solution} is the volume fraction of only the solution ($= 1 - \phi_{\text{M}}$). n is a geometric parameter that is 1, 2, and 3 for lamellar, cylindrical, and spherical domains, respectively. For phase-separated membranes, X-ray scattering experiments can characterize this domain size. These measurements show that d scales according to

$$\frac{d}{d^0} = \phi_{\text{M}}^{-m} \qquad 4\text{-}22$$

where material m is a scaling parameter.

4.8.3 Bulk Solution Parameters

The solvent/cation binding constant k_i and cation-anion interaction parameter, $\beta_{i,j}$, dictate the thermodynamic properties of the electrolyte. We use osmotic coefficient ($= \frac{\mu_0 - \mu_0^\theta}{RTM_0 \sum_i m_i}$) of binary salt of bulk electrolyte solutions across the entire range of concentrations reported in Stokes and Robinson and Bonner [172, 221] to fit these parameters simultaneously using the calculated solvent chemical potential from Table 4-1. A least-squares Trust Region Reflective algorithm minimized the difference between predicted and measured osmotic coefficient with k_i bounded between 0 and 20. SciPy package of Python implemented the algorithm. Figure 4-7 shows calculated (lines) and measured (symbols) osmotic coefficients as a function of salt molality. The median error ($= \sum_{\text{all concentrations}} 1 - \frac{\text{calculated}}{\text{measured}}$) between predicted and measured osmotic coefficients is 1.52%. Table 4-4 and Table 4-5 provides results values ions k_i and salt $\beta_{i,j}$. If solution thermodynamic data for an ion are not available, we use a value from a similarly charged ion, which Table 4-4 and Table 4-5 note.

Table 4-4. k_i values fit to bulk solution osmotic coefficients

Cation	k_i	notes
Ca^{2+}	5.38	
Cr^{3+}	20	
Cs^{+}	2.74	
Cu^{2+}	0.244	
Fe^{3+}	0.566	
H^{+}	1.14	
K^{+}	0.430	
Li^{+}	3.59	
Na^{+}	0.505	
Ni^{2+}	5.41	
VO^{2+}	5.41	Same as Ni^{2+}
VO_2^{+}	3.59	Same as Li^{+}

Table 4-5. Fit bulk solution thermodynamic parameters

Salt	$\beta_{i,j}$ (kg mol^{-1})	notes
Ca^{2+}-Br^{-}	0.159823	
Ca^{2+}-Cl^{-}	0.079505	
$Ca^{2+}I^{-}$	0.20858	
Cr^{3+}-Cl^{-}	0.3	
Cs^{+}-Br^{-}	-0.0514	
Cs^{+}-Cl^{-}	-0.04674	
Cs^{+}-I^{-}	-0.06456	
Cu^{2+}-Cl^{-}	0.093452	
Cu^{2+}-SO_4^{2-}	-0.16372	
Fe^{3+}-Cl^{-}	0.3	
H^{+}-SO_4^{2-}	0.168173	
H^{+}-Br^{-}	0.188256	
H^{+}-Cl^{-}	0.129451	
H^{+}-$TFMS^{-}$	0.148227	
K^{+}-Br^{-}	0.025083	
K^{+}-Cl^{-}	0.019728	
K^{+}-I^{-}	0.037175	
K^{+}-$TFMS^{-}$	-0.02931	
Li^{+}-Br^{-}	0.123872	
Li^{+}-Cl^{-}	0.082837	
Li^{+}-I^{-}	0.148075	
Li^{+}-$TFMS^{-}$	0.128096	
Na^{+}-Br^{-}	0.076629	
Na^{+}-Cl^{-}	0.055678	
Na^{+}-I^{-}	0.10295	
Na^{+}-$TFMS^{-}$	0.057604	
Ni^{2+}-Cl^{-}	0.228662	
Ni^{2+}-SO_4^{2-}	-0.26269	
VO^{2+}-SO_4^{2-}	-0.164	Set to Cu^{2+}-SO_4^{2-}
VO_2^{+}-SO_4^{2-}	0.168	Set to H^{+}-SO_4^{2-}
V^{3+}-Cl^{-}	0.3	Set to Fe^{3+}-Cl^{-}

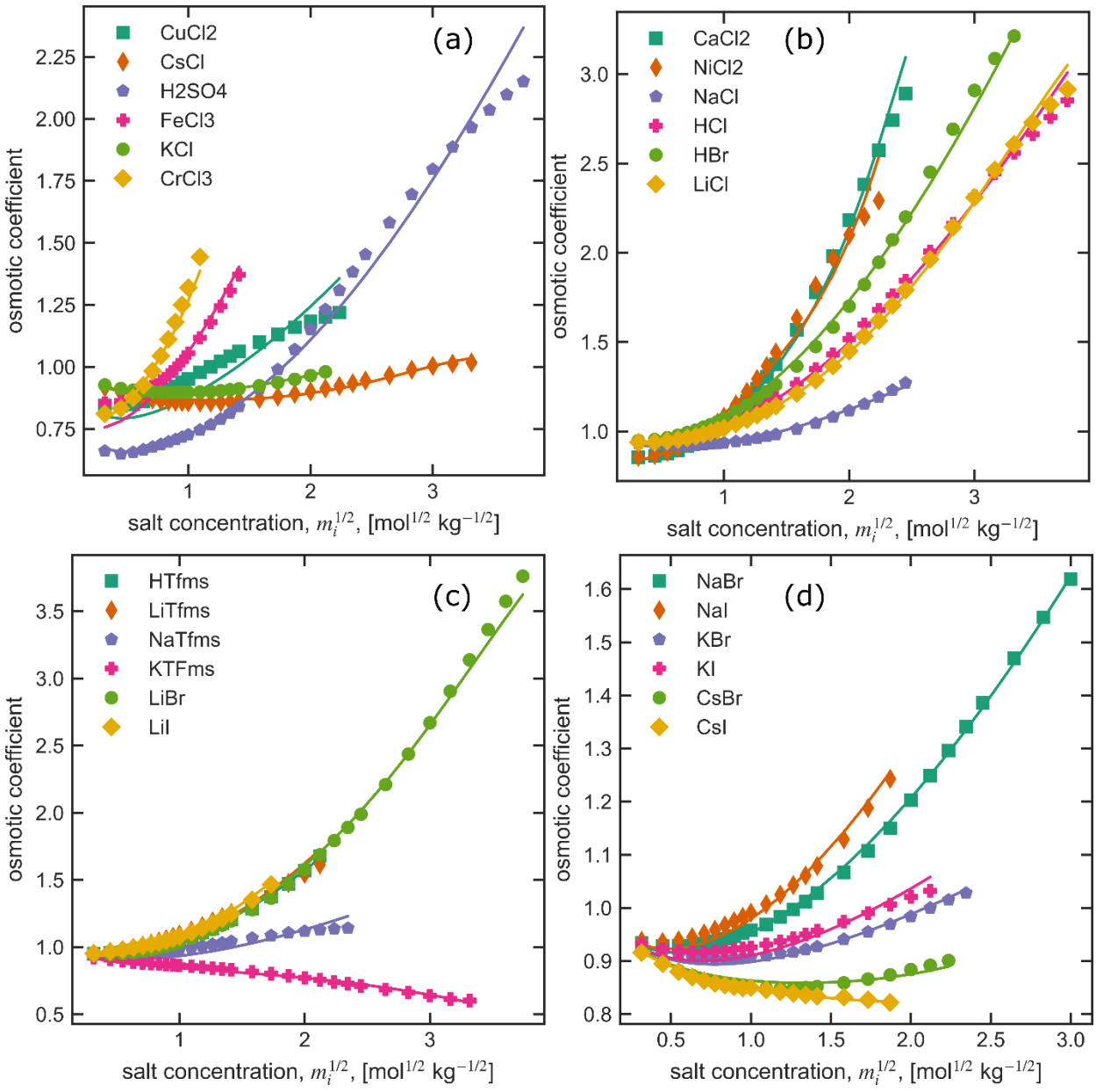

Figure 4-7. Measured (symbols) and calculated (lines) osmotic coefficient as a function of molality for different salts.

This work studies many of the species that associate with each other. Table 4-6 lists the considered reactions and their dissociation constants. These dissociation constants relate to the primary reference chemical potential and, therefore, are dimensionless. Without a report of the equilibrium constant of the V(III)-Cl and -sulfate dissociation, it is set to the value of sulfate-chromium dissociation.

Table 4-6. Speciation reactions and equilibrium constants

Reaction	Equilibrium Constant, K_{eq}	Notes and Source
$HSO_4^- \leftrightarrow H^+ + SO_4^{2-}$	1.85x10^{-4}	[233]
$NiCl^+ \leftrightarrow Ni^{2+} + Cl^-$	7.17x10^{-3}	[233]
$FeCl^{2+} \leftrightarrow Fe^{3+} + Cl^-$	5.96x10^{-4}	[233]
$CrCl^{2+} \leftrightarrow Cr^{3+} + Cl^-$	1.04x10^{-3}	[233]
$CuSO_4 \leftrightarrow Cu^{2+} + SO_4^{2-}$	7.23x10^{-5}	[233]
$NiSO_4 \leftrightarrow Ni^{2+} + SO_4^{2-}$	8.54x10^{-5}	[233]
$VOHSO_4^+ \leftrightarrow VO^{2+} + HSO_4^-$	0.01059	[223]

For membrane properties, Kusoglu et al. extensively characterized PFSA membranes using mechanical measurements and small-angle X-ray scattering experiments.[56, 211, 220] They measured a Young's modulus of 47-65 MPa for Nafion PFSA membranes in liquid water and a polymer volume fraction of 0.59. A scaling relationship scales the wet modulus of the membrane, $E_{\mathrm{b}}^{\mathrm{wet}}$, to the inherent modulus of the hydrophobic backbone: $E_{\mathrm{b}}^{0} = \frac{E_b^{\mathrm{wet}}}{1-(1-\phi_{\mathrm{M}})^{\frac{1}{2}}}$, which gives a modulus between 131-181 MPa. Additionally, the authors showed that ϕ_{domain} is 0.078, n is well-represented by 2 for a membrane in liquid water, m is 1.33, and d^0 is 2.7 nm. [56, 211, 220] The modulus of the membrane backbone equilibrated in water vapor is 320 MPa as calculated by Kusoglu et al.[56]

The distance between charged groups, b, in Nafion calculated from molecular dynamics simulations is approximately 0.48 nm,[218] which is consistent with small-angle X-ray scattering experiments.[12]

4.8.4 Domain Size in Concentrated Electrolytes

Upon using the predicted membrane water content as a function of external HBr concentration given in Figure 4-1, Equation 4-22 calculates how the domain size ($d - d^0$) changes as function of the external HBr molality, as Figure 4-8 shows.

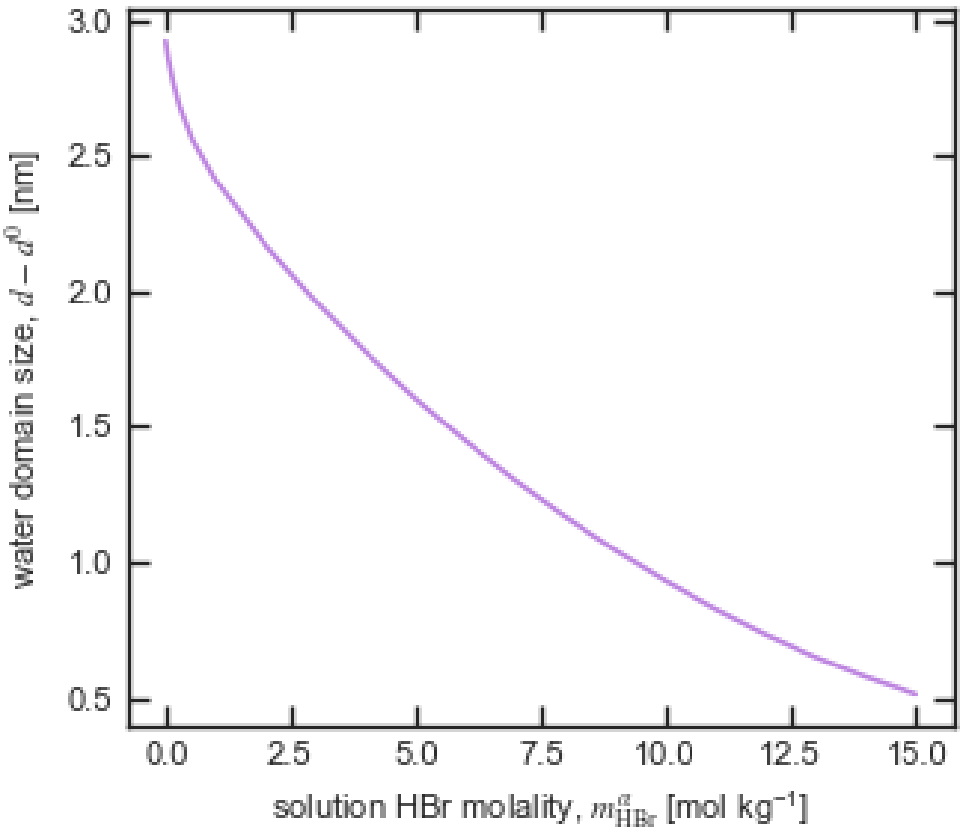

Figure 4-8. Calculated hydrophilic domain size as a function of external HBr molality.

4.8.5 Ion Partitioning in Dilute, Mixed Lithium Electrolytes

Figure 4-9 shows that the model is externally valid for lithium-alkali electrolyte mixtures by plotting predicted (lines) and measured[67] (symbols) lithium fraction in the membrane, $m^{\beta}_{\mathrm{Li}+}/m^{\beta}_{\mathrm{M}-}$, (a) and water content, λ, (b) as a function of lithium fraction in the external solution, $m^{\alpha}_{\mathrm{Li}+}/m^{\alpha}_{\mathrm{Cl}-}$, for the same alkali cations as Figure 4-4. Similar to proton-alkali mixed electrolytes, stronger cation-membrane physical interaction causes greater cation partitioning into the membrane. Agreeing with work by Pintauro and coworkers,[156, 200] the degree of physical cation-sulfonate interaction follows alkali cation ionic size with $Cs^+ > K^+ > Na^+$.

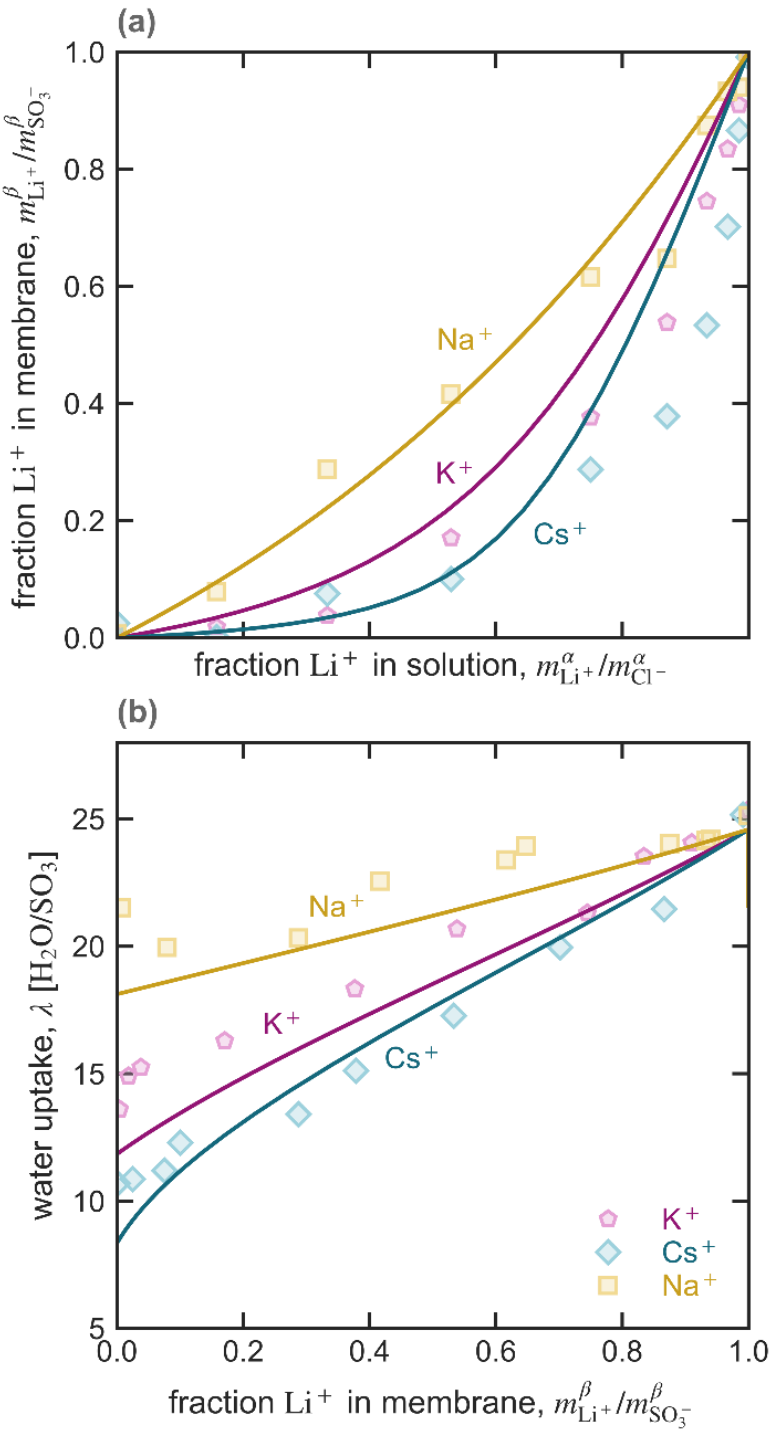

Figure 4-9. Measured[67] (symbols) and calculated (solid lines) membrane lithium fraction in the membrane $m^{\beta}_{Li^+}/m^{\beta}_{M^-}$ as a function external solution lithium fraction, $m^{\alpha}_{Li^+}/m^{\alpha}_{Cl^-}$ (a) and water content λ as a function membrane lithium fraction $m^{\beta}_{Li^+}/m^{\beta}_{M^-}$ (b), in a mixed aqueous electrolyte of lithium chloride and sodium (squares), potassium (pentagons), and cesium (tilted squares) chloride.

5 Theory of Multicomponent Phenomena in Cation-Exchange Membranes, II: Transport Model and Validation

5.1 Chapter Abstract

Multicomponent mass-transport in cation-exchange membranes involves the movement of multiple species whose motion is coupled one to another. This phenomenon mediates the performance of numerous electrochemical and water purification technologies. This work presents and validates against experiment a mathematical model for multicomponent mass transport in phase-separated cation-exchange membranes (*e.g.*, perfluorinated sulfonic-acid ionomers). Stefan-Maxwell-Onsager theory describes concentrated-solution transport. Hydrodynamic theory provides constitutive relations for the solute/solvent, solute/membrane, and solvent/membrane friction coefficients. Classical porous-medium theories scale membrane tortuosity. Electrostatic relaxation creates friction between ions. The model uses calculated ion and solvent partitioning between the external solution and the membrane from Part I (Chapter 4) of this series and incorporates the corresponding ion speciation into the transport coefficients. The proposed transport model compares favorably to properties (*e.g.*, membrane conductivity, transference numbers, electroosmosis, and permeability) measured in dilute and concentrated aqueous binary and ternary electrolytes. When combined with the findings in Part I (Chapter 4), the results reveal that the concentration and type of ions in the external solution alter the solvent volume fraction and viscosity in the hydrophilic pathways of the membrane, changing macroscale ionomer conductivity, permeability, and transference numbers. This work provides a physicochemical framework to predict ion-exchange-membrane performance in multicomponent systems exhibiting coupled transport.[**]

5.2 Introduction

Transport of multiple ions in phase-separated, solvent-filled membranes dictates performance in numerous energy-storage and conversion devices.[12, 192-193] For example, recent advances in proton-exchange-membrane (PEM) fuel cells involve new catalyst alloys and cerium additives that increase kinetic performance and durability but introduced challenges related to multi-ion transport in the cation-exchange membrane.[234-237] Similarly, low-temperature PEM electrosynthesis technologies have recently received intense interest, but the involved products and reactants can transport across the membrane.[7, 238-239] Membranes in redox-flow batteries (RFBs) absorb and transport numerous redox-active and supporting-electrolyte species. Often, these devices operate in aqueous environments and use perfluorinated sulfonic-acid (PFSA) ionomers as separators.[12] Multicomponent transport in these materials faces the conflicting goals of promoting movement of current-carrying ions between the anode and cathode while preventing crossover of redox-active species or contaminants that decrease device performance.[11-12] Although previous literature

[**] Published as Crothers, A. R.; Darling, R. M.; Radke, C. J.; Weber, A. Z., Theory of Multicomponent Phenomena in Cation-Exchange Membranes: Part II. Transport Model and Validation. *J. Electrochem. Soc.* **2020,** *167* (1), 013548.

provides useful descriptions of transport in these membranes, [14-15, 32-33, 72-73, 195-197, 240-241] multi-ion transport and thermodynamics remain poorly understood.[96]

There are two general approaches for mass-transport in ion-exchange membranes.[9, 82] In the limiting regime of negligible ion and water concentration in the membrane, dilute-solution theory is valid.[9, 82] Dilute-solution theory predicts that the flux of a species i is proportional to the concentration gradient of i plus the force an electric field applies to i.[9, 82] This theory predicts that the number of transport coefficients (*e.g.* Fickian diffusion coefficients) scales by the number of mobile species in the membrane (*i.e.* $N-1$ where N is the total number of species present, including mobile species and the membrane).[9, 82] The dilute-solution theory approach has the benefit of being relatively simple to use and understand.[9, 82] It also requires relatively few experiments to characterize fully all transport properties.[9, 82] Unfortunately, dilute-solution theory cannot describe numerous transport phenomena exhibited by ion-exchange membranes, including electroosmosis (the transport of water under an applied electric field), the flow of ions due to a water concentration gradient, and, generally, the flux of species i due to a concentration gradient of species j.[9, 79, 82, 91, 96, 235, 242] As a result, measured dilute-solution diffusion coefficients in concentrated solutions are not solely properties of the material. Rather, they are effective coefficients valid only for the operating conditions for which they are measured.[96]

The second approach is concentrated-solution theory.[9, 82] This formalism is more general and is applicable to solutions that range from highly concentrated to the dilute limit, in which case it reduces to dilute-solution theory. [9, 82] Concentrated-solution theory predicts that the flux of species i is a linear function of the electrochemical potential gradient of all but one species j present.[9, 82] Concentrated-solution theory is the general instantiation of classical nonequilibrium thermodynamics for multicomponent solutions.[9, 30, 36, 82] It naturally describes the coupling between forces on species j and transport of species i. [9, 30, 32-33, 36, 72, 78, 82, 196, 243-244] The number of independent transport coefficients in concentrated-solution theory (*e.g.* binary diffusion coefficients) scales as $(N-1)N/2$, as it should in real systems.[9] Dilute-solution theory, therefore, contains an insufficient number of transport parameters. An unfortunate consequence of a concentrated-solution description is the introduction of a large number of parameters for multicomponent systems. For example, a typical vanadium RFB with eight species necessitates 28 different experiments to characterize the transport properties completely. Further, these transport coefficients are strong functions of concentration and membrane properties (as with dilute-solution theory) and, therefore, must be quantified across relevant conditions.[32, 243]

In between the dilute and concentrated formalisms, there are compromise theories that incorporate certain but not all transport couplings into dilute-solution theory, such as making ion flux related to water transport or adding in electro-osmosis.[9, 49, 86, 245] These models provide a promising method to predict multicomponent transport while remaining relatively simple.[11, 89-90, 96, 246] However, it is not clear under what conditions these simpler approaches are valid representations of the full concentrated-solution description.

Studies of multicomponent transport in ion-exchange membranes face a choice between using dilute-solution theories and neglecting relevant transport couplings or using concentrated-solution theory but introducing an intractable number of parameters. We reduce the intractability of concentrated-solution theory by providing a mathematical formalism to calculate transport parameters at the relevant conditions based on microscale properties of the membrane. By

estimating the full set of transport properties, the model reduces the burden on extensive experimental characterization.

In this paper, we use the Stefan-Maxwell-Onsager formulation to calculate transport properties.[9, 74, 80, 82] This theory is formally equivalent to other formulations of concentrated-solution theory and attributes transport coefficients to frictional interactions between species.[9, 74, 80, 82] The frictional interactions are calculable with microscale theories.[85]

The detailed transport model in Chapter 3 informs the microscale interactions. However, the engineering model proposed in this chapter captures the essential molecular interactions without the computational complexity of Chapter 3. Chapter 3 describes transport with a semi-dilute-solution formalism whereas this chapter uses the full concentrated-solution approach.

The paper is as follows. We outline calculation of the full matrix of Stefan-Maxwell-Onsager transport coefficients based on molecular descriptors of the system. The proposed model elucidates the mechanisms driving multicomponent transport in water-filled, cation-exchange membranes. In it, we build upon the thermodynamic model of Part I (Chapter 4)[247] to calculate types, amounts, and speciation of components that move across the membrane. The theory section summarizes the pertinent concentrated-solution transport framework. It also develops a microscale-based model for transport properties and their dependence on composition and membrane material properties. The proposed model relies on physical parameters mostly available from bulk-solution measurements. In the Results and Discussion section, literature data relevant for fuel-cell and RFB membranes validate the model.

5.3 Theory

We focus on perfluorinated sulfonic-acid (PFSA) chemistry because of its extensive characterization and widespread use.[12] Nafion is the most widely-used type of PFSA.[12] This polymer consists of a hydrophobic polytetrafluoroethylene backbone (PTFE) with side chains that terminate in negatively charge sulfonate groups.[12] Upon immersion in aqueous solutions or water vapor, the domains microphase separate into into water-filled, interconnected hydrophilic domains or "pores" and hydrophobic, PTFE structural domains.[12] In this section, non-equilibrium thermodynamics is employed for multi-ion transport in the membrane structure. We provide a consistent treatment of equilibrium ionic speciation and develop a microscopic model for friction coefficients. Finally, we relate the predicted friction coefficients to macroscopic, experimentally accessible concentrated-solution transport parameters.

5.3.1 Multicomponent Mass-Transport Equations

Isothermal, isotropic, multicomponent mass transport is governed by the nonequilibrium thermodynamic driving force on species i, $\boldsymbol{d}_i$, balancing against the drag forces between i and all other species j in the system. According to the Stefan-Maxwell-Onsager theory,[9, 32, 36]

$$\boldsymbol{d}_i = \sum_{j \neq i} K_{ij}(\boldsymbol{v}_j - \boldsymbol{v}_i) \qquad 5\text{-}1$$

where K_{ij} characterizes the friction between species i and j and $\boldsymbol{v}_i$ is the velocity of species i. The driving force for transport is[36]

$$\boldsymbol{d}_i = c_i\left(\nabla\mu_i - \frac{M_i}{\rho}\nabla p - \boldsymbol{X}_i + \frac{M_i}{\rho}\sum_j \boldsymbol{X}_j c_j\right) \quad 5\text{-}2$$

where c_i, μ_i, M_i, and $\boldsymbol{X}_i$ are, respectively, the concentration (defined later), electrochemical potential, molar mass, and external body force on species i; p is pressure, and ρ is mass density. We account for electrostatic forces in the electrochemical potential μ_i rather than in a body force $\boldsymbol{X}_i$. The membrane, species M, is affixed to a support (*e.g.* a mesh or gasket) that imparts a pinning force $\boldsymbol{X}_{\mathrm{M}}$. A force balance on the membrane dictates that this force is equal to the pressure in the membrane, $\nabla p = \boldsymbol{X}_{\mathrm{M}}$.[23, 248-249] An explicit stress balance in the membrane specifies $\boldsymbol{X}_{\mathrm{M}}$.[73] Absent other external forces, substitution of Equation 5-2 into Equation 5-1 for each mobile species i in the membrane relates the electrochemical potential gradients to species velocities [9, 32, 36]

$$c_i\nabla\mu_i = K_{i\mathrm{M}}(-\boldsymbol{v}_i) + \sum_{j\neq i,\mathrm{M}} K_{ij}(\boldsymbol{v}_j - \boldsymbol{v}_i) \quad 5\text{-}3$$

For $i = \mathrm{M}$, isothermal Gibbs-Duhem demands that

$$c_{\mathrm{M}}\nabla\mu_{\mathrm{M}} - \nabla p = \sum_{i\neq\mathrm{M}} K_{i\mathrm{M}}\boldsymbol{v}_i \quad 5\text{-}4$$

where $\boldsymbol{v}_i$ is a superficial velocity and K_{ij} is the friction coefficient between species i and j. The electrochemical potential is a function of composition, pressure, temperature, T, and electric state. The pressure gradient appears in Equation 5-4 but not in Equation 5-3 because of the pinning force on the membrane.[23, 78, 249] In Equations 5-3 and 5-4, the reference velocity is that of the membrane (*i.e.* $\boldsymbol{v}_{\mathrm{M}} = 0$). Conservation of the membrane mass provides an additional constrain that relates $\boldsymbol{v}_{\mathrm{M}}$ to the laboratory frame of reference (*i.e.* to the support that affixes the membrane).[250] At steady state, the membrane is not actively swelling and the membrane velocity equals the velocity of the laboratory. We denote transport coefficients that depend on the frame-of-reference with a superscript of the reference species (*i.e.*, M). If the species are chemically independent (*i.e.*, no reactions between them), then for N species (including all species absorbed in the membrane and the membrane), there are $N-1$ independent equations of this form (the proceeding section lifts this restriction).[36] Therefore, Equation 5-3 in matrix form is[32]

$$\boldsymbol{D} = \boldsymbol{M}^{\mathrm{M}}\boldsymbol{V} \quad 5\text{-}5$$

where $\boldsymbol{D}$ and $\boldsymbol{V}$ are $N-1$ by 3 matrices in which the ith row contains, respectively, the components of the 3D vector of negative driving forces and velocities of species i (*i.e.* $D_{i*} = c_i\nabla\mu_i$ and $V_{i*} = \boldsymbol{v}_i$, where the subscript $*$ denotes a row) excluding the row and column M, due to linear dependence.[75] The transport coefficient matrix $\boldsymbol{M}^{\mathrm{M}}$ is $N-1$ by $N-1$ where $M_{ij}^{\mathrm{M}} = K_{ij}$ for $i \neq j$ and $M_{ii}^{\mathrm{M}} = -\sum_{j\neq i} K_{ij}$.

Onsager reciprocal relations dictate that the friction coefficients are symmetric, $K_{ij} = K_{ji}$.[75] Consequently, there are $N(N-1)/2$ friction coefficients. K_{ij} coefficients are related to binary interspecies diffusion coefficients according to[9]

$$\mathfrak{D}_{ij} = \frac{RTc_i c_j}{K_{ij} c_{\mathrm{T}}} \qquad 5\text{-}6$$

where c_{T} is the total molar concentration of the solution.

The molar concentration for a phase-separated membrane is defined either on a superficial basis (*e.g.*, a homogenous phase) that includes the polymer volume ($c_i' = n_i / \sum_i n_i \bar{V}_i$ where n_i and $\bar{V}_i$ are the moles and partial molar volume of species i), or an interstitial basis (*e.g.*, heterogeneous phases) that only includes the electrolyte solution in the membrane pores ($c_i = n_i / \sum_{i \neq \mathrm{M}} n_i \bar{V}_i$). We use the latter definition because it is more amenable to microscopic theories of $\mathfrak{D}_{ij}$ that are derived for bulk electrolyte solutions or porous media. We neglect changes to the total molar concentration c_{T} in the hydrophilic domains; the molar concentration of species i is $c_i = c_{\mathrm{T}}(n_i / \sum_{j \neq \mathrm{M}} n_j)$ where c_{T} is set to the molar concentration of salt-free water at 25 °C, (= 55.2 mol dm^{-3}). This assumption is rigorously valid for high water contents ($\lambda > 10$) or for membranes exchanged with cations that have molar volumes similar to water.

5.3.2 Transport with Ion Association

Many ionic species undergo ion-pair or acid-base equilibria that alter transport properties.[251] Transport measurements typically control amounts of neutral components added to the system and treat the N constituent ionic species as fully dissociated in solution (we call this the "Experimental Construct" and denote quantities in the construct with superscript exp). For example, sulfuric acid is treated as protons and sulfate ions. The Experimental Construct provides independent driving forces and fluxes for species. However, because friction between species depends on size and charge, microscopic models consider N^{mol} species in their actual, associated states (we call this the "Molecular Construct" and denote quantities in this construct with superscript mol). For example, sulfuric acid is treated as protons, bisulfate, and sulfate ions.[85]

By accounting for how driving forces in the Molecular Construct are interdependent, Appendix 5-A shows that the friction-coefficient matrix in the Molecular Construct, $\boldsymbol{M}^{\mathrm{M}^{\mathrm{mol}}}$ (a $N^{\mathrm{mol}} - 1$ by $N^{\mathrm{mol}} - 1$ matrix), is related to friction coefficients in the Experimental Construct, $\boldsymbol{M}^{\mathrm{M}^{\mathrm{exp}}}$ according to

$$\boldsymbol{M}^{\mathrm{M}^{\mathrm{exp}}} = \left(\boldsymbol{F} \left[\boldsymbol{M}^{\mathrm{M}^{\mathrm{mol}}} \right]^{-1} \boldsymbol{F}^{T} \right)^{-\mathbf{1}} \qquad 5\text{-}7$$

where $\boldsymbol{F}$ is a $N - 1$ by $N^{\mathrm{mol}} - 1$ matrix with i, j entries $f_{i,j}$, and $f_{i,j}$ is the fraction of moles of species i in the Experimental Construct, n_i^{exp}, that partially associates into n_j^{mol} moles of species j in the Molecular Construct

$$f_{i,j} = -\frac{n_j^{\mathrm{mol}} s_i}{n_i^{\mathrm{exp}} s_j} \qquad 5\text{-}8$$

Here, s_i and s_j are the stoichiometric coefficients of species i and j, respectively, in the reaction of i associating with another species to form j. For example, protons (species i) associating with sulfate ions to form bisulfate ions (species j). Note that $\sum_j f_{i,j} = 1$. Theory gives the Molecular Construct transport coefficients (*e.g.*, $\boldsymbol{M}^{\mathrm{M}^{\mathrm{mol}}}$) that we convert to the Experimental Construct

transport coefficients (*e.g.*, $\boldsymbol{M}^{\mathrm{M}^{\exp}}$) to calculate measured transport properties. In Part III (Chapter 6)[104], it is more convenient to make calculations using Equation 5-3 in the Experimental Construct. In that case, $\boldsymbol{M}^{\mathrm{M}^{\exp}}$ provides $\mathfrak{D}_{ij}^{\exp}$'s according to the definition of $\boldsymbol{M}^{\mathrm{M}}$. For convenience, we drop the superscript exp outside this section for quantities in the experimental construct.

5.3.3 Friction Coefficients

In a liquid solution consisting of solvent and ionic species in a membrane, there are six types of friction coefficients: ion/solvent, cation/anion, cation/cation, anion/anion, ion/membrane, and solvent/membrane.[32, 81, 84-85] All but the last two types are present in bulk electrolyte solutions.[84] Accordingly, we use measurements of bulk friction coefficients in solution and apply common theories for their compositional dependence to calculate their value in the hydrophilic domains of the membrane. This approach requires that the distance over which these molecular interactions occur is smaller than the size of the hydrophilic domains; this assumption is justified for the highly concentrated solutions in the membrane that strongly screen hydrodynamic influences and electrostatic interactions. A hydrodynamic model of membrane pores gives ion and solvent/membrane friction coefficients. The transport coefficients are scaled by the tortuosity τ and volume fraction, $1-\phi_{\mathrm{M}}$, of the hydrophilic membrane domains to relate the transport coefficients of a single hydrophilic domain to effective, superficial membrane fluxes used in Equations 5-3 and 5-4.[37] Tortuosity scales according to Archie's law, $\tau=(1-\phi_{\mathrm{M}})^{-\chi}$, where χ is the tortuosity scaling parameter.[252] ϕ_{M} is the volume fraction of the polymer backbone ($=\bar{V}_{\mathrm{M}}/(\bar{V}_{\mathrm{M}}+\bar{V}_0 n_0/n_{\mathrm{M}})$ neglecting the volume of absorbed ions in the membrane), $\bar{V}_{\mathrm{M}}$ is the partial molar volume of polymer per charged group (= 523.8 cm^3/mole-SO_3^- for Nafion).[12] χ is independent of water content and electrolyte concentration in the membrane.

5.3.3.1 Ion/Solvent and Ion/Ion Friction Coefficients

For ion/solvent friction coefficients, the Stokes-Einstein equation predicts the changes with solution viscosity of the binary diffusion coefficient as a result of the drag of an ion, idealized as a sphere, moving (or rotating) through a stagnant continuum solvent [85]

$$\mathfrak{D}_{i0}^{\mathrm{mol}}=\left(\frac{1-\phi_{\mathrm{M}}}{\tau}\right)\frac{\eta^{\infty}}{\eta}\mathfrak{D}_{i0}^{\infty\,\mathrm{mol}} \qquad 5\text{-}9$$

where η is the solution viscosity and the superscript ∞ denotes infinite dilution. The term in parenthesis on the right side corrects the interstitial diffusion coefficient for the tortuosity and volume fraction of hydrophilic channels. The viscosity ratio arise because the solution becomes more viscous at high ionic strengths due to increased steric interactions between ions in solution. Einstein's viscosity equation predicts how solution viscosity changes with concentration [253]

$$\eta=\frac{\eta^{\infty}\left(1+\sum_{i\neq 0,\mathrm{M}}^{N^{\mathrm{mol}}}c_i^{\mathrm{mol}}\tilde{V}_i/2\right)}{\left(1-\sum_{i\neq 0,\mathrm{M}}^{N^{\mathrm{mol}}}c_i^{\mathrm{mol}}\tilde{V}_i\right)^2} \qquad 5\text{-}10$$

where $\tilde{V}_i$ is the effective molar viscous volume of species i, that is fit to electrolyte-solution viscosity data. Stokes-Einstein theory (Equation 5-9) is widely used and generally effective at predicting the concentration dependence of ion-solvent diffusion coefficients, although agreement with experiment is imperfect.[9, 82, 85] In particular, Stokes-Einstein theory is inaccurate for associating electrolytes,[9] corrections of which are discussed later.

Although local viscous interactions govern ion/solvent friction, long-range electrostatics dominate ion/ion interactions.[169] A "cloud" of mostly oppositely charged ions surrounds an ion in solution.[169] When an external field is applied, that cloud distorts and exerts a retarding force on the ion opposing the external field.[169] From this resistive force, Debye-Hückel-Onsager theory predicts that in binary electrolytes the diffusion coefficient varies with the square-root of concentration for oppositely charged ions[9, 85]

$$\mathfrak{D}_{ij}^{\mathrm{mol}} \propto \left(\frac{1-\phi_{\mathrm{M}}}{\tau}\right)\sqrt{I^{\mathrm{mol}}} \quad \text{for} \quad z_{i\neq \mathrm{M},0} z_{j\neq \mathrm{M},0} < 0 \tag{5-11}$$

where I^{mol} is the Molecular Construct ionic strength ($= \frac{1}{2}\sum_{i\neq 0,\mathrm{M}}^{N^{\mathrm{mol}}} c_i^{\mathrm{mol}} z_i^2$) Equation 5-11 relates diffusion coefficients measured in bulk solution at a given ionic strength to those at other concentrations. Chapman[85] and Wesselingh et al.[84] suggested that, since the Debye-Hückel ion cloud is governed by the ionic strength in multicomponent electrolytes, Equation 5-11 also applies to mixtures. Experiments agrees with the Debye-Hückel-Onsager description that friction between similarly charged ions is negligible as they scarcely interact, or[32, 84]

$$\mathfrak{D}_{ij}^{\mathrm{mol}} \to \infty \quad \text{for} \quad z_{i\neq \mathrm{M}} z_{j\neq \mathrm{M}} > 0. \tag{5-12}$$

5.3.3.2 Ion and Solvent/Membrane Friction Coefficients

Debye-Hückel-Onsager theory does not apply to ionic groups attached to the polymer membrane, since they are fixed and unable to form an ionic cloud around mobile ions.[84] Still, the membrane exerts a frictional force on aqueous ions and solvent from microscale-viscous interactions with the membrane walls.[254] Microscale hydrodynamics predicts viscous interactions between a fluid and a solid wall.[83] Species velocities and concentrations discussed up to this point are macroscopic averages and correspond to experimentally measurable quantities. In developing a microscale hydrodynamic model, we invoke microscopic, local quantities that are not experimentally accessible and are denoted with a superscript loc.

Appendix 5-B shows that the area-averaged, superficial velocity v_z through the membrane (through-direction denoted as z-coordinate) where each mobile species is under an electrochemical potential gradient $\partial\mu_i/\partial z$ is

$$v_z = -\sum_{i\neq \mathrm{M}}^{N^{\mathrm{mol}}} \frac{c_i^{\mathrm{mol}}}{\mathcal{K}_i^{\mathrm{mol}}} \frac{\partial \mu_i}{\partial z} \tag{5-13}$$

where $\mathcal{K}_i^{\mathrm{mol}}$ is a hydrodynamic friction coefficient that satisfies the creeping-flow momentum balance in a pore with appropriate boundary conditions. By definition v_z is the sum of species velocities in the Molecular Construct $v_{i,z}^{\mathrm{mol}}$ weighted by their mass fractions w_i^{mol} (*i.e.*, mass-averaged velocity, $v_z = \sum_{i\neq \mathrm{M}}^{N^{\mathrm{mol}}} w_i^{\mathrm{mol}} v_{i,z}^{\mathrm{mol}}$ where $w_i^{\mathrm{mol}} = n_i^{\mathrm{mol}} M_i / \sum_{i\neq \mathrm{M}}^{N^{\mathrm{mol}}} n_i^{\mathrm{mol}} M_i$). In Appendix 5-C, we demonstrate that the expression for $K_{i\mathrm{M}}^{\mathrm{mol}}$ that satisfies both the hydrodynamic prediction of Equation 5-13 and frictional interactions in Equation 5-3 is

$$K_{i\mathrm{M}}^{\mathrm{mol}} = w_i^{\mathrm{mol}} \mathcal{K}_i^{\mathrm{mol}} + \sum_{j\neq \mathrm{M}}^{N^{\mathrm{mol}}} K_{ij}^{\mathrm{mol}} \left(\frac{\mathcal{K}_i^{\mathrm{mol}}}{\mathcal{K}_j^{\mathrm{mol}}} - 1\right) \tag{5-14}$$

where the first term on the right is due to hydrodynamic interactions directly causing friction on species i and the second term is due to hydrodynamic friction on species j that exerts friction K_{ij}^{mol} on i.

Following classic treatments of electrokinetics in microchannels,[9] Appendix 5-B shows that for a translationally invariant pore forming a channel with tortuosity τ, $\mathcal{K}_i^{\mathrm{mol}}$ is

$$\mathcal{K}_i^{\mathrm{mol}} = \frac{4G\eta}{R_{\mathrm{pore}}^2\theta_i}\left(\frac{\tau}{1-\phi_{\mathrm{M}}}\right) \qquad 5\text{-}15$$

where R_{pore} is the radius of the pore and is a function of the membrane polymer volume fraction, $R_{\mathrm{pore}} = \phi_{\mathrm{M}}^{-m}(1-\phi_{\mathrm{M}})^{1/2}/2)$[222] and m is a swelling parameter determined from microstructural characterization (= 1.33 for Nafion).[12] G is the semi-empirical geometric factor that accounts for pore shape and distribution of sizes of the hydrophilic channels; it is independent of membrane water content or ion concentration.[37] Just as in Equations 5-9 and 5-11, the term in parenthesis on the right side corrects the interstitial hydrodynamic coefficient for the tortuosity and volume fraction of hydrophilic channels. θ_i accounts for how species i distributes across the channel and equals unity when i is uniformly distributed.

To establish θ_i, we treat the negatively polymer sulfonate groups as uniformly distributed along the channel walls. Because cations are solvated, they cannot approach the walls closer than their solvated radius (*i.e.*, the Outer Helmholtz plane),[255] which we set to the diameter of a water molecule $2R_0 = 0.275$ nm;[8] Because this study deals with high membrane hydration levels where cations are fully solvated, we do not consider cation-membrane ion-pair formation (*i.e.* ions complexed with the surface by dehydrating and moving to the Inner Helmholtz plane).[255] Consequently, ionic species are distributed across a pore of effective radius $R_{\mathrm{pore}} - 2R_0$ according to the linearized Poisson-Boltzmann equation.[255] For this system, Appendix 5-B shows that θ_i is given by

$$\theta_{i\neq 0} = \beta^2\left(2-\beta^2 - z_i\varrho\left(\beta^2 + \frac{8\varrho}{\left(R_{\mathrm{pore}}k\right)^2} - \frac{4\beta I_0\left(R_{\mathrm{pore}}k\right)}{R_{\mathrm{pore}}kI_1\left(R_{\mathrm{pore}}k\right)}\right)\right) \qquad 5\text{-}16$$

where β is the ratio of the effective pore radius traversed by ions after accounting for solvation and the actual radius $\left(R_{\mathrm{pore}} - 2R_0\right)/R_{\mathrm{pore}}$, ϱ is $\sum_{i\neq \mathrm{M}}^{N^{\mathrm{mol}}} n_i^{\mathrm{mol}} z_i \,/\, \sum_{i\neq \mathrm{M}}^{N^{\mathrm{mol}}} n_i^{\mathrm{mol}} z_i^2$, k is inverse Debye length ($= \left(\sum_{i\neq \mathrm{M}}^{N^{\mathrm{mol}}} c_i^{\mathrm{mol}} z_i^2 F^2/\varepsilon_r\varepsilon_0 RT\right)^{1/2}$), ε_r is bulk solvent dielectric constant (=78.3), ε_0 is vacuum permittivity, and I_0 and I_1 are modified Bessel functions of the first kind with order 0 and 1, respectively. We neglect changes in solvent concentration across the pore so that $\theta_0 = 1$.

5.3.4 Macroscopic Transport Coefficients

Equations 5-3 and 5-4 provide a microscopic description of multi-ion transport in membranes that relate species fluxes to driving forces, whereas experiments obey a macroscopic description in which experimentally controlled driving forces cause species fluxes. Fuller showed that Equation 5-5 inverts to a macroscopic form [78]

$$\boldsymbol{N}_i = -\sum_{j\neq \mathrm{M}} L_{ij}^{\mathrm{M}} c_i c_j \nabla \mu_j \qquad 5\text{-}17$$

where $\boldsymbol{N}_i$ is the molar flux vector of species $i \neq \mathrm{M}$ and L_{ij}^{M} is a component of the $N-1$ by $N-1$ symmetric matrix $\boldsymbol{L}^{\mathrm{M}}$ defined as[37, 78]

$$\boldsymbol{L}^{\mathrm{M}} = -(\boldsymbol{M}^{\mathrm{M}})^{-1} \qquad 5\text{-}18$$

where the membrane, species M, is used as a reference.

Because experimental measurements rarely ascertain the L_{ij}^{M} transport coefficients, we rewrite Equation 5-17 in terms of transport coefficients that are measureable under well-defined experimental conditions, such that in terms of an applied gradient of electrochemical potential μ_n [9, 32]

$$\boldsymbol{N}_i = -\frac{t_i^{\mathrm{M}}\kappa}{z_i F^2}\frac{\nabla \mu_n}{z_n} - \sum_{j\neq \mathrm{M}}\left(\alpha_{ij}^{\mathrm{M}} + \frac{t_i^{\mathrm{M}} t_j^{\mathrm{M}}\kappa}{z_i z_j F^2}\right)\nabla \mu_{j,n} \qquad 5\text{-}19$$

or, equivalently, in terms of an applied current density

$$\boldsymbol{N}_i = \frac{t_i^{\mathrm{M}}\mathbf{i}}{z_i F} - \sum_{j\neq \mathrm{M}} \alpha_{ij}^{\mathrm{M}} \nabla \mu_{j,n} \qquad 5\text{-}20$$

where F is Faraday's constant, z_i is the charge number of species i, t_i^{M} is the transference number of species i, κ is conductivity, and α_{ij}^{M} is the transport coefficient between species i and j. In the absence of concentration, pressure, or temperature gradients, for a charged species i, $\nabla \mu_i = z_i F \nabla \Phi$, where Φ is the electric potential. To avoid evoking an arbitrary definition of $\nabla\Phi$ when there are concentration gradients, Equations 5-19 and 5-20 use $\mu_{i,n}$, the chemical potential of species i relative to that of species n, $\mu_{i,n} = \mu_i - \frac{z_i}{z_n}\mu_n$. $\mu_{i,n}$ is independent of Φ, depending only on the thermodynamic variables pressure, concentration, and temperature.[9] The first terms on the right sides of Equations 5-19 and 5-20 specify flux due to concentration and pressure gradients and the second terms specifies transport due to migration. Because protons are present in numerous applications of cation-exchange, a convenient choice for n is H^+.[32]

Equations 5-19 and 5-20 are general for isothermal transport. The transport coefficients appearing in these equations are related to the L_{ij}^{M}'s and are material properties of the polymer membrane that for a set composition and temperature are independent of the applied driving forces. Under certain common experimental conditions, these properties have a clear physical interpretation. Specifically, ionic conductivity, κ, and $N-2$ transference numbers, t_i^{M}, relate the fluxes and current to the applied electric potential in the absence of concentration, temperature and pressure gradients

$$\mathbf{i} = -(\kappa)\nabla\Phi = -\left(F^2 \sum_{i\neq \mathrm{M}}\sum_{j\neq \mathrm{M}} L_{ij}^{\mathrm{M}} z_i c_i z_j c_j\right)\nabla\Phi \qquad 5\text{-}21$$

$$\text{for } \nabla c_i = \nabla T = \nabla p = 0$$

and

$$\boldsymbol{N}_i = \left(\frac{t_i^{\mathrm{M}}}{z_i}\right)\frac{\mathbf{i}}{F} = \left(\frac{c_i \mathcal{F}^2}{\kappa}\sum_{j\neq \mathrm{M}} L_{ij}^{\mathrm{M}} z_j c_j\right)\frac{\mathbf{i}}{F} \qquad \text{for } \nabla c_i = \nabla T = \nabla p = 0 \qquad 5\text{-}22$$

where the second equality provides κ and t_i^{M} in terms of the L_{ij}^{M}'s. The electro-osmotic coefficient is related to the transference number of water by the ratio $t_0^{\mathrm{M}}/z_0 = \xi$, which is finite even though $z_0 = 0$.[32] Similarly, α_{ij}^{M} has a straightforward physical interpretation for experiments in the absence of current; α_{ij}^{M} is the proportionality constant relating of species fluxes under chemical potential gradients absent net ionic current ($\mathbf{i} = 0$) and relate to L_{ij}^{M} according to[32]

$$\boldsymbol{N}_i = -\alpha_{ij}^{\mathrm{M}}\nabla\mu_{j,n} = -\left(L_{ij}^{\mathrm{M}} c_i c_j - \frac{t_i^{\mathrm{M}} t_j^{\mathrm{M}}\kappa}{z_i z_j F^2}\right)\nabla\mu_{j,n} \qquad \text{for } \mathbf{i} = 0 \qquad 5\text{-}23$$

where α_{ij}^{M} is symmetric, which gives $(N-1)N/2$ α_{ij}^{M}'s of which $(N-2)(N-1)/2$ are independent.

The transmissibility of the membrane to water, $L_{\mathrm{trans},0}$, dictates the superficial velocity of water through the membrane under an applied pressure gradient. The solvent/solvent transport coefficient, α_{00}^{M}, relates to measured $L_{\mathrm{trans},0}$, as.[32]

$$L_{\mathrm{trans},0} \approx \alpha_{00}^{\mathrm{M}}\frac{\bar{V}_0^2}{l} \qquad 5\text{-}24$$

where the membrane thickness, l, increases with water content from the dry thickness, l^0; for isotropic swelling $l = l^0\left(1 + \frac{n_0\bar{V}_0}{n_{\mathrm{M}}\bar{V}_{\mathrm{M}}}\right)^{\frac{1}{3}}$.[12] Equation 5-24 is approximate because neglects volume change on mixing of the water and membrane and neglects ionic contributions to the volume of the solution.

5.4 Parameters and Calculations

Literature reports values of κ and, less frequently, ξ, $t_{\mathrm{H}^+}^{\mathrm{M}}$, and $L_{\mathrm{trans},0}$ for PFSA membranes. Here, we consider properties of membranes that are immersed in aqueous electrolyte solutions where membrane water content is relatively high. To calculate measured properties with the proposed model for a membrane in bulk solution at a given composition, we first calculate the water volume fraction ϕ_0 (neglecting the volume of ions, $\phi_0 = 1 - \phi_{\mathrm{M}}$) and molality of ions in the membrane m_i and the speciation of associating ions $f_{i,j}$ from chemical-equilibrium relations outlined in Part I (Chapter 4).[247] Although this calculation is self-consistent, model and experimental errors in electrolyte partitioning propagate to measurements and predictions of the transport properties. We relate the membrane composition to the chemical potentials of the external environment using an

equilibrium model. In the steady state, we need not include a viscoelastic response of the polymer, which may be required in a transient simulation.[12]

Equations 5-6, 5-9, 5-11, and 5-12 give K_{ij}^{mol} for species i and j excluding the membrane M while Equation 5-14 gives $K_{i\mathrm{M}}^{\mathrm{mol}}$. The K_{ij}^{mol}'s specify $\boldsymbol{M}^{\mathrm{M}^{\mathrm{mol}}}$ and Equation 5-7 gives $\boldsymbol{M}^{\mathrm{M}}$. Inversion of $\boldsymbol{M}^{\mathrm{M}}$ following Equation 5-18 provides $\boldsymbol{L}^{\mathrm{M}}$. The components of $\boldsymbol{L}^{\mathrm{M}}$ give measured transport properties outlined in Equations 5-21-5-23. Matrix inversions are performed using the Python package NumPy version 1.16.

Because of the wide availability of data, we restrict our investigation to the Nafion PFSA chemistry.[12, 67-69, 92-93, 217] Specifically, we use data for Nafion versions N117, N115, N212, and N211. The different numbered membranes have the same molecular formulae but the N11x sequence is extruded, whereas the series N21x is cast from solution; x denotes thickness in units of mils.[12] For operating parameters, we use ambient temperature (298 K) and pressure (101.3 kPa). As discussed in Chapter 5 Supporting Information (SI-5), measurements of bulk-solution transport provide most properties at these conditions (specifically, $\tilde{V}_i$, $\mathfrak{D}^{\infty\,\mathrm{mol}}_{0i\neq\mathrm{M}}$, and $\mathfrak{D}^{\mathrm{mol}}_{i\neq 0,\mathrm{M}j\neq 0,\mathrm{M}}$ at a reference concentration). Parameters of ions unavailable in the literature are set to those ions of similar charge number that are available (see SI-5).

Table 5-1 provides the two adjusted values for the parameters of Nafion membranes. These are Archie's tortuosity scaling parameter, χ, and the geometric transport factor, G. Results and Discussion show that the parameter values are the best eye-fit of calculated and measured membrane conductivity proton transference number, electroosmotic coefficient, and water-water transport coefficient. G and χ are independent of membrane water and ion content, Results and Discussion compares model predictions with experiments.

Table 5-1. Nafion membrane specific fitting parameters in the model

Parameters	Value [-]
χ	0.3 for data from [67-69, 71] 1.2 otherwise
G	4

Because membrane pretreatment and processing impact network tortuosity,[12] we use two values of Archie's parameter: $\chi = 0.3$ for the highly pretreated and conductive N117 and N115 membranes measured by Okada and co-workers reported to have a proton-form conductivity of ~0.2 S cm^{-1} in liquid water [67-69, 71], and $\chi = 1.2$ for all other datasets that consistently report $\kappa <$ 0.1 S cm^{-1} for proton-form membranes in liquid water at room temperature.[57, 93, 224] Both of these values fall within the range of χ for a range of different types of porous media (0.3-3.4)[256]. G for different pore shapes falls between 2 and 3, which correspond to circular- and slit-pore shape cross sections, respectively.[37] This range of G is lower than the value fit here. The discrepancy is likely due an extremely heterogeneous distribution of hydrophilic domain sizes that leads to a large effective G.[37] Porous media with parallel-type pore nonuniformities in which species transport through pores that are larger than average lead to G's that are greater than those predicted by pore shape alone.[37]

5.5 Results and Discussion

This section compares calculated and measured transport properties. We first consider data for membranes in dilute-aqueous solutions, partially-exchanged with proton or lithium and a mono- or multivalent cation. The external solution is sufficiently dilute so that no co-ions are present in the membrane.[67-69, 71] The absence of co-ions makes the measurements informative for fuel-cell membrane applications. These datasets also contain different transport coefficients that permit validation of various aspects of the model. We also consider membranes in external concentrated electrolytes that incorporate co-ions from the surrounding solution. Fewer transport measurements are available under these conditions, but they test model predictions when numerous species are present. Concentrated conditions are relevant for RFB operation.[93, 217] In particular, we calculate transport coefficients for membranes in aqueous solutions of sulfuric acid and vanadium sulfate that are representative of electrolytes in vanadium RFBs, which are the most studied flow-battery chemistry.[223]

5.5.1 Multicomponent Transport Properties of Mixed-Cation-Form Membranes in Water

Okada et al.[67-69, 71] extensively characterized transport properties of N115 and N117 by measuring conductivity κ, proton and lithium transference numbers t_i^{M}, electroosmotic coefficient ξ, and water transport coefficient α_{00}^{M} of membranes that are partially exchanged with different cations in liquid aqueous electrolytes.

The mathematical model outlined in Part I (Chapter 4)[247] calculates the water volume fraction ϕ_0 and molality of species in the membrane m_i (given in Figure 4-4, Figure 4-5Figure 4-9 in Chapter 4). Given these values, we calculate the transport properties of mixed-exchanged proton-alkali Nafion membrane in liquid water. Figure 5-1 shows measured[68, 70] (symbols) and calculated (lines) (a) membrane conductivity κ, (b) proton transference number $t_{\mathrm{H}^+}^{\mathrm{M}}$, (c) electroosmotic coefficient ξ, (d) and water transport coefficient α_{00}, (e) ion-water transport coefficient α_{i0}^{M} (not measured, only calculated), and (f) ion-ion transport coefficient α_{ij}^{M} (not measured, only calculated) as function of the fractional proton exchange $n_{\mathrm{H}^+}/n_{\mathrm{SO}_3^-}$ (*i.e.* the fraction of negatively charged polymer sulfonate group charge-balanced by protons) with various alkali metal cations. For membranes partially exchanged with alkali cations and protons, the transport coefficients are related according to $\alpha_{0\mathrm{A}^+}^{\mathrm{M}} = -\alpha_{0\mathrm{H}^+}^{\mathrm{M}}$ and $\alpha_{H^+H^+}^{\mathrm{M}} = -\alpha_{A^+H^+}^{\mathrm{M}} = \alpha_{A^+A^+}^{\mathrm{M}}$.[32] Best-eye fitting of the data in Figure 5-1 specifies χ and G. Figure 5-6 shows the same calculated transport properties as Figure 5-1 for lithium-form membrane exchanged with other alkali cations (α_{00} not measured).[67] The fitted χ and G in Table 5-1 calculate transport properties for mixed lithium-alkali form membranes without adjustment.

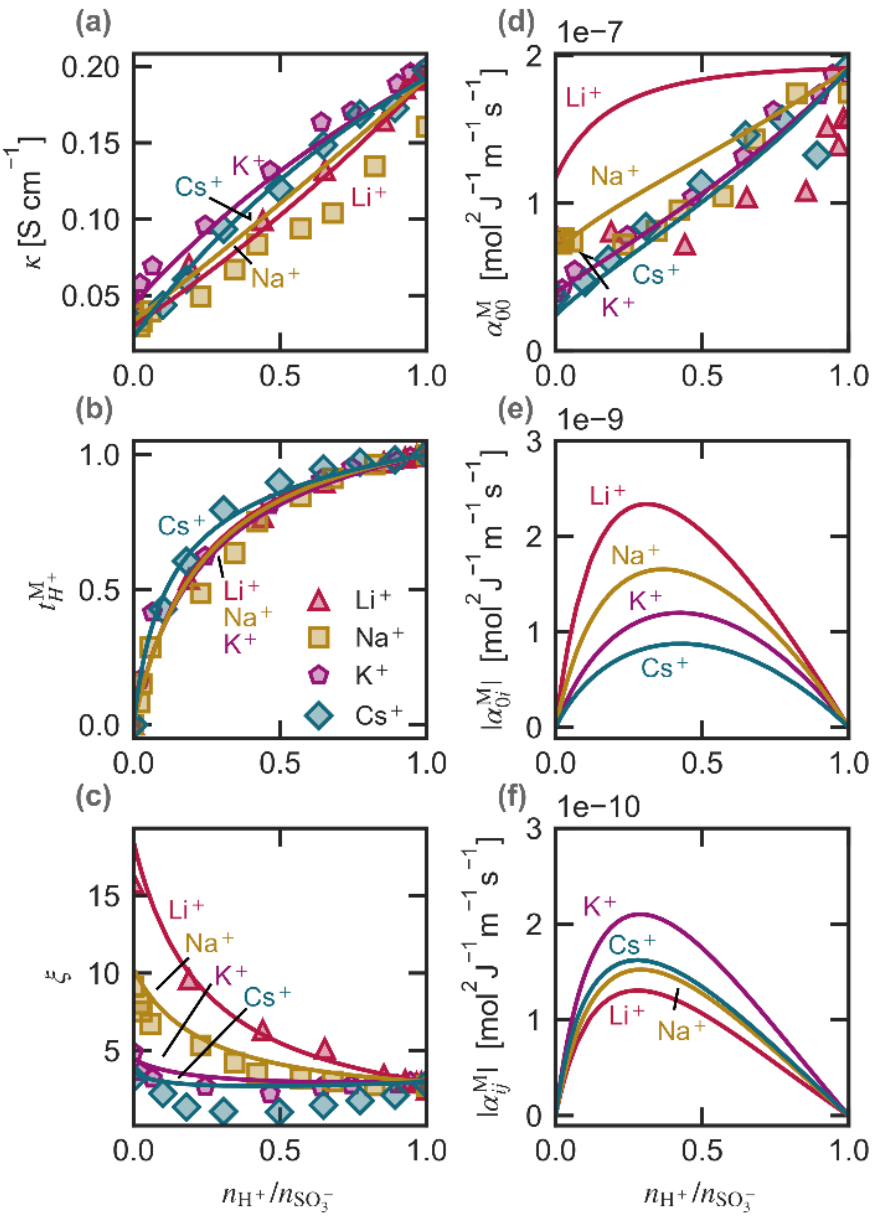

Figure 5-1. Measured[68] (symbols) and calculated (lines) N11x membrane (a) conductivity κ, (b) proton transference number $t_{\mathrm{H}^+}^{\mathrm{M}}$, (c) electroosmotic coefficient ξ, and the transport coefficients between (d) water-water α_{00}^{M}, (e) ion-water α_{i0}^{M}, and (f) ion-ion α_{ij}^{M} in liquid water as function of fractional proton exchange, $n_{\mathrm{H}^+}/n_{\mathrm{SO}_3^-}$, with lithium (triangles), sodium (squares), potassium (pentagons), and cesium (tilted squares)

Agreement in Figure 5-1 between theory and experiment is sufficient for differing membrane proton fractions and ion types. There are three cases that the model differs from experiment. The model calculates a higher sodium-exchanged membrane conductivity than does the measurement. We attribute this difference to varying experimental conditions because the measured sodium-exchanged samples have lower conductivity than the other cation-exchanged samples even when

the membranes are fully in proton form (*i.e.* they should have identical composition), as Figure 5-1a shows.[68, 70] The model significantly over-predicts α_{00}^{M} for the lithium-exchanged membranes, as Figure 5-1d shows, and ξ for partial cesium-exchanged membranes as Figure 5-1c shows. These discrepancies may be partially attributed to the high experimental uncertainty for α_{00}^{M} (calculated to be ~40% for proton-form membranes in Figure 5-1d) and to lack of experimental data. Further, we assume G and χ are independent of cation type, but cation-sulfonate interactions can alter the membrane microstructure causing disagreement between calculated and measured transport properties.[40, 54, 218]

As the membrane exchanges from alkali cation form to proton form, conductivity increases, plotted in Figure 5-1a, because protons are much more mobile than are alkali cations. Figure 5-1b shows that the high mobility of protons causes high $t_{\mathrm{H}^+}^{\mathrm{M}}$ except in membranes that are mostly exchanged with alkali cations (> 50% exchanged). Equations 5-21 and 5-22 show that conductivity increases as Nafion exchanges from alkali ions to protons and ξ decreases, consistent with Figure 5-1c.

The high mobility of protons generates less friction for water transport through the membrane (see Equation 5-6). A rising $n_{\mathrm{H}^+}/n_{\mathrm{SO}_3^-}$ ratio thus increases α_{00}^{M}, as Figure 5-1d confirms. In the absence of current, low-mobility alkali cations move down a gradient chemical potential of water as they are dragged by water, but a streaming potential develops to ensure electroneutrality and causes highly mobile protons to move up a water chemical potential gradient (*i.e.*, $\alpha_{0\mathrm{A}^+}^{\mathrm{M}} > 0$ and $\alpha_{0\mathrm{H}^+}^{\mathrm{M}} < 0$).

Figure 5-1e shows that in fully alkali ion-exchanged membranes, protons are not available to move in the opposite direction as alkali-cations and $\alpha_{0\mathrm{A}^+}^{\mathrm{M}} = \alpha_{0\mathrm{H}^+}^{\mathrm{M}} = 0$. Similarly, $\alpha_{0\mathrm{A}^+}^{\mathrm{M}} = \alpha_{0\mathrm{H}^+}^{\mathrm{M}} = 0$ for fully proton-exchanged membranes. Figure 5-1f illustrates that $\alpha_{\mathrm{H}^+\mathrm{A}^+}^{\mathrm{M}}$ similarly reaches a maximum for partially exchanged membranes and is zero for fully exchanged membranes. The values of α_{00}^{M} are more than an order of magnitude greater than $|\alpha_{i0}^{\mathrm{M}}|$ and $|\alpha_{ij}^{\mathrm{M}}|$, which demonstrates that fluxes induced by chemical-potential gradients of ions are secondary to those induced by pressure or water concentration gradients.

The general trends described in the preceding two paragraph hold for all membranes exchanged with each of the alkali cations. Variations in transport properties between the different alkali ions A^+ are due to different ion-water binary diffusion coefficient at infinite dilution $\mathcal{D}_{0\mathrm{A}^+}^{\infty}$ (given in SI-5), to the water volume fraction of the exchanged membrane ϕ_0 (given in Part I, Chapter 4,[247]), and to the molar viscous volume of the cation-exchanged sample $\tilde{V}_{\mathrm{A}^+}$ SI-5). ϕ_0 decreases with increasing alkali cation crystallographic size (*i.e.* $\mathrm{Li}^+ > \mathrm{Na}^+ > \mathrm{K}^+ > \mathrm{Cs}^+$) and $\mathcal{D}_{0\mathrm{A}^+}^{\infty}$ has the opposite trend (*i.e.* $\mathrm{Li}^+ < \mathrm{Na}^+ < \mathrm{K}^+ < \mathrm{Cs}^+$). These different physical parameters explain the variations of transport properties in Figure 5-1 for the different cation-exchanged membranes.

To explore these differences, Figure 5-2 plots calculated transport properties for a 50% alkali ion-exchanged Nafion membrane (*i.e.* $n_{\mathrm{H}^+}/n_{\mathrm{SO}_3^-} = 0.5$) on contour plots for (a) conductivity, (b) proton transference number, (c) electroosmotic coefficient, (d) and water, (e) ion-water, and (f) ion-ion transport coefficients as a function of ϕ_0 on the y-axis and $\mathfrak{D}_{0\mathrm{A}^+}^{\infty}$ on the x-axis. Each x-y point in Figure 5-2 are the transport properties of Nafion partially exchanged with a hypothetical alkali ion that has a diffusion coefficient $\mathfrak{D}_{0\mathrm{A}^+}^{\infty}$ and where the membrane water volume fraction is ϕ_0. For these calculations, we set all other properties of A^+ (*e.g.* molar viscous volume and molar mass) to those of sodium because it is in the middle of the alkali series. To provide a reference,

symbols in Figure 5-2 are the $\mathfrak{D}_{0i}^{\infty}$ and ϕ_0 for a 50% cation-exchanged Nafion membranes in liquid water for the different alkali cations.

Figure 5-2a and f show that κ and $|\alpha_{ij}^{\mathrm{M}}|$ increase with increasing cation diffusivity $\mathfrak{D}_{0\mathrm{A}^+}^{\infty}$ because more mobile ions have a higher flux for a given electric field or ion chemical-potential gradient, respectively. At low water contents, rising ϕ_0 increases κ and $|\alpha_{ij}^{\mathrm{M}}|$ because larger pores and lower tortuosity facilitate increased ion transport. However, at high ϕ_0, the relation is opposite because rising ϕ_0 decreases ion concentrations, decreasing κ and $|\alpha_{ij}|$.

This non-monotonic relationship between water content and ion-ion transport causes $|\alpha_{ij}^{\mathrm{M}}|$ of partially alkali-exchanged Nafion to follow the order $\mathrm{Li}^+ < \mathrm{Na}^+ < \mathrm{Cs}^+ < \mathrm{K}^+$, as Figure 5-1f shows. Similarly, κ has the order $\mathrm{Li}^+ < \mathrm{Na}^+ < \mathrm{Cs}^+ < \mathrm{K}^+$ because of the relationship between ϕ_0 and κ as well as because lithium and sodium cause stronger viscosification of the solution in the membrane (*i.e.* $\tilde{V}_{\mathrm{Li}^+} > \tilde{V}_{\mathrm{Na}^+} > \tilde{V}_{\mathrm{K}^+} > \tilde{V}_{\mathrm{Cs}^+}$).

Figure 5-2b shows the relatively small effects $\mathfrak{D}_{0\mathrm{A}^+}^{\infty}$ and ϕ_0 have on $t_{\mathrm{H}^+}^{\mathrm{M}}$. This explains the negligible differences in t_{H^+} for different alkali ion-exchanged membranes seen in Figure 5-1b. Figure 5-2c, d, e show that the water-transport properties, ξ, α_{00}^{M}, and α_{0i}^{M} all rise with increasing ϕ_0. Higher water content increases pore size and decreases tortuosity, increasing water transport.

The high value ξ for lithium-exchanged membrane has previous been attributed to lithium "dragging" water in its large solvation shell as it transits the membrane.[12, 68] The effect of lithium's large solvation and resulting high friction coefficient manifests as a relatively low $\mathfrak{D}_{0\mathrm{Li}^+}^{\infty}$.[8] This work shows that the low lithium diffusivity is not sufficient to explain the high value of ξ for lithium-exchanged membranes. Rather, the large ξ is due to the higher water content of the membrane and the resulting larger hydrophilic domains of these membranes. This finding is consistent with previous hydrodynamic models.[18, 257]

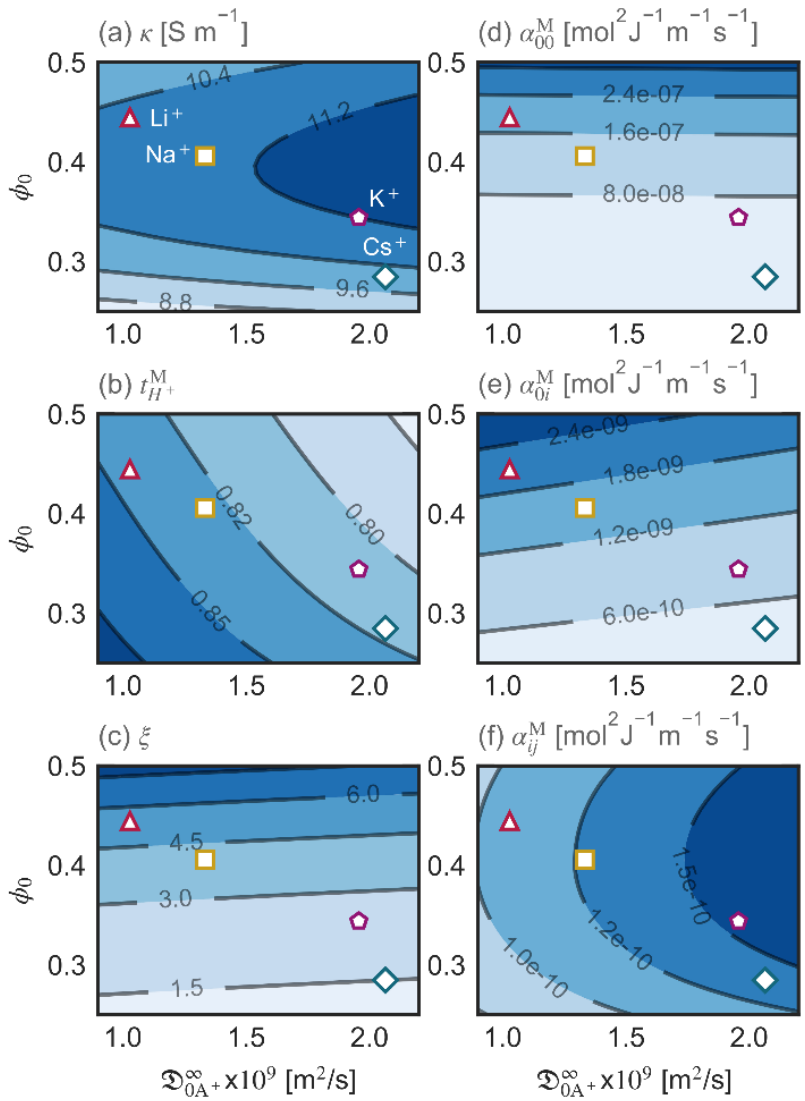

Figure 5-2. Contour plot of calculated (a) conductivity, (b) proton transference number, (c) electroosmotic coefficient, (d) and water, (e) ion-water, and (f) ion-ion transport coefficient as a function of ϕ_0 on y-axis and $\mathfrak{D}_{0A^+}^{\infty}$ on x-axis for a 50% alkali ion-exchanged Nafion membrane. Symbols plot $\mathfrak{D}_{0A^+}^{\infty}$ and ϕ_0 at 50% cation-exchanged Nafion membranes in liquid water for lithium (triangle), sodium (square), potassium (pentagon), and cesium (diamond).

The proposed model calculates transport properties of Nafion membranes exchanged with multivalent cations. Except of α_{00}^{M}, Figure 5-3 shows that the transport model (lines) is in reasonable agreement with experimental measurements[69] (symbols, same transport properties as Figure 5-1) for a proton-form membranes exchanged with various multivalent ions as a function of membrane proton fraction ($= n_{H^+}/n_{SO_3^-}$). There is relatively little difference between calculated transport properties of multivalent ion-exchanged membranes because these ions have similar $\mathfrak{D}_{0A^{z_A}}^{\infty}$ and water uptake.

Figure 5-3 shows that the model over predicts water transport. Multivalent cations strongly interact with polymer sulfonate groups, altering membrane morphology through crosslinking or domain rearrangement.[54] This change in polymer structure may be one source of disagreement between calculated and measured transport properties.[40, 54, 218] In this case, χ and G should be functions of ion-exchange and cation type, but the exact nature of this effect requires further investigation.

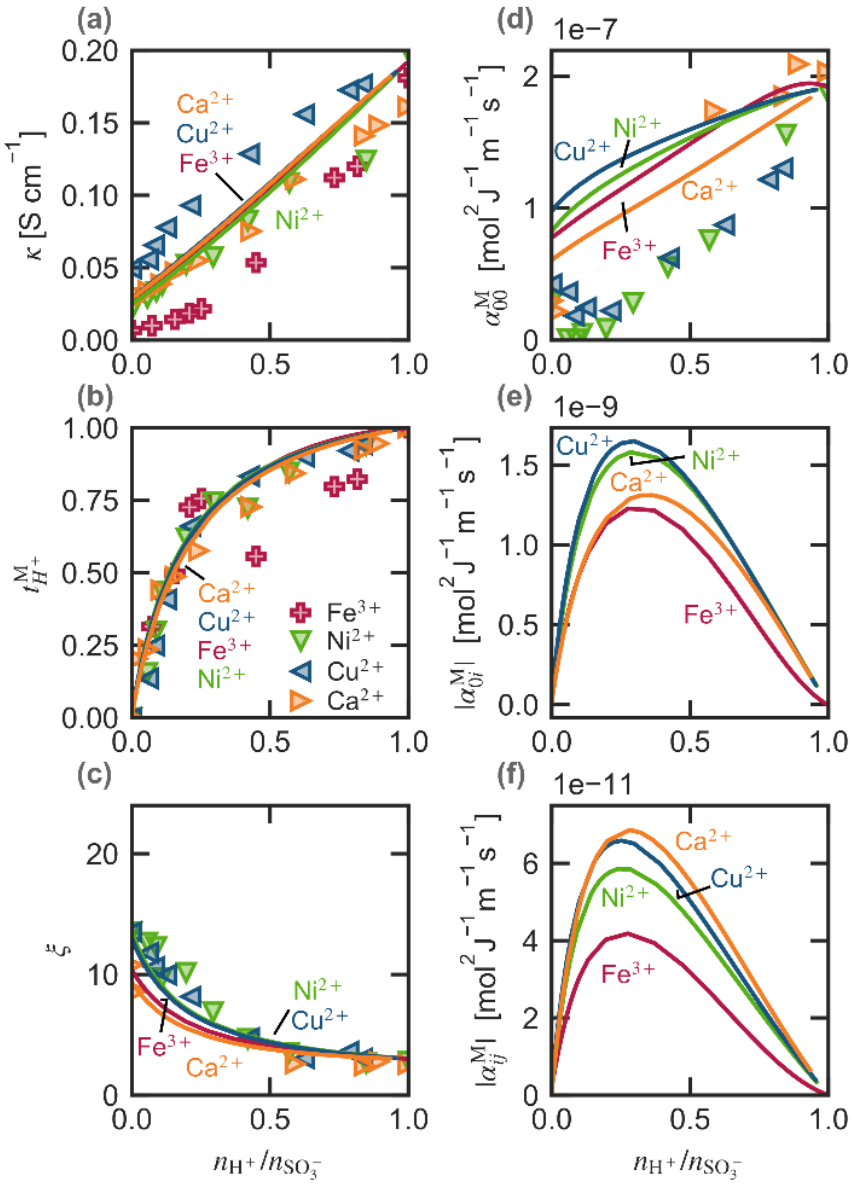

Figure 5-3. Measured[69] (symbols) and calculated (lines) (a) conductivity κ, (b) proton transference number $t^{M}_{H^+}$, (c) electroosmotic coefficient ξ (Fe-exchanged membrane not measured), and the transport coefficients between (d) water-water α^{M}_{00} (Fe-exchanged membrane not measured), (e) ion-water α^{M}_{i0} (not measured), and (f) ion-ion α^{M}_{ij} (not measured) of a Nafion membrane in liquid water as a function of fractional proton exchange, $n_{H^+}/n_{SO_3^-}$, with calcium (right triangle), nickel (down triangle), copper (left triangle), and iron (plus sign).

5.5.2 Transport in Concentrated Electrolytes

In concentrated electrolyte solutions, membrane water content and ion concentration induces large changes in transport properties. Part I (Chapter 4)[247] shows that membrane water content decreases and acid uptake increases with increasing bulk electrolyte concentration. Figure 5-4 shows measured[93, 217] (circles) and calculated (solid line) N117 membrane conductivity as a function of external sulfuric acid concentration. Conductivity increases slightly up to a bulk electrolyte concentration of 4 mol kg^{-1}. At higher concentrations, conductivity decreases with increasing electrolyte concentration.

Dashed lines in Figure 5-4 show conductivity (hypothetical) if the viscosity of the electrolyte solution in the membrane η or the membrane volume fraction ϕ_M is equal to that of the membrane in acid-free liquid water (*i.e.* $\eta = \eta(m_{H_2SO_4} = 0)$ or $\phi_M = \phi_M(m_{H_2SO_4} = 0)$, respectively). When viscosity of the electrolyte solution in the membrane is constant, membrane conductivity does not decrease as significantly at higher acid concentrations because proton mobility would be larger. When ϕ_M is held constant, the conductivity increases as the acid concentration in the membrane increases. In actuality, as bulk acid concentration increases, membrane water content decreases (see Part I, Chapter 4[247]) causing increased tortuosity and decreased pore size. In agreement with Tang et al.[93], the delicate balance between decreasing proton mobility and increased number of charge carriers leads to a maximum in membrane conductivity at moderate acid concentrations.

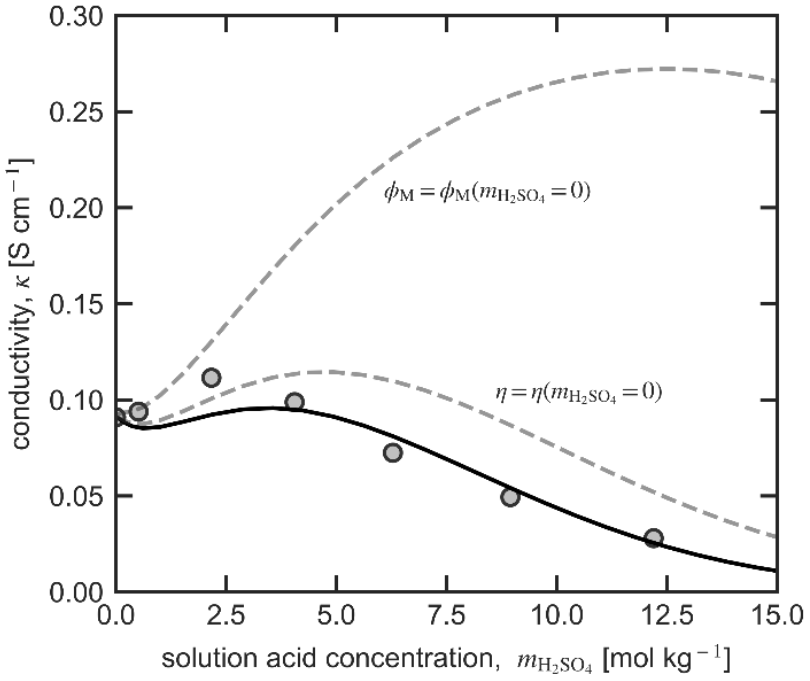

Figure 5-4. Measured [93] (circles) and calculated (solid lines) N117 conductivity as a function of external solution sulfuric acid concentration. Dashed lines denote model predictions with transport properties calculated if η and ϕ_M are that of the membrane in acid-free water (*i.e.* $\eta = \eta(m_{H_2SO_4} = 0)$ or $\phi_M = \phi_M(m_{H_2SO_4} = 0)$, respectively).

Figure 5-5 plots calculated (solid line) and measured[92] (symbols) membrane conductivity as a function of either vanadium III, IV or V concentration with sulfuric acid such that the total sulfate concentrations is 5 mol L^{-1}. The conductivity is normalized to the conductivity of the membrane in vanadium-free sulfuric acid to reduce propagation of error (see Figure 5-4). Based on the proposed model for intermolecular friction, there is no friction between like-charged ions (see Equation 5-12). Consequently, vanadium ions and protons do not directly interact at the microscopic description of the model (*i.e.* $\mathfrak{D}^{\mathrm{mol}}_{\mathrm{H^+V}^{n+}(x)} = \infty$), but the presence of one still influences the other macroscopically (see Equation 5-18). Although the current is carried mainly by mainly protons (dotted line shows this by plotting conductivity multiplied by proton transference number, $\kappa t^{\mathrm{M}}_{\mathrm{H^+}}$), as more vanadium is added to the membrane, the number of very mobile protons decreases and conductivity decreases. As Figure 5-5 shows, the triply-charged V(III) displaces more protons and predicted conductivity curves are convex, whereas the singularly-charged V(V) curve is concave.

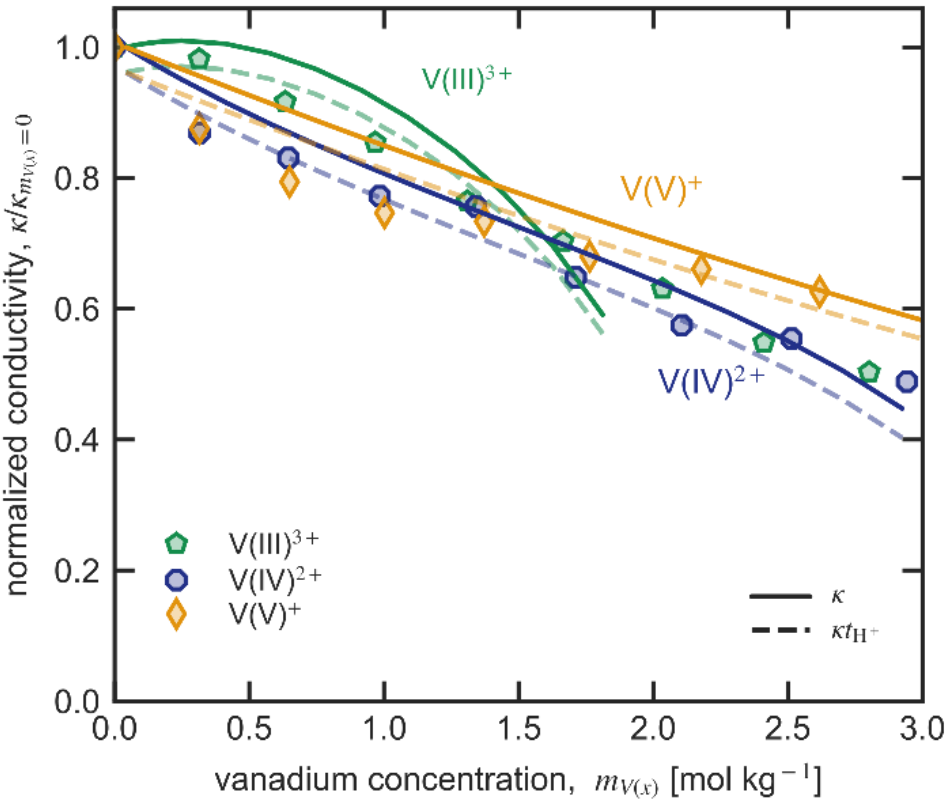

Figure 5-5. Measured[92] (symbols) and calculated (solid lines) membrane conductivity as a function of external vanadium V(III) (pentagons), V(IV) (octagons), or V(V) (diamonds) concentration in sulfuric acid with a total sulfate concentration of 5 mol dm^{-3}. Conductivity is normalized by the conductivity of the vanadium-free sulfuric acid solution, $\kappa_{m_{\mathrm{v(x)}=0}}$. Dashed lines are model of the proton contribution to conductivity, $\kappa t^{\mathrm{M}}_{\mathrm{H^+}}$.

In addition to conductivity and proton transference number, an array of other transport properties dictate multi-ion transport in ionomer membranes. Specifically, Figure 5-7 shows calculated vanadium transference numbers, electroosmotic coefficients, and α_{ij}^{M} transport coefficients of Nafion in the same electrolytes as Figure 5-5. Most of the transport properties are highly concentration dependent, and are starkly different between vanadium species. Although conductivity measurements, such as those in Figure 5-5, are crucial to understand transport in these membrane, this single transport property provides a limited view of the diverse processes involved in transport.[12, 18, 68, 92] Furthermore, dilute-solution descriptions that consider only one transport parameter for each species provide an incomplete understanding of transport in many instances. As Figure 5-7 demonstrates, the proposed concentrated-solution model facilitates complete specification of transport properties of multicomponent systems using only two microscale, adjustable parameters, χ and G.

5.6 Summary

We develop a mathematical model for multicomponent mass transport in phase-separated cation-exchange membranes based on Stefan-Maxwell-Onsager description. Microscopic theory predicts how thermodynamic and transport properties change with ion and water concentration. The model relies on two adjusted membrane-specific parameters (Archie's tortuosity parameter and pore-shape), whose values are physically reasonable and independent of water content and ion concentration. The model quantitatively agrees over wide ranges of electrolyte concentrations and compositions.

The proposed model shows that thermodynamic properties in Part I (Chapter 4)[247] impact transport properties by controlling the concentration and identity of ions and water uptake. Membranes with less water have lower ion mobilities, because the membrane tortuosity increases and the fraction that is conductive decreases. Moreover, increased ion concentration in the membrane increases the viscosity of the solution inside the hydrophilic domains of the membrane, further decreasing mobility. Consequently, the presence of mobile and fixed ions all impact transport both directly through Stefan-Maxwell-Onsager-type frictional interactions and indirectly by changing the structure of the membrane and the internal solution properties.

We fully specify the numerous transport coefficients involved in multicomponent transport by using concentrated-solution theory. The coefficients rigorously describe coupling of species transport. By building the model from physicochemical microscale description of transport, a paucity of experiments can specify model parameters. In Part III (Chapter 6), we use the proposed theory to parameterize a model for multicomponent transport in a vanadium redox-flow-battery membrane.[104] We show how concentrated-solution description in this system is essential to understand device performance.[104]

5.7 Nomenclature

Roman

$\bar{V}_i$	Partial molar volume of species i, $\mathrm{m^3\ mol^{-1}}$
$\tilde{V}_i$	Effective molar viscous volume of species i, $\mathrm{m^3\ mol^{-1}}$
K_{ij}	Friction coefficient between species i and j, $\mathrm{J\ s\ cm^{-5}}$

$L_{\text{trans},0}$	Membrane solvent transmissibility, $m^4\ J^{-1}\ s^{-1}$
L_{ij}^{M}	Inverted transport coefficient between species i and j, $cm^5\ J^{-1}\ s^{-1}$
M_i	Molar mass of species i, $g\ mol^{-1}$
M_{ij}^{M}	Components i and j of matrix $\boldsymbol{M}^{\text{M}}$ between species, $J\ s\ cm^{-5}$
R_0	Radius of water molecule, 0.1375 nm
$R_{\text{effective}}$	Effective radius of hydrophilic pore accessible to hydrated ions, m
R_{pore}	Pore radius, nm
c_T	Total molar solution concentration, $mol\ dm^{-3}$
c_i	Molar concentration of species i, $mol\ dm^{-3}$
$f_{i,j}$	Association fraction of species i into species j
m_i	Molality of species i, $mol\ kg^{-1}{}_{\text{solvent}}$
n_i	Moles of species i, moles
s_i	Stoichiometric coefficient of species i
t_i^{M}	Transference number of species i
u_i	Potential of mean force on species i from the membrane, J
v_{z}	Mass averaged velocity across the membrane, $m\ s^{-1}$
w_i	Mass fraction of species i
z_i	Charge number of species i
$\mathcal{K}_i$	Hydrodynamic friction coefficient of species i in the membrane, $J\ s\ cm^{-5}$
$\mathfrak{D}_{ij}$	Diffusion coefficient between species i and j, $m^2\ s^{-1}$
F	Faraday's constant, 96,487 $C\ mol^{-1}$
G	Domain geometric factor
I	Ionic strength, $mol\ m^{-3}$
N	Number of species
R	Gas constant, 8.3145 $J\ mole\ K^{-1}$
T	Temperature, 298 K
k	Inverse Debye length, m^{-1}
l	membrane thickness, m
m	Scaling constant
p	Pressure, Pa

Greek

α_{ij}^{M}	Transport coefficient of species i due to chemical potential gradient of j, $mol^2\ J^{-1}\ m^{-1}\ s^{-1}$
ε_0	Vacuum permittivity, $8.85\times10^{-12}\ F\ m^{-1}$
ε_r	Relative dielectric constant
θ_i	Distribution factor for species i in a hydrophilic domain
$\mu_{i,n}$	Electrochemical potential of species i relative to that of species n, $J\ mol^{-1}$
μ_i	(Electro)chemical potential of species i, $J\ mol^{-1}$
ϕ_i	Volume fraction of species i
Φ	Electric potential, V
β	Ratio of the effective pore radius and the actual radius
η	Solution viscosity, Pa s

κ	Conductivity, S cm^{-1}
λ	Membrane water content, $\mathrm{mol_{water}\,mol_{SO_3^-}^{-1}}$
ξ	Electro-osmotic coefficient
ρ	Mass density, kg m^{-3}
τ	Tortuosity
χ	Archie's tortuosity scaling parameter
ψ	Electrostatic potential, V
ϱ	Electrostatic parameter

Vectors and Arrays

$\boldsymbol{L}^{\mathrm{M}}$	Matrix of inverted friction coefficients, cm^5 J^{-1} s^{-1}
$\boldsymbol{M}^{\mathrm{M}}$	Matrix of friction coefficients, J s cm^{-5}
$\boldsymbol{N_i}$	Flux vector of species i, mol m^{-2} s^{-1}
$\boldsymbol{X}_i$	Molar body force on species i, N mol^{-1}
$\boldsymbol{d}_i$	Driving force on species i, N m^{-3}
$\boldsymbol{v_i}$	Velocity vector of species i, m s^{-1}
$\mathbf{i}$	Current density, A cm^{-2}
$\boldsymbol{D}$	Matrix of driving forces, N dm^{-3}
$\boldsymbol{F}$	Matrix of association fractions $f_{i,j}$
$\boldsymbol{V}$	Matrix of species velocities, m s^{-1}

Subscript

∞	Infinite dilution
domain	Hydrophilic domain
ref	Reference value

Superscript

$'$	Superficial quantity
exp	Experimental Construct
M	Referenced to membrane velocity
mol	Molecular Construct
loc	Local, microscopic quantity a hydrophilic domain
0	Dry Membrane

5.8 Appendix 5-A

To relate the species properties in the Experimental and Molecular Constructs, chemical equilibria of the speciation reactions give $f_{i,j}$, the fraction of moles of species i that partially associates into moles of species j,[30]

$$s_j \mu_j = -\sum_i s_i \mu_i \qquad 5\text{-}25$$

where the sum is over species i that associate to form j.

The mole-weighted velocities of a fully dissociated species is the sum of the mole-weighted average velocities of its partially associated species,

$$\frac{n_i}{s_i}\boldsymbol{v}_i^{\text{exp}} = -\sum_i \frac{n_j^{\text{mol}}}{s_j}\boldsymbol{v}_j^{\text{mol}} \tag{5-26}$$

where the summation is over all species j that that dissociate to i. Equation 5-8 shows that Equation 5-26 relates the velocity in the two constructs relates via

$$\boldsymbol{v}_i^{\text{exp}} = \sum_j f_{i,j}\boldsymbol{v}_j^{\text{mol}} \tag{5-27}$$

Taking the gradient of Equation 5-25, multiplying the left side by $c_j^{\text{mol}}/c_j^{\text{mol}}$ and the right by c_i/c_i and rearranging relates the driving forces in the two constructs

$$c_j^{\text{mol}}\nabla\mu_j = \sum_i f_{i,j}\left(c_i^{\text{exp}}\nabla\mu_i\right) \tag{5-28}$$

where the summation is over species i that associate to form j. In matrix form, Equations 5-27 and 5-28 are

$$\boldsymbol{V}^{\text{exp}} = \boldsymbol{F}\boldsymbol{V}^{\text{mol}} \tag{5-29}$$

and

$$\boldsymbol{D}^{\text{mol}} = \boldsymbol{F}^{\boldsymbol{T}}(\boldsymbol{D}^{\text{exp}}) \tag{5-30}$$

where $\boldsymbol{F}$ has elements $F_{ij} = f_{i,j}$ and is a full rank matrix with the number of columns greater than or equal to the number of rows, and the superscript T denotes the matrix transpose. Substituting the Molecular Construct form of Equation 5-5 into Equation 5-29 and using Equation 5-30, we have

$$\boldsymbol{V}^{\text{exp}} = \boldsymbol{F}\boldsymbol{V}^{\text{mol}} = \boldsymbol{F}\left[\boldsymbol{M}^{\text{M}^{\text{mol}}}\right]^{-1}\boldsymbol{D}^{\text{mol}} = \boldsymbol{F}\left[\boldsymbol{M}^{\text{M}^{\text{mol}}}\right]^{-1}\boldsymbol{F}^{T}\boldsymbol{D}^{\text{exp}} \tag{5-31}$$

where the power -1 is the matrix inverse. Rearranging the Experimental Construct form of Equation 5-5 and setting it equal to Equation 5-31 gives

$$\left[\boldsymbol{M}^{\text{M}^{\text{exp}}}\right]^{-1}\boldsymbol{D}^{\text{exp}} = \boldsymbol{F}\left[\boldsymbol{M}^{\text{M}^{\text{mol}}}\right]^{-1}\boldsymbol{F}^{T}\boldsymbol{D}^{\text{exp}} \tag{5-32}$$

Because this equality is true for any driving force on the system, $\boldsymbol{D}^{\text{exp}}$, Equation 5-32 rearranges to relate friction coefficients in the Experimental and Molecular Constructs

$$\boldsymbol{M}^{\text{M}^{\text{exp}}} = \left(\boldsymbol{F}\left[\boldsymbol{M}^{\text{M}^{\text{mol}}}\right]^{-1}\boldsymbol{F}^{T}\right)^{-1} \tag{5-33}$$

Onsager reciprocal relations holds for both K_{ij}^{exp} and K_{ij}^{mol} because the transformations in Equation 5-33 guarantees that $\boldsymbol{M}^{\text{M}^{\text{exp}}}$ is symmetric since $\boldsymbol{M}^{\text{M}^{\text{mol}}}$ is also symmetric.

5.9 Appendix 5-B

We consider a 2-D cylindrical channel with the z-direction parallel to the channel walls and the r-direction is radial. Velocity in the radial and azimuthal directions are neglected.[82] Using the continuity equation, the steady-state equation of motion in the z-direction for a Newtonian fluid with constant viscosity and density is[82]

$$\frac{\partial p}{\partial z} - \sum_{i \neq \mathrm{M}}^{N^{\mathrm{mol}}} X_{i,z} c_i^{\mathrm{loc}^{\mathrm{mol}}} = \frac{\eta}{r}\frac{\partial}{\partial r}\left(r\frac{\partial v_z^{\mathrm{loc}}}{\partial r}\right) \tag{5-34}$$

The r-velocity component is zero and where $X_{i,z}$ is the molar external force on species i in the z-direction. The average molar body force $\boldsymbol{X}$ is equal to the mole-fraction weighted sum of molar body forces on each species, $\boldsymbol{X} = \sum_i \boldsymbol{X}_i x_i$. Radial variations of η are neglected. $c_i^{\mathrm{loc}^{\mathrm{mol}}}$ and v_z^{loc} are the local concentration of species i and fluid velocity in the z-direction, respectively, with the superscript loc denoting a function of r; taking the integral average of v_z^{loc} and $c_i^{\mathrm{loc}^{\mathrm{mol}}}$ across the channel gives average, interstitial velocity and concentration v_z and c_i^{mol} (*i.e.* $\int_0^{R_{\mathrm{pore}}} v_z^{\mathrm{loc}} 2\pi r dr = \pi R_{\mathrm{pore}}^2 v_z$ and $\int_0^{R_{\mathrm{pore}}} c_i^{\mathrm{loc}^{\mathrm{mol}}} 2\pi r dr = \pi R_{\mathrm{pore}}^2 c_i^{\mathrm{mol}}$). Note that in this section, v_z is the interstitial velocity in a single pore. As such, v_z is scaled by $(1-\phi_{\mathrm{M}})/\tau$ when appearing in Equations 5-3, 5-4, and 5-13. The isothermal Gibbs-Duhem (*i.e.*, $dp = \sum_{i\neq \mathrm{M}}^{N^{\mathrm{mol}}} c_i^{\mathrm{loc}^{\mathrm{mol}}} d\mu_i$)[30] equation replaces pressure changes with species (electro)chemical potential changes

$$\sum_{i \neq \mathrm{M}}^{N^{\mathrm{mol}}} c_i^{\mathrm{loc}^{\mathrm{mol}}} \frac{\partial \mu_i}{\partial z} = \frac{\eta}{r}\frac{\partial}{\partial r}\left(r\frac{\partial v_z^{\mathrm{loc}}}{\partial r}\right) \tag{5-35}$$

where $\partial\mu_i/\partial z$ includes the external force $X_{i,z}$ (*i.e.* μ_i includes potentials from external forces such as electrostatic field or gravity). Since the r-direction is in local equilibrium, $\partial\mu_i/\partial r = 0$. Some researchers treat electrostatic fields as an external force similar to gravity, in which case the μ_i in the Gibbs-Duhem equation includes only the chemical potential,[258] whereas other researchers account for electrostatic interactions via an electrochemical potential, in which case μ_i in the Gibbs-Duhem equation is an electrochemical potential;[74] Equation 5-35 is the same with either approach.

We integrate Equation 5-35 twice with respect to r take the integral average to obtain v_z

$$v_z = \frac{\int_0^{R_{\mathrm{pore}}} v_z^{\mathrm{loc}} 2\pi r dr}{\pi R_{\mathrm{pore}}^2} = -\sum_{i\neq \mathrm{M}} \frac{c_i^{\mathrm{mol}}}{\mathcal{K}'^{\mathrm{mol}}_i}\frac{\partial \mu_i}{\partial z} \tag{5-36}$$

where

$$\mathcal{K}'^{\mathrm{mol}}_i = \pi R_{\mathrm{pore}}^2 c_i^{\mathrm{mol}} \left\{ \int_{R_{\mathrm{pore}}}^{0} 2\pi r''' \left[\int_{r'''}^{R_{\mathrm{pore}}} \left(\frac{1}{r''} \int_0^{r''} r' \frac{c_i^{\mathrm{loc}^{\mathrm{mol}}}}{\eta} dr' \right) dr'' \right] dr''' \right\}^{-1} \tag{5-37}$$

and we use the boundary conditions $\partial v_z^{\mathrm{loc}}/\partial r\,(r=0) = 0$ and $v_z^{\mathrm{loc}}\left(r = R_{\mathrm{pore}}\right) = 0$, requiring symmetry of the fluid velocity at the channel centerline and no-slip of the velocity at the channel

walls, respectively. ${\mathcal{K}'}_i^{\mathrm{mol}}$ is the hydrodynamic friction for a single pore and is scaled by $\tau/(1-\phi_{\mathrm{M}})$ to obtain $\mathcal{K}_i^{\mathrm{mol}}$ in Equation 5-15 that describes macroscopic of the membrane. Comparing Equations 5-15 and 5-37 gives θ_i

$$\theta_i = \frac{4G\eta}{R_{\mathrm{pore}}^4 c_i^{\mathrm{mol}}} \int_0^{R_{\mathrm{pore}}} 2r''' \left[\int_{r'''}^{R_{\mathrm{pore}}} \left(\frac{1}{r''} \int_0^{r''} r' \frac{{c_i^{\mathrm{loc}}}^{\mathrm{mol}}}{\eta} dr' \right) dr'' \right] dr''' \qquad 5\text{-}38$$

To obtain ${c_i^{\mathrm{loc}}}^{\mathrm{mol}}$, the potential of mean force between species i and the membrane u_i dictates how i is distributed across the channel relative to its average concentration, ${c_i^{\mathrm{loc}}}^{\mathrm{mol}}/c_i^{\mathrm{mol}}$ (*i.e.* radial distribution function of i with respect to M), according to[251]

$$\frac{{c_i^{\mathrm{loc}}}^{\mathrm{mol}}}{c_i^{\mathrm{mol}}} = \exp\left(-\frac{u_i}{RT}\right) \qquad 5\text{-}39$$

We treat the ions as fully solvated and that they cannot move past the Outer Helmholtz plane (*i.e.* $u_i = \infty$ for $r > R_{\mathrm{effective}}$ where $R_{\mathrm{effective}}$ is the effective channel radius excluding the region beyond the Outer Helmholtz plane, specifically, $R_{\mathrm{effective}} = R_{\mathrm{pore}} - 2R_0$). For the rest of the channel, we consider that the microscopic electrostatic potential ψ dictates the potential of mean force such that $u_i = z_i F\psi$ for $r < R_{\mathrm{effective}}$; ψ is referenced such that $\psi = 0$ at radial position where ${c_i^{\mathrm{loc}}}^{\mathrm{mol}} = c_i^{\mathrm{mol}}$. With these expression for u_i and linearizing B6 for small electrostatic potentials gives [169]

$${c_i^{\mathrm{loc}}}^{\mathrm{mol}} = c_i^{\mathrm{mol}} \left(1 - \frac{\psi z_i F}{RT}\right) \mathcal{H}(R_{\mathrm{effective}} - r) \qquad 5\text{-}40$$

where $\mathcal{H}(x)$ is the Heaviside step function ($= 0$ for $x < 0$ and $= 1$ for $x \geq 0$). ψ is the microscopic electrostatic potential that is a function of r and z and cannot be rigorously related the macroscopic potential Φ.[9]. Poissons equation in cylindrical coordinates with constant relative permittivity ε_r dictates that for $r \leq R_{\mathrm{effective}}$ the electrostatic potential obeys[169]

$$\frac{1}{r}\frac{\partial}{\partial r} r \frac{\partial \psi}{\partial r} + \frac{\partial^2 \psi}{\partial z^2} = -\frac{\sum_{i \neq \mathrm{M}}^{N^{\mathrm{mol}}} z_i {c_i^{\mathrm{loc}}}^{\mathrm{mol}} F}{\varepsilon_r \varepsilon_0} = -\frac{\sum_{i \neq \mathrm{M}}^{N^{\mathrm{mol}}} z_i c_i^{\mathrm{mol}} F}{\varepsilon_r \varepsilon_0} + k^2 \psi \qquad 5\text{-}41$$

where ε_0 is the permittivity of free space and the second equality uses Equation 5-40 and the definition for the inverse Debye length k defined following Equation 5-16. Because the microscopic electrostatic field across the channel is much greater than the electrostatic field applied across the membrane, $\partial\psi/\partial r \gg \partial\psi/\partial z$, we set the second term on the right side of Equation 5-41 to zero.[259] Gauss' law provides a boundary condition by dictating the total surface charge at the Outer Helmholtz plane is equal in magnitude but opposite in sign to the excess charge density in the channel,

$$(2\pi R_{\mathrm{effective}}) \frac{\partial \psi}{\partial r}(r = R_{\mathrm{effective}}) = -\frac{\sum_{i \neq \mathrm{M}}^{N^{\mathrm{mol}}} z_i c_i^{\mathrm{mol}} F}{\varepsilon_r \varepsilon_0} \left(\pi R_{\mathrm{effective}}^2\right) \qquad 5\text{-}42$$

Equations 5-41 and 5-42 dictates that $\int_0^{R_{\text{effective}}} \psi r = 0$. The second boundary condition is symmetry of electrostatic potential at the center line, $\partial\psi/\partial r(r = 0) = 0$. Equation 5-42 with these boundary conditions gives ψ for $r < R_{\text{pore}} - 2R_0$

$$\psi = \frac{\sum_{i\neq \text{M}}^{N^{\text{mol}}} z_i c_i^{\text{mol}} \mathcal{F}}{k^2 \varepsilon_r \varepsilon_0} - \frac{R_{\text{effective}} \left(\sum_{i\neq \text{M}}^{N^{\text{mol}}} z_i c_i^{\text{mol}} F\right) I_0(kr)}{(2\varepsilon_r \varepsilon_0 I_1(kR_{\text{effective}})} \quad 5\text{-}43$$

We find $\mathcal{K}_i^{\text{mol}}$ and θ_i given in Equations 5-15 and 5-16 using the solution for potential in Equation 5-43, the distribution of ionic species in Equation 5-40, and following the integration outlined in Equation 5-38.

5.10 Appendix 5-C

Substituting Equation 5-3 into Equation 5-14 and relating the mass averaged velocity to species velocities gives

$$\sum_{i\neq \text{M}} v_{i,z}^{\text{mol}} w_i^{\text{mol}} = -\sum_{i\neq \text{M}} \frac{1}{\mathcal{K}_i^{\text{mol}}} \sum_{j\neq i} K_{ij}^{\text{mol}} \left(v_{j,z}^{\text{mol}} - v_{i,z}^{\text{mol}}\right) \quad 5\text{-}44$$

Expanding the right side of Equation 5-44 and rearranging indexes gives

$$\sum_{i\neq \text{M}} v_{i,z}^{\text{mol}} w_i^{\text{mol}} = -\sum_{i\neq \text{M}} \sum_{j\neq \text{M}} \frac{K_{ji}^{\text{mol}} v_{i,z}^{\text{mol}}}{\mathcal{K}_j^{\text{mol}}} + \sum_{i\neq \text{M}} \sum_{j\neq \text{M}} \frac{K_{ij}^{\text{mol}} v_{i,z}^{\text{mol}}}{\mathcal{K}_i^{\text{mol}}} + \sum_{i\neq \text{M}} \frac{K_{i\text{M}}^{\text{mol}} v_{i,z}^{\text{mol}}}{\mathcal{K}_i^{\text{mol}}} \quad 5\text{-}45$$

Because Equation 5-45 is true for any $v_{i,z}$, the friction coefficients must satisfy

$$w_i^{\text{mol}} = -\sum_{j\neq \text{M}} \frac{K_{ji}^{\text{mol}}}{\mathcal{K}_j^{\text{mol}}} + \sum_{j\neq \text{M}} \frac{K_{ij}^{\text{mol}}}{\mathcal{K}_i^{\text{mol}}} + \frac{K_{i\text{M}}^{\text{mol}}}{\mathcal{K}_i^{\text{mol}}} \quad 5\text{-}46$$

Solving Equation 5-46 for $K_{i\text{M}}^{\text{mol}}$ and noting that $K_{ij}^{\text{mol}} = K_{ji}^{\text{mol}}$ gives Equation 5-14.

5.11 Chapter 5 Supporting Information

5.11.1 Bulk Solution Parameters

Equation 6 fits the effective viscous molar cation volume $\tilde{V}_i$ to bulk solution chloride electrolyte viscosity data. Since chloride is relatively unhydrated compared to cations,[169] the viscous volume is set to zero. Table 5-2 presents values the fitted viscous diameter ($= \left(\frac{\tilde{V}_i 6}{\text{N}_\text{A}\pi}\right)^{\frac{1}{3}}$) and the data source that fit $\tilde{V}_i$. Ion without readily available viscosity measurements are set to those of similarly charge cations. The viscous volume of ion pairs is set to that of the constituent cation.

Table 5-2. Fit bulk solution viscous size parameters

Ion	$\left(\frac{\tilde{V}_i 6}{N_A \pi}\right)^{\frac{1}{3}}$ [nm]	Notes and Source
Ca^{2+}	0.725	[260]
Cu^{2+}	0.704	[260]
Fe^{3+}	0.908	[260] Approximated from Cr^{3+}
H^{+}	0.407	[85]
K^{+}	0.251	[85]
Li^{+}	0.552	[85]
Na^{+}	0.508	[85]
Ni^{2+}	0.765	[260]
V^{3+}	0.908	[260] Approximated from Cr^{3+}
VO^{2+}	0.775	[94]
VO_2^{+}	0.552	[85] Approximated from Li^{+}
$VOHSO_4^{+}$	0.552	Set to VO_2^{+}
$VHSO_4^{2+}$	0.908	Set to V^{3+}

For transport properties, Table 5-3 lists the parameters describing binary diffusion coefficients between species. Chapman provides extensive values of ion-ion diffusion coefficients in binary alkali-chloride electrolytes.[85]

Table 5-3. Species transport and size parameters

Ion	Parameter	Value*	Notes and Source
H^+	$D_{0H^+}^{\infty}$	9.311 x10^{-9} [m^2 s^{-1}]	[173]
	$D_{H^+Cl^-}$	1.883 x10^{-9} [m^2 s^{-1}]	[85]
	$D_{H^+Br^-}$	1.88x10^{-9} [m^2 s^{-1}]	App. as HCl [85]
	$D_{H^+SO_4^{2-}}$	1.354x10^{-11} [m^2 s^{-1}] at 0.3 mol kg^{-1}	App as Na_2SO_4 [85]
	$D_{H^+HSO_4^{2-}}$	1.83x10^{-9} [m^2 s^{-1}]	App as H_2SO_4 [85]
Li^+	$D_{0Li^+}^{\infty}$	1.957 x10^{-9} [m^2 s^{-1}]	[173]
	$D_{Li^+Cl^-}$	1.251 x10^{-10} [m^2 s^{-1}]	[85]
Na^+	$D_{0Na^+}^{\infty}$	1.334 x10^{-9} [m^2 s^{-1}]	[173]
	$D_{Na^+Cl^-}$	2.631 x10^{-10} [m^2 s^{-1}]	[85]
K^+	$D_{0K^+}^{\infty}$	1.957 x10^{-9} [m^2 s^{-1}]	[173]
	$D_{K^+Cl^-}$	4.078 x10^{-10} [m^2 s^{-1}]	[85]
Cs^+	$D_{0Cs^+}^{\infty}$	2.065 x10^{-9} [m^2 s^{-1}]	[173]
	$D_{Cs^+Cl^-}$	4.078 x10^{-10} [m^2 s^{-1}]	App as KCl [85]
V^{3+}	$D_{0V^{3+}}^{\mathrm{mol}\ \infty}$	0.141x10^{-9} [m^2 s^{-1}]	[261]
	$D_{V^{3+}SO_4^-}^{\mathrm{mol}}$	6.26x10^{-12} [m^2 s^{-1}] at 0.7 mol kg^{-1}	App as $CuSO_4$ [85]
	$D_{V^{3+}HSO_4^-}^{\mathrm{mol}}$	6.63x10^{-12} [m^2 s^{-1}] at 0.05 mol kg^{-1}	App. as $LaCl_2$ [85]
	$D_{V^{3+}Cl^-}^{\mathrm{mol}}$	6.63x10^{-12} [m^2 s^{-1}] at 0.05 mol kg^{-1}	App. as $LaCl_2$ [85]
$VHSO_4^{2+}$	$D_{0VHSO_4^+}^{\mathrm{mol}\ \infty}$	0.141x10^{-9} [m^2 s^{-1}]	App. as VO [262]
	$D_{VHSO_4^+SO_4^-}^{\mathrm{mol}}$	1.78x10^{-11} [m^2 s^{-1}] at 0.3 mol kg^{-1}	App. as Na_2SO_4 [263]
	$D_{VHSO_4^+HSO_4^-}^{\mathrm{mol}}$	2.63x10^{-10} [m^2 s^{-1}]	App. as NaCl, [263]
VO^{2+}	$D_{0VO^{2+}}^{\mathrm{mol}\ \infty}$	0.14x10^{-9} [m^2 s^{-1}]	[264]
	$D_{VO^{2+}SO_4^{2-}}^{\mathrm{mol}}$	6.26x10^{-12} [m^2 s^{-1}] at 0.7 mol kg^{-1}	App. as $CuSO_4$ [263]
	$D_{VO^{2+}HSO_4^-}^{\mathrm{mol}}$	6.01x10^{-11} [m^2 s^{-1}] at 1.0 mol kg^{-1}	App. as $CaCl_2$ [263]
$VOHSO_4^+$	$D_{0VOHSO_4}^{\mathrm{mol}\ \infty}$	0.14x10^{-9} [m^2 s^{-1}]	[264]
	$D_{HSO_4VO^+SO_4^{2-}}^{\mathrm{mol}}$	2.398x10^{-11} [m^2 s^{-1}] at 0.3	App. as KSO_4 [263]
	$D_{HSO_4VO^+HSO_4^-}^{\mathrm{mol}}$	4.079x10^{-10} [m^2 s^{-1}]	App. as KCl [263]
VO_2^+	$D_{0VO_2^+}^{\mathrm{mol}\ \infty}$	0.14x10^{-9} [m^2 s^{-1}]	[264]
	$D_{VO_2^+SO_4^{2-}}^{\mathrm{mol}}$	2.398x10^{-11} [m^2 s^{-1}] at 0.3	App. as KSO_4 [263]
	$D_{VO_2^+HSO_4^-}^{\mathrm{mol}}$	4.079x10^{-10} [m^2 s^{-1}]	App. as KCl [263]
Fe^{3+}	$D_{0Fe^{3+}}^{\infty}$	0.604x10^{-9} [m^2 s^{-1}]	[173]
	$D_{Fe^{3+}Cl^-}$	6.63x10^{-12} [m^2 s^{-1}]	App. as $LaCl_3$ [263]

Ca^{2+}	$D^{\infty}_{0Ca^{2+}}$	$0.792x10^{-9}$ [m^2 s^{-1}]	[173]
	$D_{Ca^{2+}Cl^-}$	$1.96x10^{-10}$ [m^2 s^{-1}] at 1.5 mol kg^{-1}	App. as $BaCl_2$ [263]
Ni^{2+}	$D^{\infty}_{0Ni^{2+}}$	$0.661x10^{-9}$ [m^2 s^{-1}]	[173]
	$D^{\infty}_{0ClNi^{+}}$	$0.661x10^{-9}$ [m^2 s^{-1}]	App. as Ni^{2+}
	$D_{Ni^{2+}Cl^-}$	$1.96x10^{-10}$ [m^2 s^{-1}] at 1.5 mol kg^{-1}	App. as $BaCl_2$ [263]
Cu^{2+}	$D^{\infty}_{0Cu^{2+}}$	$0.714x10^{-9}$ [m^2 s^{-1}]	[173]
	$D_{Cu^{2+}Cl^-}$	$1.96x10^{-10}$ [m^2 s^{-1}] at 1.5 mol kg^{-1}	App. as $BaCl_2$ [263]
Cl^-	D_{0Cl^-}	2.032 $x10^{-9}$ [m^2 s^{-1}]	[173]
Br^-	D_{0Br^-}	2.080 $x10^{-9}$ [m^2 s^{-1}]	[173]
* reference concentration is 3 mol kg^{-1} for D_{ij} unless otherwise stated			

5.11.2 Multicomponent Transport Properties of Membranes in Dilute, Mixed Lithium Electrolytes

These trends continue in lithium-form membranes exchanged with other alkali metals. Figure 5-6 shows the same measured [67] (symbols) and predicted (lines) properties as Figure 5-1 in text for Li^+-A^+ exchange as a function of membrane lithium cation fraction, $y^{\beta}_{Li^+}$. The conductivity of Li^+-A^+ changes relatively little despite the higher affinity of A^+ for the membrane. Moreover, the lithium transference number shows that the fractional ion-exchange largely dictates the fraction of current is carried by each ion, which occurs only if the ion mobilities are similar. These finding supports the conclusions of Kamcev et al. and that ion-membrane association does not reduce mobility.[199]

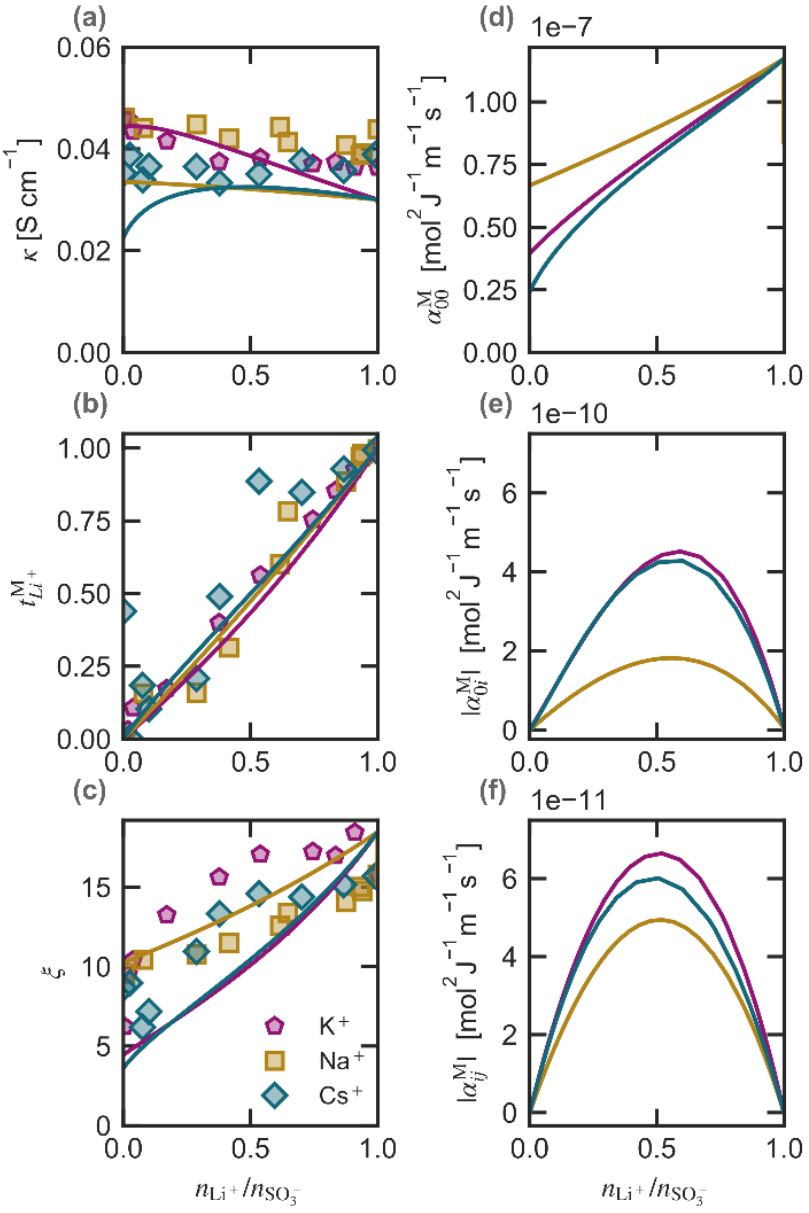

Figure 5-6. Measured[67] (symbols) and calculated (lines) Nafion membrane (a) conductivity κ, (b) proton transference number $t_{Li^+}^M$, (c) electroosmotic coefficient ξ, and the transport coefficients between (d) water-water α_{00}, (e) ion-water α_{i0}^M, and (f) ion-ion α_{ij}^M in liquid water, as function of fractional proton exchange, $n_{Li^+}/n_{SO_3^-}$, with lithium (triangles), sodium (squares), potassium (pentagons), and cesium (tilted squares).

5.11.3 Concentrated-Solution Transport Properties of Nafion in Vanadium Electrolytes

Figure 5-7 plots (a) electroosmotic coefficient ξ, (b) vanadium transference number $t^{\mathrm{M}}_{\mathrm{V(x)}}$, and the transport coefficients between (c) water-water α^{M}_{00} (d) water-sulfate $\alpha^{\mathrm{M}}_{0\mathrm{SO_4}}$, (e) water-vanadium $\alpha^{\mathrm{M}}_{0\mathrm{V(x)}}$, (f) sulfate-sulfate $\alpha^{\mathrm{M}}_{\mathrm{SO_4SO_4}}$, (g) vanadium-vanadium $\alpha^{\mathrm{M}}_{\mathrm{V(x)V(x)}}$, and (h) sulfate-vanadium $\alpha^{\mathrm{M}}_{\mathrm{SO_4V(x)}}$ a Nafion membrane in the same electrolytes as Figure 5-5. Most of the transport properties are strongly concentration dependent, and are starkly different among vanadium species. The vanadium-related transport properties $t^{\mathrm{M}}_{\mathrm{V(x)}}$, $\alpha^{\mathrm{M}}_{0\mathrm{V(x)}}$, $\alpha^{\mathrm{M}}_{\mathrm{V(x)V(x)}}$, and $\alpha^{\mathrm{M}}_{\mathrm{SO_4V(x)}}$ increase with increasing vanadium amounts in the membrane (see Part I, Chapter 4)[247]. Despite sulfate uptake remaining relatively constant with increasing concentration of vanadium in the external electrolyte (see Part I, Chapter 4)[247], sulfate transport properties $\alpha^{\mathrm{M}}_{0\mathrm{SO_4}}$ and $\alpha^{\mathrm{M}}_{\mathrm{SO_4SO_4}}$ decrease in V(IV) and V(V) electrolytes but, in V(III) electrolytes, they increase at low vanadium concentrations and then decrease at higher electrolyte concentrations. Water transport properties ξ and α^{M}_{00} change continuously with the trend depending on the vanadium oxidation state in the electrolyte.

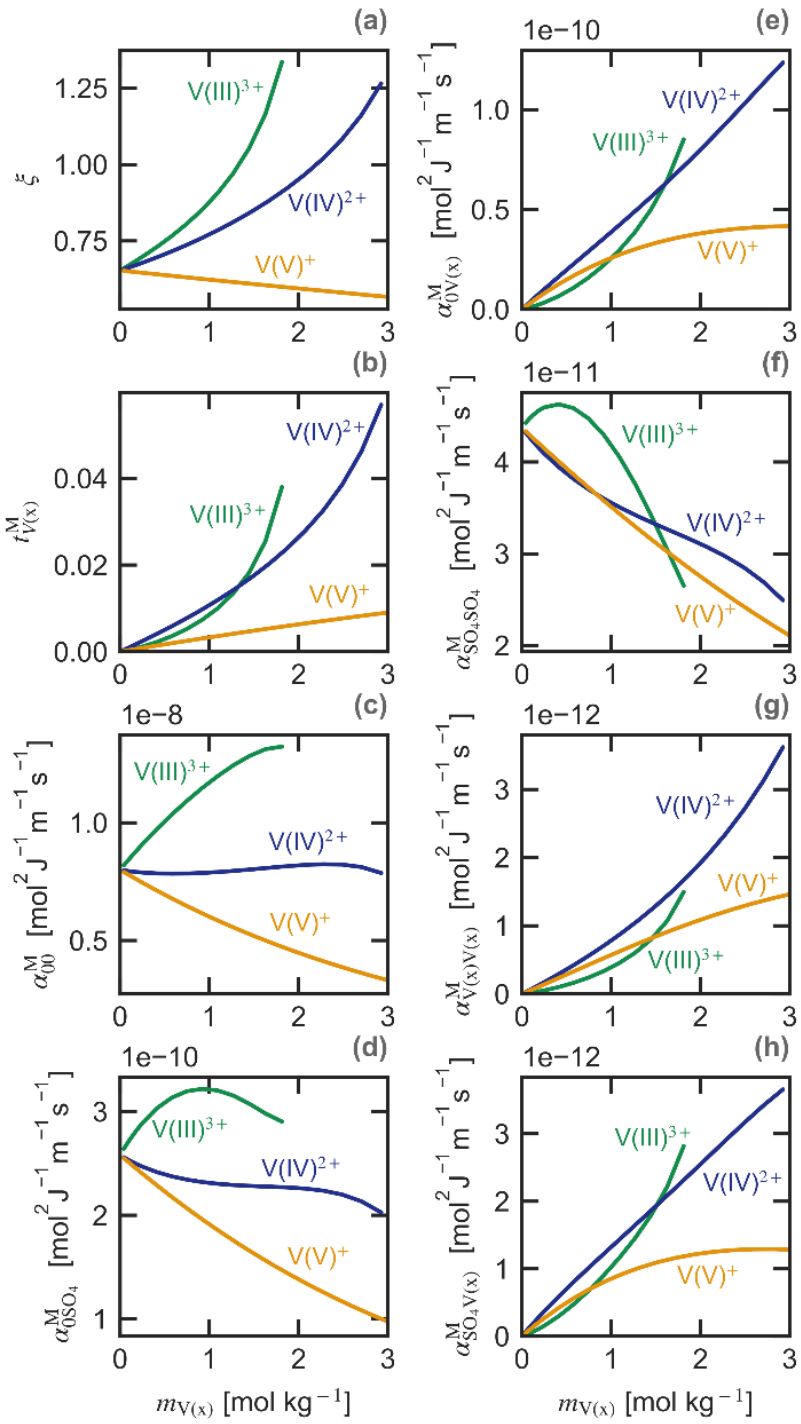

Figure 5-7. Calculated (a) electroosmotic coefficient ξ, (b) vanadium transference number $t^{M}_{V(x)}$, and the transport coefficients between (c) water-water α^{M}_{00} (d) water-sulfate $\alpha^{M}_{0SO_4}$, (e) water-vanadium $\alpha^{M}_{0V(x)}$, (f) sulfate-sulfate $\alpha^{M}_{SO_4SO_4}$, (g) vanadium-vanadium $\alpha^{M}_{V(x)V(x)}$, and (h) sulfate-vanadium $\alpha^{M}_{SO_4V(x)}$ for a Nafion membrane as a function of external vanadium V(III), V(IV), or V(V) molality, $m_{V(x)}$, in sulfuric acid with a total sulfate concentration of 5 mol dm^{-3}.

6 Theory of Multicomponent Phenomena in Cation-Exchange Membranes, III: Transport in Vanadium Redox-Flow-Battery Separators

6.1 Chapter Abstract

Transport through vanadium redox-flow-battery membranes strongly influences cell performance. In this work, we use a multicomponentconcentrated-solution model of transport and thermodynamics in phase-separated cation-exchange membranes, the most common separator type, to develop structure-performance relationships. The model incorporates species partitioning into the membrane, thermodynamic nonidealities, and Stefan-Maxwell-Onsager frictions between species. Molecular-thermodynamics and -transport theories parameterize the model. We validate the calculations against measured Coulombic and voltage efficiencies of a vanadium flow battery as a function of current density. Our model shows that species transport is the result of collective interactions between all species present in the system. The magnitude of coupling suggests that predictions made using dilute-solution theory for transport in these systems will be misleading in many situations. As a demonstration of the capabilities of the model, we predict cell performance, incorporating these interactions, as a function of electrolyte concentration and composition and membrane equivalent weight and backbone modulus. We find that electrolytes with high sulfuric acid concentrations provide the greatest cell performance (quantified by maximizing power density at a target energy efficiency). In the case of membrane properties, low equivalent-weight polymers perform better; at high equivalent-weights, a low membrane modulus is preferred.[††]

6.2 Introduction

Membrane separator properties critically impact the performance of vanadium redox flow batteries (VRFB).[11, 86-88, 119, 265-268] These separators, which are typically polymer membranes, facilitate ionic current between the positive and negative electrodes while limiting shorting and self-discharge due to crossover of vanadium active species.[11, 265] To optimize VRFB performance, there is an optimal design window between conductivity and crossover, which are at odds, as they necessitate different membrane morphology and intrinsic properties.[11, 86, 265] Thus, determining structure-performance relationships for membranes is key to successful deployment of VRFBs. As a result, the electrochemistry community has researched these transport properties using measurements and models for a variety of separator materials and operating conditions, as numerous reviews and articles outline.[11, 86-88, 106, 119, 194-195, 265-271]

Despite these efforts, transport in VRFB separators is still a poorly understood process due to the numerous species and modalities involved, as displayed in Figure 6-1.[92, 94, 96, 269-272] Such transport involves both vanadium partitioning into the separator from the external electrolyte solution,[91, 93-

[††] Published as Crothers, A. R.; Darling, R. M.; Kushner, D.; Perry, M. L.; Weber, A. Z., Theory of Multicomponent Phenomena in Cation-Exchange Membranes: Part III. Transport in Vanadium Redox-Flow-Battery Separators. *J. Electrochem. Soc.* **2020,** *167* (1), 013549.

[94, 195] followed by ion and solvent transport across the separator driven by concentration gradients (*i.e.* diffusion) and the electric field (*i.e.* migration).[86, 89-90, 95-96, 107, 195, 270, 272-273] The impact of different driving forces on species flux is particularly complicated due to the high concentration of multiple ionic species present.[96, 196] High concentrations create strongly nonideal thermodynamics (*e.g.* large excess chemical potentials), and frictional interactions between species couple transport (*e.g.* concentration gradients of species i cause transport of species j).[64, 95-96, 196, 274] As a result of these complex conditions, transport and partitioning coefficients are functions of both the composition of electrolyte in the electrodes and membrane chemistry.[91, 93-94, 118-119, 268, 274]

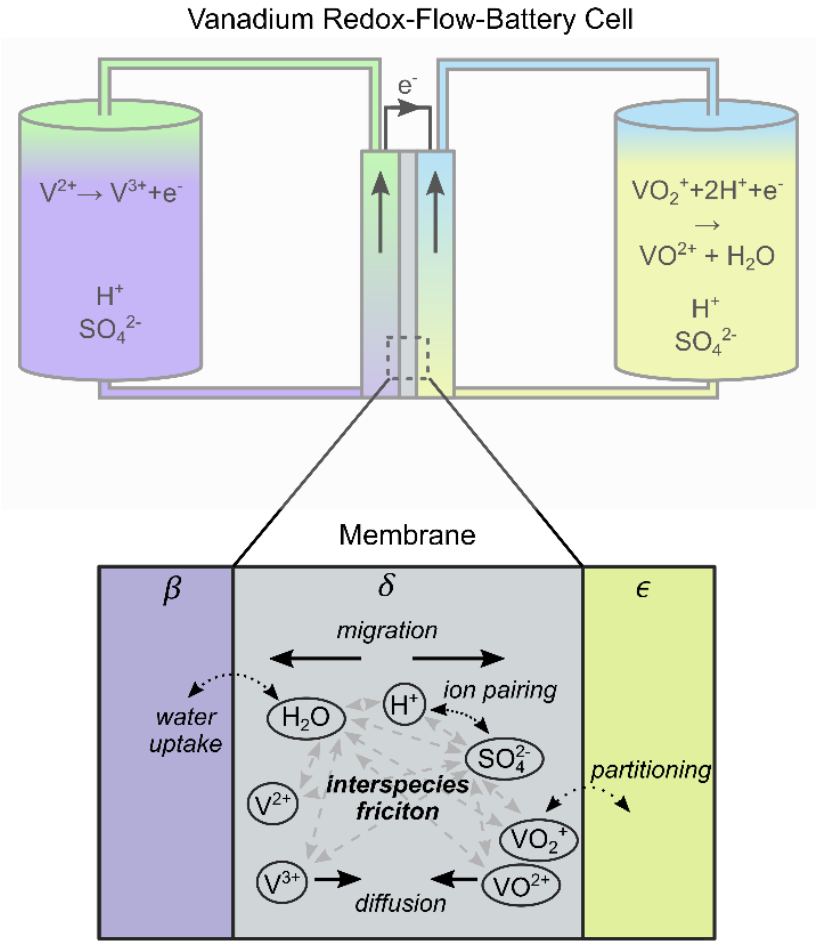

Figure 6-1. Schematic of a redox flow battery (top) and pictorial representation various multicomponent thermodynamic and transport phenomena taking place in VRFB membranes (bottom). The membrane, phase δ, seperates the negative electrode, phase β, from the positive electrode, phase ϵ.

Mathematical models for transport in membranes deconvolute these various effects.[86, 88-90, 195-196, 243, 269, 272, 274] Previously developed models have been invaluable for understanding cell performance across multiple cycles and how electrolyte transports through the cell.[86, 88-90, 195-196, 243, 269, 272, 274] However, many of these efforts are restricted to dilute-solution approximations that

do not consider coupled transport and/or account for concentration-dependent transport properties. The validity of these assumptions under flow-battery operating conditions is not known. Unfortunately, approaches that use concentrated-solution theory[196, 243, 274] are often intractable because they require numerous transport parameters, of which the few that are measured have large associated experimental error.[243] To overcome these challenges, Part I and II of this series (Chapters 4 and 5) developed and validated molecular models for coupled, multi-ion thermodynamic and transport properties in phase-separated cation-exchange membranes.[31, 247] This approach completely specifies the concentrated-solution transport properties as a function of concentration and membrane chemistry. Using these models, this paper explores the role of transport coupling and links molecular-scale behavior to macroscale performance of VRFB membranes, providing design criteria and guidelines for both cell developers and membrane chemists.

The outline of this paper is as follows. In the theory section, we summarize the relevant thermodynamic and transport equations. We then examine the extent and nature of transport coupling and the impact on membrane properties. A 1-D, quasi-steady-state model of a VRFB membrane uses the transport parameters to show how vanadium crossover is detrimental. Finally, we examine how the electrolyte composition and the structure and chemistry of the membrane impact the cell performance.

6.3 Theory

In focusing our study on the transport driving forces in VRFB membranes (see Figure 6-1 bottom), we consider the cell at quasi-steady-state in which the cell state of charge and the composition of the electrode electrolytes does not change significantly during a cycle. This work compliments previous VRFB modeling efforts that have focused on overall cell operation (see Figure 6-1 top).[89-90, 195, 269-270, 275-281] This section first summarizes the VRFB system, including relevant electrochemical and chemical reactions. We then show how ohmic overpotentials and crossover of active species impact cell operation. The final sections formulate the transport and thermodynamic equations governing species flux and chemical potential drop across the membrane.

6.3.1 Vanadium Flow-Battery System

This study examines an all-vanadium redox-flow battery, pictured in Figure 6-1. The system consists of electrolyte-filled porous electrodes that contain aqueous vanadium sulfate salts with sulfuric-acid supporting electrolyte (water, H_2O, protons, H^+, and sulfate, SO_4^{2-}, are abbreviated 0, H, and SO_4, respectively). The system is at a temperature of 295 K. The negative electrode, β, contains V^{2+} and V^{3+} (denoted V(II) and V(III), respectively, based on vanadium oxidation state) and the positive electrode, ϵ, contains VO^{2+} and VO_2^+ (denoted V(IV) and V(V) respectively). Vanadium in any oxidation state is denoted V(x). As the cell discharges, the reactions are $V(II) \rightarrow V(III)$ at the negative electrode and $V(V) \rightarrow V(IV)$ at the positive electrode. Sulfate species associate with vanadium ions and with protons to form various ion-paired products.[223] Table 6-1 details the electrochemical reactions and their half-cell potentials, the chemical reactions that occur when vanadium crosses over the membrane separating the electrodes (phase δ), and the ion association equilibrium reactions.

Table 6-1. Electrochemical and chemical reaction and ion-pair equilibria in VRFBs.[107, 223]

Electrochemical Reactions	
$V^{2+} \leftrightarrows V^{3+} + e^-$	$E^0 = -0.26\ V$ vs. SHE
$VO^{2+} + H_2O \leftrightarrows VO_2^+ + 2H^+ + e^-$	$E^0 = 1.00\ V$ vs. SHE
Chemical Crossover Reactions	
$V^{2+} + 2VO_2^+ + 2H^+ \rightarrow 3VO^{2+} + H_2O$	At Positive Electrode
$V^{3+} + VO_2^+ \rightarrow 2VO^{2+}$	At Positive Electrode
$VO^{2+} + V^{2+} + 2H^+ \rightarrow 2V^{3+} + H_2O$	At Negative Electrode
$VO_2^+ + 2V^{2+} + 4H^+ \rightarrow 3V^{3+} + 2H_2O$	At Negative Electrode
Ion Association Equilibria	
$H^+ + SO_4^{2-} \rightleftarrows HSO_4^-, \quad K_{eq} = 1.85\text{x}10^{-4}$ (Ref [233])	
$HSO_4^- + V^{3+} \rightleftarrows HSO_4V^{2+}, \quad K_{eq} = 1.8\text{x}10^{-6}$ (fit)	
$HSO_4^- + VO^{2+} \rightleftarrows HSO_4VO^+, \quad K_{eq} = 0.01059$ (Ref [223])	

6.3.2 Cell Performance

Cell performance is typically characterized by the power density on discharge, Ψ_d, and the round-trip energy efficiency, ε_e.[34] Ψ_d is the product of the discharge current density i_d and the cell potential on discharge V_d [9]

$$\Psi_d = i_d V_d \tag{6-1}$$

The energy efficiency is the ratio of the integrated cell power density on discharge to charge and is typically treated as the product of the voltage efficiency, ε_v, and the Coulombic efficiency, ε_q, [119]

$$\varepsilon_e = \left(\frac{V_d}{V_c}\right)\left(\frac{\int_d i_d dt}{\int_c i_c dt}\right) = \varepsilon_v \varepsilon_q \tag{6-2}$$

where t is time, the subscript c or d denotes charge or discharge, and the cell voltage is approximated as constant during charge or discharge. ε_v characterizes efficiency losses due to cell overpotentials (*e.g.* kinetic and ohmic) and decreases with increasing current density.[11] ε_q quantifies efficiency losses due to vanadium passing through the membrane between electrode solutions, mixing, and reacting chemically rather than electrochemically. ε_q tends to increase with rising current density because the total charge extracted from the cell generally grows compared to the amount of charge lost to chemical reactions.[11] A typical operating goal is maximizing power density at a target energy efficiency.[34] The next two sections present the governing equations for cell potential, which is required to calculate power density and voltage efficiency, and the state-of-charge loss during cycling, which dictates Coulombic efficiency.

6.3.2.1 Cell Potential

The cell potential is the difference in the electrochemical potential of the electrons μ_{e^-} in the metal at the negative electrode α' and the positive electrode α''; these are related to the electrochemical

potential of species i, μ_i^{ϕ}, participating in the oxidation/reduction reactions in electrode ϕ as outlined in Table 6-1[9]

$$FV = \mu_{e^-}^{\alpha'} - \mu_{e^-}^{\alpha''} = \left(\mu_{V(II)}^{\beta} - \mu_{V(III)}^{\beta} - F\eta^{\beta}\right) - \left(\mu_{V(IV)}^{\epsilon} + \mu_0^{\epsilon} - \mu_{V(V)}^{\epsilon} - 2\mu_H^{\epsilon} - F\eta^{\epsilon}\right) \quad 6\text{-}3$$

where F is Faraday's constant and η^{ϕ} is ionic potential drop between the metal and the electrolyte in electrode ϕ due to mass-transport resistances, surface overpotentials, or other non-membrane cell resistances.

To put Equation 6-3 in terms of the electrochemical potentials of species in the membrane, chemical equilibrium requires that the electrochemical potential of charged species (and the chemical potential of neutral species) must be equal at the interface of electrode phase ϕ and membrane phase δ[30]

$$\mu_i^{\delta} = \mu_i^{\phi} \quad 6\text{-}4$$

where μ_i is a function of chemical variables – temperature, pressure, composition – and, for charged species, the ionic potential.

It is convenient to group electrostatic dependences into a single variable with the remaining variables depending only on composition, temperature, and pressure. We reference the electrochemical potential of species i to the electrochemical potential of the membrane M to define

$$\mu_{i,M}^{\delta} = \mu_i^{\delta} - \frac{z_i}{z_M}\mu_M^{\delta}, \quad 6\text{-}5$$

which is an electroneutral pairing of species and is independent of electrostatic potential.[9, 74] To track the electrical state through the membrane, we set the ionic potential Φ equal to the electrochemical potential of the membrane, $z_M F\Phi = \mu_M^{\delta}$. This assignment is equivalent to measuring the ionic potential using a hypothetical reference electrode selective to the ionic groups on the membrane at the same conditions.[9] Using Equation 6-4 and $\mu_{i,M}^{\delta}$, the cell potential is then

$$V = U + \eta + \Delta\Phi \quad (6\text{-}6)$$

where $\eta = \eta^{\epsilon} - \eta^{\beta}$ groups non-membrane overpotentials in the cell. U is the equilibrium cell potential

$$FU = \left[\left(\mu_{V(II),M}^{\delta'} - \mu_{V(III),M}^{\delta'}\right) - \left(\mu_{V(IV),M}^{\delta''} + \mu_0^{\delta''} - \mu_{V(V),M}^{\delta''} - 2\mu_{H,M}^{\delta''}\right)\right] \quad 6\text{-}7$$

where δ' is and δ'' are the membrane phase at the negative and positive electrode interfaces, respectively. $\Delta\Phi = \Phi^{\delta''} - \Phi^{\delta'}$ is the potential drop across the membrane due to ohmic and diffusion overpotentials. During discharge (charge), η and $\Delta\Phi$ become more negative (positive) with increasing current density, causing the cell voltage efficiency to decrease.[11] We set U to the measured open-circuit potential (= 1.42 V)[11] by neglecting the diffusion potential, which tends to be small.[9] η is modeled as an ohmic potential drop with resistance R_{Ω}

$$\eta = \pm|i|R_{\Omega}. \quad 6\text{-}8$$

where η is negative for discharge and positive for charge.

6.3.2.2 State-of-Charge Loss

Vanadium crossover causes the cell to self-discharge. The cell state of charge, SOC, characterizes the extent the cell is in the charged state; it is the ratio of the sum of the moles of vanadium in the charged state (namely, V(II) in the negative electrode and V(V) in the positive electrode) to the total moles of vanadium in the system

$$SOC = \frac{n^{\beta}_{\mathrm{V(II)}} + n^{\epsilon}_{\mathrm{V(V)}}}{n^{\beta}_{\mathrm{V(II)}} + n^{\beta}_{\mathrm{V(III)}} + n^{\epsilon}_{\mathrm{V(V)}} + n^{\epsilon}_{\mathrm{V(IV)}}} \tag{6-9}$$

where n_i^{ϕ} is the moles of i in electrode ϕ.

The rate at which the state of charge changes during discharging or charging is a function of the cell current density i and the crossover current density i_{x} [11, 86-87]

$$\frac{Fn_{\mathrm{t}}}{2A}\frac{dSOC}{dt} = -i - i_{\mathrm{x}} \tag{6-10}$$

where A is the active area of the membrane and n_{t} is the total moles of vanadium in the system ($i.e.\ n^{\beta}_{\mathrm{V(II)}} + n^{\beta}_{\mathrm{V(III)}} + n^{\epsilon}_{\mathrm{V(V)}} + n^{\epsilon}_{\mathrm{V(IV)}}$). i_{x} characterizes how vanadium crossover decreases the state of charge of the cell and is a function of the flux of vanadium species i through the membrane, N_i, according to [11, 86-87]

$$i_{\mathrm{x}} = F\frac{3N_{\mathrm{V(II)}} - 3N_{\mathrm{V(V)}} + N_{\mathrm{V(III)}} - N_{\mathrm{V(IV)}}}{2}. \tag{6-11}$$

The membrane/negative electrode interface is set at $z = 0$ and the membrane/positive electrode interface is at $z = l_{\mathrm{M}}$ so that N_i is positive for species that move towards the positive electrode (*e.g.* V(II) and V(III)) and negative for species that move toward the negative electrode (*e.g.* V(IV) and V(V)). With this convention for the direction of flux, the ionic current density i through the membrane is positive on discharge and is also the electronic current leaving the positive electrode normalized by A (*i.e.* positive on discharge).[86] A subsequent section shows that N_i is constant across the membrane.

The first term on the right side of Equation 6-10 is the consumption/production of species due to electrochemical charge/discharge, the second term is due to the loss of V(II) and V(V) from crossover to the opposing electrode and from reactions with vanadium species that transport from the opposing electrode (Table 6-1 specifies the stoichiometry incorporated in Equation 6-11). Based on the low concentration of absorbed vanadium in the membrane, the chemical reactions in Table 6-1 occur in the electrode solutions and not in the membrane. The supporting electrolyte provides an excess of protons, and the high concentration of vanadium in the electrode solution rapidly reacts with any vanadium that crosses the membrane into the electrode.[107] The factor of 1/2 on the left side of Equation 6-10 results from considering the combined state of charge of the positive and negative electrodes. i_{x} is a function of current density and cell state of charge (see Equation 6-11).[270, 277]

As a result of vanadium crossover, the amount of charge extracted from the cell during discharge, $\int_{\mathrm{d}} i_{\mathrm{d}} A dt$, is less than the amount put into the cell to recharge it to its original state of charge during charging, $-\int_{\mathrm{c}} i_{\mathrm{c}} A dt$.[86] Integrating Equation 6-10 over a discharge/charge cycle with no net change

in SOC for a constant discharge and constant charge current density and crossover current, i_{x}, and solving for ε_{q} gives[86]

$$\varepsilon_{\mathrm{q}} = \frac{1 + \frac{i_{\mathrm{x,c}}}{i_{\mathrm{c}}}}{1 + \frac{i_{\mathrm{x,d}}}{i_{\mathrm{d}}}} \qquad 6\text{-}12$$

where i_{c} is negative and i_{d}, $i_{\mathrm{x,c}}$, $i_{\mathrm{x,d}}$ are positive. Because i_{x} is a function cell state of charge, the condition for Equation 6-12 of constant i_{x} is achieved by small change to SOC over charge/discharge.

6.3.3 Membrane Phenomena

The following two sections discuss how the electrolyte partitions into and how it transports across the membrane. These expressions provide for calculation of ε_{q}, ε_{v}, and $\Delta\Phi$. Although the following expressions are general for any flow-battery membrane, the specific microscale theories we use to calculate thermodynamic and transport coefficient are specific to phase-separated polymer cation-exchange membrane that Parts I and II present.[31, 247] The most common class of these materials are perfluorinated sulfonic-acid (PFSA) ionomers, such as Nafion.[12] These materials consists of nanoscale, interconnected hydrophilic domains filled with aqueous electrolyte solution and side-chains terminated with anionic moieties that are tethered to the PFSA polymer.[12] Surrounding these domains are hydrophobic polytetrafluoroethylene backbone that provides structural support.[12]

6.3.3.1 Membrane Thermodynamics

Requisite for species to transport across the membrane, they must sorb from the electrode electrolyte into the membrane as Equation 6-4 specifies. Chemical thermodynamics quantifies how these potentials are related to measurable quantities. The chemical potential of a neutral species is[30]

$$\mu_i = \mu_i^{\theta} + RT \ln x_i + \mu_i^{\mathrm{ex}} \qquad 6\text{-}13$$

where R is the universal gas constant, T is temperature, and x_i is the mole fraction of i ($= \sum_j n_i/n_j$ where n_j is the moles of species j). The mole fraction of charged polymer groups in the membrane is x_{M} and the charge for most cation-exchange membranes is $z_{\mathrm{M}} = -1$. The reference chemical potential of i, μ_i^{θ}, is for a hypothetical ideal solution at unit mole fraction x_i and is a function of temperature and pressure.[30] The second term on the right side of Equation 6-13 is the ideal solution contribution.[30] In this paper, the ideal-solution contribution is for fully-dissociated electrolyte (*i.e.* the Experimental Construct discussed in Part I, Chapter 4).[247] The excess chemical potential accounts for ion/ion, ion/membrane, solvent/membrane, and solvent/ion interactions including ion-pair formation (see Table 6-1), electrostatic interactions, ion solvation, steric confinement, and membrane swelling. Part I (Chapter 4) details calculation of the excess chemical potential μ_i^{ex}.[247]

For a charged species, the electrochemical potential has the same form as Equation 6-13 but further depends on the electrical state of the phase and charge number z_i.[9] However, expressing the electrochemical chemical potential using only neutral pairings of two charged of species (*i.e.* $\mu_i - \frac{z_i}{z_j}\mu_j$) eliminates the dependence on electrical potential.[9] Substitution of these neutral pairings of

Equation 6-13 into Equation 6-4 relates species mole fraction in the membrane and electrode electrolyte[62]

$$\frac{x_i^{\delta}\left(x_j^{\delta}\right)^{-\frac{z_i}{z_j}}}{x_i^{\phi}\left(x_j^{\phi}\right)^{-\frac{z_i}{z_j}}} = \exp\left[\frac{\left(\mu_i^{\mathrm{ex},\phi} - \mu_i^{\mathrm{ex},\delta}\right) - \frac{z_i}{z_j}\left(\mu_j^{\mathrm{ex},\phi} - \mu_j^{\mathrm{ex},\delta}\right)}{RT}\right] = \Gamma_{ij} \tag{6-14}$$

For neutral species (*e.g.* water) $z_i = 0$ and, therefore, the *j*th species does not need to be specified in Equation 6-14. Electroneutrality inside the membrane adds a constraint that fully specifies ion partitioning[30]

$$F\sum_i z_i x_i^{\delta} = 0 \tag{6-15}$$

If oppositely charged ions are used for i and j (such as the anion and cation of a salt) and Γ_{ij} is unity, the oppositely charged pairs i and j partition into the membrane according to ideal Donnan equilibrium.[62] If $\Gamma_{ij} > 1$, i and j favorably partition into the membrane whereas if partitioning is unfavorable, $\Gamma_{ij} < 1$.[62] For context, Part I (Chapter 4) shows that for a Nafion cation-exchange membrane in an aqueous hydrobromic-acid solution at concentration of 5 mol/kg-solvent, the term on the right side of Equation 6-14 is ~0.75 for HBr and 0.95 for water.[247]

6.3.3.2 Membrane Transport

Upon sorption into the membrane, species transport according to their molar flux N_i across the membrane (z-direction in the 1-D model). The molar flux obeys species conservation at steady-state[82]

$$-\frac{\partial N_i}{\partial z} = 0 \tag{6-16}$$

Although the concentration of species in the electrodes changes during cell operation, transport in the membrane is assumed to be at steady-state because the concentration and pressure gradients in the membrane develop much faster (*i.e.* pseudo steady-state approximation).[82]

Absent temperature and hydraulic-pressure gradients, transport is driven by electrochemical potential gradients. Friction between species introduces drag that reduces total flux. Stefan-Maxwell-Onsager theory describes the balance between driving force and drag on i not equal to M as [9, 32, 36]

$$c_i\frac{\partial \mu_i}{\partial z} = \sum_{j\neq i,\mathrm{M}}\frac{RT}{\mathfrak{D}_{ij}c_{\mathrm{T}}}\left(c_i N_j - c_j N_i\right) - \frac{RTc_{\mathrm{M}}}{\mathfrak{D}_{i\mathrm{M}}c_{\mathrm{T}}}N_i, \tag{6-17}$$

and for the membrane as

$$c_{\mathrm{M}}\frac{\partial \mu_{\mathrm{M}}}{\partial z} = \sum_{j\neq \mathrm{M}}\frac{RTc_{\mathrm{M}}}{\mathfrak{D}_{j\mathrm{M}}c_{\mathrm{T}}}N_j \tag{6-18}$$

where c_i is the molar concentration of species i and c_T is the total molar concentration in the membrane. (For convenience in this section, we do not superscript variables for quantities in the membrane phase δ). As discussed in the preceding section, μ_i is a function of temperature, pressure, composition, and ionic potential Φ. $\mathfrak{D}_{ij}$ is the binary diffusion coefficient between species i and j. $\mathfrak{D}_{j\mathrm{M}}$ is related to the friction coefficient between species i and the membrane, $K_{i\mathrm{M}}$, that is described in Part II (Chapter 5), according to $\mathfrak{D}_{i\mathrm{M}} = c_i c_\mathrm{M} RT/c_\mathrm{T} K_{i\mathrm{M}}$.[31] The membrane is stationary (*i.e.* is the reference velocity) and the membrane concentration c_M is set as the molar concentration of charged groups on the polymer. Onsager reciprocal relations dictate that the diffusion coefficients are symmetric so that $\mathfrak{D}_{ij} = \mathfrak{D}_{ji}$. Consequently, for a VRFB with eight species (water, sulfate ions, protons, the membrane, and four vanadium species), there are 28 transport coefficients. In this paper, Equations 6-17 and 6-18 consider ionic species as fully dissociated (*i.e.* uses the Experimental Construct discussed in Part II, Chapter 5).[31] Transport coefficients $\mathfrak{D}_{ij}$ include the effect of ion-pair formation to ensure that this model is consistent with the various ion-paired species that exist. Part II (Chapter 5) outlines calculation of $\mathfrak{D}_{ij}$ and $K_{i\mathrm{M}}$ as a function of membrane water content and ion concentration.[31]

Equations 6-17 and 6-18 are rigorous but inconvenient because they involve gradients in electrochemical potential that are not readily characterized and frame the driving force in terms of species fluxes, whereas experiments measure fluxes under applied forces. Appendix 6-A shows that for constant total molar concentration, c_T, eliminating the electrostatic dependence of the driving forces (*i.e.* making the substituting $\mu_i = \mu_{i,\mathrm{M}} + \frac{z_i}{z_\mathrm{M}}\mu_\mathrm{M}$ as shown in Equation 6-5),[74] and expanding chemical potential gradients in terms of composition variables gives the flux of species i as the sum of migration and diffusion terms:

$$N_i = \frac{t_i i}{z_i F} - \sum_{j \neq \mathrm{M},n} D_{ij} \frac{\partial c_{j,\mathrm{M}}}{\partial z} \qquad 6\text{-}19$$

for $i \neq \mathrm{M}, n$, where n is a reference species with charge number different from M, t_i is the transference number of species i, and D_{ij} are multicomponent diffusion coefficient between species i and j based on concentration driving forces. We assign protons as reference species n. Although t_0 and z_0 are zero for water, the ratio t_0/z_0 is definite and equal to the electroosmotic coefficient ξ. $\partial c_{j,\mathrm{M}}/\partial z$ is the concentration gradient of a (potentially hypothetical) salt consisting of $|z_\mathrm{M}|$ ions j and $|z_j|$ charged polymer groups M

$$\frac{\partial c_{j,\mathrm{M}}}{\partial z} = \frac{1}{s_{j,\mathrm{M}}}\left(\frac{\partial c_j}{\partial z} - \frac{z_j c_j}{z_\mathrm{M} c_\mathrm{M}}\frac{\partial c_\mathrm{M}}{\partial z}\right) \qquad 6\text{-}20$$

where $s_{j,\mathrm{M}}$ is the number of particles constituting j,M ($s_{j,\mathrm{M}} = |z_j| + |z_\mathrm{M}|$ for $z_j \neq 0$). For neutral species (*e.g.* water), $s_{j,\mathrm{M}} = 1$ so that the concentration gradient of j,M is simply the concentration gradient of j (*i.e.* $\partial c_{j,\mathrm{M}}/\partial z = \partial c_j/\partial z$). This formalism generalizes the treatment of concentration gradients in binary electrolytes[9] to an arbitrary number of species; the concentration gradient of j,M reduces to the concentration gradient of the salt for a binary electrolyte with $|z_-|$ cations and $|z_+|$ anions.

Appendix 6-A shows how D_{ij} is related to the binary diffusion coefficients $\mathfrak{D}_{ij}$'s and chemical potential gradients. Specifically, D_{ij}'s are components of the $N-2$ by $N-2$ diffusion matrix $\boldsymbol{D}$

that is the product of the matrix inverse of $\boldsymbol{B}$, an $N-2$ by $N-2$ matrix containing transport coefficients, and $\boldsymbol{\chi}$, an $N-2$ by $N-2$ matrix containing multicomponent thermodynamic factors

$$\boldsymbol{D} = \boldsymbol{B}^{-1}\boldsymbol{\chi}\boldsymbol{S} \tag{6-21}$$

where $\boldsymbol{S}$ is a diagonal matrix with entries $s_{j,\mathrm{M}}$, and the entries of $\boldsymbol{B}$ for $i \neq j$ are

$$B_{ij} = x_i\left[\frac{z_i}{z_{\mathrm{M}}\mathfrak{D}_{j\mathrm{M}}} + \frac{z_j}{z_n}\left(\frac{1}{\mathfrak{D}_{in}} - \frac{z_i}{z_{\mathrm{M}}\mathfrak{D}_{n\mathrm{M}}}\right) - \frac{1}{\mathfrak{D}_{ij}}\right] \tag{6-22}$$

and for $i = j$,

$$B_{ii} = \frac{z_i x_i}{z_n}\left(\frac{z_n}{z_{\mathrm{M}}\mathfrak{D}_{i\mathrm{M}}} + \frac{1}{\mathfrak{D}_{in}} - \frac{z_i}{z_{\mathrm{M}}\mathfrak{D}_{n\mathrm{M}}}\right) + \sum_{k\neq i}\frac{x_k}{\mathfrak{D}_{ik}}. \tag{6-23}$$

$\boldsymbol{B}^{-1}$ is a matrix of thermodynamic diffusion coefficients. The entries of $\boldsymbol{\chi}$ are

$$\chi_{ij} = \delta_{ij} + \frac{x_i}{x_j}\frac{\partial \mu_{i,\mathrm{M}}^{\mathrm{ex}}}{\partial RT\ln(x_j/x_{\mathrm{M}}^{z_j/z_{\mathrm{M}}})} \tag{6-24}$$

where δ_{ij} is the Kronecker delta function ($\delta_{ii} = 1$ and $\delta_{ij} = 0$ for $i \neq j$). Equation 6-21 reduces to a well-established form for the salt diffusion coefficients in the case of a binary electrolyte.[9]

The $N-2$ vector $\boldsymbol{t}$ of charge number-normalized transference numbers t_i/z_i is

$$\boldsymbol{t} = \boldsymbol{B}^{-1}\boldsymbol{\varsigma} \tag{6-25}$$

where $\boldsymbol{\varsigma}$ is an $N-2$ vector with entries

$$\varsigma_i = \frac{x_i}{z_n}\left(\frac{z_i}{z_{\mathrm{M}}\mathfrak{D}_{n\mathrm{M}}} - \frac{1}{\mathfrak{D}_{in}}\right). \tag{6-26}$$

In this approach, t_i and D_{ij} use a reference velocity of the membrane (*i.e.* $N_{\mathrm{M}} = 0$), unlike other research that uses water velocity as the frame of reference.[86] Due to this choice of the laboratory frame of reference, Equation 6-19 should not include additional terms for solvent convection. The choice for species n does not change the flux N_i but does change the value of D_{ij}. Since Equation 6-19 is applicable to $i \neq n$, we specify the flux of n using the current density and fluxes of species $i \neq n$ (*i.e.* $N_n = (i/F - \sum_{i\neq \mathrm{M},n} N_i z_i)/z_n$).

For negligible mass-transport resistance between the electrode electrolyte and membrane, chemical equilibria (*i.e.* Equations 6-14 and 6-15) specifies $c_{i,\mathrm{M}}$ at the interface of the membrane with the two electrodes. Solving Equations 6-16 and 6-19 using these concentrations as boundary conditions gives the concentration profiles and fluxes of species across the membrane for a set current density.

With specified fluxes, Equation 6-18 calculates the ionic potential gradient because it is proportional to the electrochemical potential of the membrane,

$$\frac{\partial \Phi}{\partial z} = \frac{RT}{z_{\mathrm{M}}Fc_{\mathrm{T}}}\sum_{j\neq \mathrm{M}}\frac{N_j}{\mathfrak{D}_{j\mathrm{M}}}. \tag{6-27}$$

Integration of Equation 6-27 across the membrane shows that $\Delta\Phi$ is a function of applied current density (ohmic overpotential) and flux of species at the open-circuit cell potential (diffusion overpotential). In the absence of concentration gradients, substitution of Equation 6-19 into Equation 6-27 identifies the membrane conductivity, κ, as

$$\frac{\partial\Phi}{\partial z} = -i\kappa^{-1} = -i\left\{-\frac{RT}{c_{\mathrm{T}}F^2 z_{\mathrm{M}}}\left[\frac{1}{z_n\mathfrak{D}_{n\mathrm{M}}} + \sum_{j\neq\mathrm{M},n}\frac{t_j}{z_j}\left(\frac{1}{\mathfrak{D}_{j\mathrm{M}}} - \frac{z_j}{z_n\mathfrak{D}_{n\mathrm{M}}}\right)\right]\right\}. \qquad 6\text{-}28$$

As κ increases for a fixed current density and concentration gradient, the potential drop across the membrane decreases.

6.3.4 Parameters

Parts I and II discuss calculation of μ_i^{ex} and $\mathfrak{D}_{ij}$, respectively, as functions of concentration and water content as well as membrane equivalent weight and the modulus of the hydrophobic matrix of a dry membrane;[31, 247] the required system parameters for these calculations are discussed therein. The properties specific to VRFBs are the infinite dilution diffusion coefficients in water and viscous volume of vanadium ions and vanadium-bisulfate ion pairs in solution, $\mathfrak{D}_{i,0}^{\infty}$ and $\tilde{V}_i$, respectively, the vanadium-sulfate binary diffusion coefficient $\mathfrak{D}_{i,\mathrm{SO_4}}$, the vanadium-sulfate and vanadium-membrane interaction parameters $\beta_{i,\mathrm{SO_4}}$ and $\beta_{i,\mathrm{M}}$, V(III)- and V(IV)-bisulfate association constants $K_{i-\mathrm{HSO_4}}$, and solvent/vanadium binding constant k_i.

Unfortunately, there are relatively few measurements of vanadium thermodynamic and transport properties in all its oxidation states at well-defined conditions. As described in Chapter 6 Supporting Information (SI-6), reported experimental values are used when available, and otherwise, parameters of cations of similar charge number approximate those of the vanadium ions. For V(IV) and V(V) we fit $\beta_{i,\mathrm{M}}$ to measured vanadium, sulfate, and water uptake in the membrane as a function of sulfuric acid and vanadium sulfate concentration detailed in Part I (Chapter 4).[247] Similarly, for V(III), we fit $\beta_{i,\mathrm{M}}$, $\beta_{i,\mathrm{SO_4}}$ and k_i to isotherm measurements. These parameters are plausible values for this system; however, they are estimates. Consequently, there is a strong need for fundamental thermodynamic studies of vanadium-ion properties in their different oxidation states (*i.e.* activity and osmotic coefficients as a function of concentration).

Throughout this paper, we will consider a reference VRFB system containing electrodes at a fixed composition and a membrane with fixed properties, which are provided in Table 6-2. Calculations are made for this system unless stated. The electrolyte concentrations match those in experimental cells as described in Refs[11, 86, 282] unless otherwise stated. In those studies, an initial solution of 1.5 mol dm^{-3} vanadium IV sulfate in 2.6 mol dm^{-3} sulfuric acid was twice charged with the positive electrolyte replaced after each charge. As outlined in SI-6, after this charging process and at a state of charge of 50%, the negative electrolyte has 0.75 mol dm^{-3} of both V(II) and V(III) and a total sulfate concentration of 4.66 mol dm^{-3}. The positive electrolyte has the same concentrations of V(IV) and V(V) and a total sulfate concentration of 4.11 mol dm^{-3}. The electrolyte solution mass density was 1.19 g cm^{-3}.[282] The separator in the reference system is a Nafion 212 membrane with a dry-membrane thickness, l_{M}^0, of 51 μm. The membrane equivalent weight, EW (mass-polymer per mole-sulfonate group) is 1100.

Table 6-2. Properties of the reference VRFB system

Properties	Parameter	Value
Negative electrode composition	$c^{\beta}_{\mathrm{V(II)}}$	0.75 mol dm^{-3}
	$c^{\beta}_{\mathrm{V(III)}}$	0.75 mol dm^{-3}
	$c^{\beta}_{\mathrm{SO_4}}$	4.66 mol dm^{-3}
Positive electrode composition	$c^{\epsilon}_{\mathrm{V(IV)}}$	0.75 mol dm^{-3}
	$c^{\epsilon}_{\mathrm{V(V)}}$	0.75 mol dm^{-3}
	$c^{\epsilon}_{\mathrm{SO_4}}$	4.11 mol dm^{-3}
Polymer backbone modulus	E_b^0	154 MPa
Membrane equivalent weight	EW	1100 g-polymer/mol SO_3

Other membrane properties considered are hydrophobic matrix modulus of the dry membrane, E^0_{b}, Archie's tortuosity scaling parameter, χ, hydrophilic domain geometric transport factor, G, and spacing between hydrophilic domain in dry membrane, d^0. EW sets the intrinsic concentration of ions in the membrane absent co-ions, E^0_{b} limits the extent the membrane can swell with water from the surrounding environment, G affects friction between the membrane and absorbed water and aqueous ions, and d^0 and χ dictate the hydrophilic domain size and network tortuosity, respectively, at a given water volume fraction. Unless otherwise stated, membrane properties are those of the Nafion PFSA separator and are detailed in Parts I and II.[31, 247]

6.3.5 Numerical Implementation

SI-6 outlines calculation of membrane properties, fluxes, and performance metrics. For a specified electrolyte composition in the negative and positive electrodes, Equations 6-14 and 6-15 specify x_i at δ' and δ''. Part I (Chapter 4) outlines calculation of μ_i^{ex}.[247] Given the composition of the species in the membrane, Part II (Chapter 5) outlines calculation of $\mathfrak{D}_{ij}$.[31] Equation 6-24 gives χ_{ij} where the Python package Numdifftools V.0.9.39 calculates the Jacobian, $\partial \mu^{\mathrm{ex}}_{i,\mathrm{M}}/\partial RT \ln(x_j/x_{\mathrm{M}}^{z_j/z_{\mathrm{M}}})$ using a first-order, forward-finite-difference approximation with a step size of $(1-x_0)/100$ for water and $x_i/100$ for ions. Given χ_{ij} and $\mathfrak{D}_{ij}$, Equation 6-21 calculates $\boldsymbol{D}$. The total concentration c_{T} is set to 55.3 mol dm^{-3}. For ideal volumetric mixing and isotropic swelling, the membrane thickness is $l_{\mathrm{M}} = l^0_{\mathrm{M}}(1+\lambda \bar{V}_0 \rho^0_{\mathrm{M}}/EW)^{1/3}$, λ is the average water content ($= x_0/x_{\mathrm{M}}$), $\bar{V}_0$ is the partial molar volume of water (= 18.1 cm^3 mol^{-1}), and ρ^0_{M} is the mass density of the dry membrane (= 2.1 g cm^{-3}).

To solve Equation 6-19 for each species, we extend to electrolyte systems a method outlined by Krishna et al.[283-284] for uncharged systems. Using this approach, Appendix 6-B shows that for a specified current density, the species fluxes are specified by iterating over a set of six transcendental algebraic equations and neglecting changes across the membrane of: the thermodynamic factor χ_{ij} because the solution composition from the most abundant species (sulfate, the membrane, water, and protons) changes relatively little across the membrane; c_{T} because the molar density of the membrane change only slightly with composition; $\mathfrak{D}_{ij}$ because the dominant factors they depends upon -ionic strength and water content inside the membrane- are relatively constant; and $\partial \ln x_{\mathrm{M}}/\partial z$ because the membrane concentration changes little

between the electrodes. We evaluate $\mathfrak{D}_{ij}$, χ_{ij}, and λ using the mean of the composition of the membrane at the interface with the two electrodes $x_i^{\bar{\delta}}$ $(= (x_i^{\delta'} + x_i^{\delta''})/2)$, calculating the fraction of vanadium and protons that form ion pairs with sulfate at this composition. SI-6 shows that the error introduced by these assumption is small. The derivative of $\ln x_{\mathrm{M}}$ is approximated as $\partial \ln x_{\mathrm{M}} / \partial z \approx \ln(x_{\mathrm{M}}(z)/x_{\mathrm{M}}(z=0)) / l_{\mathrm{M}}$. In Results and Discussion, we show this assumption is also reasonable.

Upon specifying species fluxes at a given charge and discharge current density, Equation 6-11 gives i_{x} and, using Equation 6-12, ε_{q}. Integration of Equation 6-27 gives Φ. Φ is a linear function of z for the assumption of constant $\mathfrak{D}_{ij}$. Upon calculating $\Delta\Phi$, Equations (6-6), 2-1, and 6-1 give V, ε_{v}, ε_{e}, and Ψ_{d}. To find the maximum discharge cell power density Ψ_{d} at $\varepsilon_{\mathrm{e}} = 80\%$ (our adopted design criteria), we iteratively solve these equations for varying i until finding the maximum.[285] As previously stated, the electrode composition and N_i are assumed constant during charge or discharge. This condition is achieved for incremental changes in SOC during cycling.

We performed sample-based sensitivity analysis for the impact of membrane properties EW, E_{b}^0, χ, G, and d^0 on transport properties and cell performance. SI-6 details the sampling technique and range for these properties. The sensitivity analysis uses a cell current density of 200 mA cm^{-2} and the electrolyte composition is that of the reference conditions (see Table 6-2).

6.4 Results and Discussion

6.4.1 Representative VRFB Membrane Transport

This section discusses transport in the reference system (see Table 6-2) consisting of the quintessential VRFB membrane, Nafion, under typical electrolyte concentrations.

6.4.1.1 Transport Properties

Equation 6-21 shows that the diffusion matrix $\boldsymbol{D}$ captures transport coupling between all species due to thermodynamic interactions that $\boldsymbol{\chi}$ specifies and for and frictional interactions that $\boldsymbol{B^{-1}}$ incorporates. For a thermodynamically ideal solution, $\chi_{ii} = 1$ and $\chi_{ij} = 0$. In a dilute solution ($x_i \to 0$ and $x_{\mathrm{M}} \to 1$), the matrix $\boldsymbol{D}$ has the species/membrane diffusion coefficients on the diagonal while off-diagonal elements are equal to zero.

For Nafion in a VRFB, Figure 6-2a plots the mean calculated diffusion coefficients D_{ij} on a heat map colored from dark blue (large positive coefficients) through white (coefficient equal to zero) to dark red (large negative coefficient) and the thermodynamic factor χ_{ij} is given in parenthesis. The calculations show that transport in this system is far more complex than diffusion in an ideal, dilute solution. Although some off-diagonal terms of the diffusion matrix are small, they are not categorically negligible and in some cases are larger than the on-diagonal terms. For example, a concentration gradient of $\mathrm{V(IV)M_2}$ causes more than twice the flux of V(V) compared to an equal concentration gradient in V(V)M. A few of the diffusion coefficients are negative, indicating that the flux of one species will take place up the concentration gradient of another, holding all else constant. In particular, for all vanadium species i, $D_{\mathrm{SO_4}i}$ is negative and large in magnitude.

Thermodynamic nonidealities contribute to transport coupling in particular. χ_{ij} for vanadium species i and j are close to ideal because positively charged ions do not significantly change the

excess chemical potential of other positively charged species. χ_{ij} for vanadium/water and /sulfate are mostly large because of the significant effect interactions between these species have on the excess free energy of the system.

Figure 6-2b shows a heat map of charge number-normalized transference numbers. Absent concentration gradients, protons will carry most of the current because $t_{\mathrm{H}} = 0.94$. Sulfate ions are the second largest carrier, and vanadium species each transport about 1% of the current.

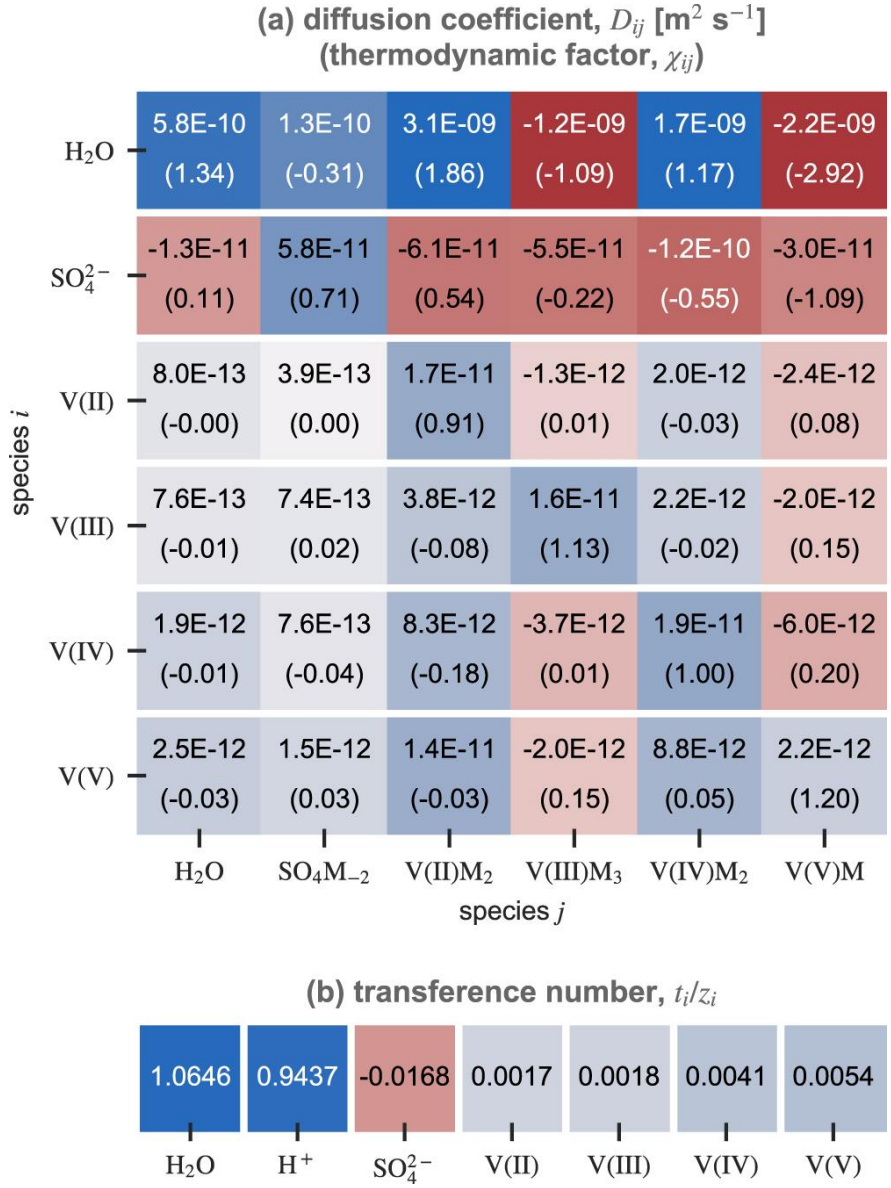

Figure 6-2. Heat map colored from blue (positive), to white (zero), to red (negative) of (a) diffusion coefficient matrix $\boldsymbol{D}$ with given tabulated values of D_{ij} (and χ_{ij} in parenthesis) and (b) charge number-normalized transference numbers t_i/z_i with values tabulated for the reference system (see Table 6-2).

6.4.1.2 Transport at Open Circuit

The concentration difference between electrodes creates concentration gradients in the membrane. Figure 6-3 shows the mole-fraction profile of each species in the membrane between the interfaces with the negative electrode ($z = 0$) and the positive electrode ($z = l_{\mathrm{M}}$) calculated using the procedure outlined in Appendix 6-B with the no current density (*i.e.* $i = 0$). For transport that is not coupled (*i.e.* dilute-solution approximation), the mole-fractions of the species will decrease linearly between the two electrodes. This behavior is not present in this system indicating that transport coupling plays an important role.

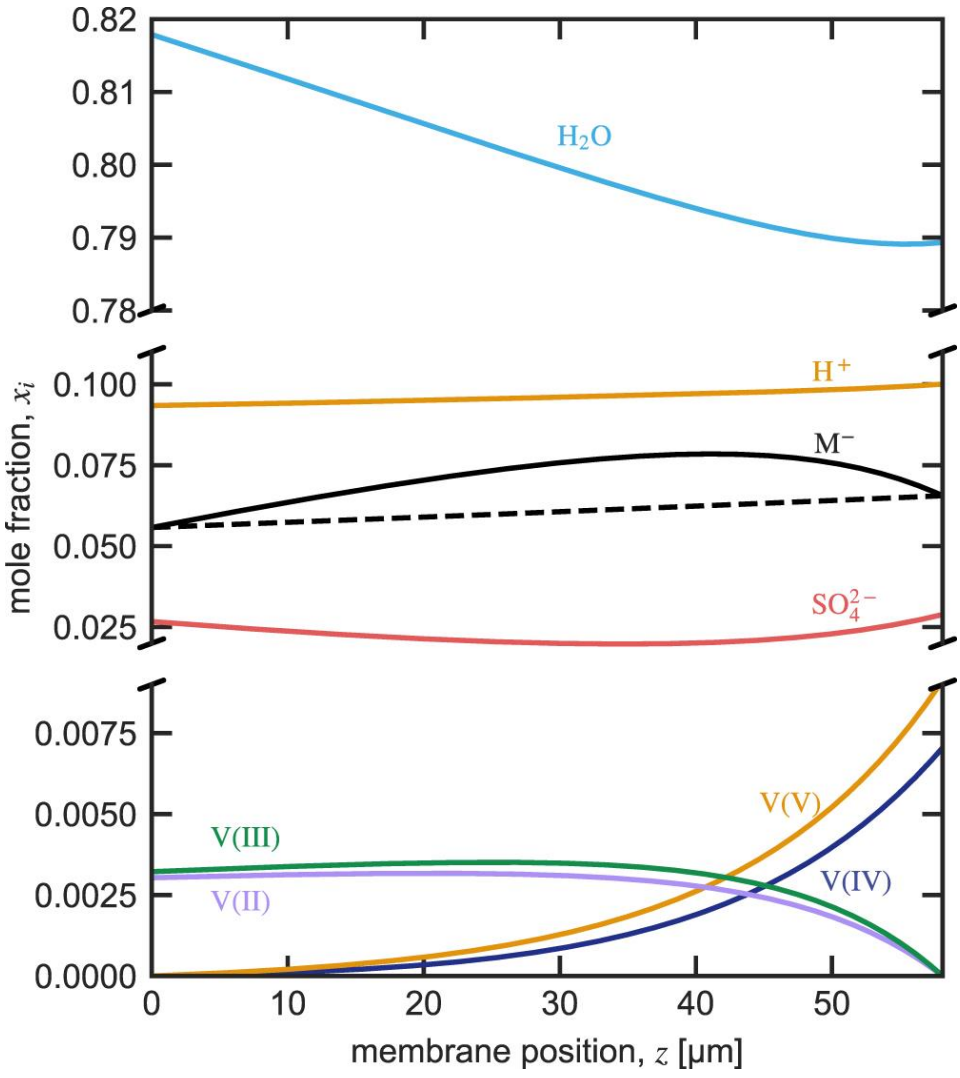

Figure 6-3. Calculated mole fractions as a function of position in the membrane from $z = 0$ (interface with negative electrode) to $z = l_{\mathrm{M}}$ (interface with positive electrode) for current density $i = 0$ for the reference system (see Table 6-2). Note change of scales on mole fraction-axis.

The vanadium species mole fractions in the negative electrode (V(II) and V(III)) goes to zero on approaching the positive electrode-interface, and the vanadium species mole fractions in the positive electrode (V(IV) and V(V)) decrease towards the negative electrode/membrane interface. The mole fractions of sulfate, protons, and membrane fixed-charged groups are relatively constant across the membrane with the latter two showing a slight decrease towards the negative electrode and having a maximum away from the electrode interfaces. The dotted line in Figure 6-3 shows $\ln(x_{\mathrm{M}}(z)/x_{\mathrm{M}}(z=0))\,/l_{\mathrm{M}}$, which closely matches $\partial \ln x_{\mathrm{M}}\,/\partial z$ and illustrates that the assumption equating the two is reasonable.

The water mole fraction decreases from the negative electrode to the positive electrode/membrane interface. Although the water mole fraction of the two electrode electrolytes are nearly the same, Γ_0 at the negative electrode is larger than at the positive electrode causing the concentration gradient inside the membrane.

The concentration gradients (see Figure 6-3) drive fluxes according to the matrix of diffusion coefficients (see Figure 6-2). Using V(II) as an example, Figure 6-4 plots the contribution to $N_{\mathrm{V(II)}}$ (see Equation 6-19) from the concentration gradient of species j referenced to the membrane (*i.e.* $D_{\mathrm{V(II)}j}\partial c_{j,\mathrm{M}}$, where we abbreviate $\partial/\partial z$ as ∂) as a function of position across the membrane. Each species plays an important role in driving transport with their contribution varying across the membrane. Where a concentration gradient is large, that species drives more transport. For example, around $z = 45$ μm, vanadium gradients are largest and contribute substantially to V(II) transport. Approaching the positive electrode interface ($z = 58$ μm), $x_{\mathrm{V(II)}} \to 0$, and leading to $D_{\mathrm{V(II)}j\neq\mathrm{V(II)}} \to 0$; as this point, V(II) transport is then solely caused by the V(II) concentration gradient.

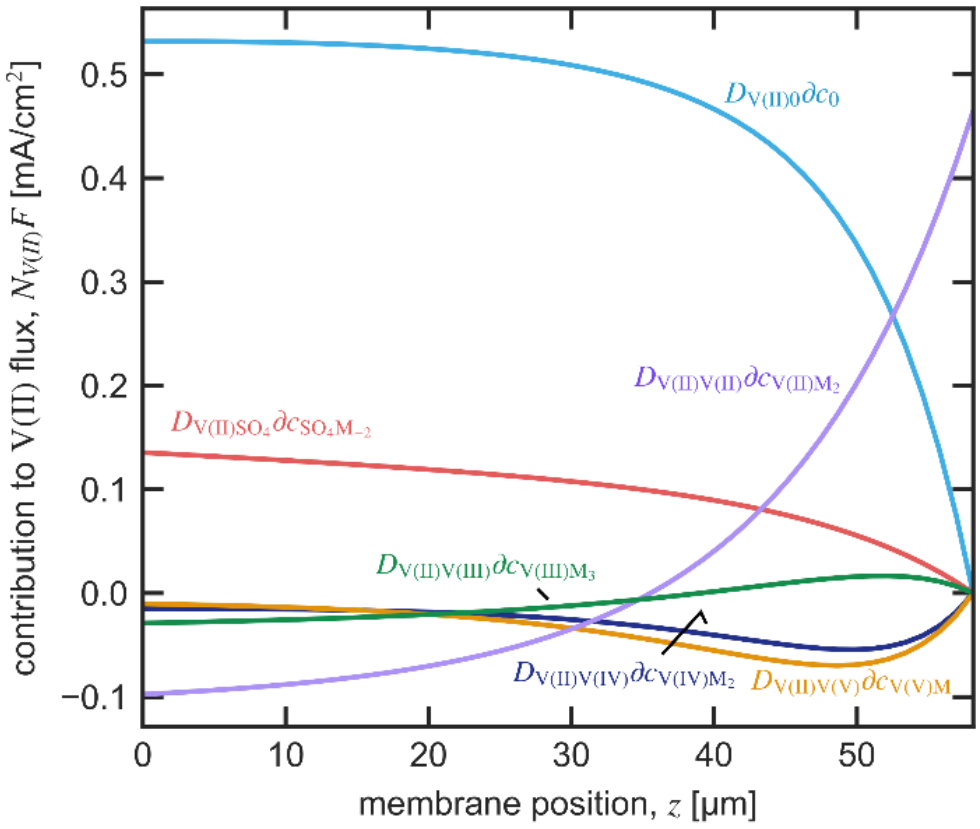

Figure 6-4. Flux of V(II) multipled by Faraday's constant, $N_{\mathrm{V(II)}}F$, caused by a concentration gradient of j, M, $\partial c_{j\mathrm{M}}$, calculated from Equation 6-19 (*i.e.* $FD_{\mathrm{V(II)}j}\partial c_{j,\mathrm{M}}$) as a function of position in the membrane.

The water concentration gradient is a key transport driving force. Although the water-driven diffusion coefficient $D_{\mathrm{V(II)}0}$ is not large (see Figure 6-2, Row 3, Column 1), the water concentration gradients are (see Figure 6-3), causing high water-related fluxes. The term $\partial c_{\mathrm{SO_4M_{-2}}}$ $(= \partial c_{\mathrm{SO4}} - \frac{c_{\mathrm{SO_4}} z_{\mathrm{SO4}}}{c_{\mathrm{M}} z_{\mathrm{M}}} \partial c_{\mathrm{M}})$ also contributes significantly to transport. Although $\partial c_{\mathrm{SO4}}$ is relatively small, as Figure 6-3 shows, $-\frac{c_{\mathrm{SO_4}} z_{\mathrm{SO4}}}{c_{\mathrm{M}} z_{\mathrm{M}}} \partial c_{\mathrm{M}}$ is large and positive and $D_{\mathrm{V(II)SO_4}}$ is negative. As a consequence, the term $-D_{\mathrm{V(II)SO_4}}\,\partial c_{\mathrm{SO_4M_{-2}}}$ drives V(II) towards the positive electrode. Moreover, at the negative electrode ($z = 0$), $\partial c_{\mathrm{V(II)}}$ is small but $-\frac{c_{\mathrm{V(II)}} z_{\mathrm{V(II)}}}{c_{\mathrm{M}} z_{\mathrm{M}}} \partial c_{\mathrm{M}}$ and $D_{\mathrm{V(II)V(II)}}$ are large and negative. The result is that $-D_{\mathrm{V(II)V(II)}}\,\partial c_{\mathrm{V(II)M_2}}$ pulls vanadium towards the negative electrode.

Figure 6-5 shows the calculated normalized mean flux contribution of each species i due to the concentration gradients of each other species j referenced to M (*i.e.* $\int D_{ij}\partial c_{j,\mathrm{M}} dz / \sum_{k\neq \mathrm{M},n} |\int D_{ik}\partial c_{k,\mathrm{M}} dz|$). The left side of Figure 6-5 gives the total flux of each species multiplied by F. The points show species fluxes for an thermodynamically ideal solution (*i.e.* $\chi_{ij} = 0$ for $i \neq j$ and $\chi_{ii} = 1$).

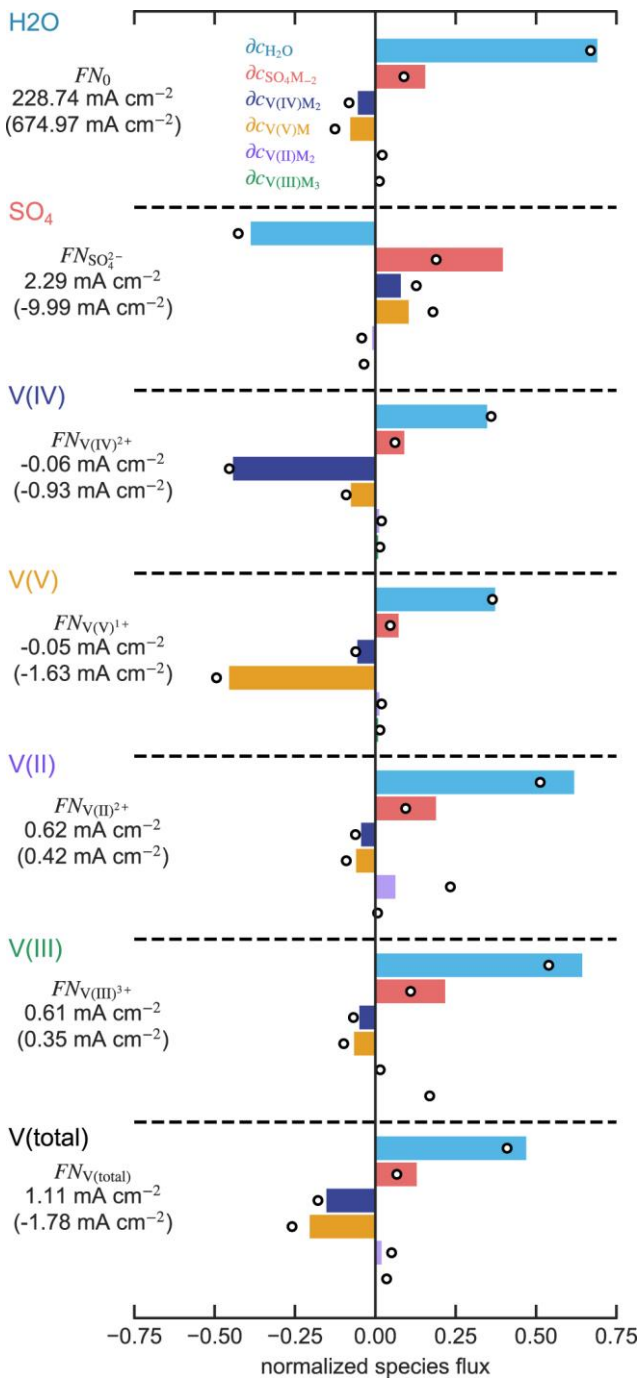

Figure 6-5. Bar chart of flux of i, N_i, caused by a concentration gradient of j, M, normalizing by the sum of absolute values of each contribution and averaged over the membrane (*i.e.* $\int D_{ij}\partial c_{j,\mathrm{M}}dz/\sum_{k\neq \mathrm{M},n}|\int D_{ik}\partial c_{k,\mathrm{M}}dz|$) for the reference system (see Table 6-2). The dotted lines group contributions to species i and the bars are for each species j. The circles show the same calculation with a thermodynamically ideal solution (*i.e.* $\chi_{ij}=0$ for $i\neq j$ and $\chi_{ii}=1$). The left side gives the total flux of each species multiplied by Faraday's constant and the term in parenthesis is the flux calculated for no interspecies friction (*i.e.* $\mathfrak{D}_{ij\neq \mathrm{M}}\to\infty$).

As the large magnitude off-diagonal elements in Figure 6-2 show, concentration gradients of species i causes transport of species j. This finding is further evidence that dilute-solution theories in which a species transport is driven by only its own concentration gradient (*i.e.* $N_i = f(\partial c_i)$) is not sufficient to calculate transport accurately. To quantify this error, the term in parenthesis on the left side of Figure 6-5 shows that the dilute-solution approximation (*i.e.* that the only friction on a species is due to the membrane, $\mathfrak{D}_{ij\neq \mathrm{M}} \to \infty$) predicts fluxes that, on average (*i.e.* mean), deviate from the concentrated-solution model by 772%.

For all species, the principle transport driving force is the water concentration gradient. Water drives positively charged species to the positive electrode, resulting in a curvature of the vanadium species concentration gradients towards the positive electrode. To maintain electroneutrality, the water concentration gradient pushes sulfate to the negative electrode.

Mass-transport of ions and water is coupled because both the frictional interactions between species are nonzero and the excess chemical potential of species depends on the concentration of other species. When describing the solution as thermodynamically ideal (circles in Figure 6-5), the qualitative behavior of the coupling between species is captured. However, the thermodynamic nonidealities lead to quantitative differences from the ideal-solution approximation.

In practice, an operating cell will undergo numerous cycles and electrolyte rebalancing so that the composition in the electrodes will vary, changing the concentration gradients. Consequently, the specific direction and contributions to fluxes in Figure 6-5 do not apply throughout VRFB operation. Incorporating concentrated-solution theory into a fully transient model of VRFB operation would give insight into how these driving forces change during cell operation.

6.4.1.3 Transport under Applied Potentials

Under an applied potential, charged species migrate with the current. Figure 6-6 shows the flux of each vanadium species i (multiplied by $z_i F$) as a function of current density i. When current is positive, the concentration gradients acting on V(II) and V(III) are aligned and increasing current linearly increases vanadium flux. At negative currents, migration and diffusion are opposed causing the fluxes of V(II) and V(III) to go to zero. V(V) and V(IV) follow opposite scenarios than V(II) and V(III). This description is qualitatively consistent with previous work using a dilute-solution theory framework. For these electrolyte concentrations, the diffusional contributions causes a net flux of vanadium towards the positive electrode when the current is zero as shown in Figure 6-5.

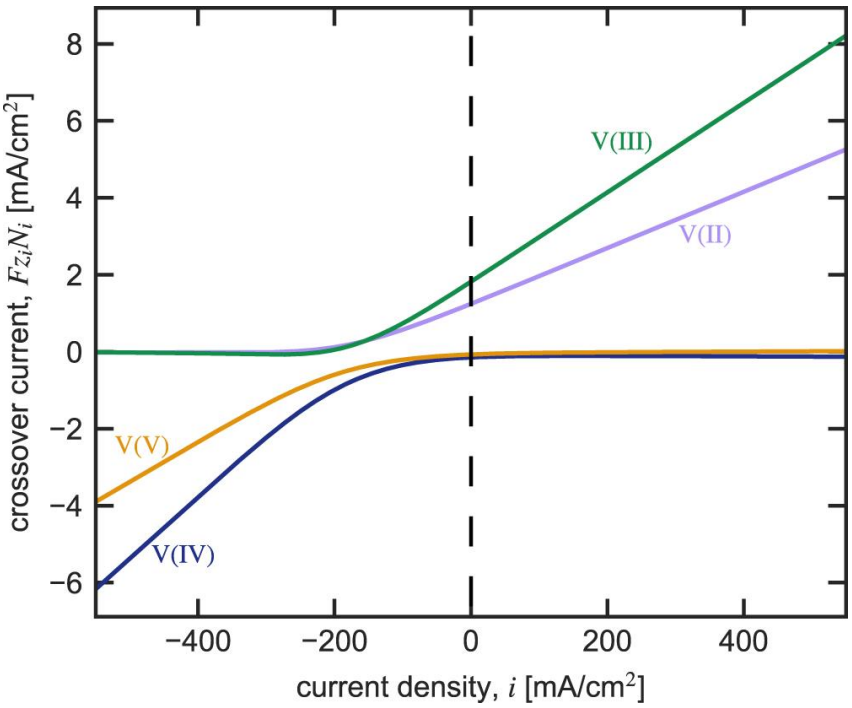

Figure 6-6. Vanadium flux N_i multiplied by charge number z_i and Faraday's constant F as a function of current density i for the reference system (see Table 6-2).

Figure 6-7 shows the mean contributions outlined in Equation 6-19 to the V(II) flux $N_{\mathrm{V(II)}}$ from each diffusion term, $D_{\mathrm{V(II)}j}\partial c_{j,\mathrm{M}}$, (see Figure 6-5) and migration, $it_{\mathrm{V(II)}}/z_{\mathrm{V(II)}}F$ as a function of current density. As the current density increases, the fraction of flux due to migration increases. The contributions to flux from diffusion changes slightly as the current density increases because migration alters the concentration gradients across the membrane. Above 250 mA/cm^2, the majority of the vanadium V(II) flux is due to migration.

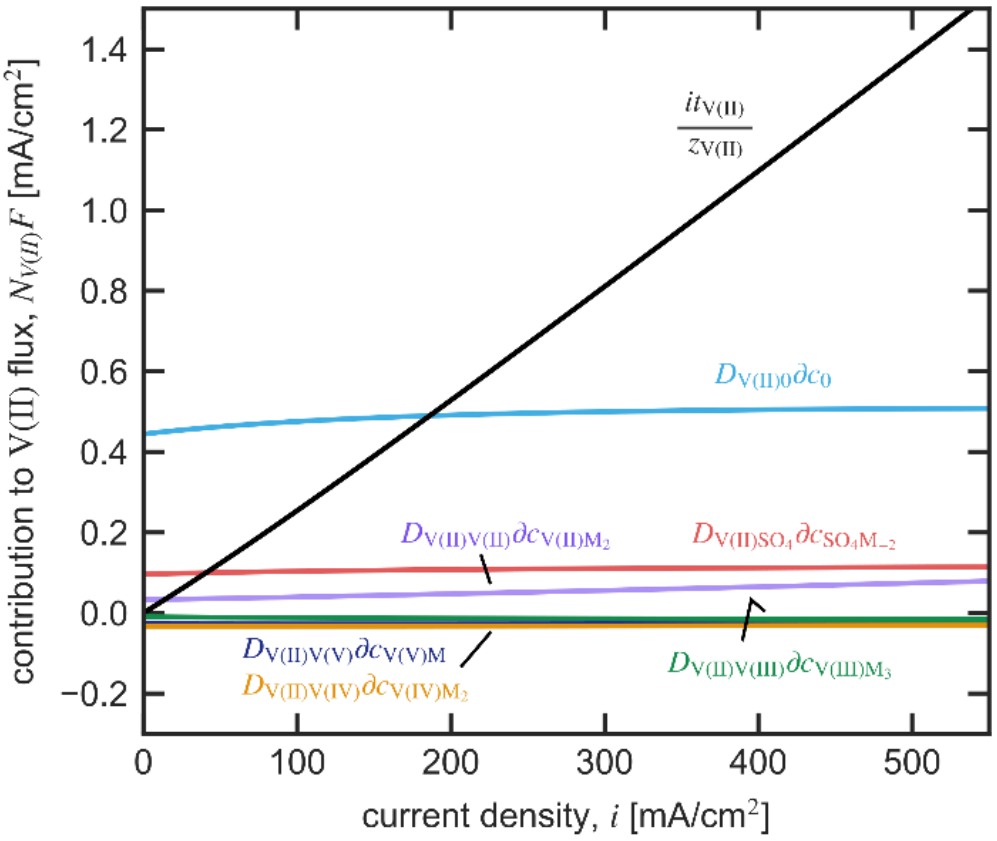

Figure 6-7. Mean contributions to the flux of V(II), $N_{\mathrm{V(II)}}$, from each diffusion term, $D_{\mathrm{V(II)}i}\partial c_{i,\mathrm{M}}$, (see Figure 6-5) and migration, $it_{\mathrm{V(II)}}/z_{\mathrm{V(II)}}$ averaged across the membrane as a function of current density for the reference system (see Table 6-2).

Figure 6-4, Figure 6-5, and Figure 6-7 show that coupling plays an important role in transport though VRFB membranes. The contributions from water concentration gradients are particularly large.[30] The calculations show that in cases that require only semi-quantitative predictions, neglecting the terms $D_{ij}\partial c_{j,\mathrm{M}}$ for $j \neq i, 0$ will cause ~25% error to the calculated fluxes at OCP with the error decreasing with increasing current density. As a result, mathematical models and experimental analysis that rely on extended versions of dilute-solution theories that incorporate the effect of water on vanadium fluxes will be qualitatively correct in many cases.

6.4.1.4 Cell Performance

Figure 6-8 shows that the calculated (lines) and measured[11] (symbols) voltage and Coulombic efficiencies, ε_{v} and ε_{q}, respectively, as a function of current density. The calculated and measured efficiencies correspond to slightly different scenarios. The model calculates performance at a constant 50% SOC (*i.e.* transport coefficients and concentration gradients are constant), whereas in the experiments charge and discharge between two voltage windows corresponding to different SOCs. Despite these slightly different conditions, the model and experiment are in good agreement.

As the current density increases, the Coulombic efficiency generally increases as the effects of crossover are reduced in comparison to the energy extracted from the cell. However, rising current density decreases voltage efficiency because the membrane and cell incur larger ohmic losses. As a consequence, the energy density increases initially, reaches a maximum, and then decreases with increasing current density. In the absence of resistance from the membrane $R_{\mathrm{M}} = 0$ (*i.e.* $\Delta\Phi = 0$), ε_{v} is higher, but non-membrane resistances limit the benefits of ultra-high conductivity membranes.

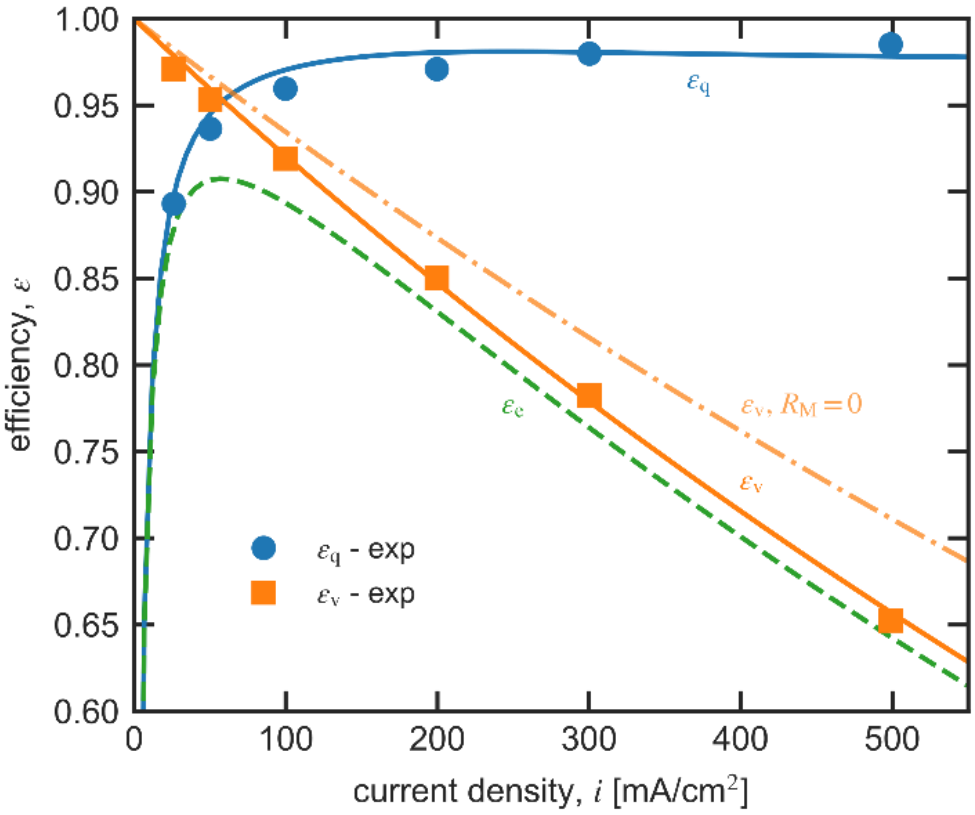

Figure 6-8. Measured (symbols, data from [11]) and calculated (lines) Coulombic efficiency ε_{q} (circles), voltage efficiency ε_{v} (squares), and energy efficiency ε_{e} as a function of current density for the reference system (see Table 6-2). Dot-dashed line shows ε_{v} for $\Delta\Phi = 0$ (*i.e.* without ohmic losses in the membrane).

Figure 6-15 shows voltage and Coulombic efficiency calculated using dilute-solution theory that only accounts for friction with the membrane (*i.e.* $\mathfrak{D}_{ij\neq\mathrm{M}} \to \infty$) and an extended dilute-solution theory that also accounts for frictions with water (*i.e.* $\mathfrak{D}_{ij\neq 0,\mathrm{M}} \to \infty$). The dilute-solution theory severely miscalculates cell efficiencies. For Coulombic efficiency, the extended-dilute-solution theory closely agrees with concentrated-solution theory but slightly overestimates voltage efficiency. Based on this analysis, researchers should account for the effect of coupled-transport modes and, in particular, the role of ion-water interactions on cell performance.

6.4.2 Impact of System Properties

The molecular transport and thermodynamic models presented in Parts I and II calculate properties as a function of external electrolyte composition and membrane chemistry.[31, 247] The following sections use these models to determine how changes away from the reference system (see Table 6-2) to operating conditions and membrane properties affect performance.

6.4.2.1 Impact of Electrolyte Concentration

In this section, we calculate the effect of changing the composition of the electrolyte in the electrodes. Specifically, varying the vanadium concentration (*i.e.* $c^{\epsilon}_{\mathrm{V(IV)}} + c^{\epsilon}_{\mathrm{V(V)}}$ and $c^{\beta}_{\mathrm{V(II)}} + c^{\beta}_{\mathrm{V(III)}}$) between 0.1-1.8 mol dm^{-3} and the mean sulfate concentration in the electrodes (*i.e.* $(c^{\beta}_{\mathrm{SO_4}} + c^{\epsilon}_{\mathrm{SO_4}})/2$) between 3.95-4.82 mol dm^{-3}. This analysis neglects vanadium solubility limits in sulfuric acid that may be exceeded under certain conditions at high sulfate concentrations.[223] Furthermore, we assume fast mass transfer from the bulk electrolyte to the carbon electrodes of the VRFB; at low vanadium concentrations mass-transport limitations may be important depending on the cell design.[276, 279, 282, 286]

6.4.2.1.1 Transport Properties

Concentration of species in the external electrolyte solution strongly impact membrane transport properties. Figure 6-9 shows membrane conductivity κ (a), V(II)0 diffusion coefficient $D_{\mathrm{V(II)0}}$ (b), and V(II) transference number $t_{\mathrm{V(II)}}$ (c) calculated at membrane composition $x_i^{\overline{\delta}}$ as a function of the total vanadium molarity in the electrodes, and the lines are varying arithmetic average sulfate concentration in the electrodes. Figure 6-16 shows the membrane water content (a), proton molality (b), and V(II) molality (c) at the same conditions. For brevity, we plot the properties of V(II), which are representative of the transport properties of the other vanadium species.

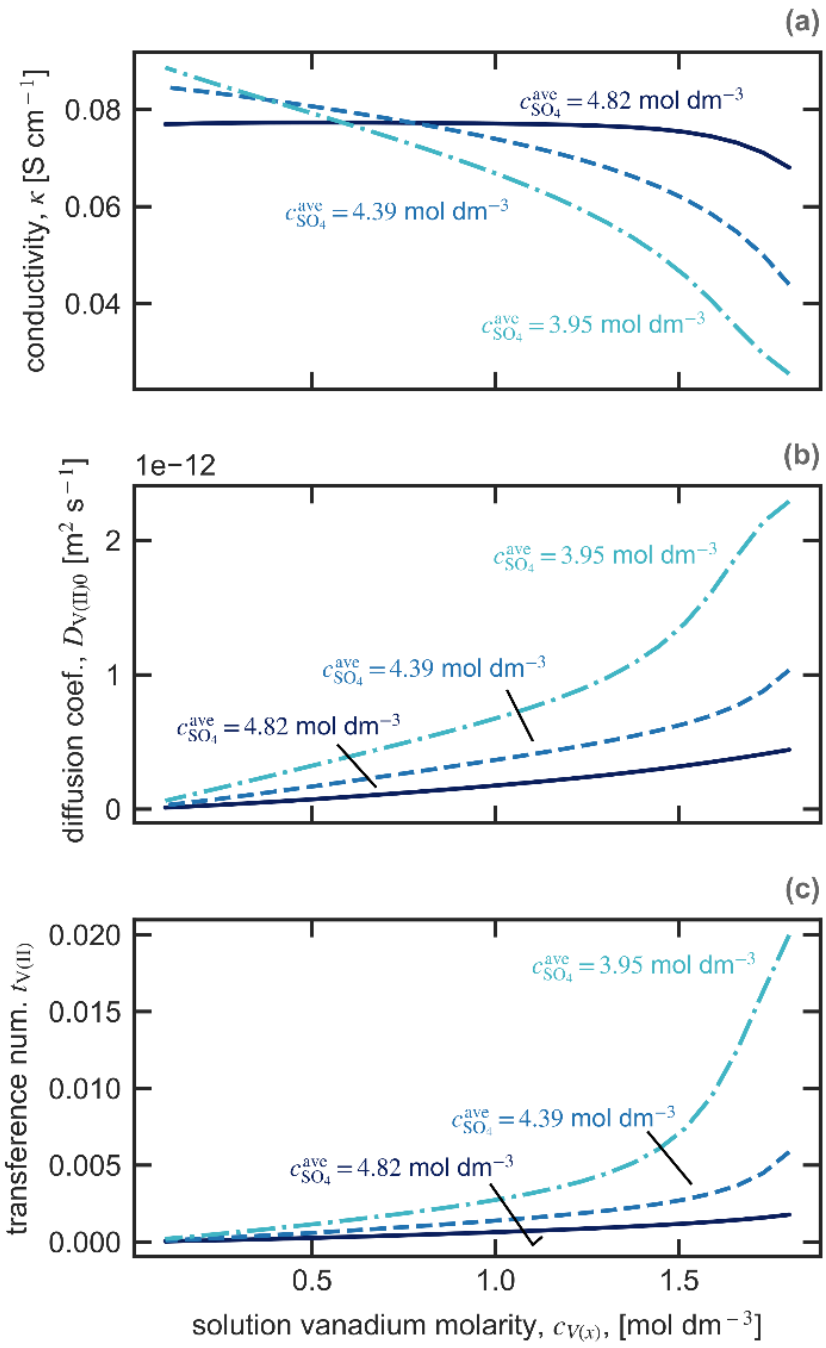

Figure 6-9. Calculated membrane (a) conductivity κ, (b) V(II)/0 diffusion coefficient $D_{V(II)0}$, and (c) V(II) transference number $t_{V(II)}$ evaluated at composition $x_i^{\overline{\delta}}$ as a function of the total vanadium molarity in the electrodes where the SOC of the cell is 50% and the different lines are for different mean sulfate concentration in the electrodes of 4.82 mol dm^{-3} (solid lines), 4.39 mol dm^{-3} (dashed line), to 3.95 mol dm^{-3} (dot-dashed line).

As the concentration of vanadium in the external electrolyte rises, the proton content in the membrane decreases, as Figure 6-16b shows. The loss of protons, which have high mobility, decreases membrane conductivity. As Figure 6-16c shows, the vanadium content in the membrane also increases with rising vanadium concentration in the electrolyte leading to larger vanadium transport properties $D_{\mathrm{V(II)}0}$ and $t_{\mathrm{V(II)}}$. Adding sulfuric acid increases the membrane proton concentration. Higher proton concentrations displace vanadium from the membrane, as Figure 6-17b and c show. Consequently, at high vanadium concentrations in the electrode, rising sulfate concentration increases conductivity and decreases vanadium transport properties, as Figure 6-9 shows. However, adding sulfuric acid in the external electrolyte also dehydrates the membrane, as Figure 6-16a shows and Part I (Chapter 4) discusses.[247] At low vanadium concentration in the electrodes, the dehydrating effects of additional sulfate dominates, causing membrane conductivity to decrease.

6.4.2.1.2 Cell Performance

Figure 6-10 shows the calculated Coulombic and voltage efficiencies, ε_{q} and ε_{v} respectively, (a) and discharge power density Ψ_{d} (b) at the current density that maximizes Ψ_{d} at ε_{e} = 80% (termed optimal power density) as a function of the vanadium concentration and for different mean sulfate concentrations in the electrodes. To show how sensitive the optimal power density is to the target energy efficiency, shaded regions in Figure 6-10b show power density at ±0.2% of the target energy density. As Figure 6-9 shows, rising vanadium concentration in the electrode electrolyte increases the vanadium transference numbers and diffusion coefficients, decreasing Coulombic efficiency. To maintain an 80% energy efficiency, the current density decreases to lower ohmic losses and increase voltage efficiency. The cumulative effect lowers the optimal power density with increasing vanadium concentration. Moreover, the lower Coulombic efficiency at high vanadium concentration makes the optimal power density less sensitive to the required energy efficiency (*i.e.* narrower shaded region in Figure 6-10).

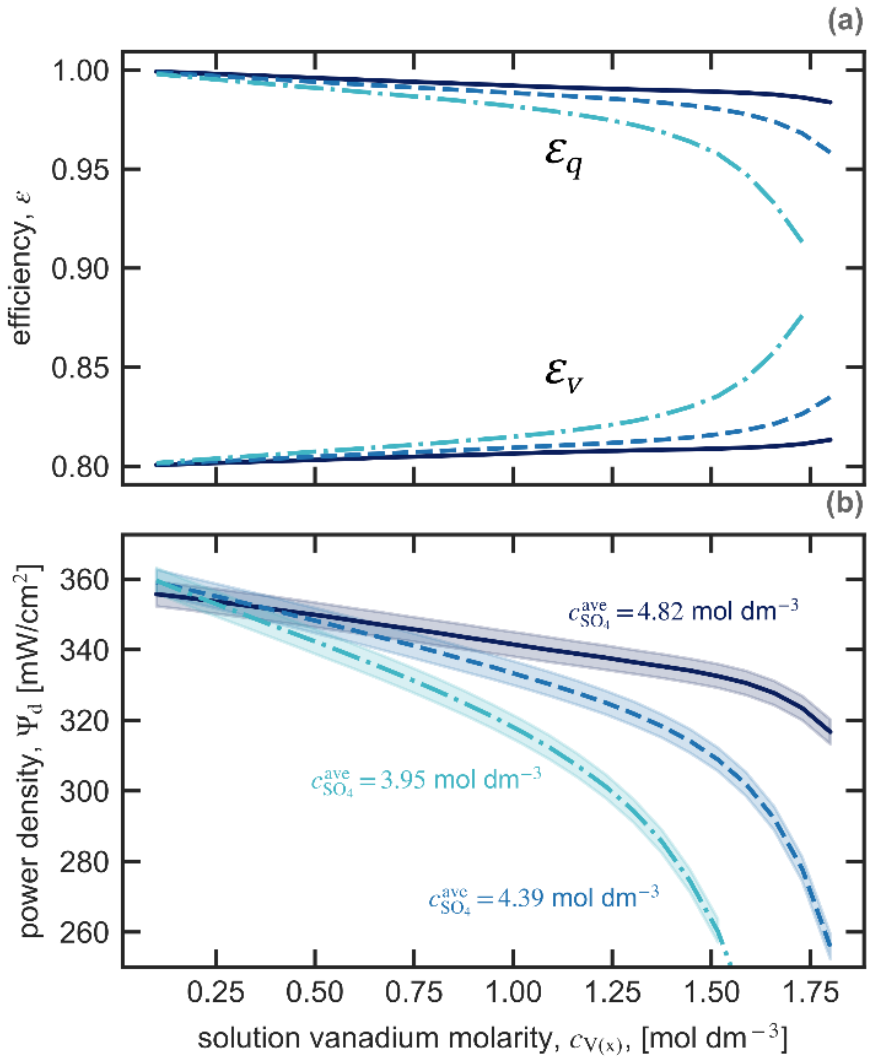

Figure 6-10. Calculated (a) Coulombic ε_q and voltage ε_v efficiencies and (b) the maximum discharge power density Ψ_d at 80% energy efficiency (shaded region is ±0.2%) at the optimal power density as a function of the total vanadium concentration in each electrode at 50% SOC and for mean sulfate concentration in the electrodes of 4.82 mol dm^{-3} (solid lines), 4.39 mol dm^{-3} (dashed line), to 3.95 mol dm^{-3} (dot-dashed line).

Increasing sulfuric acid concentration in the electrolyte (shown in Figure 6-10 as moving from dot-dashed, to dashed line, to solid line) exchanges vanadium in the membrane for protons, increasing membrane conductivity and decreasing vanadium transport coefficients, as Figure 6-9 shows. The larger resulting Coulombic efficiency allows the system to incur more ohmic losses by operating at higher current densities while maintaining the target energy efficiency. As a result, increasing sulfuric acid concentration in the electrolyte increases the optimal power density. However, at low vanadium concentrations, increasing sulfate concentration lowers membrane conductivity, as Figure 6-9 shows. The addition of sulfuric acid will therefore be less effective at low active-species concentrations. Moreover, the improved optimal power density at low

vanadium and high sulfuric acid concentrations may not result in higher return on investment for VRFB systems if balance-of-plant costs increase due lower energy density or higher pumping costs.[34]

6.4.2.2 Impact of Membrane Properties

The chemistry of the membrane impacts its transport properties. Here we focus on two common changes to the membrane: equivalent weight (EW, mass dry polymer per mole of charged group in the membrane, *i.e.*, inverse of the ion-exchnage capacity) and membrane modulus. EW is tuned by changing chemistry.[119, 266, 268] For PFSA membranes the EW is typically in the range 700-1500 g/mol.[12] PFSA membrane pretreatment changes its modulus by varying the number of physical crosslinks in the materials or its crystallinity.[56, 87, 267] Annealing tends to increase and boiling tends to decreases the membrane modulus.[56] In practice, EW and modulus are not independent because lower EW membranes tend to have lower moduli because the additional ionic groups on the polymer disrupt crystalization and crosslink formation.[12]

6.4.2.2.1 Transport Properties

Figure 6-11 shows membrane conductivity κ (a), V(II)/0 diffusion coefficient $D_{\mathrm{V(II)0}}$ (b), and V(II) transference number $t_{\mathrm{V(II)}}$ (c) calculated at membrane composition $x_i^{\overline{\delta}}$ as a function of EW and different dry-membrane moduli E_{b}^0. Figure 6-17 shows the membrane water content λ (a), proton molality $m_{\mathrm{H}}^{\overline{\delta}}$ (b), and V(II) molality $m_{\mathrm{V(II)}}^{\overline{\delta}}$ (c) at the same conditions.

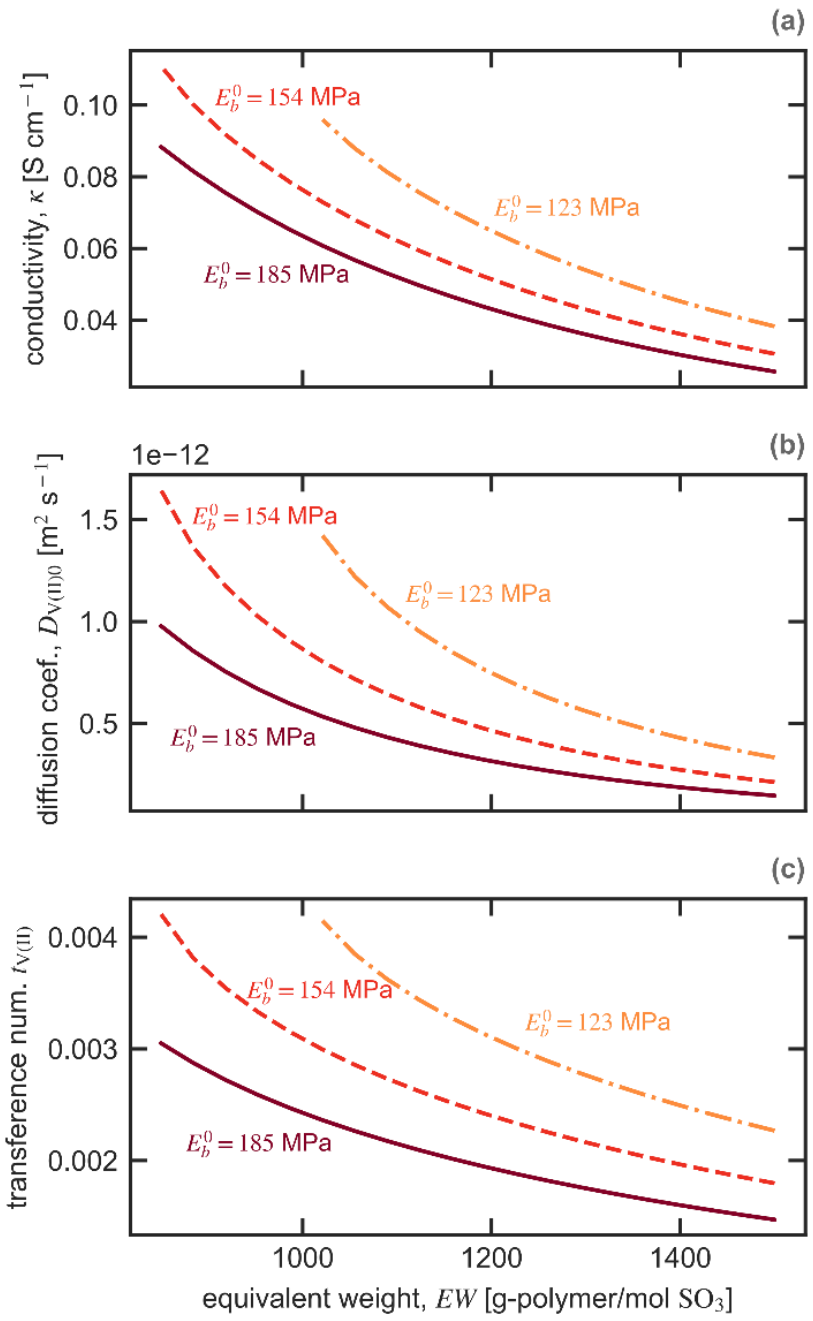

Figure 6-11. Calculated membrane (a) conductivity κ, (b) V(II)/water diffusion coefficient $D_{\mathrm{V(II)0}}$, and (c) V(II) transference number $t_{\mathrm{V(II)}}$ evaluated at composition $x_i^{\bar{\delta}}$ as a function of equivilent weight, EW, for a dry-membrane modulus E_{b}^0 of 185 MPa (solid lines), 154 MPa (dashed lines), and 123 MPa (dot-dashed lines).

Increasing EW decreases membrane water content, as Figure 6-17a shows, thereby decreasing hydophilic water volume fraction, increasing tortuosity of the hydophilic domains, and decreasing the pore size. As a result, membrane conductivity κ and V(II)/water diffusion coefficient $D_{\mathrm{V(II)0}}$

decrease, as Figure 6-11a and b show. Furthermore, increasing EW decreases the concentration of vanadium and protons in the membrane because there are fewer oppositely charged sulfonate groups for these ions to interact with. As EW increases, the vanadium concentration decreases more rapidly than proton concentration in the membrane, as Figure 6-17b and c show, decreasing the vanadium transference number, as Figure 6-11c shows.

Figure 6-11 shows (moving from dot-dashed to solid lines) that increasing the membrane modulus impacts transport properties similary to increasing EW. Raising the membrane modulus decreases water content, as Figure 6-17a shows. The lower water content of the higher modulus membranes results in lower membrane conductivity and vanadium-water diffusion coefficients. As with EW, increasing the membrane modulus decreases the vanadium content in the membrane more rapdily than the proton content, decreasing the vanadium transference number.

6.4.2.2.2 Cell Performance

Figure 6-12 shows the calculated Coulombic ε_q and voltage ε_v efficiencies (a) and discharge power density Ψ_d (b) at the current density that maximizes Ψ_d at ε_e = 80% as a function of equivalent weight EW and dry-membrane modulus E_b^0. As Figure 6-11 shows, increasing EW decreases the vanadium transference numbers and diffusion coefficients, increasing Coulombic efficiency. However, conductivity also falls with increasing EW, lowering voltage efficiency and cell potential. The benefits of higher Coulombic efficiency do not outweigh the costs to voltage efficiency and cell potential. The net effect of increasing EW is a lower optimal power density.

Decreasing the membrane modulus (shown in Figure 6-12 as moving from dot-dashed, to dashed, to solid lines) increases membrane conductivity, vanadium diffusion coefficients, and vanadium transference numbers, as Figure 6-11 indicates. At high EWs, the resulting increase in cell potential and voltage efficiency more than compensates for lower Coulombic efficiency, leading to a higher optimal power density. These findings agree with experimental studies of cell performance with different EW membrane and varying mechanical reinforcement.[118-119, 268] At low EWs (< 900 g-polymer / mole SO_4), ameliorating the poor Coulombic efficiency by increasing membrane modulus offsets the voltage-efficiency losses and results in highest optimal power density.

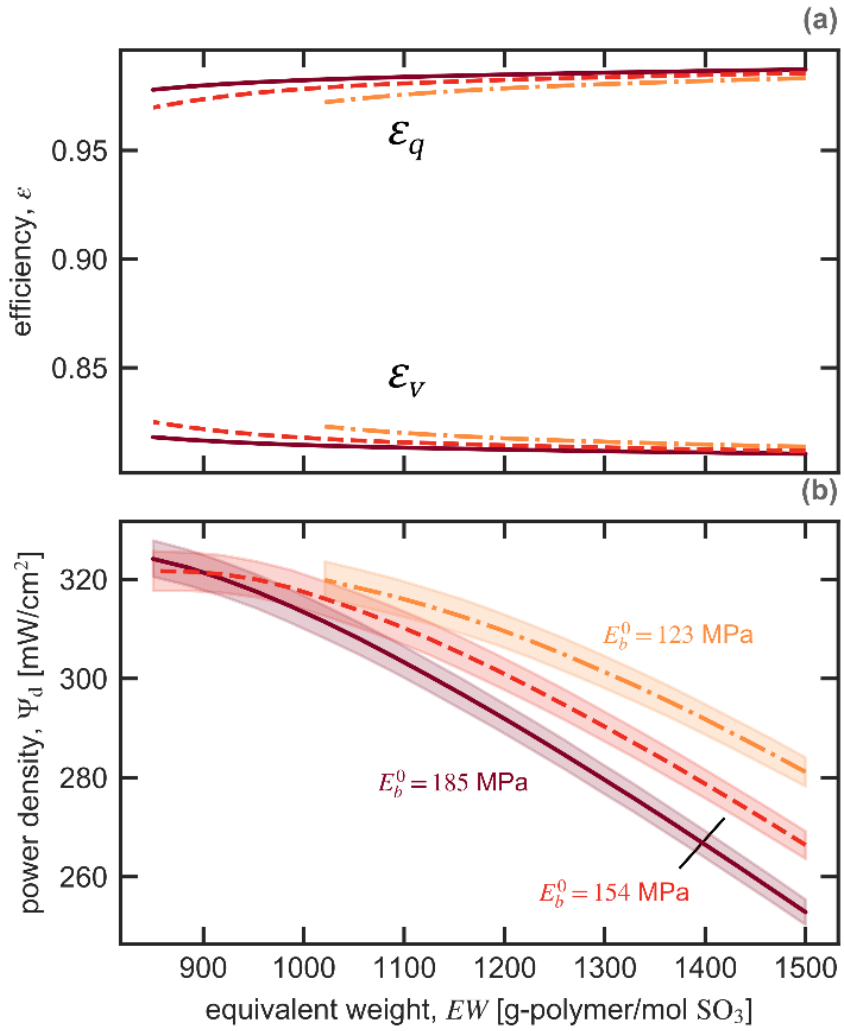

Figure 6-12. Calculated (a) Coulombic ε_q and voltage ε_v efficiencies and (b) discharge power density Ψ_d at 80% energy efficiency (shaded region is ±0.2%) as a function of equivilent weight EW for a dry-membrane modulus E_b^0 of 185 MPa (solid lines), 154 MPa (dashed lines), and 123 MPa (dot-dashed lines).

6.4.3 Structure-Property-Performance Relationships

The model results show that transport properties in VRFB membranes (*e.g.* conductivity, diffusivities, etc.) result from a complex interplay of multiple phenomena that are mediated by structural characteristics of the membrane (*e.g.* membrane modulus and EW). These transport properties, in turn, dictate VRFB performance (*e.g.* Coulombic efficiency). To provide general structure-property-performance relationships, we perform sample-based sensitivity analysis. This analysis (see Numerical Implementation) calculates properties and the performance of membranes over a range of equivalent weights, moduli, tortuosities, and hydrophilic domain shapes and sizes. This method is analogous to synthesizing a thousand membranes with attributes spanning this parameter space and measuring their properties and in-cell performance.

Figure 6-18, Figure 6-19, and Figure 6-20, show pair plots of structural attributes (EW, E_b^0, χ, G, and d^0), exemplar transport and uptake properties (κ, t_{II}, D_{0II}, D_{IIII}, m_{II}, m_H, and λ), and cell performance at a current density of 200 mA cm^{-2} (Ψ_d, ε_q, and ε_v) and reference conditions (see Table 6-2). Figure 6-21 gives the least-squares linear regression coefficients between the natural log of each variable. Based on the sample-based sensitivity analysis, Figure 6-13 shows a chord diagram of correlation between (a) structural attributes of the membrane and transport and uptake properties and (b) membrane properties and cell performance metrics scaling the chord size by the Spearman rank correlation coefficient r_s squared (Figure 6-22 provides all values of the Spearman coefficients between variables). Spearman coefficient is a measure of correlated monotonicity between variables.

Figure 6-13a illustrates that dry-membrane domain spacing, d^0, and membrane modulus, E_b^0, are highly correlated to the molality of ions in the membrane and water uptake, respectively, because they directly affect the energetics of membrane partitioning (see Part I, Chapter 4).[247] The shape and tortuosity of the hydrophilic domains, quantified by G and χ, respectively, correlate with transport properties. The domain shape affects the transference number of vanadium, whereas the tortuosity influences the conductivity and diffusion coefficients. EW correlates with all of these membrane properties, but typically to a lesser extent than the other membrane attributes. Figure 6-13a suggests which membrane design approaches are likely to influence a property of interest. However, the structure-function correlations are not high (*i.e.* at most 0.8), indicating that varying the structure of the membrane does not guarantee altered properties. Moreover, structural attributes impact multiple transport properties such that properties cannot be tuned independently.

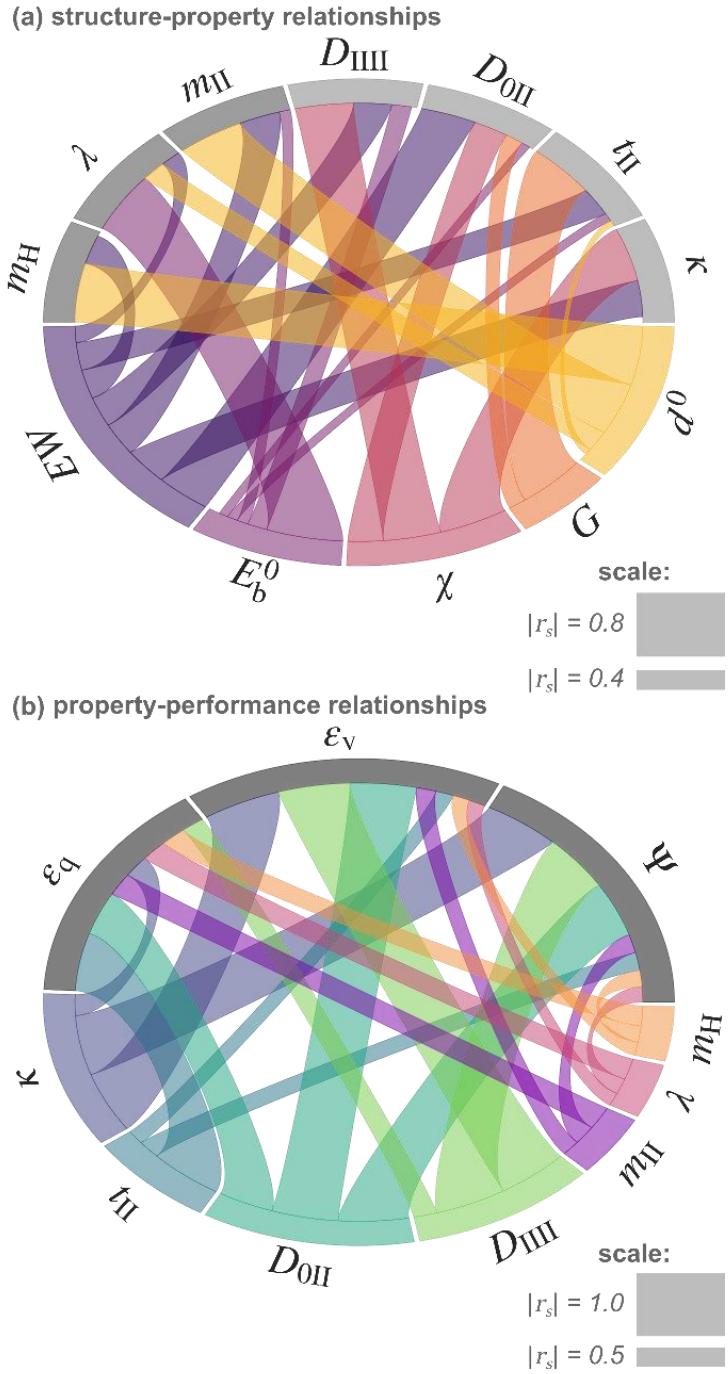

Figure 6-13. Chord diagrams of parameter sensitivity as measured by the Spearman correlation coefficient, r_s, between (a) structural parameters of the membrane and exemplar transport and uptake properties and (b) membrane properties and cell performance metrics at the reference electrolyte conditions with current density of 200 mA cm^{-2}. The arch-length of the chord's intersection with the outer circle scales as the square of the Spearman coefficient (see Figure 6-22 for values). For clarity, connections with $|r_s| < 0.05$ and between variables in the same group are not included.

Figure 6-13b correlates the membrane properties with in-situ VRFB performance. Membrane conductivity directly governs voltage efficiency, ε_v, and discharge power density, Ψ_d, at a current density of 200 mA cm^{-2} (see Equations 6-1, (6-6), and 6-28), giving $r_s = 1$ between these variables. Because conductivity is highly correlated with vanadium diffusivity, vanadium diffusion coefficients are also correlated with ε_v and Ψ_d but do not have a causal effect (see Figure 6-20). The sensitivity analysis shows that Coulombic efficiency is highly correlated with vanadium transference number ($r_s = -0.98$) and water-vanadium diffusion coefficient ($r_s = -0.84$) and only weakly correlated with vanadium-vanadium diffusion coefficient ($r_s = -0.55$). These correlations are consistent with Figure 6-7 in showing the crucial roles of migration and water-driven transport in cell operation. Water and ion uptake are weakly correlated to cell performance metrics. As such, screening membranes using ex-situ measurements of conductivity and vanadium transference number are most indicative of cell performance in these conditions.

6.5 Summary

This work develops a multicomponent, concentrated-solution model of transport in VRFB membranes that accounts for Stefan-Maxwell-Onsager transport couplings between species and thermodynamic nonidealities. The molecular-thermodynamics model outlined in Part I (Chapter 4) calculates ion and water partitioning into the membrane from the electrolyte in the electrodes and provides thermodynamic factors that influence species diffusion. The molecular-transport model outlined in Part II (Chapter 5) describes binary-diffusion coefficients between ions, water, and the membrane as a function of water content and composition.[31, 247] The resulting multicomponent diffusion coefficient matrix has large off-diagonal elements that dilute-solution theory neglects and that impact the net transport of the species through the membrane. Transport is highly coupled because of both thermodynamic and frictional interactions between species. In particular, water concentration gradients play a dominant role in vanadium crossover. Under an applied current, contributions to net flux from these diffusional modes and migration are aligned or opposed, depending on the direction of transport. Migration dominates at high current densities (>250 mA cm^{-2}). The magnitude of coupling suggests that predictions made using dilute-solution theories for VRFB will be misleading. Extended-dilute-solution theories that account for the impact of water chemical potential gradients on vanadium transport are more reliable. Furthermore, membrane-permeation experiments that measure flux under ill-defined concentration gradients will not provide diffusion coefficients that are predictive of transport under other conditions. Even in the case of carefully designed experiments, the magnitude of measured diffusion coefficients should be interpreted in the context of the collective interactions between all species present in the system. Sensitivity analysis indicate that membrane conductivity and vanadium transference number are the best predictors of cell performance metrics.

The cell performance in terms of power density and energy efficiency depends on the complex interplay of the thermodynamic and frictional interactions of all species and their gradients. We studied the effect of sulfate and vanadium concentration in the electrode electrolyte and membrane equivalent weight and modulus on membrane properties, species transport, and cell performance. For a metric of maximum power density at 80% energy efficiency, low-vanadium and high-sulfuric acid concentration electrolytes perform best. However, the solubility of vanadium in sulfuric acid limits the success of this strategy. Membranes with low equivalent weights (*i.e.* high ion-exchange capacity) perform better. Specifically, decreasing EW from 1500 to 900 improves

performance by 20% by increasing membrane conductivity. Whereas at high equivalent weights, a low modulus is superior, although perhaps not readily synthesizable.

6.6 Appendix 6-A

Adding Equation 6-18 to Equation 6-17 puts the driving force in terms of ionic potential-independent term $\mu_{i,\mathrm{M}}$

$$c_i \frac{\partial \mu_i}{\partial z} - \frac{c_i z_i}{z_\mathrm{M}} \frac{\partial \mu_\mathrm{M}}{\partial z} = c_i \frac{\partial \mu_{i,\mathrm{M}}}{\partial z} = \sum_{j \neq i,\mathrm{M}} \frac{RT}{\mathcal{D}_{ij} c_\mathrm{T}} \left(c_i N_j - c_j N_i\right) - \frac{c_\mathrm{M} RT}{c_\mathrm{T} \mathcal{D}_{i\mathrm{M}}} N_i - \frac{c_i z_i}{c_\mathrm{T} z_\mathrm{M}} \sum_{j \neq \mathrm{M}} \frac{RT}{\mathcal{D}_{j\mathrm{M}}} N_j \tag{6-29}$$

where $D_{i\mathrm{M}} = c_i c_j RT / c_\mathrm{T} K_{ij}$. For an isothermal, isobaric system, the gradient of $\mu_{i,\mathrm{M}}$ is a function of $N-2$ species compositions because the Gibbs-Duhem equation and electroneutrality reduces the degrees of freedom by 2. We expand left side of Equation 6-29 using the composition variable $\ln(x_j / x_\mathrm{M}^{z_j/z_\mathrm{M}})$

$$c_i \frac{\partial \mu_{i,\mathrm{M}}}{\partial z} = c_\mathrm{T} x_i \sum_{j \neq \mathrm{M},n}^{N} \frac{\partial \mu_{i,\mathrm{M}}}{\partial \ln\left(\frac{x_j}{x_\mathrm{M}^{z_j/z_\mathrm{M}}}\right)} \frac{\partial \ln\left(\frac{x_j}{x_\mathrm{M}^{z_j/z_\mathrm{M}}}\right)}{\partial z} = RT c_\mathrm{T} \sum_{j \neq \mathrm{M},n}^{N} \left[\chi_{ij} \left(\frac{\partial x_j}{\partial z} - \frac{z_j x_j}{z_\mathrm{M} x_\mathrm{M}} \frac{\partial x_\mathrm{M}}{\partial z}\right)\right] \tag{6-30}$$

Substitution of Equation 6-30 into Equation 6-29 gives

$$c_\mathrm{T} \sum_{j \neq \mathrm{M},n}^{N} \chi_{ij} \frac{\partial x_j}{\partial z} = \sum_{j \neq i,\mathrm{M}} \frac{(x_i N_j - x_j N_i)}{\mathcal{D}_{ij}} - \frac{x_\mathrm{M}}{\mathcal{D}_{i\mathrm{M}}} N_i - \frac{x_i z_i}{z_\mathrm{M}} \sum_{j \neq \mathrm{M}} \frac{N_j}{\mathcal{D}_{j\mathrm{M}}} + c_\mathrm{T} \sum_{j \neq \mathrm{M},n}^{N} \chi_{ij} \frac{z_j x_j}{z_\mathrm{M}} \frac{\partial \ln x_\mathrm{M}}{\partial z} \tag{6-31}$$

By choosing species n such that it has a charge number different from M, we can eliminate the mole fraction of species n and M on the right side by using the dependence of mole fractions ($1 = \sum_i x_i$) and electroneutrality ($\sum_i x_i z_i = 0$), specifically giving $x_n = (z_n + \sum_{j \neq \mathrm{M},n} x_j (z_j - z_n))/(z_n - z_\mathrm{M})$ and $x_\mathrm{M} = (z_\mathrm{M} + \sum_{j \neq \mathrm{M},n} x_j (z_j - z_\mathrm{M}))/(z_\mathrm{M} - z_n)$. Rearranging Equation 6-31 into a matrix form gives

$$\boldsymbol{\chi x'} = \boldsymbol{\Psi x} + \boldsymbol{\zeta} \tag{6-32}$$

where $\boldsymbol{x}'$ and $\boldsymbol{x}$ are $N-2$ vectors with entries $\partial x_i/\partial z$ and x_i, respectively; $\boldsymbol{\Psi}$ is a $N-2$ by $N-2$ matrix containing entries

$$\Psi_{ii} = -\frac{N_i}{c_\mathrm{T}}\left(\frac{z_i - z_n}{\mathcal{D}_{i\mathrm{M}}(z_n - z_\mathrm{M})} + \frac{z_i - z_\mathrm{M}}{\mathcal{D}_{in}(z_\mathrm{M} - z_n)}\right) + \sum_{k\neq \mathrm{M},i} \frac{N_k}{c_\mathrm{T}\mathcal{D}_{ik}} + \frac{z_i}{z_\mathrm{M}}\left(\chi_{ii}\frac{\partial \ln x_\mathrm{M}}{\partial z} - \sum_{k\neq \mathrm{M}} \frac{N_k}{c_\mathrm{T}\mathcal{D}_{k\mathrm{M}}}\right) \quad 6\text{-}33$$

and

$$\Psi_{ij} = \chi_{ij}\frac{z_j}{z_\mathrm{M}}\frac{\partial \ln x_\mathrm{M}}{\partial z} - \frac{N_i}{c_\mathrm{T}}\left(\frac{1}{\mathcal{D}_{ij}} + \frac{z_j - z_n}{\mathcal{D}_{i\mathrm{M}}(z_n - z_\mathrm{M})} + \frac{z_j - z_\mathrm{M}}{\mathcal{D}_{in}(z_\mathrm{M} - z_n)}\right) \quad 6\text{-}34$$

for $i \neq j$; and $\boldsymbol{\zeta}$ is a $N-2$ vector containing entries

$$\zeta_i = -\frac{N_i}{c_\mathrm{T}}\left(\frac{z_n}{\mathcal{D}_{i\mathrm{M}}(z_n - z_\mathrm{M})} + \frac{z_\mathrm{M}}{\mathcal{D}_{in}(z_\mathrm{M} - z_n)}\right) \quad 6\text{-}35$$

Equations 6-33 through 6-35 are for i and j not equal to species M or n.

6.7 Appendix 6-B

Krishna et al. [283-284]showed that with boundary conditions on x_i at $z = 0$ and $= l_\mathrm{M}$ the solution to Equation 6-32 for constant χ_{ij}, c_T, and $\frac{\partial \ln x_\mathrm{M}}{\partial z}$ (we approximate $\frac{\partial \ln x_\mathrm{M}}{\partial z}$ as $\ln\left(\frac{x_\mathrm{M}(z=l_\mathrm{M})}{x_\mathrm{M}(z=0)}\right)/l_\mathrm{M}$) is

$$\boldsymbol{x} - \boldsymbol{x}(z=0) = [\exp(\boldsymbol{\Theta}^{-1}\boldsymbol{\Psi}z) - \mathbf{I}][\exp(\boldsymbol{\Theta}^{-1}\boldsymbol{\Psi}l_\mathrm{M}) - \mathbf{I}]^{-1}\,[\boldsymbol{x}(z=l_\mathrm{M}) - \boldsymbol{x}(z=0)] \quad 6\text{-}36$$

where $\mathbf{I}$ is the identity matrix, the superscript -1 denotes the matrix inverse, and the exp is the matrix exponential. The concentration gradient vector is then

$$\boldsymbol{x}' = [\boldsymbol{\Theta}^{-1}\boldsymbol{\Psi}\exp(\boldsymbol{\Theta}^{-1}\boldsymbol{\Psi}z)][\exp(\boldsymbol{\Theta}^{-1}\boldsymbol{\Psi}l_\mathrm{M}) - \mathbf{I}]^{-1}\,[\boldsymbol{x}(z=l_\mathrm{M}) - \boldsymbol{x}(z=0)] \quad 6\text{-}37$$

We calculate the matrix exponential by diagonalizing the matrix argument and computing the exponential element-wise of the matrix eigenvalues. Equations 6-36 and 6-37 give the species concentration and concentration gradients as a function of species fluxes.

Equation 6-37 in conjunction with Equation 6-19 calculate flux. The equations are an implicit set of algebraic equations that calculate flux. Krishna et al.[283-284] showed that the following numerical method specifies flux: (1) calculate $\boldsymbol{\Psi}$ for $\boldsymbol{N} = 0$; (2) calculate $\boldsymbol{x}'$ from Equation 6-37 at $z = 0$; (3) use calculated $\boldsymbol{x}'$ at $z = 0$ to calculate $\boldsymbol{N}$ using Equation 6-19; (4) recalculate $\boldsymbol{\Psi}$ using the calculated $\boldsymbol{N}$; (5) repeat steps 2-4 until achieving convergence (here, set to $1\text{x}10^{-3}$ relative change in flux over an iterations).

6.8 Chapter 6 Supporting Information

6.8.1 Calculation of Electrolyte Concentrations

We calculate the composition in the electrodes after each charging step by setting the sulfate and proton salt concentration in the electrode equal (*i.e.* $\left(c_{\mathrm{SO_4}}^{\beta}\right)^{1/2} c_{\mathrm{H}}^{\beta} = \left(c_{\mathrm{SO_4}}^{\epsilon}\right)^{1/2} c_{\mathrm{H}}^{\epsilon}$) where c_i is the molar concentration of i in electrode ϕ), conserving the total mass of sulfate across a charging step (*i.e.* $c_{\mathrm{SO_4}}^{\beta} + c_{\mathrm{SO_4}}^{\epsilon}$ is the same at the end of charging), and satisfying electroneutrality ($\sum z_i c_i^{\phi} = 0$). We neglect the crossover of a small amount of vanadium during charging.

6.8.2 Parameters

Table 6-3 gives model parameters for vanadium ions (generically denoted with subscript $\mathrm{V(x)}$) where $\mathfrak{D}_{ij}^{\mathrm{mol}}$ is the binary diffusion coefficient between i and j accounting for ion pairing, $\tilde{V}_{\mathrm{V(x)}}$ is the viscous volume, $k_{\mathrm{V(x)}}$ is the solvent/cation binding constant, $K_{\mathrm{V(x)HSO_4}}$ is the vanadium/bisulfate equilibrium constant, and $\beta_{\mathrm{V(x)}i}$ is the interaction parameter between vanadium and species i. Parts I and II detail the definition of these parameters.[31, 247] As discussed in Part II (Chapter 5), superscript mol on the diffusion coefficients denotes accounting for ion-pair formation (*i.e.* Molecular Construct).[31] Superscript ∞ denotes infinite dilution. In parenthesis we note the reference concentration in units of mol dm^{-3} (M) for ion/ion diffusion coefficients. Where there are incomplete measurements for a vanadium ions, the species that have known parameters that approximate those of vanadium are given. β_{ij} and k_i for ion pairs that are positively charged (*e.g.* V(III)HSO_4) are set to those of the highest charge number participating cation; for ion pairs that are negatively charged (*e.g.* HSO_4) these thermodynamic parameters are set to the involved anion.

Table 6-3. Properties of vanadium ions

	V(II)	V(III)	V(IV)	V(V)
$\mathfrak{D}_{0V(x)}^{\infty,mol}$	1.41^{-10} [m^2/s] (Ref [261])	1.41^{-10} [m^2/s] (Ref [261])	$1.4x10^{-10}$ [m^2/s] (Ref [264])	$1.4x10^{-10}$ [m^2/s] (Ref [264])
$\mathfrak{D}_{0HSO_4V(x)}^{\infty,mol}$	1.41^{-10} [m^2/s] (Ref [261])	1.41^{-10} [m^2/s] (Ref [261])	$1.4x10^{-10}$ [m^2/s] (Ref [264])	$1.4x10^{-10}$ [m^2/s] (Ref [264])
$\mathfrak{D}_{SO_4V(x)}^{mol}$	$6.26x10^{-12}$ [m^2/s] at 0.7 M ($CuSO_4$, Ref [85])	$6.26x10^{-12}$ [m^2/s] at 0.7 M ($CuSO_4$, Ref [85])	$6.26x10^{-12}$ [m^2/s] at 0.7 M ($CuSO_4$, Ref [85])	$2.40x10^{-11}$ [m^2/s] at 0.3 M (KSO_4 Ref [85])
$\mathfrak{D}_{HSO_4V(x)}^{mol}$	$6.01x10^{-11}$ [m^2/s] ($CaCl_2$, Ref [85]) at 1 M	$6.63x10^{-12}$ [m^2/s] at 0.05 M ($LaCl_3$, Ref [85])	$6.01x10^{-11}$ [m^2/s] ($CaCl_2$, Ref [85]) at 1 M	$4.08x10^{-10}$ [m^2/s] at 3 M (KCl, Ref [85])
$\mathfrak{D}_{SO_4HSO_4V(x)}^{mol}$	N/A	$1.78x10^{-11}$ [m^2/s] at 0.3 M (Na_2SO_4, Ref [85])	$2.40x10^{-11}$ (KSO_4, Ref [85]) at 0.3 M	N/A
$\mathfrak{D}_{HSO_4HSO_4V(x)}^{mol}$	N/A	$2.63x10^{-10}$ [m^2/s] at 3 M (NaCl Ref [85])	$4.08x10^{-10}$ (KCl, Ref [85]) at 3M	N/A
$\left(\frac{\tilde{V}_{V(x)}6}{N_A\pi}\right)^{\frac{1}{3}}$	0.765 [nm] $(Ni^{2+})^{II}$	0.908 [nm] $(Cr^{3+})^{II}$	0.76 [nm] $(Ni^{2+})^{II}$	0.552 [nm] $(Li^{+})^{II}$
$k_{V(x)}$	0.244 $(Cu^{2+})^{I}$	0.566 $(Fe^{3+})^{I}$	5.41 $(Ni^{2+})^{I}$	3.59 $(Li^{+})^{I}$
$K_{V(x)HSO_4}$	No Association	$1.8x10^{-6}$ (fit)	0.01059 (Ref [223])	No Association
$\beta_{V(x)M}$	0.08 $(Cu^{2+})^{I}$	0.45 (fit)	0.08 (fit)	0.25 $(fit)^{I}$
$\beta_{V(x)SO_4}$	-0.164 $(Cu^{2+})^{I}$	0 (fit)	- 0.164 $(Cu^{2+})^{I}$	0.168 $(H^{+})^{I}$

I from Part I (Chapter 4)[247]
II from Part II (Chapter 5)[31]

6.8.3 *Flowchart of VRFB membrane model*

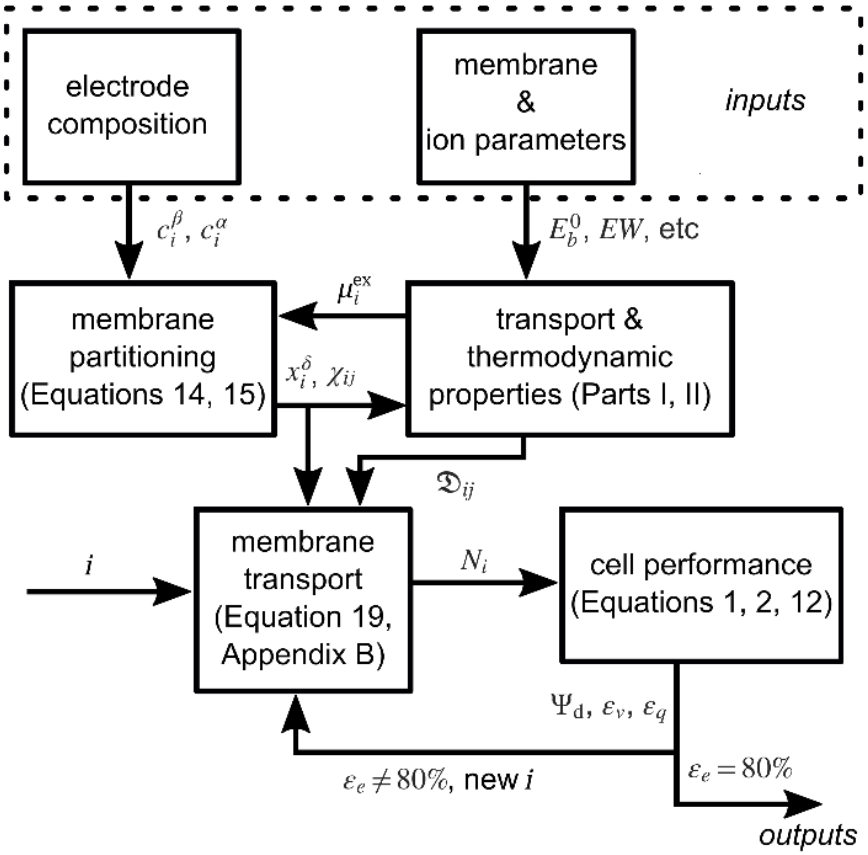

Figure 6-14. flowchart outlining the model of VRFB membrane transport and thermodynamics.

6.8.4 *Validity of Constant-Transport-Coefficients Assumption*

The validity of neglecting changes in $\mathfrak{D}_{ij}$ and χ_{ij} over the composition in the membranes is considered here. We compare $\mathfrak{D}_{ij}$ and χ_{ij} evaluated at a composition that is 90% and 10% of the composition of the negative electrode (*i.e* $x_i^{\bar{\delta}_{90\%}} = (0.9x_i^{\delta'} + 0.1x_i^{\delta''})$ and $x_i^{\bar{\delta}_{10\%}} = (0.1x_i^{\delta'} + 0.9x_i^{\delta''})$, respectively). Table 6-4 shows the average absolute relative deviation (AARD) of $\mathfrak{D}_{ij}$ calculated at these composition relative to the average membrane composition that we use in the main text (*i.e.* $x_i^{\bar{\delta}} = (0.5x_i^{\delta'} + 0.5x_i^{\delta''})$)

$$\mathrm{AARD}_{\mathfrak{D}_{ij}} = \frac{\left|\frac{\mathfrak{D}_{ij}\left(x_i^{\bar{\delta}_{90\%}}\right) - \mathfrak{D}_{ij}\left(x_i^{\bar{\delta}}\right)}{\mathfrak{D}_{ij}\left(x_i^{\bar{\delta}_{90\%}}\right)}\right| + \left|\frac{\mathfrak{D}_{ij}\left(x_i^{\bar{\delta}_{10\%}}\right) - \mathfrak{D}_{ij}\left(x_i^{\bar{\delta}}\right)}{\mathfrak{D}_{ij}\left(x_i^{\bar{\delta}_{10\%}}\right)}\right|}{2}$$

The small values of AARD show that assuming constant $\mathfrak{D}_{ij}$ across the membrane is justified. Table 6-5 shows the average absolute deviation of χ_{ij} at compositions of $x_i^{\bar{\delta}_{90\%}}$ and $x_i^{\bar{\delta}_{10\%}}$ relative to $x_i^{\bar{\delta}}$.

$$\mathrm{AAD}_{\chi_{ij}} = \frac{\left|\chi_{ij}\left(x_i^{\bar{\delta}_{90\%}}\right) - \chi_{ij}\left(x_i^{\bar{\delta}}\right)\right| + \left|\chi_{ij}\left(x_i^{\bar{\delta}_{10\%}}\right) - \chi_{ij}\left(x_i^{\bar{\delta}}\right)\right|}{2}$$

The AAD is a superior measure of deviation for χ_{ij} since some entries go to zero, such as the off-diagonal elements of an ideal solution. χ_{ij} is of order 1, and some values of $\mathrm{AAD}_{\chi_{ij}}$ are of the same order. Therefore, the assumption of constant χ_{ij} is approximate. To quantify how these errors impact calculated fluxes, Table 6-6 shows the AAD of the calculated species fluxes using χ_{ij} and $\mathfrak{D}_{ij}$ at $x_i^{\bar{\delta}_{90\%}}$ and $x_i^{\bar{\delta}_{10\%}}$ relative those calculated at $x_i^{\bar{\delta}}$. Using transport parameters from the range of compositions in the membrane to calculate fluxes of water and vanadium does not significantly change their value. The flux of SO_4 does vary depending on how the membrane phase composition is averaged. However, these errors are not concerning here as the interest of this paper is principally vanadium crossover. As such, the approximations made to solve the system of equations outlined in the Theory section do not significantly bias out results.

Table 6-4. AARD of $\mathfrak{D}_{ij}$

	0	SO4	V(IV)	V(V)	V(II)	V(III)	M
0	NA	4%	4%	4%	4%	5%	6%
SO4	4%	NA	7%	4%	4%	2%	19%
V(IV)	4%	7%	NA	7%	10%	3%	3%
V(V)	4%	4%	7%	NA	23%	7%	2%
V(II)	4%	4%	10%	23%	NA	8%	3%
V(III)	5%	2%	3%	7%	8%	NA	3%
M	6%	19%	3%	2%	3%	3%	NA

Table 6-5. AAD of χ_{ij}

	0	SO4	V(IV)	V(V)	V(II)	V(III)
0	0.073	0.124	0.127	0.317	0.133	0.302
SO4	0.022	0.081	0.093	0.118	0.080	0.224
V(IV)	0.017	0.011	0.097	0.199	0.201	0.381
V(V)	0.023	0.013	0.041	0.156	0.080	0.057
V(II)	0.004	0.009	0.011	0.044	0.051	0.100
V(III)	0.008	0.018	0.043	0.112	0.169	0.269

Table 6-6. Calculated N_iF for transport coefficients at $x_i^{\bar{\delta}}$ and the AAD

	0	SO4	V(IV)	V(V)	V(II)	V(III)
$\boldsymbol{N_iF}$ [mA/cm^2]	275.75	0.81	-0.10	-0.06	0.50	0.90
AAD [mA/cm^2]	11.585	1.096	0.078	0.032	0.017	0.066

6.8.5 Sample-Based Sensitivity Analysis Parameters

Values of membrane properties were sampled using Saltelli's extension of the Sobol sequence as implemented in the SALib package for python.[287] The sequence consisted of 1001 samples over the range of parameters listed in Table 6-7.

Table 6-7. Ranges of membrane parameters sampled for sensitivity analysis

Parameter	Lower Limit	Upper Limit
Equivalent Weight, EW	950 [g-polymer/mole SO_3]	1250 [g-polymer/mole SO_3]
Backbone Modulus, E_b^0	139 [MPa]	169 [MPa]
Archie's Parameter, χ	0.9	1.5
Geometric Transport Factor, G	3	6
Dry-membrane domain spacing, d^0	2.2 [nm]	3.3 [nm]

6.8.6 *Predicted Cell Performance with Different Transport Models*

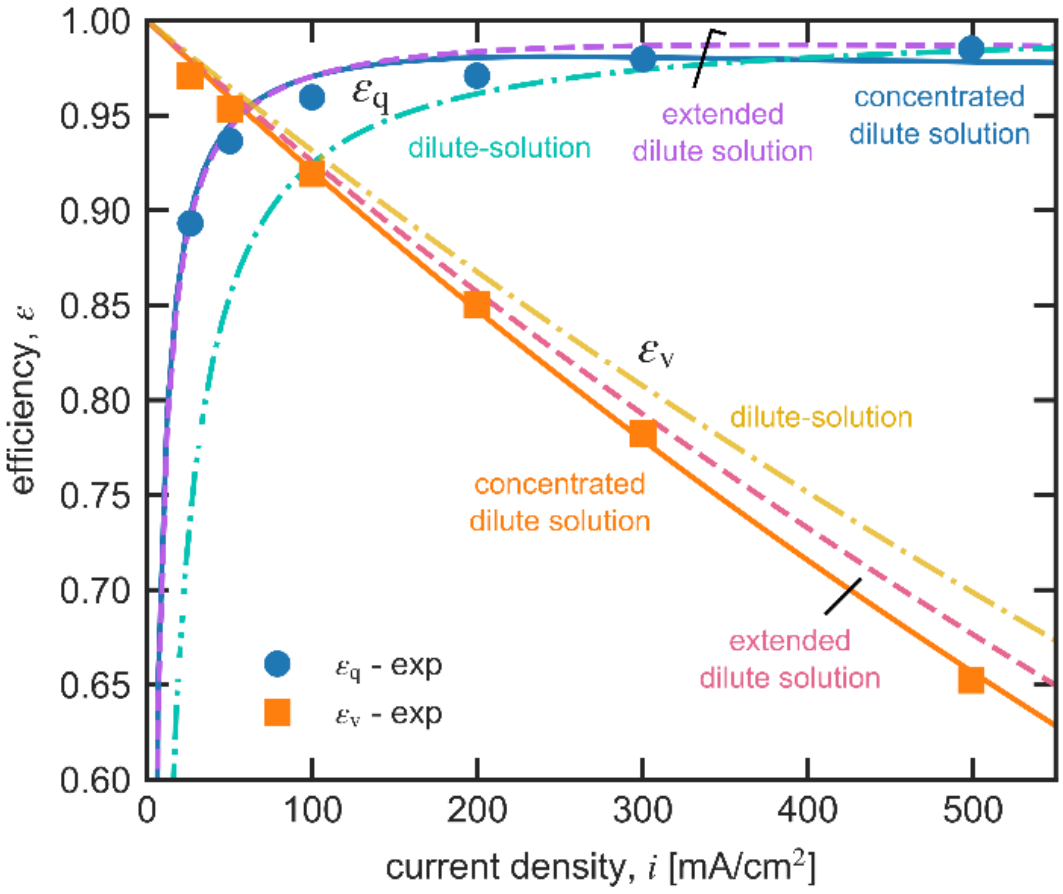

Figure 6-15. Coulombic efficiency ε_q and voltage efficiency ε_v calculated using the proposed concentrated-solution theory model, the dilute-solution theory that accounts only for interactions with the membrane (*i.e.* $\mathfrak{D}_{ij\neq M} \to \infty$) and an extended dilute-solution theory that also accounts for frictional interactions with water (*i.e.* $\mathfrak{D}_{ij\neq 0,M} \to \infty$).

6.8.7 *Impact of EW, Modulus, and Supporting and Vanadium Electrolyte Concentration*

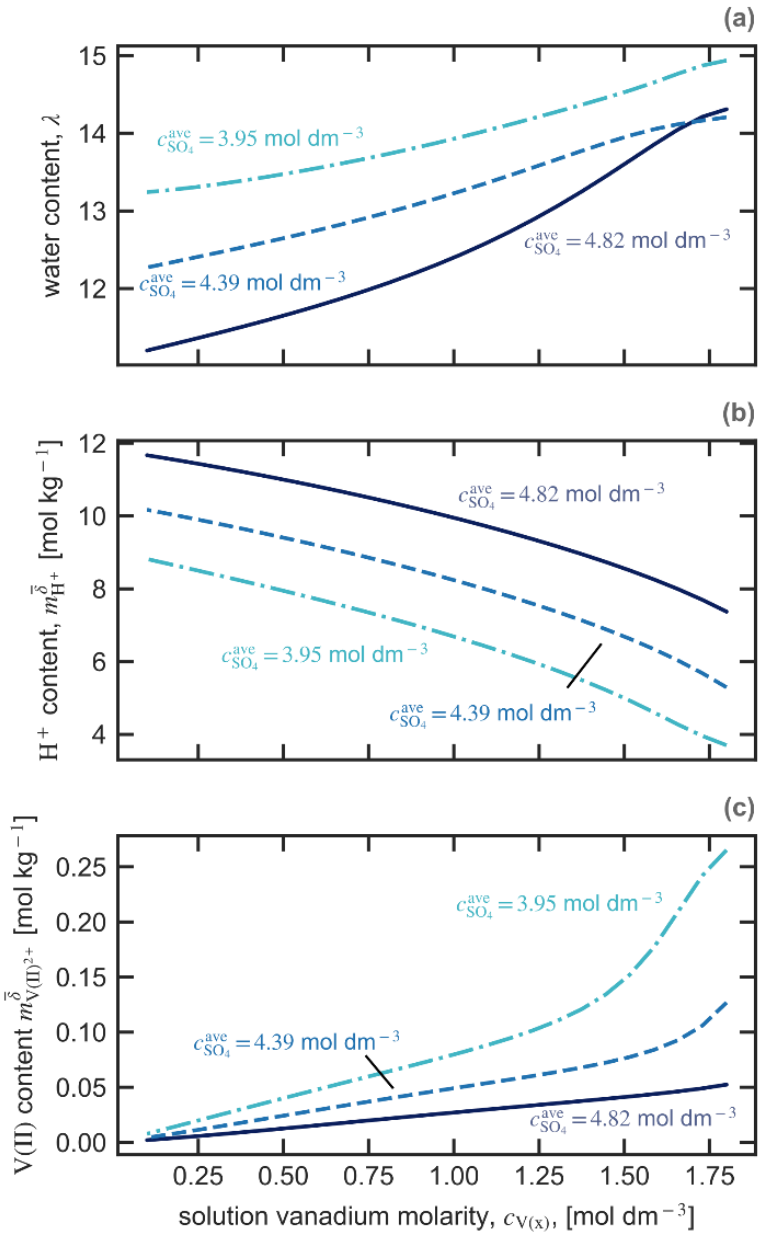

Figure 6-16. Calculated membrane water uptake λ (a), proton molarity $m_{\mathrm{H}}^{\overline{\delta}}$ (b), and V(II) molarity $m_{\mathrm{V(II)}}^{\overline{\delta}}$ (c) evaluated at composition $x_i^{\overline{\delta}}$ as a function of the total vanadium molarity in the electrodes where the SOC of the cell is 50% and the different lines are for different arithmetic average sulfate concentration in the electrodes of 4.82 mol dm^{-3} (solid lines), 4.39 mol dm^{-3} (dashed line), to 3.95 mol dm^{-3} (dot-dashed line).

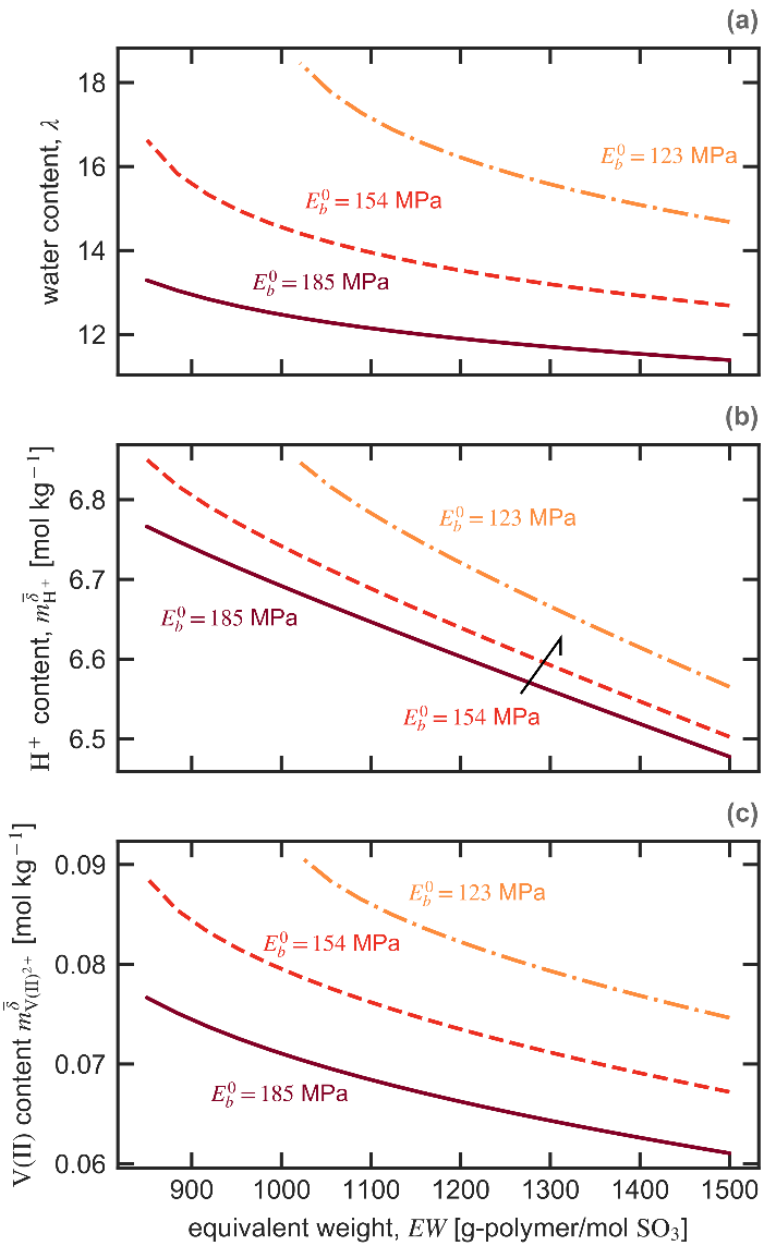

Figure 6-17. Calculated membrane water uptake λ (a), proton molarity $m_{\mathrm{H}}^{\bar{\delta}}$ (b), and V(II) molarity $m_{\mathrm{V(II)}}^{\bar{\delta}}$ (c) evaluated at composition $x_i^{\bar{\delta}}$ as a function of equivilent weight EW for different dry-membrane moduli E_{b}^0 of 185 MPa (solid lines), 154 MPa (dashed lines), and 123 MPa (dot-dashed lines).

6.8.8 Sample-Based Sensitivity Analysis

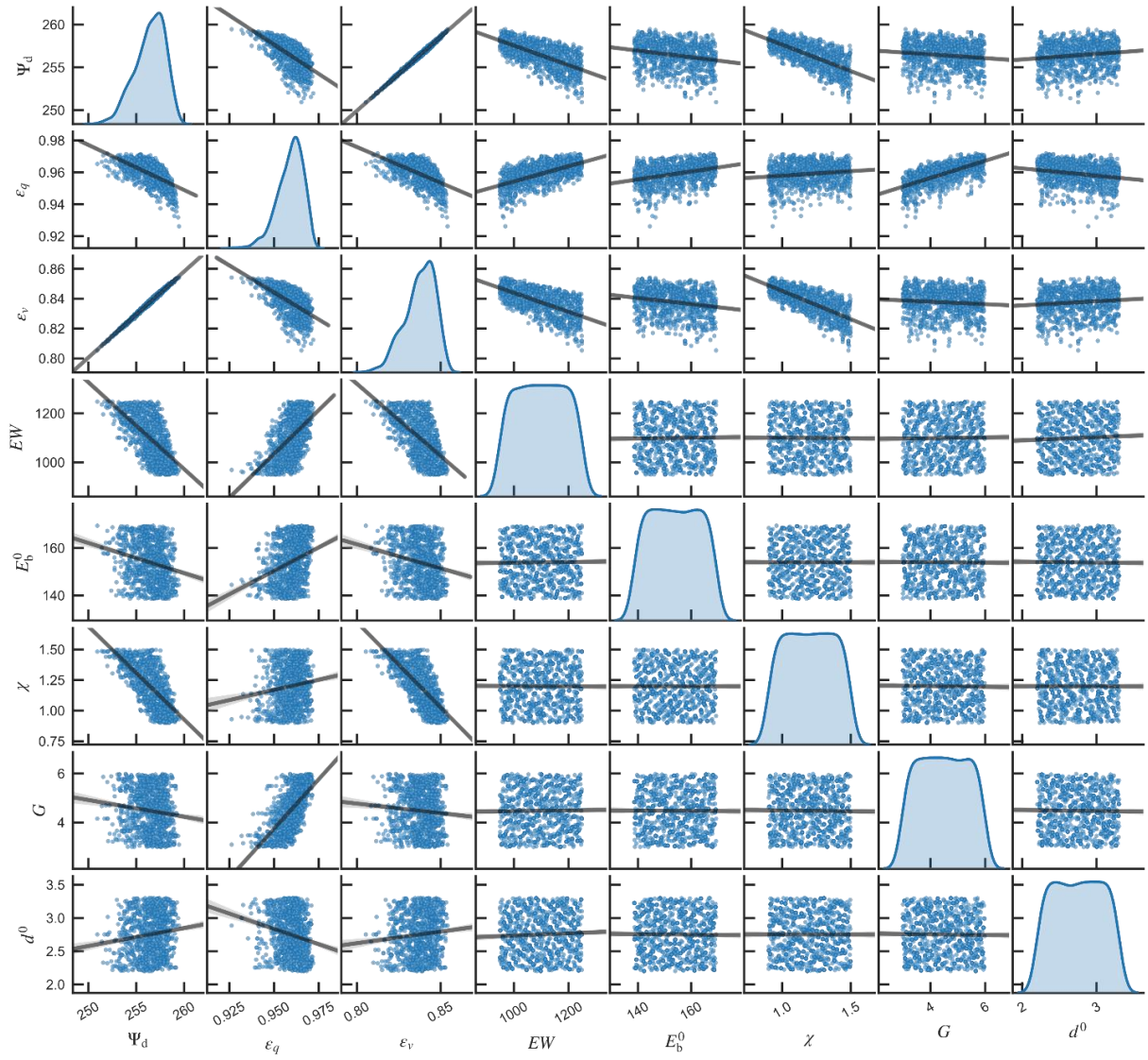

Figure 6-18. Pair plot of membrane structure-performance properties sample-based sensitivity analysis. Diagonals show kernel density estimate of variable distribution. Points in off-diagonal plots are the calculated values of a specific sample. Lines show best-fit least-squares linear regression.

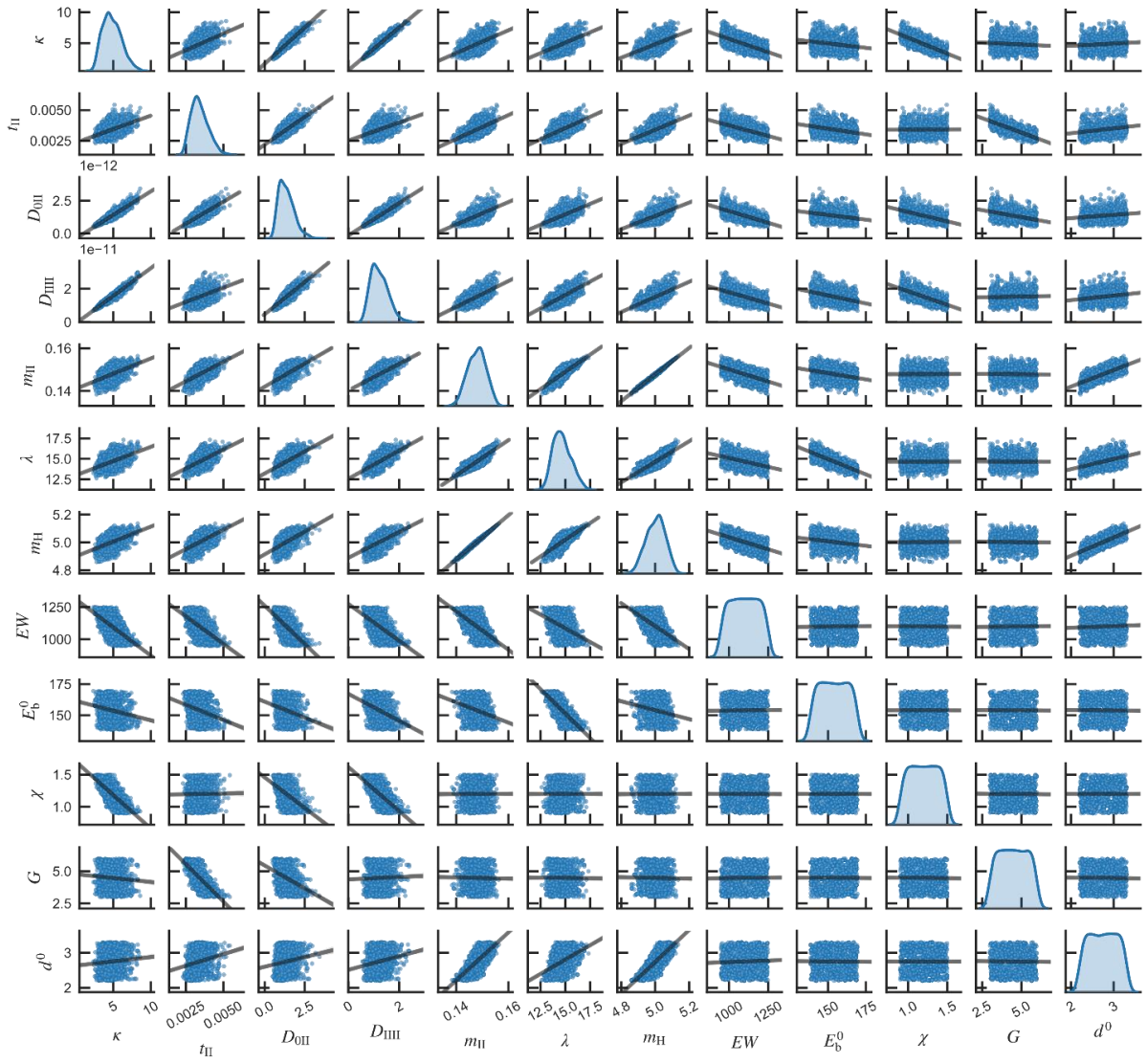

Figure 6-19. Pair plot of membrane structure-property properties sample-based sensitivity analysis. Diagonals show kernel density estimate of variable distribution. Points in off-diagonal plots are the calculated values of a specific sample. Lines show best-fit least-squares linear regression.

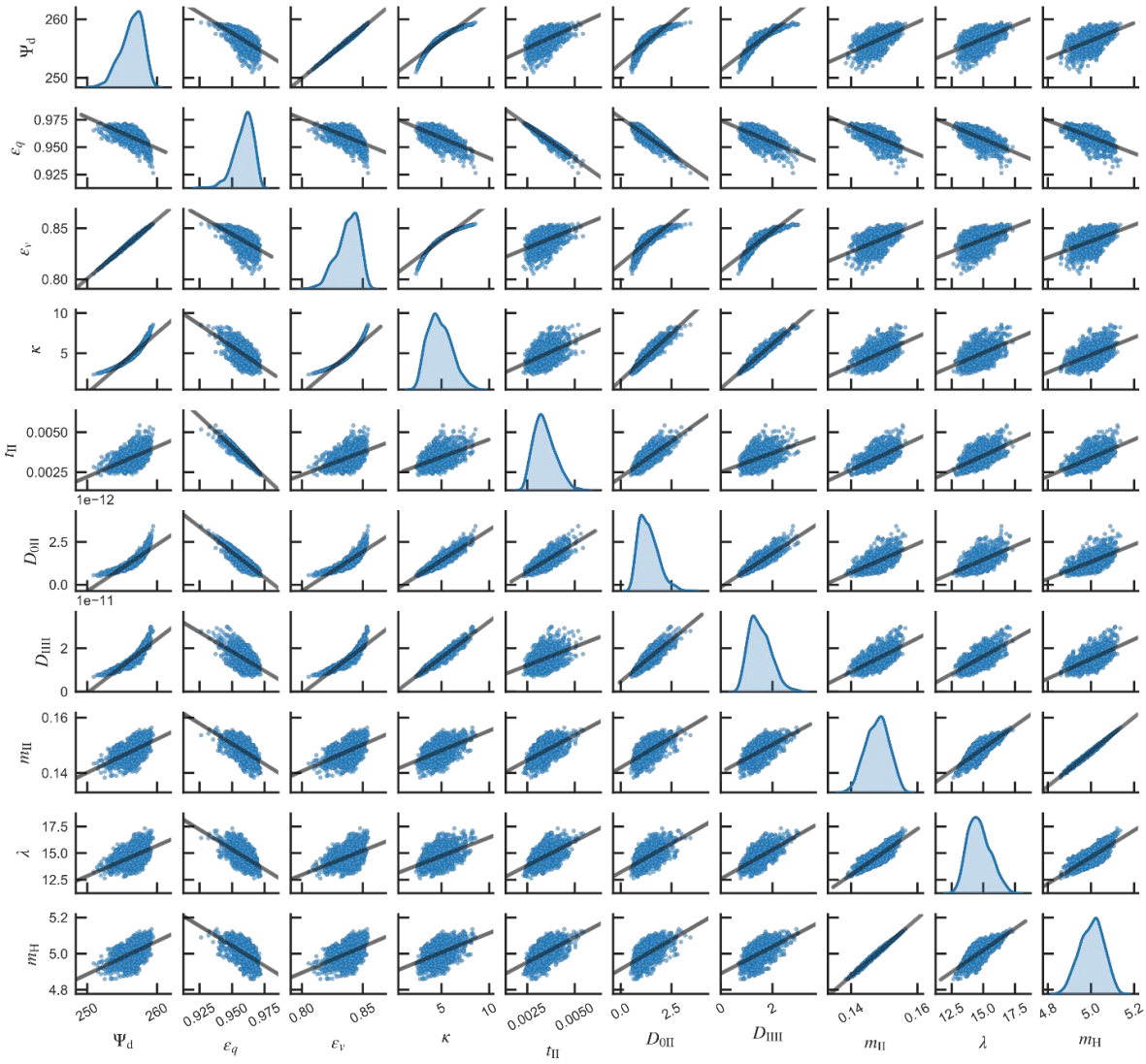

Figure 6-20. Pair plot of membrane function-performance properties sample-based sensitivity analysis. Diagonals show kernel density estimate of variable distribution. Points in off-diagonal plots are the calculated values of a specific sample. Lines show best-fit least-squares linear regression.

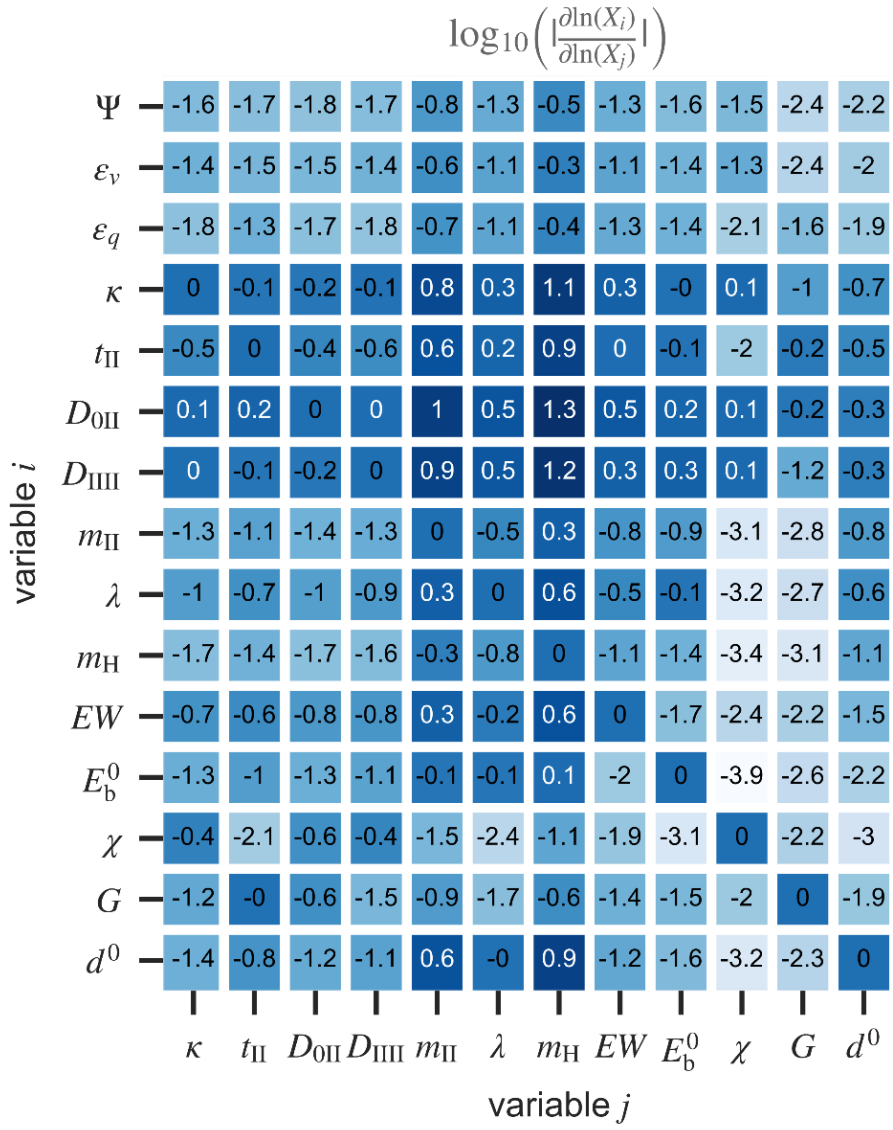

Figure 6-21. Heat map matrix of the $\log_{10}$-absolute value-effect coefficients obtained by linearly regressing the natural log of each structure-property-performance components against one another. Heatmap is colored from white (negative values) to blue (positive values). The coefficient represents the $\log_{10}$ of the fractional change in variable i given a fractional change to variable j.

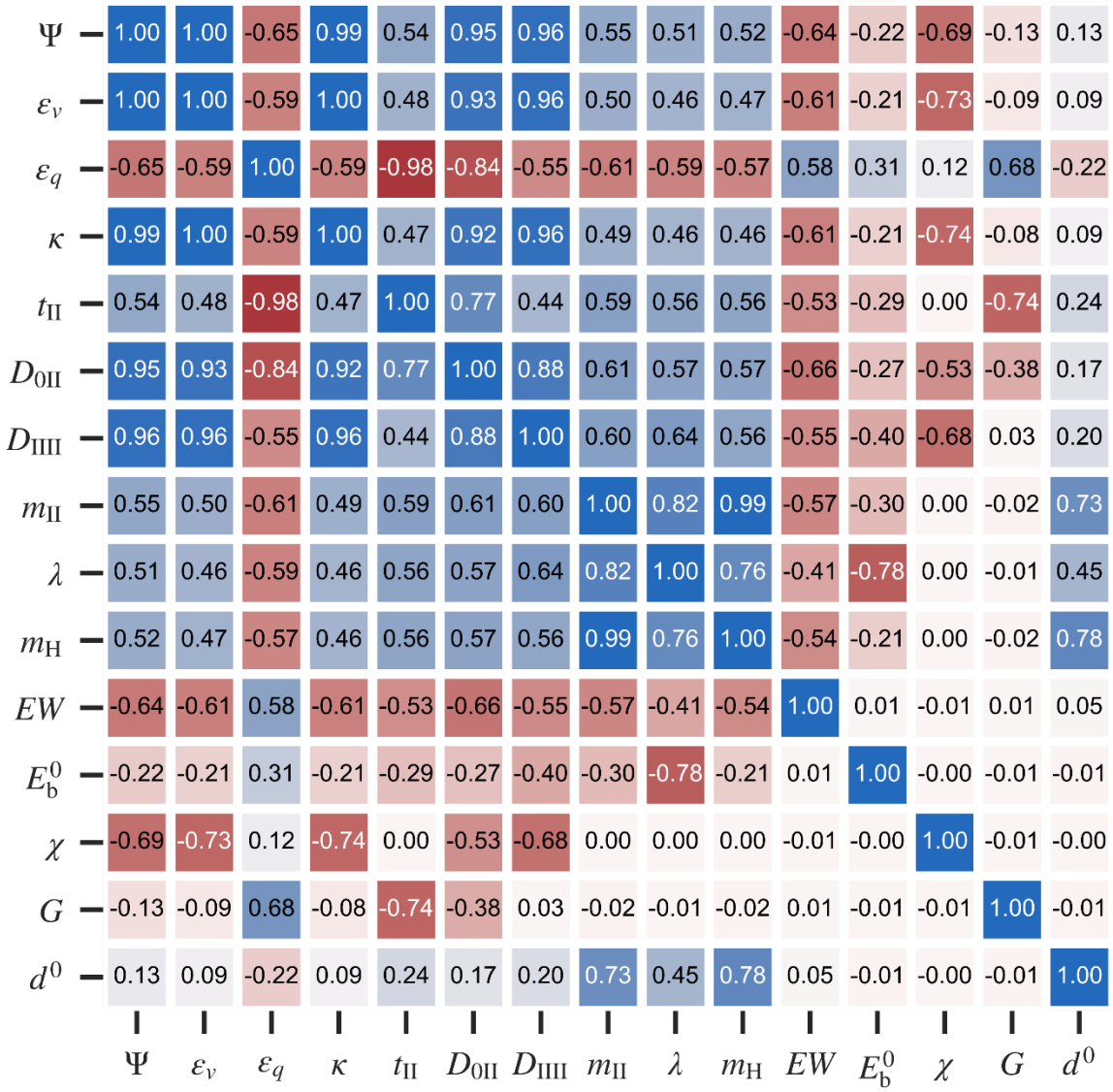

Figure 6-22. Heat map matrix of Spearman rank correlation coefficients between structure-property-performance components colored from red (negative values) to white (zero) to blue (positive values).

7 The Influence of Mesoscale Interactions on Proton, Water, and Electrokinetic Transport in Solvent-Filled Membranes: Theory and Simulations

7.1 Chapter Abstract

Transport of protons and water through water-filled, phase-separated cation-exchange membranes occurs through a network of connected hydrophilic water-filled channels. This paper uses simulations and theory to explore the role of this network (i.e. at the mesoscale) on water, proton, and electrokinetic transport, in perfluorinated sulfonic-acid (PFSA) membranes, pertinent to fuel cells. A concentrated-solution theory describes microscale transport. Network simulations model mesoscale effects and calculate macroscopic properties. An experimentally consistent 3D Voronoi network topology characterizes the interconnected channels in the membrane. Experimental water, proton, and electrokinetic transport properties validate calculations of macroscopic properties from network simulations and from effective medium theory. The results show that the hydrophilic channel size affects the different microscale transport modes dissimilarly, resulting in different distributions of microscale coefficients for different modes of transport. As a result, the network mediates transport of species non-uniformly. Dissimilar calculated tortuosities arise for water, proton, and electrokinetic transport coefficients (i.e. 4.7, 3.0 and 6.1, respectively, at a water content of 8 H_2O per polymer charge equivalent). The pathways that water travels across the membrane is different than those of protons. The distribution of transport properties across the network induces local electrokinetic flows that couple water and proton transport. Specifically, local electrokinetic transport induces water gradients that decrease macroscopic conductivity by up to a factor of 3. Macroscopic proton, water, and electrokinetic transport coefficients depend on the collective microscale transport properties of all modes of transport and their distribution across hydrophilic channels.

7.2 Introduction

Research of water-swollen phase-separated ion-exchange membranes often seeks physical bases for the measured values of transport properties, such as conductivity and water permeation, in terms of the molecular interactions among species.[12, 14-15, 18, 44, 64, 105, 240, 257, 288-291] To this end, a microscale description of transport in a single representative (e.g., average) water-filled domain accounting for molecular interactions to provides a transport property L^* (superscript * denotes a microscale property).[31, 37, 84, 257, 292-294] The transport property is upscaled to compare with measured macroscopic properties by considering (1) that L^* describes transport in a water-filled channel (i.e., an interstitial property), whereas the membrane as a whole contains a water volume fraction ϕ with the polymeric component of the membrane remaining inert to aqueous transport making its measured properties superficial, and (2) that transport occurs across a network of connected channels forming a meandering pathways characterized by a single tortuosity τ.[37] These two factors scale the microscale property L^* to a macroscopic, measurable property L according to[37, 295]

$$L = \frac{\phi}{\tau} L^*. \tag{7-1}$$

In principle, tortuosity characterizes the transport path length and depends on the topology of the material (i.e., how the various sized channels are connected) and, in particular, the distribution of channel transport properties.[37] Tortuosity quantifies how the lengthscales over which channels are connected and distributed (i.e., the mesoscale) influences macroscopic properties. It is, however, is not well recognized that tortuosity also varies with the particular transport property under consideration.[37] As a pedagogical example of the importance of property distribution, consider the tortuosity of a network consisting of two channels a and b connected in series with the same cross-sectional area and width with different transport properties L^{*a} and L^{*b} that is, as Appendix 7-A shows,

$$\tau = \frac{\phi L^*}{L} = \frac{1}{2} + \frac{(L^{*a})^2 + (L^{*b})^2}{4L^{*a}L^{*b}}. \tag{7-2}$$

The tortuosity is unity when the transport property of the segments are equal and $\tau > 1$ when transport properties are unequal.

In practice, τ is often an adjustable parameter.[37] Equation 7-1 is the so-called capillary model for transport and is widely used to understand transport in membranes and porous media.[37, 84, 240, 257, 289, 292-293, 295-296] Specifically, Chapters 3 and 5 invoke Equation 7-1 to upscale microscale properties to macroscopic transport coefficients. This work studies the application of the capillary model and the nature of τ and, consequently, the mesoscale in proton-exchange membranes in which proton and water transport occur simultaneously.

Phase-separated, water-filled proton-exchange membranes a challenge for the capillary model because the presence of water and a mobile cation gives rise to multiple modes of transport.[12, 18, 72, 257] Ion electrochemical-potential gradients, $\nabla\mu_+$, generate an ion flux, $\boldsymbol{N}_+$, (e.g., an electric field generates current). Likewise, water chemical-potential gradients, $\nabla\mu_0$, induce a water flux, $\boldsymbol{N}_0$, (i.e., water diffusion or permeation). Because the (electro)chemical potential depends on pressure, a pressure gradient also drives mass transport accordingly. Additionally, transport driving forces are coupled by electrokinetics such that ion electrochemical-potential gradients initiate a water flux (i.e., electroosmosis) and water chemical-potential gradients initiate an ion flux (i.e., streaming current). This paper explores how the capillary model represents these multiple modes of transport in proton-exchange membranes (see Table 6 in Ref [12]).

Transport in these systems is mathematically described by non-equilibrium thermodynamics of concentrated solutions. For our system with a cation, water, and a membrane (with fixed anionic charges) the governing flux equations are[78, 295, 297]

$$\boldsymbol{N}_+ = -L_{++}\nabla\mu_+ - L_{+0}\nabla\mu_0 \tag{7-3}$$

and

$$\boldsymbol{N}_0 = -L_{0+}\nabla\mu_+ - L_{00}\nabla\mu_0 \tag{7-4}$$

where μ_0 is the water chemical potential, μ_+ is the proton electrochemical potential, L_{00} is the transport coefficient relating a flux of water to its chemical potential gradient (proportional to water permeance), L_{++} is the transport coefficient relating a flux of cations to its electrochemical

potential gradient (proportional to ionic conductivity), and L_{+0} is the electrokinetic transport coefficient relating the flux of ions to a water chemical potential gradient[‡‡]. Onsager's reciprocal relationship dictates that $L_{+0} = L_{0+}$.[295]

In network of inter-connected channels, the presence of coupling between transport modes makes effective transport properties challenging to rationalize in terms of microscale properties and simple upscaling.[257] For example, in the case of two channels a and b connected in series with different conductive transport properties L_{++}^{*a} and L_{++}^{*b} with mean L_{++}^{*} but the same cross-sectional area, width, and water and electrokinetic transport coefficients L_{00}^{*} and L_{0+}^{*} respectively, the proton transport (i.e. conductive) tortuosity is, as Appendix 7-A shows,

$$\tau_{++} = \frac{\phi L_{++}^{*}}{L_{++}} = \frac{(L_{0+}^{*})^2 - L_{00}^{*} L_{++}^{*}}{(L_{0+}^{*})^2 - L_{00}^{*}\left(\frac{L_{++}^{*a} L_{++}^{*b}}{L_{++}^{*}}\right)} \qquad 7\text{-}5$$

As in the case of uncoupled transport (Equation 7-2), in coupled transport $\tau_{++} = 1$ if the transport channels have the same transport properties. However, in the coupled case, transport coefficients for water transport and electrokinetics influence the tortuosity of proton transport coefficient. This phenomena arises because the difference between L_{++}^{*a} and L_{++}^{*b} induces an electrokinetic water chemical-potential gradient that drives additional proton flux. Even if there is no net water chemical potential difference across both segments, there is a chemical potential difference across the individual segment. It is therefore impossible to describe completely the effective ionic transport coefficient of this system without accounting for the water transport and electrokinetic properties. For example, in the limiting case that the water transport coefficient is zero, $L_{00}^{*} = 0$, the tortuosity for proton transport is actually unity no matter the proton transport coefficients. This result is starkly different than when considering uncoupled transport (Equation 7-2). This simple toy model of two channel in series illustrates that coupling between water and ion transport mediates macroscopic transport properties at the mesoscale. The complexity of this phenomena increases when considering real systems that contain numerous connected channels with a heterogeneous size distribution.

Previous literature studies the effect of transport couplings in network structures transporting gas and electrokinetic phenomena in porous media.[97-98, 298] We explore this relationship in the context of water-filled, phase-separated, cation-exchange membranes, building on prior network simulations of this material.[48, 76, 143, 299] In particular, we study perfluorinated-sulfonic-acid (PFSA) membranes (such as Nafion) because they are an essential component of energy conversion applications and are widely characterized experimentally, allowing for model validation.[12]

PFSAs are nanophase separated with water-filled channels exhibiting sizes on the order of nanometers.[12, 18, 58] The hydrophilic channels of PFSA membranes contain water and cations with negatively charged sulfonate (SO_3^-) groups imbedded in the hydrophobic channel walls.[12, 18, 58] This study considers Nafion PFSA membranes exchanged with protons. The equivalent weight (EW) of the membrane is the average mass of polymer per sulfonate group. For the Nafion membrane in this study EW is 1020 (based on manufacture-reported titration and lower than the nominal 1100 in most literature).[12, 300] The water content of the membrane is quantified by λ, the

[‡‡] In some literature (see Chapter 5) the transport coefficient L_{ij} is written as $c_i c_j L_{ij}$. This formulation is convenient when relating to Stefan-Maxwell concentrated-solution formalism

molecules of water per sulfonate group and spans from ~0 when fully dried to ~22 when fully hydrated, with the water activity of the environment controlling the average hydration level of the material.[12] The sizes of the hydrophilic channels or "pores" is widely distributed.[12, 58, 99, 137] PFSA materials are dissimilar to classic porous media in that, in the dry state, the hydrophilic channels collapse and are not filled with gas or vapor.[12]

This paper is outlined as follows. First, we summarize a microscale model for transport coefficients L_{ij}^* of single water-filled channel of a PFSA membrane as a function of water content and channel size. Second, the microscale model parameterizes the mesoscale network simulations of PFSA membranes using realistic network topologies (represented by a 3D Voronoi tessellation) and channel-size distributions informed by structural characterization. Network nodes exhibit no transport resistance. Effective-medium theory rationalizes the findings of these simulations. The Network simulations and effective-medium theory calculate the macroscopic transport properties L_{ij}. Measured transport properties validate the model predictions. Finally, we examine the implications of our work and the nature of the capillary model and tortuosity in PFSA materials.

7.3 Microscale Transport Description

We calculate microscale transport properties L_{ij}^* by accounting for binary frictional interactions between cations, water, and the membrane using the Stefan-Maxwell formalism.[9, 31] As outlined in prior work,[31] in a cation-exchange membrane with polymer (denoted M), water (denoted 0), and a proton (denoted +), nonequilibrium thermodynamics dictates that the (electro)chemical potential gradient drives mass transport. According to Gibbs-Duhem, only two of these three electrochemical potential are independent.[9] In a Stefan-Maxwell form, this driving force is balanced by frictional drag interactions between species i and j and is proportional to their difference in species velocities, $\boldsymbol{v}_i^*$ and $\boldsymbol{v}_j^*$, multiplied by a friction coefficient K_{ij}^* [31, 78]

$$c_+^* \nabla \mu_+ = K_{+0}^* (\boldsymbol{v}_0^* - \boldsymbol{v}_+^*) + K_{+\mathrm{M}}^* (-\boldsymbol{v}_+^*) \qquad 7\text{-}6$$
$$c_0^* \nabla \mu_0 = K_{0+}^* (\boldsymbol{v}_+^* - \boldsymbol{v}_0^*) + K_{0\mathrm{M}}^* (-\boldsymbol{v}_0^*)$$

where c_i^* is the concentration of species i. A reference velocity must be specified because only 2 of the three velocities are independent.[31] There is no superscript $*$ on the (electro)chemical potentials because they are the same at the microscale and macroscale. The membrane provides the reference velocity, $\boldsymbol{v}_{\mathrm{M}}^* = 0$, because the membrane is typically fixed (relative to the laboratory frame of reference). Solving Equations 7-6 for $\boldsymbol{v}_0^*$ and $\boldsymbol{v}_+^*$ and noting that flux is proportional to the species velocity ($\boldsymbol{N}_i^* = c_i^* \boldsymbol{v}_i^*$) gives Equations 7-3 and 7-4. To specify K_{ij}^*, this work uses the microcontinuum model described previously,[31] with several modifications detailed in Appendix 7-B details; a brief summary included here.

We treat water/cation friction coefficients as equivalent to those of a bulk-aqueous-electrolyte at the same cation concentration. The short-range water-cation interactions justify the implicit assumption that the presence of the channel walls do not alter interactions between mobile species in solution. Proton/water friction in bulk solution exhibit a very low friction (high diffusion coefficient) at high water contents but a high friction coefficient (low diffusion coefficient) at low water contents (see Appendix 7-B).[8, 18, 85] The strong dependence on water content is due to a transition from protons transporting via hopping along hydrogen bond networks (i.e. Grotthuss

mechanisms) to a vehicular transport mechanism at low water contents as anions and bound water disrupt hydrogen bonding.[8, 18]

A classic electrokinetic treatment specifies the water/membrane and mobile cation/membrane friction coefficients.[31] Specifically, the Navier-Stokes equation describes an aqueous solution flowing through charged channels with no-slip boundary conditions.[9, 31] The linearized Poisson-Boltzmann equation specifies the distribution of cations throughout the channel.[9, 31] The solution to this system of equations specifies the interspecies friction coefficients as a function of membrane water content, λ, and channel size.

Chemical equilibrium specifies the fraction of cation immobilized due to desolvation and pairing with the fixed, anionic sulfonate groups as a function of water content. The ion-pariring equilibrium constant is adjusted such that the calculated fraction of cations paired with sulfonate groups agrees with molecular-dynamics simulations of PFSAs.[42]

In quantifying water/membrane and mobile cation/membrane friction, the hydrophilic PFSA domains are considered locally flat channels with sulfonates distributed along the domain/polymer interface.[58] For the flat-channel geometry, the local channel height H^* is a function of water content λ and the local channel interfacial area per sulfonate charges $A^*_{SO_3}$

$$H^* = \frac{\bar{V}_0 \lambda}{N_A A^*_{SO_3}} \qquad 7\text{-}7$$

where the volume of cations is negligible, $\bar{V}_0$ is the partial molar volume of water (approximated as equal to the molar volume of pure water), and N_A is Avogadro's number. For a channel with an average (mean) height, H^{ave}, fitting small-angle X-ray scattering (SAXS) to Equation 7-7 specifies the surface area per sulfonate group as $A^{ave}_{SO_3}$ (for Nafion, $A^{ave}_{SO_3}$ = 0.23 nm^2).[12] We consider the sulfonate groups arrayed on a square-lattice at the hydrophilic/hydrophobic domain interface, giving a spacing between sulfonate groups as $l^*_{SO_3} = \sqrt{A^*_{SO_3}}$. The distance between sulfonate groups of the average-height-domain is denoted $l^{ave}_{SO_3}$ (because the mean and square-root functions are not permutable, the mean of $l^*_{SO_3}$ is not equivalent to $l^{ave}_{SO_3}$).

Figure 7-1 shows calculated (a) microscale proton transport coefficient L^*_{++}, (b) electrokinetic transport coefficient L^*_{0+}, (c) and water transport coefficient L^*_{00}, as a function of water content λ and the ratio of channel height to average channel height H^*/H^{ave} (see Appendix 7-B). Up to moderate water contents ($\lambda \sim 10$), the proton transport coefficient L^*_{++} increases with water content as the cations solvate, encounter less hydrodynamic resistance with the channel walls, and increasingly transport via the hopping mechanism. At high water contents, increasing water content dilutes protons and reduces the cation transport coefficient.

For small, thin channels (small H^*/H^{ave}), increasing channel height decreases hydrodynamic resistance with the walls, thereby increasing the cation transport coefficient L^*_{++}. However, the dependence of L^*_{++} on H^* reverses for thick channels. At high H^*/H^{ave} , the cations are confined to the walls due to electrostatic attraction to the closely packed sulfonate groups. Increasing channel height further confines protons near to the walls, increasing hydrodynamic resistance and decreasing cation transport.

Hydrodynamic interactions with the channel walls govern electrokinetic transport coefficient L_{0+}^{*} and the water transport coefficient L_{00}^{*}. As water content and channel height increase, the electrokinetic and water transport coefficients increase monotonically.

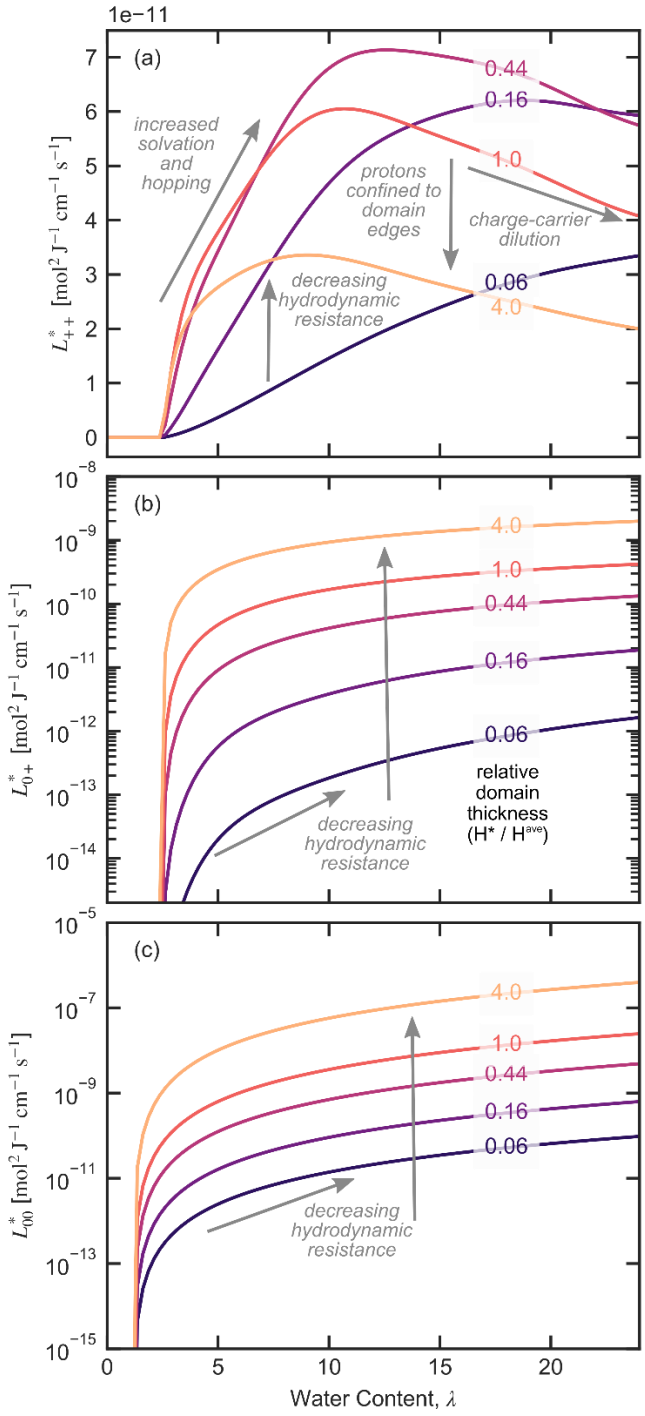

Figure 7-1. Microscale channel transport coefficients for cation transport L^*_{++} (a), electrokinetic transport L^*_{0+} (b) and water transport L^*_{00} (c) as a function of water content λ for different channel heights relative to the average height, H^*/H^{ave}. Appendix 7-B details the calculations.

7.4 Upscaling and Macroscopic Transport Description

An important finding from Figure 7-1 sis that the L_{ij}^{*} transport coefficients values have dependencies on different channel sizes at the same water content. As we show later, this finding leads to different tortuosities and different pathways for water and protons to traverse the membrane. The following subsections first discuss the distribution of channel heights in the membrane. Then, we outline Voronoi tessellation resistor-network simulations, where each segment is parameterized by the microscale model, to determine effective, macroscale transport properties. To overcome the reductionist limitations of simulations, an effective-medium theory rationalizes the results of the simulations.

7.4.1 Microscale Channel-Size Distribution

There is a wide range of channel heights in PFSA membranes[12, 58, 99, 137] and, consequently, from Figure 7-1, a distribution of transport properties. The thickest channels correspond to channels with sulfonate groups packed to their distance of closest approach on the top and bottom domain walls, $l_{\mathrm{SO_3}}^{*} = l_{\mathrm{SO_3}}^{\mathrm{DCA}}$. The distance of closest approach between sulfonate groups is 0.4 nm.[43] Because sulfonate groups are present on both the top and bottom walls of the domain, $l_{\mathrm{SO_3}}^{\mathrm{DCA}}$ is half this distance, or 0.2 nm. To calculate the channel-size distribution, we quantify the probability that a channel has a given spacing between sulfonate groups beyond the distance of closest approach $l_{\mathrm{SO_3}}^{*} - l_{\mathrm{SO_3}}^{\mathrm{DCA}}$ with[301]

$$PDF\left(l_{\mathrm{SO_3}}^{*} - l_{\mathrm{SO_3}}^{\mathrm{DCA}}\right) = \frac{1\ [\mathrm{m}]}{\left(l_{\mathrm{SO_3}}^{*} - l_{\mathrm{SO_3}}^{\mathrm{DCA}}\right)\sigma_{l_{SO_3}}\sqrt{2\pi}} \exp\left(-\frac{\left[\ln\left(l_{\mathrm{SO_3}}^{*} - l_{\mathrm{SO_3}}^{\mathrm{DCA}}\right) - \mu_{l_{SO_3}}\right]^2}{2{\sigma_{l_{SO_3}}}^2}\right) \quad 7\text{-}8$$

where PDF is a log-normal probability distribution function, $l_{\mathrm{SO_3}}^{*} - l_{\mathrm{SO_3}}^{\mathrm{DCA}}$ and $\sigma_{l_{SO_3}}$ and $\mu_{l_{SO_3}}$ are parameters of the distribution. Equations 7-7 and 7-8 and the microscale properties in Appendix 7-B provide the distribution of channel sizes and transport properties. These distributions parameterize the network simulations that are discussed in the next section. We fit the network simulations of macroscopic proton, water, and electrokinetic transport properties with measured values by adjusting $\sigma_{l_{SO_3}}$. The best-fit $\sigma_{l_{SO_3}}$ is 1.52 (dimensionless). Integration of the product of Equation 7-8 and $1/\left(l_{\mathrm{SO_3}}^{*}\right)^2$ specifies its mean, $1/A_{\mathrm{SO_3}}^{\mathrm{ave}}$, according to the Law of the Unconscious Statistician.[301] We numerically solve for $\mu_{l_{SO_3}}$ (= –21.36 m) using Brent's method[302] so that the mean of $1/\left(l_{\mathrm{SO_3}}^{*}\right)^2$ with Equation 7-8 is equal to the SAXS measurements of $1/A_{\mathrm{SO_3}}^{\mathrm{ave}}$.[12]

Figure 7-2a show the calculated PDF of channel height $PDF(H^{*})$ for $\lambda = 20$ using random variants of $l_{\mathrm{SO_3}}^{*}$ from Equation 7-8 and from calculation of height using Equation 7-7. The probability distribution extracted from transmission electron microscopy (TEM) of a hydrated Nafion film ($\lambda \sim 20$) provides comparison.[99, 137] The proposed model-fit distribution is wide and slowly decreases with increasing H^{*} whereas the distribution from TEM is more narrow and peaks around 0.75 nm.

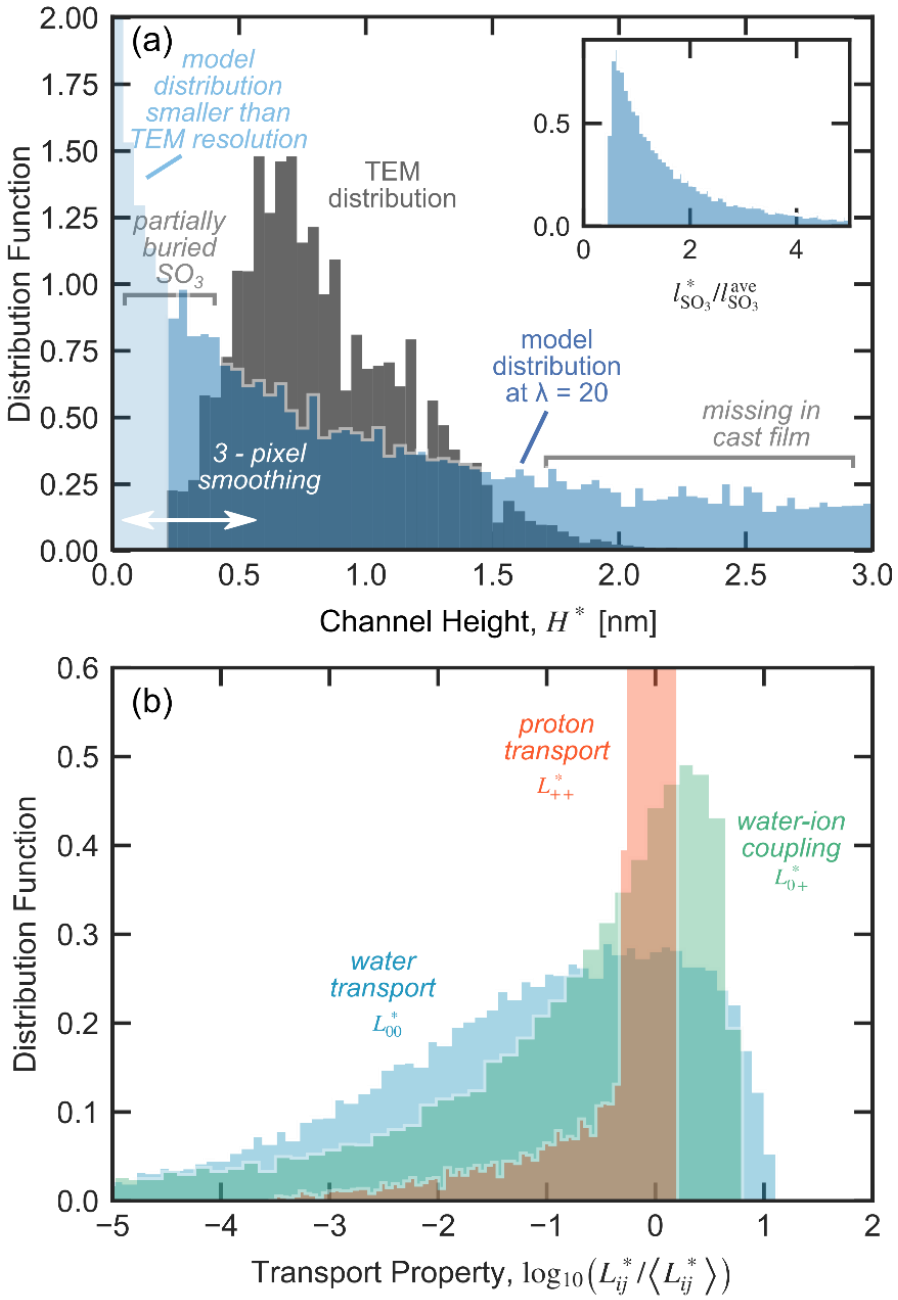

Figure 7-2. Probability distribution function of channel heights from (a) transmission electron microscopy[99, 137] and using 20,000 random variants of $l^*_{SO_3}$ sampled using Equation 7-8 and calculating channel height using Equation 7-7 each at $\lambda = 20$ (b) and the probability distribution of proton, water, and electrokinetic transport coefficients corresponding to the channel size distribution as Appendix 7-B details. Insert in (a) shows random variants of $l^*_{SO_3}$ normalized to $l^{ave}_{SO_3}$ sampled using Equation 7-8.

Three limitations of TEM analysis and sample preparation help rationalize the discrepancies between the model-fit and TEM distributions for small channels sizes. First, TEM does not capture very small channels because they are below the limit of detection of the image, which has a pixel size of 0.224 nm.[137] Second, to identify the interface between hydrophilic and hydrophobic channels and to reduce noise, a 3-pixel median filter was applied to the TEM image.[99] The de-noising process means that some small channels (up to 3-pixels across a dimension, or 0.672 nm) do not appear in the TEM distribution. These small channels consist of sulfonate groups that are partially buried in the hydrophobic matrix that allow only a small amount of water or ions to move through them.[303-304] Further, a wide distribution of $l^*_{SO_3}$ is consistent with the measured wide distribution of EWs for the same membrane chemistry[305] (see Figure 7-2a inset showing probability distribution function of $l^*_{SO_3}/l^{ave}_{SO_3}$ where the spacing between sulfonate groups scales with the EW of membrane in the channel). Finally, TEM required microtomed 100 nm thick cast-thin films whereas the model distribution is fit to experiments of bulk membranes that have undergone various pretreatment or processing conditions.[12, 137] As a result, the model distribution contains large channels that could have resulted from sample preparation that was not present in the TEM sample.

Figure 7-2b shows the probability distribution of the proton, water, and electrokinetic transport coefficients at $\lambda = 20$ calculated as Appendix 7-B details and shown in Figure 7-1. Water transport properties varies an order of magnitude with channel height whereas proton transport coefficient is relatively independent of channel height (Figure 7-1). As a result, the water and electrokinetic transport coefficients have a wide distribution whereas the proton transport coefficient distribution is narrow. Each transport property has a different distribution because they depend differently on channel size (see Figure 7-1).

7.4.2 Resistor-Network Simulations

A 3D network of connected channels simulates the effective transport properties. Segments of the network represent water-filled channels and zero-volume nodes represent connections between channels. We use a Voronoi tessellation to represent the topology of PFSA membranes. The tessellation edges representing water-filled domains. A Voronoi tessellation is a realistic representation of the PFSA microstructure, with a coordination number of 3 (average number of segments connected to a node) and with slit channels anisotropically oriented locally but, on average, isotropic.[12, 162] Appendix 7-C details network construction that gives n_S segments connecting n_N nodes distributed across a 3D cube of dimensions W.

The walls of each channel have a sulfonate spacing $l^*_{SO_3}$ sampled from the probability distribution in Equation 7-8, giving each channel a height at a specific water content (see Equation 7-7) with corresponding cation, water, and electrokinetic transport properties (see Appendix 7-B). Let $Q_i^{\alpha,\beta}$ be the net molar flow rate (mol/s) of water or cation into each node α from connecting node β. At steady state, the net (scalar) flow into or out of each non-boundary node α, from all connecting nodes β is zero, or

$$-\sum_{\beta} Q_i^{\alpha,\beta} = 0 \qquad 7\text{-}9$$

where the molar flow is the product of the interstitial molar flux and the cross-sectional area of the segment (i.e. product of channel height $H^{\alpha,\beta}$ and depth, $D^{\alpha,\beta}$),

$$Q_i^{\alpha,\beta} = N_i^{\alpha,\beta} H^{\alpha,\beta} D^{\alpha,\beta} \quad 7\text{-}10$$

The depth of each channel is set as the same and equal to D^{ave}.

The interstitial flux through a segment connecting nodes α from β, $N_i^{\alpha,\beta}$, obeys the flux Equations 7-3 and 7-4 written for each segment

$$N_+^{\alpha,\beta} = -L_{++}^{\alpha,\beta} \frac{\Delta^{\alpha,\beta}\mu_+}{W^{\alpha,\beta}} - L_{+0}^{\alpha,\beta} \frac{\Delta^{\alpha,\beta}\mu_0}{W^{\alpha,\beta}} \quad 7\text{-}11$$

and

$$N_0^{\alpha,\beta} = -L_{0+}^{\alpha,\beta} \frac{\Delta^{\alpha,\beta}\mu_+}{W^{\alpha,\beta}} - L_{00}^{\alpha,\beta} \frac{\Delta^{\alpha,\beta}\mu_0}{W^{\alpha,\beta}} \quad 7\text{-}12$$

where $L_{ij}^{\alpha,\beta}$ is the transport coefficient L_{ij}^* of the segment connecting α and β, $W^{\alpha,\beta}$ is the width of the channel normal to the direction of transport, and $\Delta^{\alpha,\beta}\mu_i$ is the drop of electrochemical potential of protons or chemical potential of water from node β to α, $\Delta^{\alpha,\beta}\mu_i = \mu_i^{\alpha} - \mu_i^{\beta}$. Equations 7-11 and 7-12 require a constant transport coefficient $L_{ij}^{\alpha,\beta}$ across the segment between α and β so that the (electro)chemical potential changes linearly. Application of a small (electro)chemical potential change across the network satisfies this requirement. This assumption is justified in that macroscopic gradients necessarily cause small microscale water content changes.

To specify the effective network transport coefficients (i.e., the macroscopic transport properties), the algorithm sets the (electro)chemical potential of the nodes on the left boundary ($x = 0$) as the zero reference (i.e, $\mu_i = 0$) for both species. On the right boundary nodes, a small potential drop relative to the left boundary, $\Delta^{\text{net}}\mu_i$ is set for both species in turn. As Appendix 7-D details, solving Equation 7-9 for each internal node (i.e. non-boundary node) with Equations 7-11 and 7-12 for each segment specifies the water and cation flow through the nodes and segments. We treat the water content as constant across the membrane, corresponding to a small $\Delta^{\text{net}}\mu_i$. Therefore, L_{ij}^* is independent of $\Delta^{\text{net}}\mu_i$ and Q_i^* is linear with $\Delta^{\text{net}}\mu_i$.

Figure 7-3 shows calculated flows of proton (a)-(c) and water (d)-(f) under a proton electrochemical potential difference across the network and water flow (g)-(i) with a water chemical potential drop. Each line is a network channel with its thickness scaled proportionally with its height. The circle sizes scale proportionally to the species flow through the channel (see Equation 7-10). (a), (d), and (g) shows flows at low hydration, (b), (e), and (h) are at moderate hydration, and (g), (f), and (i) show fluxes high hydration. To make qualitative inferences possible, visualizations in Figure 7-3 are in 2D, whereas network simulations are 3D for reporting quantitative properties.

Figure 7-3 demonstrates that flows increase with increasing water content for the same $\Delta^{\text{net}}\mu_i$ as the channels expand and transport properties generally increase. However, different modes of transport take considerably different pathways across the membrane. Due to the narrow distribution of proton transport properties (see Figure 7-2), protons transport across most segments. In contrast to proton transport, water and electrokinetic transport properties are widely distributed giving a strong preference for some pathways over others, as Figure 7-3i reveals.

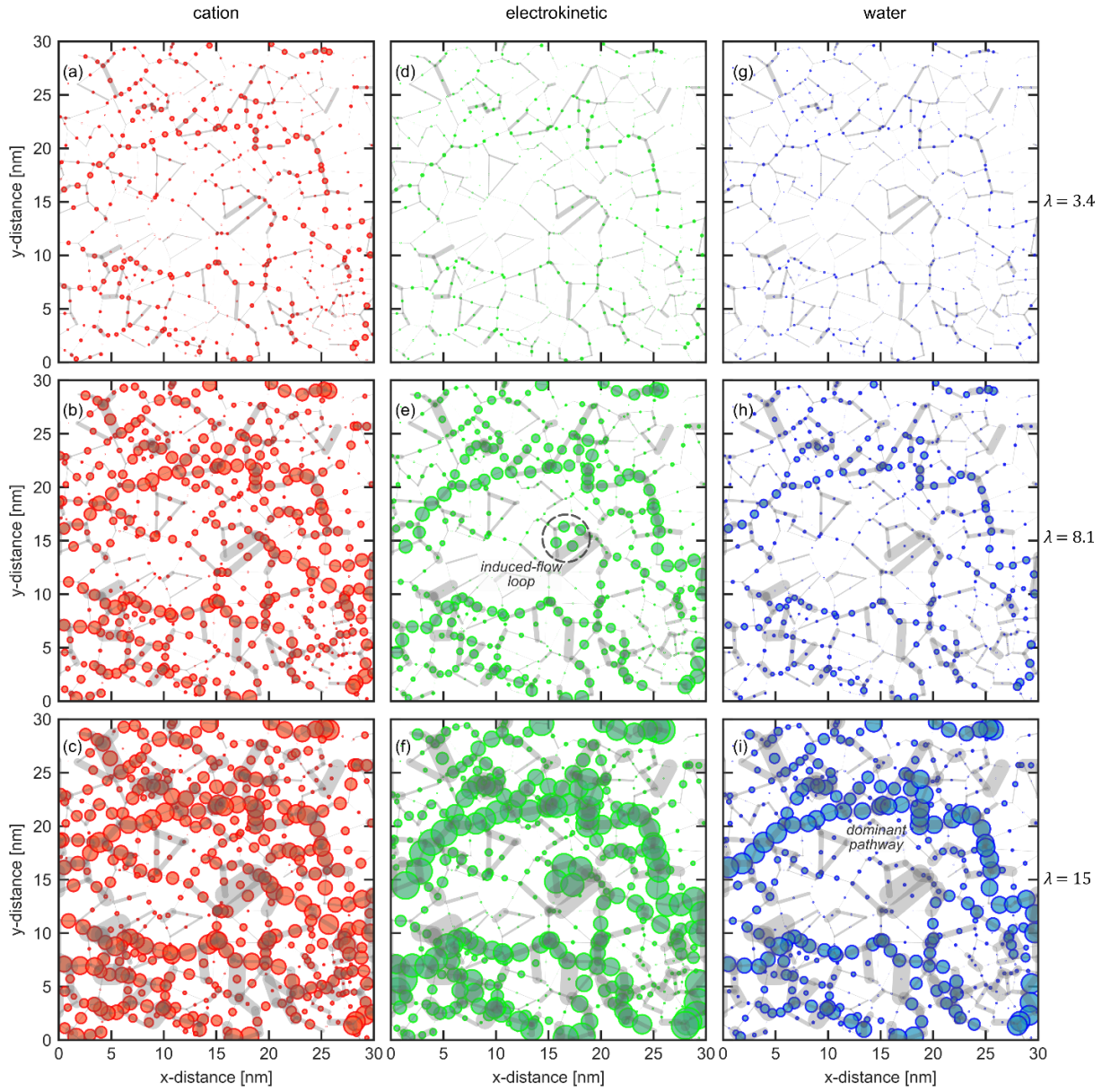

Figure 7-3. Network simulation flows of cations (a)-(c) and water (d)-(f) under a cation electrochemical potential difference and (g)-(i) with a water chemical potential drop. Lines are network channels scaled proportionally with the channel height. Circle area is scaled proportional to species flow. (a), (d), and (g) show flows at a $\lambda = 3.4$, (b), (e), and (h) are at $\lambda = 8.1$, and (g), (f), and (i) show fluxes $\lambda = 15$. Note the induced-flow loop (e).

All else being equal, species transport pathways favor channels with large heights. As Figure 7-3 shows, however, this criterion is insufficient to predict high flows through a domain. Transport through a channel also depends on the (electro)chemical potential drop across it that, in turn, is a function of the collective transport properties of nearby channels. The distribution of transport properties induces local (electro)chemical potential gradients. The figure in Appendix 7-D shows

calculated proton electrochemical potential (a) and water chemical potential (b) of each node under a proton electrochemical potential difference across the network (using Equation 7-34 in Appendix 7-D) as a function of position at $\lambda = 15$. The proton electrochemical-potential declines across the network, but does not decrease uniformly between the left and right sides of the network. Even with no macroscopic water chemical-potential drop (i.e., $\Delta^{\text{net}}\mu_0 = 0$), the distribution of transport properties generates local water chemical-potential gradients. Local gradients induce electrokinetic flow loops that pump flow in circles, as Figure 7-3e notes, and which have been observed in saturated porous media under electric fields.[97]

To understand how mesoscale flows dictate macroscopic properties, we sum the flows passing through the network and normalize by the total cross-sectional area of the network (including both hydrophilic and hydrophobic phase-separated area) to specify the macroscopic (superficial) fluxes in the network of species i, N_i^{net} (see Appendix 7-D for details). Network fluxes, width of the network W^{net}, and applied potential govern the macroscopic effective network transport coefficients. When $\Delta^{\text{net}}\mu_0 = 0$ we have that

$$L_{++}^{\text{net}} = -N_+^{\text{net}} \frac{W^{\text{net}}}{\Delta^{\text{net}}\mu_+} \tag{7-13}$$

and

$$L_{0+}^{\text{net}} = -N_0^{\text{net}} \frac{W^{\text{net}}}{\Delta^{\text{net}}\mu_+} \tag{7-14}$$

and when $\Delta^{\text{net}}\mu_+ = 0$ we recover

$$L_{00}^{\text{net}} = -N_0^{\text{net}} \frac{W^{\text{net}}}{\Delta^{\text{net}}\mu_0} \tag{7-15}$$

Network simulations obey Onsager's reciprocal relation such that $L_{0+} = L_{+0}$.

Transport properties L_{ij} are rarely measured directly experimentally.[78] Rather, experiments characterize slightly different sets of transport properties that are measurable under well-defined conditions. Under an applied electric field with constant water chemical potential, the conductivity κ and electroosmotic coefficient ξ characterize ion and water transport, respectively.[78] The water transport coefficient α characterizes water transport across a membrane due to a water chemical-potential gradient in the absence of current.[§§] These transport coefficients relate to the L_{ij} coefficients according to[78]

[§§] The properties are defined $\kappa = -i(W/\Delta\Phi)$ and $\xi = N_0/Fi$ for $\Delta\mu_0 = 0$, and $\alpha = -N_0(W/\Delta\mu_0)$ for $i = 0$, where i is the current density across the membrane (scalar), $\Delta\Phi$ is the applied electric potential drop across the membrane of width W, and $\Delta\mu_0$ is the water chemical-potential drop across the membrane.

$$\kappa = L_{++}F^2 \qquad 7\text{-}16$$

$$\xi = \frac{L_{0+}}{L_{++}}$$

$$\alpha = L_{00} - \frac{L_{0+}^2}{L_{++}}$$

We followed Weber and Newman[23] to convert water-tracer diffusion coefficients measurements (i.e. from pulse-field-gradient nuclear magnetic resonance) to α and the procedure by Delacourt and Newman[32] to convert water permeance measurements to α.

Figure 7-4 shows network-calculated transport properties (dashed line) and measured transport properties (symbols) of macroscopic (a) conductivity κ [53-54, 306-314], (b) electroosmotic coefficient ξ [310, 315-319], and (c) water transport coefficient α [44, 68, 312, 320-324] as a function of water content λ. Calculations are the average of 5 randomly seeded network simulations with 80-nm characteristic system sizes and using Equations 7-13 through 7-16 to obtain the transport coefficients. As a previous section details (Microscale Channel-Size Distribution), we adjusted the sulfonate spacing distribution parameter σ_{SO_3} to fit these data sets.

The Voronoi network simulations agree with experiments for all transport properties up to high water contents ($\lambda \sim 17$). The under-prediction of conductivity for high water contents is likely to our treatment of electrostatic interactions between the proton and the sulfonate groups that pushes the cation towards to the domain walls. Including the forces on protons from cation solvation restores protons towards the center of the channels, increasing conductivity at high water contents.

7.4.3 Comparison to Effective Medium Theory

Simulations, like experiments, demonstrates what occurs (given a set of rules) in a systems, but do not directly provide a theory that describes the system. For PFSA membranes, network simulations reveal that protons and water take different pathways across the membrane and that the distribution of channel transport coefficients induce local (electro)chemical-potential gradients. Effective medium theory (EMT) models the network simulations observations.[101] EMT, developed by Kirkpatrick, calculates effective transport coefficients of transport networks.[101] The theory considers a single segment with transport property L_{ij}^* interacting with an "effective medium" network with each segment having a transport property L_{ij}^{EMT}. For a network entirely consisting of segments with transport properties L_{ij}^{EMT}, an external field (i.e., an (electro)chemical potential gradient) causes a uniform (electro)chemical potential drop between cross sections of the network normal to the direction of transport. The presence of L_{ij}^* causes an additional local field that decays over a large region of the network. For L_{ij}^{EMT} to represent accurately an actual network containing a distribution of segments with different transport properties L_{ij}^*, EMT requires that the internal fields induced by the presence of each segment sum to zero.

We adapt the method of Bonilla and Bhatia for multicomponent EMT, as detailed in Appendix 7-E.[100] EMT accounts for the local proton electrochemical-potential gradient caused by variations of L_{++}^* and the local water chemical-potential gradient induced by variations of L_{00}^*. Multicomponent

EMT also incorporates how electrokinetic coupling between water and proton transport link variations of L_{+0}^{*} and L_{00}^{*} to induced local proton electrochemical-potential gradients.

The solid lines in Figure 7-4 show conductivity (a), electroosmotic coefficient (b), and water transport coefficient (c) calculated using EMT Equation 7-39 in Appendix 7-E). EMT shows agreement with network simulations. The success of multicomponent EMT in this case suggests a useful upscaling method for others microscale theories of membrane transport without requiring computationally intensive network simulations. However, EMT complements but does not replace network simulations.

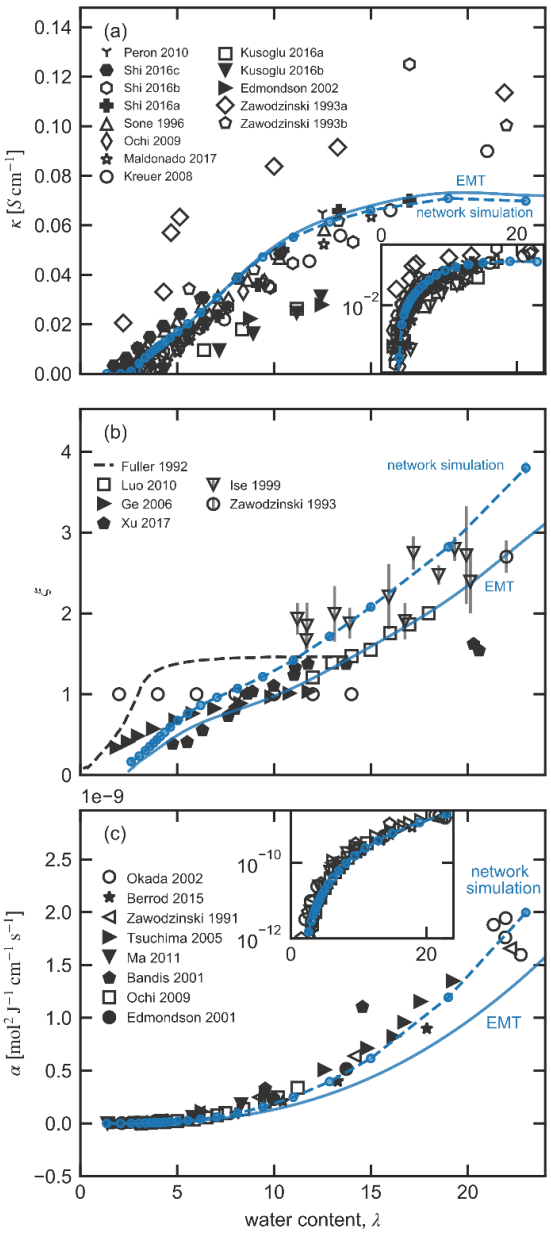

Figure 7-4. Experimental (symbols) and calculated (lines) (a) macroscopic conductivity κ (data from Refs [53-54, 306-314]), (b) electroosmotic coefficient ξ (data from Refs [310, 315-319]), and (c) water transport coefficient α (data from Refs [44, 68, 312, 320-324]) calculated by averaging five randomly seeded network simulations of an 80-nm dimension system and Equations 7-13 through 7-16 (dashed lines) and effective medium theory, Equation 7-39 (solid lines) and measured coefficient from literature (symbols) as a function of water content λ for systems at temperatures between 22-30°C. Inserts show same plot on a $\log_{10}$ y-axis scale. Open symbols are from datasets characterizing pretreated membranes and filled symbols are from datasets of membranes without pretreatments.

7.5 Effect of the Mesoscale on Transport

To quantify the impact the mesoscale has on transport, we compute a tortuosity. According to Equation 7-1, tortuosity is the ratio the effective macroscopic properties from the network simulations (see Figure 7-4) to the microscale transport properties of a representative channel with an average height H^{ave} (see Figure 7-1). Figure 7-5a shows the tortuosity τ_{ij} of transport coefficient L_{ij} as a function of water content. The tortuosity of each transport property is strikingly different. The tortuosity of proton transport decreases with water content, the tortuosity of water transport is constant for different water contents, and the tortuosity of electrokinetic transport increases with water content. For $\lambda > 3$, the tortuosity of proton transport is smallest, then water transport, and it is largest for electrokinetic transport. The network visualization in Figure 7-3 corroborates this result: proton flux become more homogenous with increasing water content, whereas electrokinetic fluxes are more widely distributed at higher hydrations.

To understand the role of electrokinetic coupling on tortuosity, dashed lines in Figure 7-5a show the tortuosity of water and cation transport predicted from the network simulations with no electrokinetic coupling, i.e., $L_{0+}^{*} = 0$. When electrokinetic coupling is removed, local water gradients induced by variations in proton transport properties increase the path length of protons transport through the membrane via electrokinetic coupling. Upon setting $L_{00}^{*} = 0$, simulations calculate an even lower proton-transport tortuosity, as the dot-dashed line in Figure 7-5a shows. The results demonstrate that macroscopic transport coefficients are partially a function of the collective microscale cation, water, and electrokinetic transport properties and their distributions.

Figure 7-5a and Figure 7-3 both show that the tortuosity, a crude measure of the mesoscale length of transport pathways, is different for each mode of transport. To quantify the overlap between transport pathways of different transport modes, we calculate the correlation coefficient between water, proton, and electrokinetic flows through domain segments that the network simulations calculate.[301] A correlation coefficient of 1 corresponds to a complete positive linear correlation between flows of different transport modes (i.e, transport takes place in the same network segments) and the coefficient has a value of 0 if there is no linear correlation between fluxes of different transport modes. Figure 7-5b plots the correlation coefficient of proton/water fluxes, proton/electrokinetic fluxes, and water/electrokinetic fluxes as a function of water content. The correlation coefficients quantifies what Figure 7-3 shows qualitatively, namely, water and electrokinetic flow transport through similar channels, but these channels are rather different from those used for proton transport. These results are, again, the result of different transport-property distributions influencing pathways.

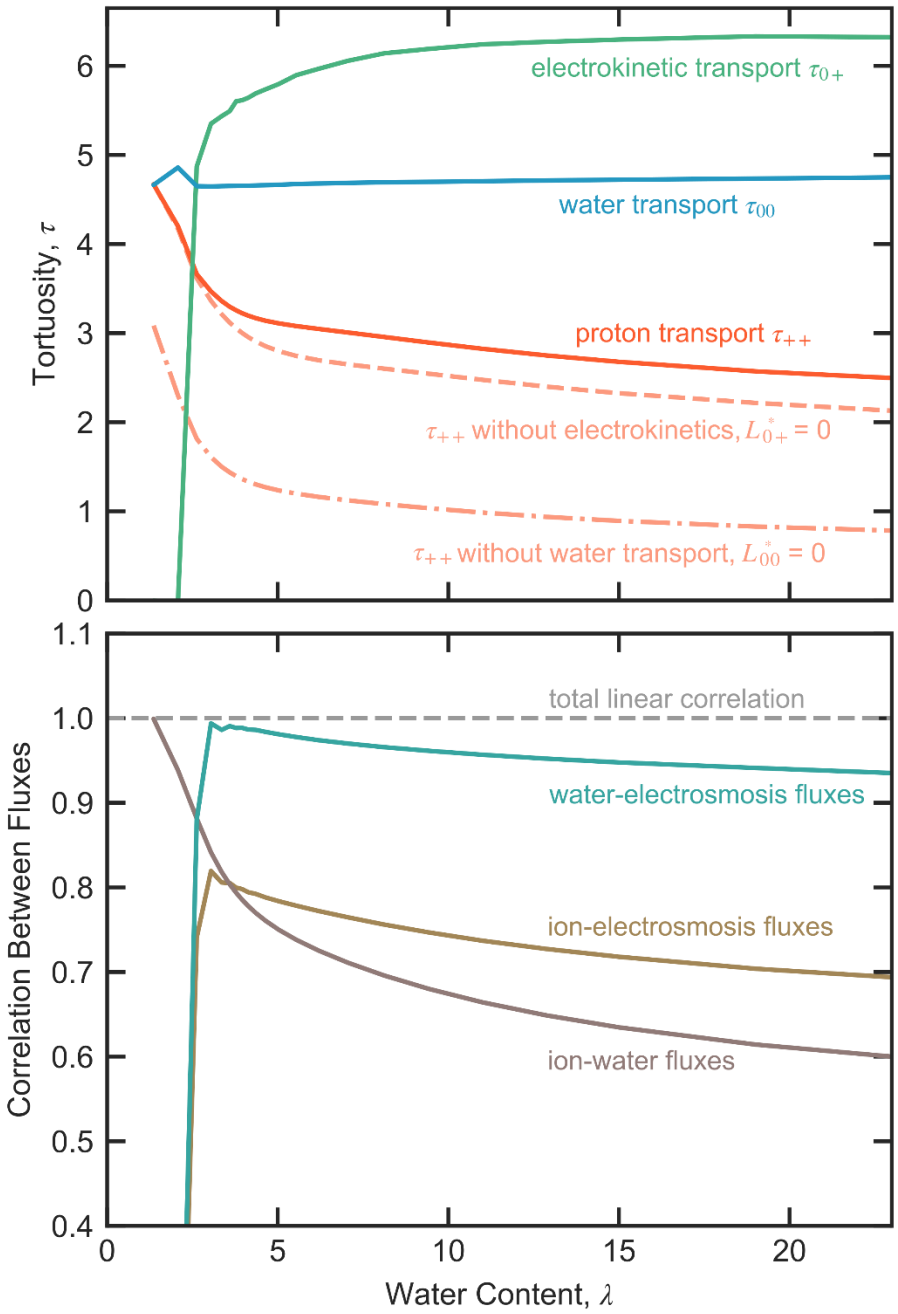

Figure 7-5. Tortuosity from network simulations at 80 nm and microscale theory (a) using Equation 7-1 for proton τ_{++}, water τ_{00}, and electro kinetic τ_{0+} transport coefficients and (b) correlation coefficient between ion/water, ion/electrokinetic, and water/electrokinetic flows through segments in the 80 nm network simulations as a function of water content, λ. Dashed and dot-dashed lines in (a) show simulated network proton tortuosity, τ_{++}, for $L_{0+}^{*} = 0$ and $L_{0+}^{*} = 0$, respectively.

In explanation of these simulation results, EMT predicts that "local" (electro)chemical potential gradients develop due to the distribution of segment transport properties (see Figure 7-3). These local gradients influence these transport pathways and, in turn, the macroscopic transport coefficients. EMT does not quantify the distance over which these gradients are important. To quantify this length scale, Figure 7-6 plots effective transport properties predicted from network simulation L_{++}^{net} (circles), L_{0+}^{net} (triangles), and L_{00}^{net} (squares) as a function of the characteristic dimensions network size at $\lambda = 8.1$. Each point results from a network simulation with a different seeds (i.e. different Voronoi tessellations and different random samplings of the segment sulfonate spacing from Equation 7-8). All transport properties are normalized to those simulated with 80-nm networks. Lines provide the corresponding multicomponent EMT-calculated transport properties (from Equation 7-39 in Appendix 7-E). All system sizes are periodic in planes perpendicular to transport.

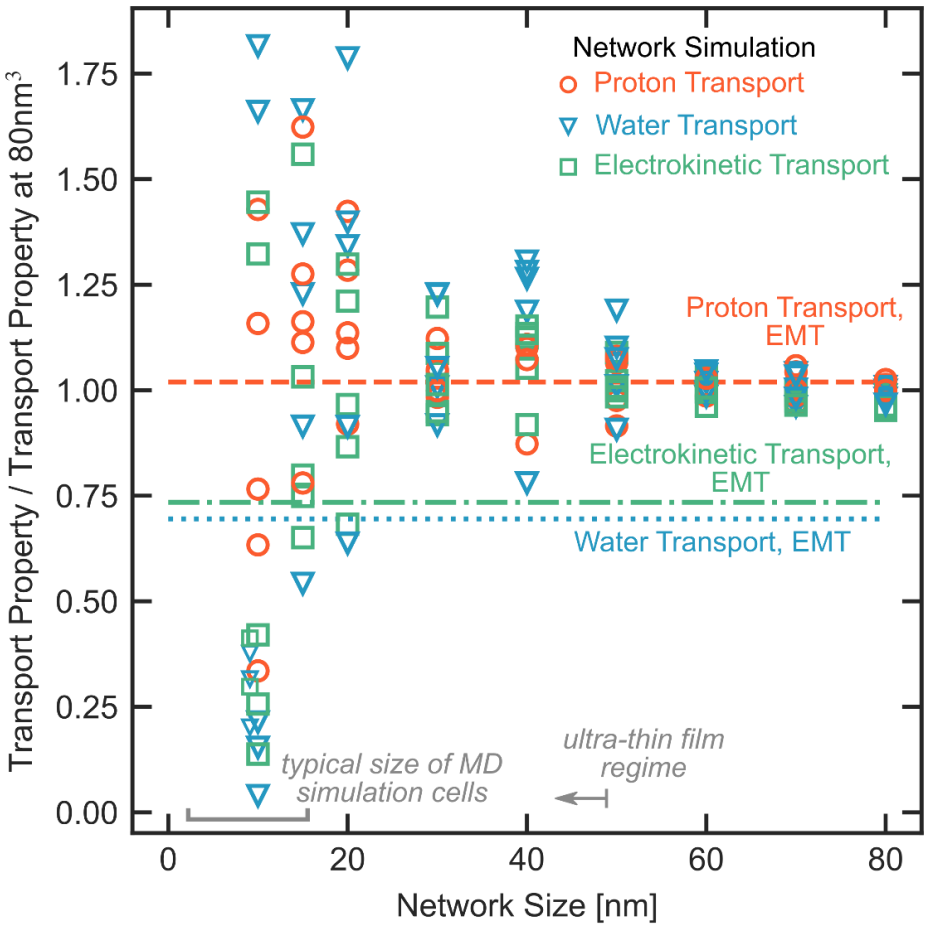

Figure 7-6. Network simulated transport coefficients L_{++}^{net} (circles), L_{0+}^{net} (triangles), and L_{00}^{net} (squares) as a function of the network dimension at $\lambda = 8.1$. Each point represents result of a random seeding. Transport properties are normalized to those simulated with 80-nm network. Lines provide the corresponding EMT-calculated transport properties normalized to network normalized to network simulation at 80 nm.

For small system sizes, different network instantiations predict drastically different transport properties. Properties with a wider distribution of microscale transport properties (water and electrokinetic transport) vary more between different networks configurations of the same network size. The representative volume element (the network size above which properties do not change and is, therefore, large enough to behave as a macroscopic system) has a characteristic dimensions greater than 60 nm. Variations in channel transport coefficients, L_{ij}^{*}, create local gradients on this scale.

This representative volume is much larger than the size most molecular simulations can achieve given the computation cost of simulating large systems (< 10 nm dimension cubes).[40, 43, 325] This limitation could explain some of the difference between properties simulated with molecular dynamics and experiments. Moreover, this representative volume corresponds to the size below which PFSA thin-films experimentally exhibit anomalous transport properties relative to the bulk system. Previous literature attributes this behavior to confinement of the polymer to length scale of its persistence length. The results in Figure 7-6 show that these experiments also take place on the same length scale as locally induced transport gradients.

7.6 Summary

This paper explores the nature of mesoscale transport in PFSA membranes including the role of electrokinetic coupling. We use a microscale concentrated-solution theory to calculate water, proton, and electrokinetic transport properties of water-filled hydrophilic channels in PFSA membranes as a function of channel height and water content. The microscale model parameterizes resistor network simulations that ascertain macroscopic transport coefficients. Effective medium theory provides a framework to understand the simulation results.

Using this methodology, we show that channel size impacts microscale properties of proton, water, and electrokinetic transport. Because there is a distribution of water-filled channel sizes in PFSA membranes, the corresponding distribution of microscale transport properties is different for each mode of transport. Consequently, the transport pathways that water and protons take through the membrane are different. Moreover, the distribution of properties induces local gradients of water chemical potential (and proton electrochemical potential) that act on proton (and water) transport through electrokinetic coupling. As a result, mesoscale effects, as characterized by the transport coefficient tortuosity, leads to starkly different behavior for different modes of transport. These effects are relatively long-range and can create system size-dependent behavior for experiments and simulations probing this length scale.

7.7 Appendix 7-A

The superficial flux of a species N^{*} across a transport segment is proportional to the chemical-potential drop across the segment $\Delta^{*}\mu$ – absent additional driving forces (e.g. no electrokinetic coupling) and the transport coefficient of the segment L^{*}, and inversely proportional to the width of the segment, W^{*}

$$N^{*} = -L^{*}\frac{\Delta^{*}\mu}{W^{*}} \qquad 7\text{-}17$$

The fluxes through two segments connected in series with the same area are equal. Segment a, connecting node α to node β, and segment b, connecting node β with node δ, each have width W^* and transport coefficients L^{*a} and L^{*b}, respectively. The superficial flux through the network N^{net} is

$$N^{\text{net}} = -L^{\text{net}}\frac{\left(\mu^{\delta} - \mu^{\alpha}\right)}{2W^*} = -\phi L^{*a}\frac{\left(\mu^{\beta} - \mu^{\alpha}\right)}{2W^*} = -\phi L^{*b}\frac{\left(\mu^{\delta} - \mu^{\beta}\right)}{2W^*} \tag{7-18}$$

where L^{net} is the effective transport property of the network, and μ^{α} is the chemical potential at node α. The conductive volume fraction (e.g., water volume fraction), ϕ, relates the interstitial microscale flux N^* to the superficial network flux N^{net}. Solving Equations 7-18 for L^{net} and eliminating the variable μ^{β} gives an expression for the transport property of resistors in series

$$\frac{1}{L^{\text{net}}} = \frac{1}{2\phi}\left(\frac{1}{L^{*a}} + \frac{1}{L^{*b}}\right) \tag{7-19}$$

Setting the representative microscale transport property L^* as the mean of L^{*a} and L^{*b}, the tortuosity τ, defined in Equation 7-1, is given by Equation 7-2.

For the case of coupled transport of water and protons (Equations 7-3 and 7-4), the superficial fluxes of each species through two segments in series (with equal cross-sectional area and width) are equal. The network flux of cations is related to the (electro)chemical potential drop of each species across the entire network and effective, network transport coefficients. The network flux of cations is also equal to the superficial flux through each segment,

$$\begin{aligned} N_{+}^{\text{net}} &= -L_{++}^{\text{net}}\frac{\left(\mu_{+}^{\delta} - \mu_{+}^{\alpha}\right)}{2W^*} - L_{+0}^{\text{net}}\frac{\left(\mu_{0}^{\delta} - \mu_{0}^{\alpha}\right)}{2W^*} \\ &= -\phi L_{++}^{*a}\frac{\left(\mu_{+}^{\beta} - \mu_{+}^{\alpha}\right)}{W^*} - \phi L_{+0}^{*}\frac{\left(\mu_{0}^{\beta} - \mu_{0}^{\alpha}\right)}{W^*} = \\ &= -\phi L_{++}^{*b}\frac{\left(\mu_{+}^{\delta} - \mu_{+}^{\beta}\right)}{W^*} - \phi L_{+0}^{*}\frac{\left(\mu_{0}^{\delta} - \mu_{0}^{\beta}\right)}{W^*} \end{aligned} \tag{7-20}$$

Similarly, for water flux,

$$\begin{aligned} N_{0}^{\text{net}} &= -L_{0+}^{\text{net}}\frac{\left(\mu_{+}^{\delta} - \mu_{+}^{\alpha}\right)}{2W^*} - L_{00}^{\text{net}}\frac{\left(\mu_{0}^{\delta} - \mu_{0}^{\alpha}\right)}{2W^*} \\ &= -\phi L_{0+}^{*}\frac{\left(\mu_{+}^{\beta} - \mu_{+}^{\alpha}\right)}{W^*} - \phi L_{00}^{*}\frac{\left(\mu_{0}^{\beta} - \mu_{0}^{\alpha}\right)}{W^*} = \\ &= -\phi L_{0+}^{*}\frac{\left(\mu_{+}^{\delta} - \mu_{+}^{\beta}\right)}{W^*} - \phi L_{00}^{*}\frac{\left(\mu_{0}^{\delta} - \mu_{0}^{\beta}\right)}{W^*} \end{aligned} \tag{7-21}$$

For the example in the introduction, the electrokinetic and water transport properties, L_{0+}^{*} and L_{00}^{*}, are the same in both segments. Solving Equations 7-20 and 7-21 for L_{++}^{net}, gives

$$L_{++}^{\text{net}} = \phi\frac{(L_{0+}^{*})^2 L_{++}^{*} - L_{00}^{*}L_{++}^{*a}L_{++}^{*b}}{(L_{0+}^{*})^2 - L_{00}^{*}L_{++}^{*}} \tag{7-22}$$

where L_{++}^* is the mean of L_{++}^{*a} and L_{++}^{*b}, $L_{++}^* = (L_{++}^{*a} + L_{++}^{*b})/2$. Using a representative microscale transport property, L_{++}^*, and following the definition of tortuosity gives τ_{++} in Equation 7-5.

7.8 Appendix 7-B

The L_{ij} coefficients are algebraic functions of the friction coefficients,[31, 78]

$$L_{00}^* = -(c_0^*)^2 \frac{K_{0+}^* + K_{+\mathrm{M}}^*}{K_{0\mathrm{M}}^* K_{+\mathrm{M}}^* + K_{0+}^*(K_{0\mathrm{M}}^* + K_{+\mathrm{M}}^*)} \qquad 7\text{-}23$$

$$L_{0+}^* = -c_0^* c_+^* \frac{K_{0+}^*}{K_{0\mathrm{M}}^* K_{+\mathrm{M}}^* + K_{0+}^*(K_{0\mathrm{M}}^* + K_{+\mathrm{M}}^*)}$$

$$L_{++}^* = -(c_+^*)^2 \frac{K_{0+}^* + K_{0\mathrm{M}}^*}{K_{0\mathrm{M}}^* K_{+\mathrm{M}}^* + K_{0+}^*(K_{0\mathrm{M}}^* + K_{+\mathrm{M}}^*)}$$

Although Equations 7-3 and 7-4 are equivalent to Equations 7-6, they are convenient for developing a microscale model of transport because the accompanying K_{ij}'s embody binary molecular interactions.[31] The next two subsections outline calculation of concentrations and frictional interactions between water and proton and the membrane, $K_{0\mathrm{M}}^*$ and $K_{+\mathrm{M}}^*$. and between water and cations, K_{0+}^*.

7.8.1.1 Water and Proton Concentration

Although water content fully specifies the microscale concentrations in the hydrophilic channels. We neglect the volume of protons giving a water concentration of $1/\bar{V}_0$ where $\bar{V}_0$ is the partial molar volume of water and we treat as constant and equal to 18.01 mol cm^{-3}. To specify the concentration of mobile protons, c_+^*, we consider that for protons to dissociate from the sulfonate groups, they must be solvated by water according to the equilibria

$$\mathrm{HSO_3} + s\mathrm{H_2O} \rightleftharpoons \mathrm{SO_3^-} + (\mathrm{H_2O})_s\mathrm{H^+} \qquad 7\text{-}24$$

where s is the number of water in proton's first solvation shell. We treat the activity of proton-sulfonate pairs and free sulfonate groups as proportional to the fraction total sulfonate in these two states, f_{bound} and $1 - f_{\mathrm{bound}}$, respectively. The activity of free protons is given by its mole fraction x_+^*,

$$x_+^* = \frac{1 - f_{\mathrm{bound}}}{\lambda - \lambda_{\mathrm{res}} - s(1 - f_{\mathrm{bound}}) + (1 - f_{\mathrm{bound}})} \qquad 7\text{-}25$$

where λ is water content and the numerator is the number of free protons per sulfonate group and the denominator is the fraction of free water molecules (total water subtracting the residual water that always solvates the salt, λ_{res}, the water solvating free protons, $s(1 - f_{\mathrm{bound}})$) and free cations. Water activity is taken as unity. Chemical equilibrium dictates that[30]

$$\frac{f_{\mathrm{bound}}\big(\lambda - \lambda_{\mathrm{res}} - s(1 - f_{\mathrm{bound}}) + (1 - f_{\mathrm{bound}})\big)}{(1 - f_{\mathrm{bound}})^2} = K_{\mathrm{eq}} \qquad 7\text{-}26$$

where K_{eq} is the equilibrium constant of Equation 7-24. λ_{res} sets a threshold water content above which water can dissociate from sulfonate groups, which is set to 2.5, in agreement with *ab-initio* quantum chemical calculations.[28] The number of water molecules in the proton solvation shell is

set to 4, within the ranges reported in literature.[12, 59] We fit K_{eq} to the fraction of free protons, $1 - f_{bound}$, found in *ab-initio* molecular dynamics simulations of PFSA that report the fraction of protons beyond the sulfonate groups' first solvation shell (giving $K_{eq} = 3$).[42] Figure 7-7 plots $1 - f_{bound}$ given by Equation 7-26 (line) and predicted by molecular dynamics simulations of Nafion membranes as a function of water content. Solving for f_{bound} specifies the microscale concentration of mobile protons, $c_+^* = (1 - f_{bound})/\lambda \bar{V}_0$.

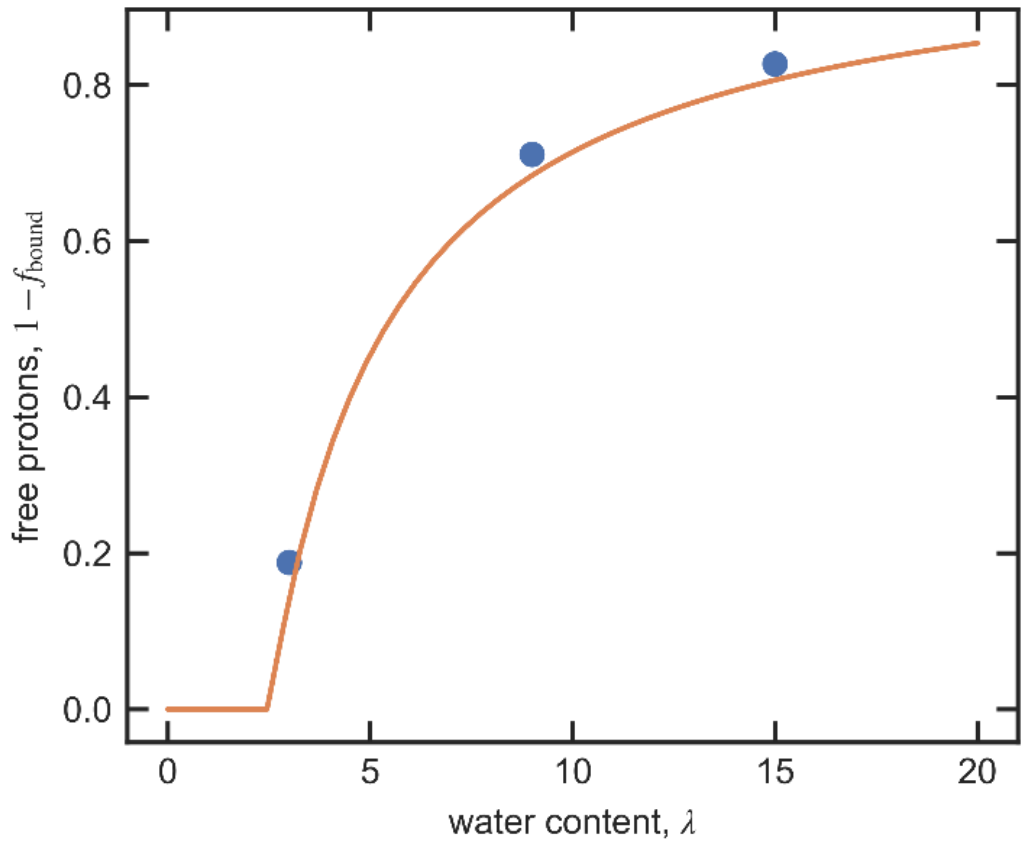

Figure 7-7. Fraction of solvated protons, $1 - f_{bound}$, as a function of water content λ from Equation 7-26 (line) and *ab-initio* molecular-dynamics simulations (points) from Ref [42].

7.8.1.2 Water/Membrane and Cation/Membrane Friction Coefficient

The membrane interacts with the aqueous proton and water moving through its hydrophilic channels. Electrolyte solution flowing through channels with charged walls has been modeled extensively.[9, 255] A momentum balance (i.e. Navier-Stokes) dictates that the driving forces on the aqueous solution balance the viscous resistance the solution exerts on the channel walls.[9, 31, 255] The Navier-Stokes equation for a Newtonian fluid specifies the mass-averaged velocity through a channel, v_z, (in the z-direction) with an invariant cross-section under the influence of a (electro)chemical potential gradient, $\partial \mu_i / \partial z$, as[31]

$$v_z^* = -\frac{c_0^*}{\mathcal{K}_0^*}\frac{\partial \mu_0}{\partial z} - \frac{c_+^*}{\mathcal{K}_+^*}\frac{\partial \mu_+}{\partial z} \quad 7\text{-}27$$

where $\mathcal{K}_i^*$ is a hydrodynamic friction coefficient of i that satisfies the momentum balance with no-slip boundary conditions at the channel walls for a slit geometry[31]

$$\mathcal{K}_i^* = \frac{12\eta}{(H^*)^2\theta_i} \quad 7\text{-}28$$

where η is the viscosity of the solution in the hydrophilic channel and θ_i is a distribution coefficient specifying how a species i is distributed across the channel. Einstein's viscosity equation[253] calculates how the viscosity of the solution changes with proton concentration c_+^*,

$$\eta = \eta^\infty \frac{\left(1 + \frac{c_+^* \tilde{V}_+}{2}\right)}{\left(1 - c_+^* \tilde{V}_+\right)^2} \quad 7\text{-}29$$

where η^∞ is viscosity of water (= 0.89 cP),[173] and $\tilde{V}_+$ is the molar viscous volume of water and is a constant fit to measured viscosity of bulk electrolyte HCl (= 0.021 mol L^{-1}), because HCl shows little ion-pair formation at high concentrations.[85] Water is considered uniformly distributed across the water-filled channel, yielding $\theta_0 = 1$. Following the same procedure outlined previously,[31] the linearized Poisson-Boltzmann equation specifies the distribution coefficient for protons across the cross section of the channel with a fixed charge density at the walls that, when coupled to the Navier-Stokes equation for flow in a slit, gives[31]

$$\theta_+ = \frac{12 + 6k^*H^*}{(k^*H^*)^2 \tanh\left(\frac{k^*H^*}{2}\right)} \quad 7\text{-}30$$

where k^{*-1} is the Debye length, $= 1.359\text{x}10^{-8}\ (c_+^*)^{-1/2}$ where the constant has units of $mol^{1/2}\ m^{-1/2}$ in water at 25°C.[31] The charge density at the hydrophilic/hydrophobic channel interface is not in Equation 7-30 because the water content λ (and, protons concentration, accordingly) and the channel height H^* specify the charge density from geometric arguments.

Satisfying the Navier-Stokes equation and the Stefan-Maxwell equations shows that the hydrodynamic coefficient $\mathcal{K}_i^*$ relates to the friction with the membrane $K_{i\mathrm{M}}$ according to[31]

$$K_{i\mathrm{M}} = \mathcal{K}_i^* w_i + \sum_{j \neq i} K_{ij}^* \left(\frac{\mathcal{K}_i^*}{\mathcal{K}_j^*} - 1\right) \quad 7\text{-}31$$

where w_i is the mass fraction of species i.

7.8.1.3 Water/Cation Friction Coefficient

Friction between water and cation, K_{0+}, is a function of proton concentration c_+^*, water concentration c_0^*, and the Stefan-Maxwell proton-water diffusion coefficient D_{0+}^* [31]

$$K_{ij}^* = \frac{c_0^* c_+^* RT}{(c_+^* + c_0^*) D_{0+}^*} \quad 7\text{-}32$$

We equate D_{0+}^{*} to the water/proton diffusion coefficient in a bulk electrolyte solution of hydrochloric acid, HCl, at the same proton concentration. Following the method outlined by Chapman,[85] measured electrolyte transport and thermodynamic properties determine the water/proton binary diffusion coefficient. We use measured HCl solution conductivity, density, electrolyte activity coefficient, and proton transference number compiled from literature by Chapman and Newman[326] and electrolyte diffusion coefficient from Rizzo.[327] HCl is chosen because it exhibits little ion-pair formation at low concentrations.[172] Because the experiments are conducted at different electrolyte concentrations and the analysis requires the derivative of the natural log of activity coefficient, a smooth spline fit the data (implemented with the SciPy 1.4.1 using a univariate spline method with a cubic spline for all properties, except the natural log of activity coefficient which utilized a 4th order spline, and with a smoothing factor of 0.01 for all properties). We also extracted the water/water diffusion coefficient in HCl using NMR diffusion measurements[328] with the approach outlined previously.[329] Figure 7-8 shows the extracted diffusion coefficients for water/proton (solid line) and water/water (dashed line) as a function of solvent ratio (mol H_2O / mol HCl, analogous to λ but for a bulk electrolyte). The water/proton diffusion coefficient is very large at high water contents (dilute electrolyte), due to the Grotthuss hopping mechanism that facilitates rapid transport of a positive charge of an excess proton along hydrogen-bond networks[8]. However, at lower water contents (concentrated electrolyte), much of the water is highly structured, solvating the protons. At these high concentrations, the structured water does not facilitate proton hopping and the diffusion coefficient of protons converges with the diffusion coefficient of water, suggesting that protons are moving entirely by vehicular transport.[328, 330]

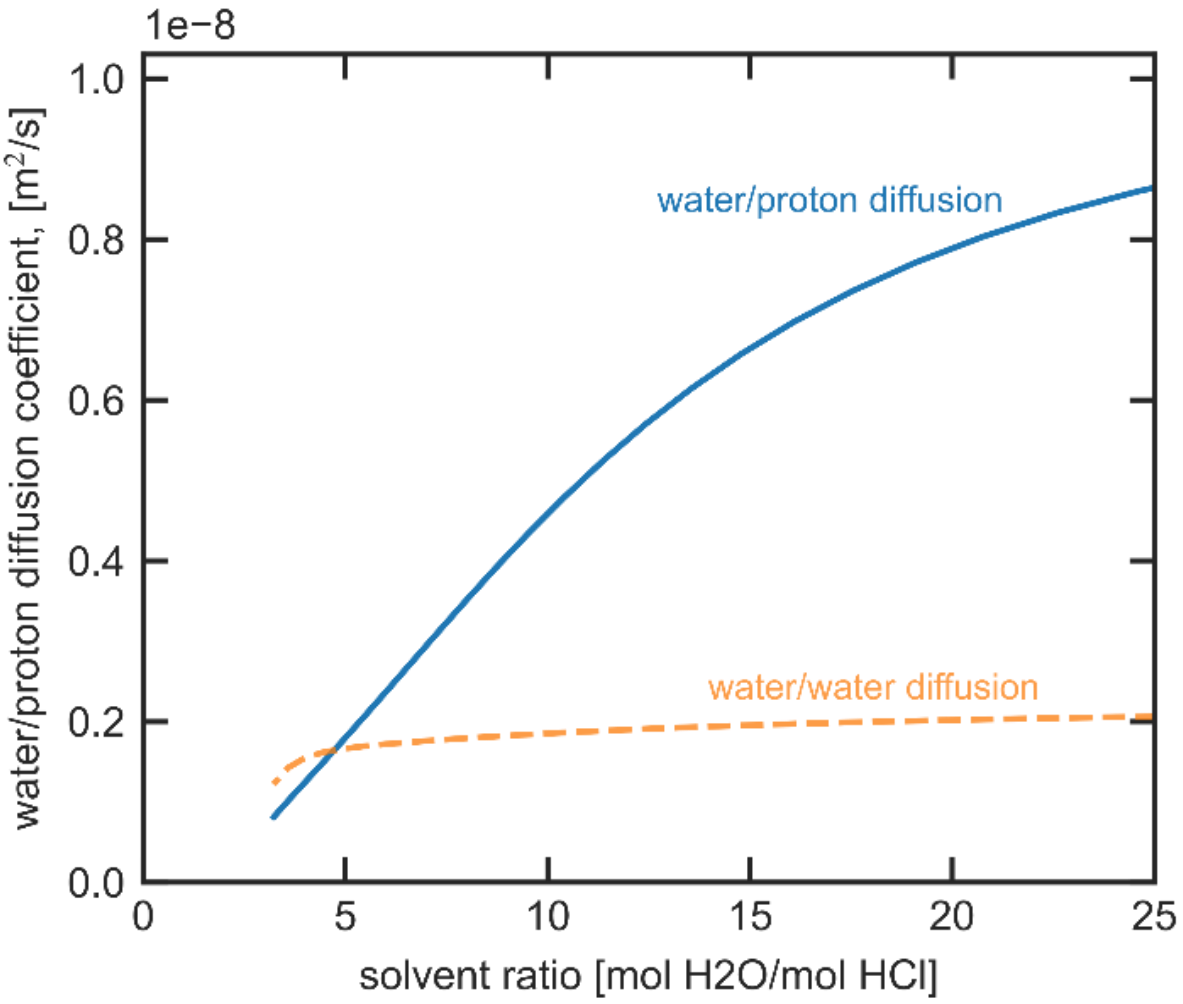

Figure 7-8. Water/proton (solid line) and water/water (dashed line) diffusion coefficient of bulk solution of HCl extracted from transport experiments[85, 326, 328] as a function the ratio of moles of solvent to moles of salt.

7.9 Appendix 7-C

The network-assembly algorithm places n_{R} seed points randomly in a 3D cube of dimension W^{net} (e.g., point 0 is placed with coordinates $0 < x_0 < W^{\mathrm{net}}$, $0 < y_0 < W^{\mathrm{net}}$, $0 < z_0 < W^{\mathrm{net}}$) with an average spacing between closest points equal to the domain spacing of the dry membrane (2.95 nm). The membrane swell isotopically such that the ratio of microscale channel width and network width is constant. Boundary conditions require a clearly defined interface over which to apply the conditions. To achieve well-defined boundaries in the direction of transport (x-direction), the algorithm reflects the positions of the n_{R} seed points about the y-z plane at $x = 0$ and $x = W^{\mathrm{net}}$ (e.g. a point at x_0, y_0, z_0 is reflected to $-x_0, y_0, z_0$ and $2W^{\mathrm{net}} - x_0, y_0, z_0$), creating an additional n_{R}x2 seeds. To facilitate periodic boundary conditions, the algorithm translates the original n_{R} points in the y- and z- directions with a constant x-coordinate (e.g. a point at x_0, y_0, z_0 is translated to $x_0, y_0 \pm W^{\mathrm{net}}, z_0$ and $x_0, y_0, z_0 \pm W^{\mathrm{net}}$), creating an additional n_{R}x4 seeds.

The total of n_{R}x7 points constitute the seeds for the Voronoi tessellation cells. There are seven cubes with a central cube and six cubes bordering the central cube's faces. The points reflected about the y-z plane at $x = 0$ and $x = W$ form a well-defined interface. Voronoi nodes and segments for $x < 0$ and $x > W$ are trimmed (i.e., deleted). For any node in the central cube that connects across the x-y and x-z planes at $z, y = 0, = W$ to a node in one of the translated cubes, the algorithm reconnects to the corresponding node in the central cube to create periodic boundary conditions (e.g., initially Node 0 at x_0, y_0, z_0 with coordinates between 0 and W^{net} is connected to Node 1 at x_1, y_1, z_1 with x_1 and z_1 between 0 and W^{net} and y_1 between W^{net} and $2W^{\mathrm{net}}$. The algorithm connects Node 0 to Node 2 that is the image of Node 1 in the central cube with coordinates x_1, $y_1 - W^{\mathrm{net}}$, z_1. The length of phantom segment connecting Node 0 to Node 2 is set as that of the segment connecting Node 0 to Node 1.) The algorithm now trims the nodes with $y, z < 0, > W^{\mathrm{net}}$. The nodes at $x = 0$ and $x = W^{\mathrm{net}}$ are boundary nodes. The resulting network contains n_{S} segments connected by n_{N} nodes of which $n_{\mathrm{N,B}}$ are boundary nodes and $n_{\mathrm{N,I}}$ are internal nodes. All algorithms are written in Python, using the packages OpenPNM 1.6.2[331] to structure the network and extract incidence matrixes (with modifications to incorporate periodic boundary conditions as discussed above), and SciPy 1.4.1 and NumPy 1.18.1 to perform numerical and array computations.

7.10 Appendix 7-D

Substitution of Equations 7-11 and 7-12 into Equation 7-9 for each internal node creates a matrix equation

$$\boldsymbol{A\mu} = \boldsymbol{b} \tag{7-33}$$

where $\boldsymbol{A}$ is a $2n_{\mathrm{N,I}}$ x $2n_{\mathrm{N,I}}$ matrix of transport coefficients as Equations 7-11 and 7-12 prescribe, $\boldsymbol{\mu}$ **is** a $2n_{\mathrm{N,I}}$ column vector (electro)chemical potentials of each node, and $\boldsymbol{b}$ is a $2n_{\mathrm{N,I}}$ column vector describing the flow balance on each node and is equal to zero for all nodes except those connected to boundary nodes. These latter entries specify the flux from boundary into connected nodes based on the (electro)chemical potential applied at the boundaries. The size of $2n_{\mathrm{N,I}}$ comes from specifying the water and proton (electro)chemical potentials. Inversion of $\boldsymbol{A}$ in Equation 7-33 calculates the potentials at each node.

Upon solving for the (electro)chemical potential at each node, Equations 7-11 and 7-12 provide the flux into each node. Summing the cation or water flow passing through boundary nodes (leaving the left boundary nodes or entering the right boundary nodes), and normalizing by the total area (product of network height H^{net} and depth D^{net}) including hydrophilic and hydrophobic regions specifies the macroscopic (superficial) flux through the membrane

$$N_i = \frac{\sum_{\alpha}^{n_{\mathrm{N,B,right/left}}} \sum_{\beta} Q_i^{\alpha,\beta}}{H^{\mathrm{net}} D^{\mathrm{net}}} \tag{7-34}$$

where the first summation is over all nodes α at a boundary (right or left) and the second summation is over all segments connecting α to neighboring node β. Upon substituting the definition of segment flow into Equation 7-34, the results is a sum segment fluxes

$$N_i = \frac{\sum_{\alpha}^{n_{\mathrm{N,B,right/left}}} \sum_{\beta} N_i^{\alpha,\beta} H^{\alpha,\beta} D^{\alpha,\beta}}{H^{\mathrm{net}} D^{\mathrm{net}}} = \frac{\sum_{\alpha}^{n_{\mathrm{N,B,right/left}}} \sum_{\beta} N_i^{\alpha,\beta} H^{\alpha,\beta} D^{\mathrm{ave}}}{\phi H^{\mathrm{ave}} D^{\mathrm{ave}} n_{\mathrm{N,B,right/left}}} = \frac{\sum_{\alpha}^{n_{\mathrm{N,B,right/left}}} \sum_{\beta} N_i^{\alpha,\beta} \phi \left(\frac{H^{\alpha,\beta}}{H^{\mathrm{ave}}}\right)}{n_{\mathrm{N,B,right/left}}} \quad 7\text{-}35$$

where the first equality imposes the equality $D^{\alpha,\beta} = D^{\mathrm{ave}}$ and the product of the water volume fraction, ϕ, and the total area of the network is equals the hydrophilic area of the network face, which is the sum of the hydrophilic areas of each domain, $\phi D^{\mathrm{net}} H^{\mathrm{net}} = \sum_{\alpha}^{n_{\mathrm{N,B,right/left}}} H^{\alpha,\beta} D^{\mathrm{ave}}$. The domain is sufficiently large such that $H^{\mathrm{net}} n_{\mathrm{N,B,right/left}} = \sum_{\alpha}^{n_{\mathrm{N,B,right/left}}} H^{\alpha,\beta}$. Note that D^{ave} cancels in the analysis. We treat the membrane as swelling isotopically over a sufficiently large length scale such that the ratio $W^{\mathrm{net}}/W^{\alpha,\beta}$ is constant for all water contents. As such, for a given random seed, simulations over all water contents (i.e., swelling) only require one network construction, drastically decreasing computation time. To illustrate these calculations, Figure 7-9 shows calculated proton electrochemical potential (a) and water chemical potential (b) of each node under a proton electrochemical potential difference across the network using Equation 7-33 as a function position at $\lambda = 15$.

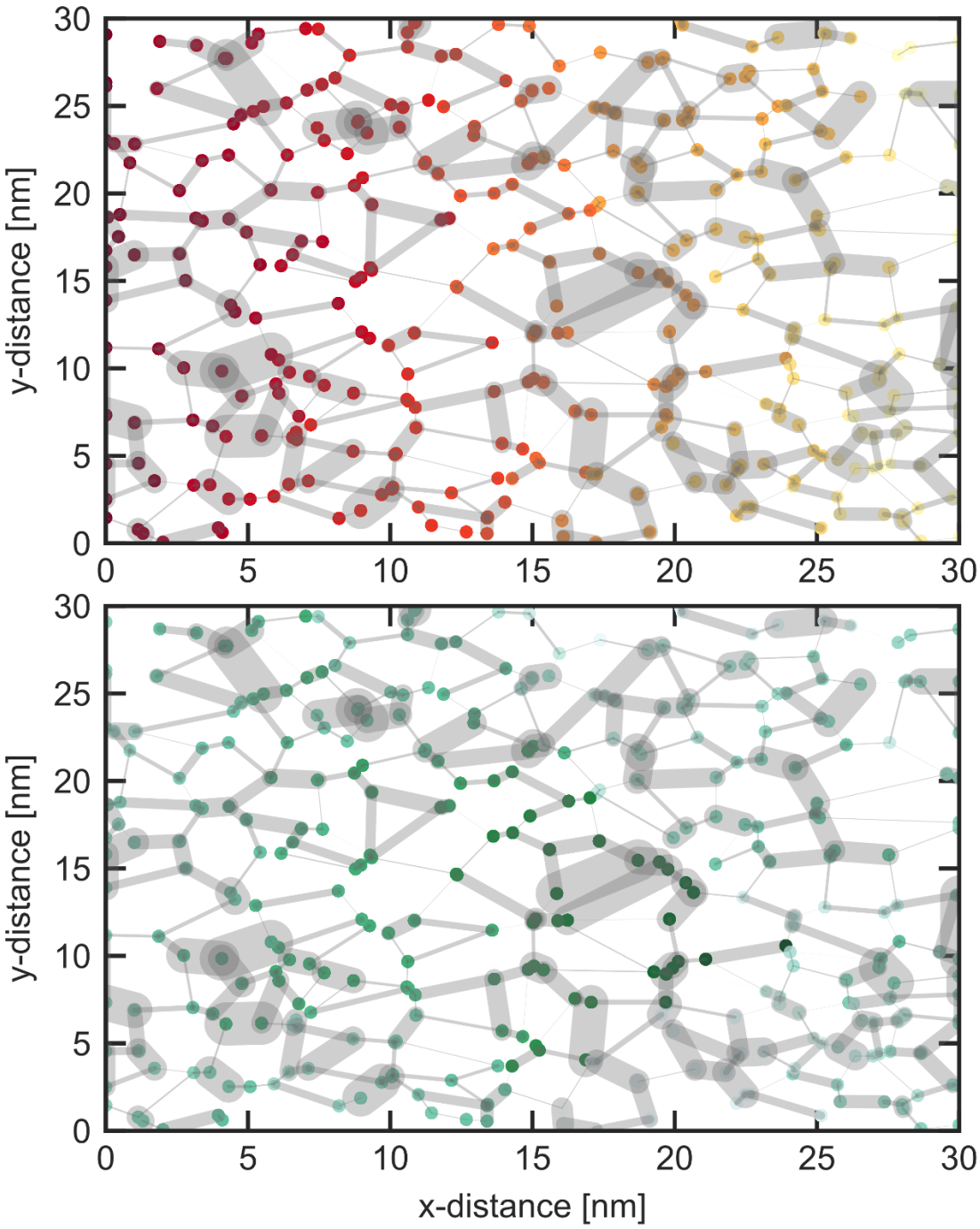

Figure 7-9. Calculated proton electrochemical potential (a) and water chemical potential (b) of each node under a proton electrochemical potential difference across the network using Equation 7-33 as a function position at $\lambda = 15$. Each line is a network channel with its thickness scaled proportionally with the channel height and each node is colored and sized based on its (electro)chemical potential.

7.11 Appendix 7-E

Bonilla and Bhatia provide a general expression for multicomponent effective medium theory (EMT).[100]

$$\int_0^\infty \int_0^\infty \int_0^\infty \left[\left(\frac{z}{2}-1\right)\boldsymbol{g}^{\mathrm{EMT}} + \boldsymbol{g}^*(H^*,W^*,D^*)\right]^{-1} [\boldsymbol{g}^{\mathrm{EMT}} - \boldsymbol{g}^*(H^*,W^*,D^*)] PDF(H^*,W^*,D^*) dH^* dW^* dD^* = 0 \quad (7\text{-}36)$$

where $\boldsymbol{g}^{\mathrm{EMT}}$ is the matrix of macroscale transport conductances, $\boldsymbol{g}^*$ is the matrix of microscale transport segment conductances, z is the coordination number of the network, and $PDF(H^*,W^*)$ is the probability distribution function of channel heights, H^*, and widths, W^*, and depths, D^*. Conductances relate to the transport properties according to

$$\boldsymbol{g}^* = \boldsymbol{L}^* \phi \frac{H^* D^*}{W^*} \quad (7\text{-}37)$$

and

$$\boldsymbol{g}^{\mathrm{EMT}} = \boldsymbol{L}^{\mathrm{EMT}} \frac{H^{\mathrm{ave}} D^{\mathrm{ave}}}{W^{\mathrm{ave}}} \quad (7\text{-}38)$$

where $\boldsymbol{L}$ is a matrix of transport properties with L_{++} and L_{00} along the diagonal and L_{+0} and L_{0+} on the off-diagonal entries and the superscripts EMT refer to the effective medium coefficients and $*$ refers to the microscopic coefficient. The volume fraction of water, ϕ, in Equation 7-37 corrects L^* from a interstitial property to a superficial property. H^{ave}, D^{ave}, and W^{ave} are the average height, depth, and width of segments, respectively. Consistent with network simulations, $D^* = D^{\mathrm{ave}}$. As there is a narrow distribution of W^*, compared to the distribution of H^*, we set $W^* = W^{\mathrm{ave}}$. This second approximation does not significantly bias Equation 7-36 as it still agrees with test simulations of a network with a binomial distribution of heights (0 or 1) that we conducted. Test simulations also showed that, although the coordination number for Voronoi tesselation is 3, its non-regular lattice makes the apparent z equal to 4.

Here, we apply the multicomponent EMT to transport coefficients of water, cation, and electrokinetic. To satisfy the EMT requirement that the induced local (electro)chemical potential gradients average to zero, the effective transport property matrix $\boldsymbol{L}^{\mathrm{EMT}}$ obeys

$$\int_0^\infty \left[\left(\frac{z}{2}-1\right)\boldsymbol{L}^{\mathrm{EMT}} + \left(\frac{H^*\phi}{H^{\mathrm{ave}}}\right)\boldsymbol{L}^*(H^*)\right]^{-1} \left[\boldsymbol{L}^{\mathrm{EMT}} - \left(\frac{H^*\phi}{H^{\mathrm{ave}}}\right)\boldsymbol{L}^*(H^*)\right] PDF(H^*) dH^* = 0 \quad (7\text{-}39)$$

The EMT expression, Equation 7-39, differ from that of Bonilla and Bhatia[100] because they considered cylinders rather than slits and because they used a modified smooth-field approximation to relate $\boldsymbol{g}^{\mathrm{EMT}}$ to $\boldsymbol{L}^{\mathrm{EMT}}$ that did not markedly improve agreement between the EMT and our test simulations. However, in the network simulations with a distribution of H^*, the use of Equation 7-38 rather than the smooth-field approximation equivalent may be a source of discrepancy between the model and simulations.

8 Conclusions and Suggested Future Directions

Phase-separated water-swollen cation-exchange membranes are an important component in numerous electrochemical energy-conversion devices.[12] This dissertation develops mathematical models of thermodynamics and transport properties for these membrane under different environmental conditions. These models provide for high-fidelity prediction and optimization of electrochemical cell performance and give insights into the molecular underpinnings of membrane properties. Perfluorinated sulfonic-acid (PFSA) polymer chemistry is the primary focus of this work, but the methodology in this dissertation is valid for other chemistries. Individual chapters provide detailed conclusions. This chapter presents three reoccurring and general findings from this work:

(1) *The specific behavior of ions in the water-swollen membrane is largely explained by their behavior in bulk solution.* For example, the variations of membrane conductivity exchanged with different cations scales with variations of mobility of the ions in aqueous solution (see Chapters 3 and 5). Similarly, the affinity of counter-ions for the membrane is comparable to that ion's attraction to the small-molecule equivalent of the polymer charge group (e.g., triflic acid anion for a PFSAs) in bulk-electrolyte (see Chapter 4). This general conclusion supports previous literature.[44, 54, 290, 332-333] Properties of solvent-swollen phase-separated membranes should, therefore, be compared to analogous bulk-solution electrolytes. The physics of solution electrolytes are relatively well understood[8] and can be applied to solvent-swollen membranes. Differences between the behavior of bulk-electrolyte solutions and that of membranes are then due to membrane-specific interactions.

(2) *The concentrated nature of solvent-swollen phase-separated membranes gives rise to important phenomena.* Concentrated-solution effects manifest themselves in transport properties, such as the electroosmotic coefficient and solute-solute diffusion coefficient (see Chapters 2, 5, 6, and 7). Thermodynamic properties also display concentrated-solution effects. Species activity coefficients are far from unity and ions form pairs with one another (see Chapters 3 and 4). This conclusion implies that dilute-solution theories are insufficient to fully understand and characterize PFSA membranes. Often times concentrated-solution theories are not tractable. Judicious simplifications need to be made. For example, Chapter 6 showed that many solute-solute interactions are negligible, but making that assumption *a priori* can lead to misleading conclusions about the validity and physical nature of measured transport coefficients.

(3) *Mesoscale phenomena strongly impact solvent-swollen phase-separated membrane properties.* The tortuosity of the transport networks of solvent-swollen phase-separated membranes reduce macroscopic transport far more than does microscale friction (see Chapter 3). When mesoscale phenomena and concentrated-solution transport are combined, the emergent macroscopic properties are not readily computed by a corresponding microscale property (see Chapter 7).

Each of these conclusions has implications to the application of solvent-swollen, phase-separated membranes in electrochemical energy-conversion devices (see Chapters 2 and 6). In general, tailoring the properties of the membranes improves cell performance. Conclusion 1, however, suggests that bulk-electrolyte properties of the involved electrolytes dictate many of membrane properties (see Chapters 3, 4 and 5). For example, the transport selectivity of ions through the membrane (i.e., the ratio of species' diffusion coefficients) is unlikely to differ drastically from this ratio of the corresponding ions in solution. Conclusion 2 warns that a property measured within a dilute-solution framework can be a convolution of multiple concentrated-solution effects (see

Chapter 6). For example, the flux of an ion through a membrane depends upon not only on ion/membrane interactions (as dilute-solution theory predicts), but also upon ion electrochemical potential differences of all the species present, water/ion interactions, and osmotic-pressure differences, among others factors (see Chapter 7). Conclusions 2 and 3 emphasize the need to consider higher-order effects (i.e., water/solute interactions and electrolyte filled-channel/channel interactions, respectively) that introduce additional complexity while providing unexplored avenues to tune or improve membrane properties.

8.1 Suggested Future Directions

There are numerous future directions for this work.

1) *Develop new membrane chemistries or electrochemical-device design strategies that take advantage of concentrated-solution and mesoscale effects.* For example, osmotic molecular stressors in redox-flow-battery electrolytes could take advantage of concentrated-solution effects by imposing advantageous osmotic pressure differences that reduce detrimental crossover of redox-active species. Alternatively, the distribution of hydrophilic domain sizes in the membrane can be tuned to favor ion or solvent transport properties as required by device requirements.
2) *Adapt the mathematical models proposed in this dissertation to other membrane materials and systems of interest.* The proposed models and their frameworks in this dissertation readily extend to non-aqueous and mixed-solvent transport and partitioning. They are useful for electrochemical energy-conversion devices that require wider voltage windows than aqueous electrolytes allow.[4, 334] The role of neutral solutes on membrane properties can be incorporated to predict transport of non-ionic electrosynthesis products.[3, 335] Extension of the model to include transport of species dissolved in the polymer backbone, such as hydrogen and oxygen, allows modeling of gas crossover and permeability.[336] Although this dissertation focused on PFSAs, extension to hydrocarbon cation- and anion-exchange membranes is straightforward as well as to hydrogels used in applications beyond electrochemical-energy conversion.
3) *Develop reduced-order models*. The mathematical models presented in this dissertation are complex, often requiring numerical solutions to coupled partial differential and/or transient algebraic equation. Model-order reduction that retains the essential physics of the full model while decreasing computational complexity is a fruitful area of further research. The multicomponent models in Chapters 4 and 5 and the network model in Chapter 7 make accurate predictions, but the required theoretical and numerical complexity hinder adoption. Simplified models reduce the barriers to implementation so that they can be incorporated into larger systems-level models without increasing computational effort.
4) *Extend current mathematical models to transient behavior.* Because the polymer membranes are viscoelastic, water and ion uptake are functions of time since exposed to a changed environment.[12] Extending water and ion-uptake models in Chapter 4 to include time-dependent response of the polymer can explain diffusion and swelling dynamics.[12]
5) *Develop mathematical models of mesoscale thermodynamics.* Chapter 7 proposes a mesoscale transport model. Model calculations show that the distribution of hydrophilic domain sizes has a distinct impact on different transport properties. Developing analogous network-simulations to model thermodynamic properties can address whether different uptake and mechanical properties are also affected differently by the mesoscale.

6) *Incorporate the role interfaces have on membrane thermodynamics and transport*. In electrochemical energy-conversion devices, ionomer (e.g., PFSA) thin films in catalyst layers provide ionic conduction pathways to reaction sites.[337] The properties of the thin-film ionomers confined at catalyst sites are considerably different from those of bulk membranes made from the same polymer.[12, 337] Incorporating confinement-dependent tortuosity can quantify how transport properties change as a function of ionomer-film thickness including anisotropy.[12, 338] Modifying the molecular-thermodynamic model developed in Chapter 4 to account for confinement can explain different water and ion uptake properties.[12, 339] These anomalous thin-film behaviors arises from confinement effects as well as from interactions of the mobile ions and polymer with the catalyst interface. A compelling area of exploration is coupling the current thermodynamic theory to a model of the electrochemical double-layer adjacent to charged surfaces, such as a catalyst particle. This model can answer fundamental questions about the thermodynamics of local environments that violate electroneutrality as well as application-specific questions about catalyst layers. Combining a double-layer model and transient-membrane properties (see 4 above), allows prediction of surface-charging and capacitive-impedance effects.
7) *Characterize thermodynamic and transport properties of concentrated bulk-electrolytes that are used in electrochemical energy-conversion devices*. As Chapter 4-6 showed, optimizing the performance of energy-conversion devices requires multicomponent bulk-electrolyte thermodynamic and transport data.[340] There are extensive datasets available on the thermodynamic and transport properties of the most common dilute single-salt aqueous electrolytes.[85] However, there is limited measured thermodynamic properties and transport coefficients of concentrated electrolytes and for electrolytes of many electrochemical energy-conversion devices (e.g., vanadium sulfate).[223] Moreover, many energy-conversion devices contain mixed-solvent or mixed-salt electrolytes.[336, 340] There is little if any complete transport and thermodynamic characterizations of such multicomponent systems.[9, 251] It is not guaranteed that existing molecular theories, which are validated against binary electrolytes, are applicable to systems with additional components.[9, 66, 340-341] Despite over a hundred years of studies on the transport and thermodynamic properties of electrolyte solutions, this field still requires additional research.[8]

9 References

1. *Global Warming of 1.5°C. An IPCC Special Report on the impacts of global warming of 1.5°C above pre-industrial levels and related global greenhouse gas emission pathways, in the context of strengthening the global response to the threat of climate change, sustainable development, and efforts to eradicate poverty*; Intergovernmental Panel on Climate Change, World Meteorological Organization: Geneva, Switzerland, 2017.
2. *Global Energy Perspective*; McKinsey and Company: 2019.
3. De Luna, P.; Hahn, C.; Higgins, D.; Jaffer, S. A.; Jaramillo, T. F.; Sargent, E. H., What would it take for renewably powered electrosynthesis to displace petrochemical processes? *Science* **2019,** *364* (6438), eaav3506.
4. Schiffer, Z. J.; Manthiram, K., Electrification and Decarbonization of the Chemical Industry. *Joule* **2017,** *1* (1), 10-14.
5. Moliner, R.; Lázaro, M. J.; Suelves, I., Analysis of the strategies for bridging the gap towards the Hydrogen Economy. *International Journal of Hydrogen Energy* **2016,** *41* (43), 19500-19508.
6. Na, J.; Seo, B.; Kim, J.; Lee, C. W.; Lee, H.; Hwang, Y. J.; Min, B. K.; Lee, D. K.; Oh, H.-S.; Lee, U., General technoeconomic analysis for electrochemical coproduction coupling carbon dioxide reduction with organic oxidation. *Nature Communications* **2019,** *10* (1), 5193.
7. Daniela, B.; Purnima, P.; Kaylee, D.; Miguel, M., *Design Guidelines for Membrane-separated Organic Electrosynthesis: The Case of Adiponitrile Production*. 2019.
8. Bockris, J. O. M.; Reddy, A. K. N.; Gamboa-Aldeco, M. E., *Modern electrochemistry*. 2nd ed.; Plenum Press: New York, 1998.
9. Newman, J.; Thomas-Alyea, K. E., *Electrochemical Systems*. John Wiley & Sons: 2004.
10. West, A. C., *Electrochemistry and Electrochemical Engineering: An Introduction*. Alan C. West: 2012.
11. Darling, R.; Gallagher, K.; Xie, W.; Su, L.; Brushett, F., Transport Property Requirements for Flow Battery Separators. *J. Electrochem. Soc.* **2016,** *163* (1), A5029-A5040.
12. Kusoglu, A.; Weber, A. Z., New Insights into Perfluorinated Sulfonic-Acid Ionomers. *Chem. Rev.* **2017,** *117* (3), 987-1104.
13. Prausnitz, J. M.; Lichtenthaler, R. N.; de Azevedo, E. G., *Molecular thermodynamics of fluid-phase equilibria*. Pearson Education: 1998.
14. Yang, Y.; Pintauro, P. N., Multicomponent space-charge transport model for ion-exchange membranes with variable pore properties. *Ind. Eng. Chem. Res* **2004,** *43* (12), 2957-2965.
15. Geise, G. M.; Paul, D. R.; Freeman, B. D., Fundamental water and salt transport properties of polymeric materials. *Prog. Polym. Sci.* **2014,** *39* (1), 1-42.
16. Park, H. B.; Kamcev, J.; Robeson, L. M.; Elimelech, M.; Freeman, B. D., Maximizing the right stuff: The trade-off between membrane permeability and selectivity. *Science* **2017,** *356* (6343).
17. Dursch, T. J.; Taylor, N. O.; Liu, D. E.; Wu, R. Y.; Prausnitz, J. M.; Radke, C. J., Water-soluble drug partitioning and adsorption in HEMA/MAA hydrogels. *Biomaterials* **2014,** *35* (2), 620-629.
18. Kreuer, K.-D.; Paddison, S. J.; Spohr, E.; Schuster, M., Transport in Proton Conductors for Fuel-Cell Applications: Simulations, Elementary Reactions, and Phenomenology. *Chem. Rev.* **2004,** *104* (10), 4637-4678.

19. Mauritz, K. A.; Moore, R. B., State of Understanding of Nafion. *Chem. Rev.* **2004,** *104* (10), 4535-4586.
20. Hickner, M. A.; Ghassemi, H.; Kim, Y. S.; Einsla, B. R.; McGrath, J. E., Alternative Polymer Systems for Proton Exchange Membranes (PEMs). *Chem. Rev.* **2004,** *104* (10), 4587-4612.
21. Varcoe, J. R.; Atanassov, P.; Dekel, D. R.; Herring, A. M.; Hickner, M. A.; Kohl, P. A.; Kucernak, A. R.; Mustain, W. E.; Nijmeijer, K.; Scott, K.; Xu, T.; Zhuang, L., Anion-exchange membranes in electrochemical energy systems. *Energy & Environmental Science* **2014,** *7* (10), 3135-3191.
22. Weber, A. Z.; Newman, J., Modeling Transport in Polymer-Electrolyte Fuel Cells. *Chem. Rev.* **2004,** *104* (10), 4679-4726.
23. Weber, A. Z.; Newman, J., Transport in Polymer-Electrolyte Membranes II. Mathematical Model. *J. Electrochem. Soc.* **2004,** *151* (2), A311-A325.
24. Weber, A. Z.; Newman, J., Transport in Polymer-Electrolyte Membranes I. Physical Model. *J. Electrochem. Soc.* **2003,** *150* (7), A1008-A1015.
25. Wang, C.; Paddison, S. J., Mesoscale modeling of hydrated morphologies of sulfonated polysulfone ionomers. *Soft Matter* **2014,** *10* (6), 819.
26. Promislow, K.; Jones, J.; Xu, Z.; Gavish, N.; Christlieb, A., Variational Models of Pore Networks in Ionomer Membranes: The Role of Electrostatics. *ECS Transactions* **2013,** *50* (2), 161-173.
27. Paddison, S. J., Proton Conduction in PEMs: Complexity, Cooperativity and Connectivity. In *Device and Materials Modeling in PEM Fuel Cells*, Paddison, S. J.; Promislow, K. S., Eds. Springer New York: 2009; pp 385-412.
28. Wang, C.; Clark Ii, J. K.; Kumar, M.; Paddison, S. J., An ab initio study of the primary hydration and proton transfer of CF3SO3H and CF3O(CF2)2SO3H: Effects of the hybrid functional and inclusion of diffuse functions. *Solid State Ionics* **2011,** *199–200*, 6-13.
29. Costamagna, P.; Grosso, S.; Di Felice, R., Percolative model of proton conductivity of Nafion® membranes. *Journal of Power Sources* **2008,** *178* (2), 537-546.
30. Guggenheim, E. A., *Thermodynamics-an advanced treatment for chemists and physicists*. North-Holland Publishing Company: Amsterdam, 1985.
31. Crothers, A. R.; Darling, R. M.; Radke, C. J.; Weber, A. Z., Theory of Multicomponent Phenomena in Cation-Exchange Membranes: Part II. Transport Model and Validation. *J. Electrochem. Soc.* **2020,** *167* (1), 013548.
32. Delacourt, C.; Newman, J., Mathematical Modeling of a Cation-Exchange Membrane Containing Two Cations. *J. Electrochem. Soc.* **2008,** *155* (11), B1210-B1217.
33. Weber, A. Z.; Delacourt, C., Mathematical Modelling of Cation Contamination in a Proton-exchange Membrane. *Fuel Cells* **2008,** *8* (6), 459-465.
34. Darling, R. M.; Gallagher, K. G.; Kowalski, J. A.; Ha, S.; Brushett, F. R., Pathways to low-cost electrochemical energy storage: a comparison of aqueous and nonaqueous flow batteries. *Energy & Environmental Science* **2014,** *7* (11), 3459-3477.
35. Perry, M. L.; Weber, A. Z., Advanced Redox-Flow Batteries: A Perspective. *J. Electrochem. Soc.* **2016,** *163* (1), A5064-A5067.
36. Hirschfelder, J. O.; Curtiss, C. F.; Bird, R. B.; Mayer, M. G., *Molecular theory of gases and liquids*. Wiley New York: 1954; Vol. 26.
37. Dullien, F. A., *Porous media: fluid transport and pore structure*. Academic press: 2012.

38. Eck, N. v.; Waltman, L., Software survey: VOSviewer, a computer program for bibliometric mapping. **2009,** *84* (2), 523.
39. Noack, A., Modularity clustering is force-directed layout. *Physical Review E* **2009,** *79* (2), 026102.
40. Savage, J.; Voth, G. A., Proton Solvation and Transport in Realistic Proton Exchange Membrane Morphologies. *J. Phys. Chem. C* **2016,** *120* (6), 3176-3186.
41. Feng, S.; Savage, J.; Voth, G. A., Effects of Polymer Morphology on Proton Solvation and Transport in Proton-Exchange Membranes. *J. Phys. Chem. C* **2012,** *116* (36), 19104-19116.
42. Devanathan, R.; Idupulapati, N.; Baer, M. D.; Mundy, C. J.; Dupuis, M., Ab Initio Molecular Dynamics Simulation of Proton Hopping in a Model Polymer Membrane. *J. Phys. Chem. B* **2013,** *117* (51), 16522-16529.
43. Devanathan, R.; Venkatnathan, A.; Dupuis, M., Atomistic Simulation of Nafion Membrane: I. Effect of Hydration on Membrane Nanostructure. *J. Phys. Chem. B* **2007,** *111* (28), 8069-8079.
44. Berrod, Q.; Lyonnard, S.; Guillermo, A.; Ollivier, J.; Frick, B.; Manseri, A.; Améduri, B.; Gébel, G., Nanostructure and Transport Properties of Proton Conducting Self-Assembled Perfluorinated Surfactants: A Bottom-Up Approach toward PFSA Fuel Cell Membranes. *Macromolecules* **2015,** *48* (17), 6166-6176.
45. Bontha, J. R.; Pintauro, P. N., Prediction of ion solvation free energies in a polarizable dielectric continuum. *J. Phys. Chem.* **1992,** *96* (19), 7778-7782.
46. Yang, Y.; Pintauro, P. N., Multicomponent space-charge transport model for ion-exchange membranes. *AIChE J.* **2000,** *46* (6), 1177-1190.
47. Berg, P.; Benjaminsen, B. E., Effects of Finite-size Ions and Relative Permittivity in a Nanopore Model of a Polymer Electrolyte Membrane. *Electrochim. Acta* **2014,** *120*, 429-438.
48. Eikerling, M.; Kornyshev, A. A.; Kuznetsov, A. M.; Ulstrup, J.; Walbran, S., Mechanisms of Proton Conductance in Polymer Electrolyte Membranes. *J. Phys. Chem. B* **2001,** *105* (17), 3646-3662.
49. Bazant, M. Z.; Kilic, M. S.; Storey, B. D.; Ajdari, A., Towards an understanding of induced-charge electrokinetics at large applied voltages in concentrated solutions. *Adv. Colloid Interface Sci.* **2009,** *152* (1–2), 48-88.
50. Paddison, S. J.; Paul, R.; Jr, T. A. Z., Proton friction and diffusion coefficients in hydrated polymer electrolyte membranes: Computations with a non-equilibrium statistical mechanical model. *J. Chem. Phys.* **2001,** *115* (16), 7753-7761.
51. Paddison, S. J.; Paul, R.; Zawodzinski, T. A., A Statistical Mechanical Model of Proton and Water Transport in a Proton Exchange Membrane. *J. Electrochem. Soc.* **2000,** *147* (2), 617-626.
52. Karraker, K. A.; Radke, C. J., Disjoining pressures, zeta potentials and surface tensions of aqueous non-ionic surfactant/electrolyte solutions: theory and comparison to experiment. *Adv. Colloid Interface Sci.* **2002,** *96* (1–3), 231-264.
53. Shi, S.; Dursch, T. J.; Blake, C.; Mukundan, R.; Borup, R. L.; Weber, A. Z.; Kusoglu, A., Impact of hygrothermal aging on structure/function relationship of perfluorosulfonic-acid membrane. *J. Polym. Sci., Part B: Polym. Phys.* **2016,** *54* (5), 570-581.
54. Shi, S.; Weber, A. Z.; Kusoglu, A., STRUCTURE-TRANSPORT RELATIONSHIP OF PERFLUOROSULFONIC-ACID MEMBRANES IN DIFFERENT CATIONIC FORMS. *Electrochim. Acta* **2016,** *220*, 517-528.

55. Hwang, G. S.; Parkinson, D. Y.; Kusoglu, A.; MacDowell, A. A.; Weber, A. Z., Understanding Water Uptake and Transport in Nafion Using X-ray Microtomography. *ACS Macro Lett.* **2013,** *2* (4), 288-291.
56. Kusoglu, A.; Savagatrup, S.; Clark, K. T.; Weber, A. Z., Role of Mechanical Factors in Controlling the Structure–Function Relationship of PFSA Ionomers. *Macromolecules* **2012,** *45* (18), 7467-7476.
57. Kusoglu, A.; Cho, K. T.; Prato, R. A.; Weber, A. Z., Structural and transport properties of Nafion in hydrobromic-acid solutions. *Solid State Ionics* **2013,** *252*, 68-74.
58. Kreuer, K.-D.; Portale, G., A Critical Revision of the Nano-Morphology of Proton Conducting Ionomers and Polyelectrolytes for Fuel Cell Applications. *Adv. Funct. Mater.* **2013,** *23* (43), 5390-5397.
59. Kreuer, K.-D., The role of internal pressure for the hydration and transport properties of ionomers and polyelectrolytes. *Solid State Ionics* **2013,** *252*, 93-101.
60. Liu, D.; Dursch, T.; Oh, Y.; Bregante, D.; Chan, S.; Radke, C., Equilibrium water and solute uptake in silicone hydrogels. *Acta biomaterialia* **2015,** *18*, 112-117.
61. Kotsmar, C.; Sells, T.; Taylor, N.; Liu, D. E.; Prausnitz, J. M.; Radke, C. J., Aqueous Solute Partitioning and Mesh Size in HEMA/MAA Hydrogels. *Macromolecules* **2012,** *45* (22), 9177-9187.
62. Manning, G. S., Limiting Laws and Counterion Condensation in Polyelectrolyte Solutions I. Colligative Properties. *J. Chem. Phys.* **1969,** *51* (3), 924-933.
63. Kamcev, J.; Paul, D. R.; Freeman, B. D., Ion activity coefficients in ion exchange polymers: Applicability of Manning's counterion condensation theory. *Macromolecules* **2015,** *48* (21), 8011-8024.
64. Kamcev, J.; Paul, D. R.; Manning, G. S.; Freeman, B. D., Accounting for frame of reference and thermodynamic non-idealities when calculating salt diffusion coefficients in ion exchange membranes. *Journal of Membrane Science* **2017,** *537*, 396-406.
65. Freger, V., Elastic energy in microscopically phase-separated swollen polymer networks. *Polymer* **2002,** *43* (1), 71-76.
66. Zerres, H.; Prausnitz, J. M., Thermodynamics of phase equilibria in aqueous-organic systems with salt. *AIChE J.* **1994,** *40* (4), 676-691.
67. Okada, T.; Arimura, N.; Satou, H.; Yuasa, M.; Kikuchi, T., Membrane transport characteristics of binary cation systems with Li+ and alkali metal cations in perfluorosulfonated ionomer. *Electrochim. Acta* **2005,** *50* (16), 3569-3575.
68. Okada, T.; Satou, H.; Okuno, M.; Yuasa, M., Ion and Water Transport Characteristics of Perfluorosulfonated Ionomer Membranes with H+ and Alkali Metal Cations. *J. Phys. Chem. B* **2002,** *106* (6), 1267-1273.
69. Okada, T.; Ayato, Y.; Yuasa, M.; Sekine, I., The Effect of Impurity Cations on the Transport Characteristics of Perfluorosulfonated Ionomer Membranes. *J. Phys. Chem. B* **1999,** *103* (17), 3315-3322.
70. Okada, T.; Møller-Holst, S.; Gorseth, O.; Kjelstrup, S., Transport and equilibrium properties of Nafion® membranes with H+ and Na+ ions. *J. Electroanal. Chem.* **1998,** *442* (1–2), 137-145.
71. Okada, T.; Nakamura, N.; Yuasa, M.; Sekine, I., Ion and Water Transport Characteristics in Membranes for Polymer Electrolyte Fuel Cells Containing H + and Ca2 + Cations. *J. Electrochem. Soc.* **1997,** *144* (8), 2744-2750.

72. Pintauro, P. N.; Bennion, D. N., Mass transport of electrolytes in membranes. 1. Development of mathematical transport model. *Ind. Eng. Chem. Fundam.* **1984,** *23* (2), 230-234.
73. Goyal, P.; Monroe, C. W., New Foundations of Newman's Theory for Solid Electrolytes: Thermodynamics and Transient Balances. *J. Electrochem. Soc.* **2017,** *164* (11), E3647-E3660.
74. Monroe, C. W.; Delacourt, C., Continuum transport laws for locally non-neutral concentrated electrolytes. *Electrochim. Acta* **2013,** *114*, 649-657.
75. Monroe, C. W.; Newman, J., Onsager Reciprocal Relations for Stefan− Maxwell Diffusion. *Ind. Eng. Chem. Res* **2006,** *45* (15), 5361-5367.
76. Gostick, J. T.; Weber, A. Z., Resistor-Network Modeling of Ionic Conduction in Polymer Electrolytes. *Electrochim. Acta* **2015,** *179*, 137-145.
77. Weber, A. Z.; Newman, J., Transport in Polymer-Electrolyte Membranes III. Model Validation in a Simple Fuel-Cell Model. *J. Electrochem. Soc.* **2004,** *151* (2), A326-A339.
78. Fuller, T. F. Solid-polymer-electrolyte fuel cells. Ph.D., University of California Berkeley, Ann Arbor, 1992.
79. Meyers, J. P.; Newman, J., Simulation of the Direct Methanol Fuel Cell II. Modeling and Data Analysis of Transport and Kinetic Phenomena. *J. Electrochem. Soc.* **2002,** *149* (6), A718-A728.
80. Curtiss, C. F.; Bird, R. B., Multicomponent Diffusion. *Ind. Eng. Chem. Res* **1999,** *38* (7), 2515-2522.
81. Krishna, R.; Wesselingh, J. A., The Maxwell-Stefan approach to mass transfer. *Chem. Eng. Sci.* **1997,** *52* (6), 861-911.
82. Bird, R. B.; Lightfoot, E. N.; Stewart, E. W., *Transport phenomenon*. Wiley: 2007.
83. Lightfoot, E. N.; Bassingthwaighte, J. B.; Grabowski, E. F., Hydrodynamic models for diffusion in microporous membranes. *Annals of Biomedical Engineering* **1976,** *4* (1), 78-90.
84. Wesselingh, J. A.; Vonk, P.; Kraaijeveld, G., Exploring the Maxwell-Stefan description of ion exchange. *The Chemical Engineering Journal and the Biochemical Engineering Journal* **1995,** *57* (2), 75-89.
85. Chapman, T. W. The Transport Properties of Concentrated Electrolyte Solutions. University of California, Berkeley, 1967.
86. Darling, R. M.; Weber, A. Z.; Tucker, M. C.; Perry, M. L., The Influence of Electric Field on Crossover in Redox-Flow Batteries. *J. Electrochem. Soc.* **2016,** *163* (1), A5014-A5022.
87. Xie, W.; Darling, R. M.; Perry, M. L., Processing and Pretreatment Effects on Vanadium Transport in Nafion Membranes. *J. Electrochem. Soc.* **2016,** *163* (1), A5084-A5089.
88. Agar, E.; Knehr, K. W.; Chen, D.; Hickner, M. A.; Kumbur, E. C., Species transport mechanisms governing capacity loss in vanadium flow batteries: Comparing Nafion® and sulfonated Radel membranes. *Electrochim. Acta* **2013,** *98*, 66-74.
89. Knehr, K. W.; Agar, E.; Dennison, C. R.; Kalidindi, A. R.; Kumbur, E. C., A Transient Vanadium Flow Battery Model Incorporating Vanadium Crossover and Water Transport through the Membrane. *J. Electrochem. Soc.* **2012,** *159* (9), A1446-A1459.
90. Knehr, K. W.; Kumbur, E. C., Role of convection and related effects on species crossover and capacity loss in vanadium redox flow batteries. *Electrochem. Commun.* **2012,** *23*, 76-79.
91. Lawton, J. S.; Jones, A. M.; Tang, Z.; Lindsey, M.; Zawodzinski, T., Ion Effects on Vanadium Transport in Nafion Membranes for Vanadium Redox Flow Batteries. *J. Electrochem. Soc.* **2017,** *164* (13), A2987-A2991.

92. Elgammal, R. A.; Tang, Z.; Sun, C.-N.; Lawton, J.; Zawodzinski, T. A., Species Uptake and Mass Transport in Membranes for Vanadium Redox Flow Batteries. *Electrochim. Acta* **2017,** *237*, 1-11.
93. Tang, Z.; Svoboda, R.; Lawton, J. S.; Aaron, D. S.; Papandrew, A. B.; Zawodzinski, T. A., Composition and Conductivity of Membranes Equilibrated with Solutions of Sulfuric Acid and Vanadyl Sulfate. *J. Electrochem. Soc.* **2013,** *160* (9), F1040-F1047.
94. Lawton, J. S.; Jones, A.; Zawodzinski, T., Concentration Dependence of VO2+ Crossover of Nafion for Vanadium Redox Flow Batteries. *J. Electrochem. Soc.* **2013,** *160* (4), A697-A702.
95. Sing, D. C.; Meyers, J. P., Direct Measurement of Vanadium Crossover in an Operating Vanadium Redox Flow Battery. *ECS Transactions* **2013,** *50* (45), 61-72.
96. Ashraf Gandomi, Y.; Aaron, D. S.; Mench, M. M., Coupled Membrane Transport Parameters for Ionic Species in All-Vanadium Redox Flow Batteries. *Electrochim. Acta* **2016,** *218*, 174-190.
97. Alizadeh, S.; Bazant, M. Z.; Mani, A., Impact of network heterogeneity on electrokinetic transport in porous media. *J. Colloid Interface Sci.* **2019,** *553*, 451-464.
98. Alizadeh, S.; Mani, A., Multiscale Model for Electrokinetic Transport in Networks of Pores, Part I: Model Derivation. *Langmuir* **2017,** *33* (25), 6205-6219.
99. Crothers, A. R.; Radke, C. J.; Weber, A. Z., Nano- and Mesoscale Ion and Water Transport in Perfluorosulfonic-Acid Membranes. *ECS Transactions* **2017,** *80* (8), 593-604.
100. Bonilla, M. R.; Bhatia, S. K., Multicomponent Effective Medium–Correlated Random Walk Theory for the Diffusion of Fluid Mixtures through Porous Media. *Langmuir* **2012,** *28* (1), 517-533.
101. Kirkpatrick, S., Percolation and Conduction. *Reviews of Modern Physics* **1973,** *45* (4), 574-588.
102. Chalamala, B. R.; Soundappan, T.; Fisher, G. R.; Anstey, M. R.; Viswanathan, V. V.; Perry, M. L., Redox Flow Batteries: An Engineering Perspective. *Proc. IEEE* **2014,** *102* (6), 976-999.
103. Skyllas-Kazacos, M.; Chakrabarti, M. H.; Hajimolana, S. A.; Mjalli, F. S.; Saleem, M., Progress in Flow Battery Research and Development. *Journal of The Electrochemical Society* **2011,** *158* (8), R55-R79.
104. Crothers, A. R.; Darling, R. M.; Kushner, D.; Perry, M. L.; Weber, A. Z., Theory of Multicomponent Phenomena in Cation-Exchange Membranes: Part III. Transport in Vanadium Redox-Flow-Battery Separators. *J. Electrochem. Soc.* **2020,** *167* (1), 013549.
105. Sasidhar, V.; Ruckenstein, E., Electrolyte osmosis through capillaries. *J. Colloid Interface Sci.* **1981,** *82* (2), 439-457.
106. Xu, Q.; Zhao, T. S., Fundamental models for flow batteries. *Prog. Energy Combust. Sci.* **2015,** *49*, 40-58.
107. Sun, C.; Chen, J.; Zhang, H.; Han, X.; Luo, Q., Investigations on transfer of water and vanadium ions across Nafion membrane in an operating vanadium redox flow battery. *Journal of Power Sources* **2010,** *195* (3), 890-897.
108. Yan, L.; Li, D.; Li, S.; Xu, Z.; Dong, J.; Jing, W.; Xing, W., Balancing Osmotic Pressure of Electrolytes for Nanoporous Membrane Vanadium Redox Flow Battery with a Draw Solute. *ACS Appl Mater Interfaces* **2016,** *8* (51), 35289-35297.
109. Li, B.; Luo, Q.; Wei, X.; Nie, Z.; Thomsen, E.; Chen, B.; Sprenkle, V.; Wang, W., Capacity Decay Mechanism of Microporous Separator-Based All-Vanadium Redox Flow Batteries and its Recovery. *ChemSusChem* **2014,** *7* (2), 577-584.

110. Xie, W.; Darling, R. M.; Perry, M. L., Processing and Pretreatment Effects on Vanadium Transport in Nafion Membranes. *Journal of The Electrochemical Society* **2015,** *163* (1), A5084-A5089.
111. Integration and Optimization of Novel Ion-Conducting Solids (IONICS). Advanced Research Projects Agency - Energy - U.S. Department of Energy (ARPA-E): 2016.
112. Cho, K. T.; Tucker, M. C.; Ding, M.; Ridgway, P.; Battaglia, V. S.; Srinivasan, V.; Weber, A. Z., Cyclic Performance Analysis of Hydrogen/Bromine Flow Batteries for Grid-Scale Energy Storage. *Chempluschem* **2015,** *80* (2), 402-411.
113. Teng, X.; Zhao, Y.; Xi, J.; Wu, Z.; Qiu, X.; Chen, L., Nafion/organically modified silicate hybrids membrane for vanadium redox flow battery. *J Power Sources* **2009,** *189* (2), 1240-1246.
114. Kim, S.; Yuk, S.; Kim, H. G.; Choi, C.; Kim, R.; Lee, J. Y.; Hong, Y. T.; Kim, H.-T., A hydrocarbon/Nafion bilayer membrane with a mechanical nano-fastener for vanadium redox flow batteries. *Journal of Materials Chemistry A* **2017,** *5* (33), 17279-17286.
115. Jung, M.; Lee, W.; Nambi Krishnan, N.; Kim, S.; Gupta, G.; Komsiyska, L.; Harms, C.; Kwon, Y.; Henkensmeier, D., Porous-Nafion/PBI composite membranes and Nafion/PBI blend membranes for vanadium redox flow batteries. *Appl. Surf. Sci.* **2018,** *450*, 301-311.
116. Yuan, Z.; Duan, Y.; Zhang, H.; Li, X.; Zhang, H.; Vankelecom, I., Advanced porous membranes with ultra-high selectivity and stability for vanadium flow batteries. *Energy & Environmental Science* **2016,** *9* (2), 441-447.
117. Xi, J.; Wu, Z.; Qiu, X.; Chen, L., Nafion/SiO2 hybrid membrane for vanadium redox flow battery. *J Power Sources* **2007,** *166* (2), 531-536.
118. Vijayakumar, M.; Luo, Q.; Lloyd, R.; Nie, Z.; Wei, X.; Li, B.; Sprenkle, V.; Londono, J. D.; Unlu, M.; Wang, W., Tuning the Perfluorosulfonic Acid Membrane Morphology for Vanadium Redox-Flow Batteries. *ACS Applied Materials & Interfaces* **2016,** *8* (50), 34327-34334.
119. Vrána, J.; Charvát, J.; Mazúr, P.; Bělský, P.; Dundálek, J.; Pocedič, J.; Kosek, J., Commercial perfluorosulfonic acid membranes for vanadium redox flow battery: Effect of ion-exchange capacity and membrane internal structure. *Journal of Membrane Science* **2018,** *552*, 202-212.
120. Luo, Q.; Zhang, H.; Chen, J.; Qian, P.; Zhai, Y., Modification of Nafion membrane using interfacial polymerization for vanadium redox flow battery applications. *Journal of Membrane Science* **2008,** *311* (1), 98-103.
121. Wang, L.; Pingitore, A. T.; Xie, W.; Yang, Z.; Perry, M. L.; Benicewicz, B. C., Sulfonated PBI Gel Membranes for Redox Flow Batteries. *J. Electrochem. Soc.* **2019,** *166* (8), A1449-A1455.
122. Shin, H. Y.; Cha, M. S.; Hong, S. H.; Kim, T.-H.; Yang, D.-S.; Oh, S.-G.; Lee, J. Y.; Hong, Y. T., Poly(p-phenylene)-based membrane materials with excellent cell efficiencies and durability for use in vanadium redox flow batteries. *Journal of Materials Chemistry A* **2017,** *5* (24), 12285-12296.
123. Peng, S.; Wu, X.; Yan, X.; Gao, L.; Zhu, Y.; Zhang, D.; Li, J.; Wang, Q.; He, G., Polybenzimidazole membranes with nanophase-separated structure induced by non-ionic hydrophilic side chains for vanadium flow batteries. *Journal of Materials Chemistry A* **2018,** *6* (9), 3895-3905.
124. Peng, S.; Yan, X.; Wu, X.; Zhang, D.; Luo, Y.; Su, L.; He, G., Thin skinned asymmetric polybenzimidazole membranes with readily tunable morphologies for high-performance vanadium flow batteries. *RSC Advances* **2017,** *7* (4), 1852-1862.
125. Zhang, S.; Yin, C.; Xing, D.; Yang, D.; Jian, X., Preparation of chloromethylated/quaternized poly(phthalazinone ether ketone) anion exchange membrane

materials for vanadium redox flow battery applications. *Journal of Membrane Science* **2010,** *363* (1), 243-249.
126. Dai, J.; Dong, Y.; Gao, P.; Ren, J.; Yu, C.; Hu, H.; Zhu, Y.; Teng, X., A sandwiched bipolar membrane for all vanadium redox flow battery with high coulombic efficiency. *Polymer* **2018,** *140*, 233-239.
127. Qiu, J.; Zhai, M.; Chen, J.; Wang, Y.; Peng, J.; Xu, L.; Li, J.; Wei, G., Performance of vanadium redox flow battery with a novel amphoteric ion exchange membrane synthesized by two-step grafting method. *Journal of Membrane Science* **2009,** *342* (1), 215-220.
128. Xing, D.; Zhang, S.; Yin, C.; Zhang, B.; Jian, X., Effect of amination agent on the properties of quaternized poly(phthalazinone ether sulfone) anion exchange membrane for vanadium redox flow battery application. *Journal of Membrane Science* **2010,** *354* (1), 68-73.
129. Jia, C.; Liu, J.; Yan, C., A significantly improved membrane for vanadium redox flow battery. *Journal of Power Sources* **2010,** *195* (13), 4380-4383.
130. Luo, X.; Lu, Z.; Xi, J.; Wu, Z.; Zhu, W.; Chen, L.; Qiu, X., Influences of Permeation of Vanadium Ions through PVDF-g-PSSA Membranes on Performances of Vanadium Redox Flow Batteries. *J. Phys. Chem. B* **2005,** *109* (43), 20310-20314.
131. Jin, S.; Jing, Y.; Kwabi, D. G.; Ji, Y.; Tong, L.; De Porcellinis, D.; Goulet, M.-A.; Pollack, D. A.; Gordon, R. G.; Aziz, M. J., A Water-Miscible Quinone Flow Battery with High Volumetric Capacity and Energy Density. *ACS Energy Letters* **2019,** *4* (6), 1342-1348.
132. Hatakeyama-Sato, K.; Nagano, T.; Noguchi, S.; Sugai, Y.; Du, J.; Nishide, H.; Oyaizu, K., Hydrophilic Organic Redox-Active Polymer Nanoparticles for Higher Energy Density Flow Batteries. *ACS Applied Polymer Materials* **2019,** *1* (2), 188-196.
133. Freger, V., Selectivity and polarization in water channel membranes: lessons learned from polymeric membranes and CNTs. *Faraday Discuss.* **2018**.
134. Baran, M. J.; Braten, M. N.; Sahu, S.; Baskin, A.; Meckler, S. M.; Li, L.; Maserati, L.; Carrington, M. E.; Chiang, Y.-M.; Prendergast, D.; Helms, B. A., Design Rules for Membranes from Polymers of Intrinsic Microporosity for Crossover-free Aqueous Electrochemical Devices. *Joule* **2019**.
135. Beers, K. M.; Hallinan, D. T.; Wang, X.; Pople, J. A.; Balsara, N. P., Counterion Condensation in Nafion. *Macromolecules* **2011,** *44* (22), 8866-8870.
136. Weber, A. Z.; Borup, R. L.; Darling, R. M.; Das, P. K.; Dursch, T. J.; Gu, W.; Harvey, D.; Kusoglu, A.; Litster, S.; Mench, M. M.; Mukundan, R.; Owejan, J. P.; Pharoah, J. G.; Secanell, M.; Zenyuk, I. V., A Critical Review of Modeling Transport Phenomena in Polymer-Electrolyte Fuel Cells. *J. Electrochem. Soc.* **2014,** *161* (12), F1254-F1299.
137. Allen, F. I.; Comolli, L. R.; Kusoglu, A.; Modestino, M. A.; Minor, A. M.; Weber, A. Z., Morphology of Hydrated As-Cast Nafion Revealed through Cryo Electron Tomography. *ACS Macro Lett.* **2015,** *4* (1), 1-5.
138. Marcus, Y.; Hefter, G., Ion Pairing. *Chem. Rev.* **2006,** *106* (11), 4585-4621.
139. Paul, R.; Paddison, S. J., Effects of dielectric saturation and ionic screening on the proton self-diffusion coefficients in perfluorosulfonic acid membranes. *J. Chem. Phys.* **2005,** *123* (22), 224704.
140. Petersen, M. K.; Voth, G. A., Characterization of the Solvation and Transport of the Hydrated Proton in the Perfluorosulfonic Acid Membrane Nafion. *J. Phys. Chem. B* **2006,** *110* (37), 18594-18600.
141. Feng, S.; Voth, G. A., Proton Solvation and Transport in Hydrated Nafion. *J. Phys. Chem. B* **2011,** *115* (19), 5903-5912.

142. Devanathan, R.; Venkatnathan, A.; Dupuis, M., Atomistic Simulation of Nafion Membrane. 2. Dynamics of Water Molecules and Hydronium Ions. *J. Phys. Chem. B* **2007,** *111* (45), 13006-13013.
143. Hwang, G. S.; Kaviany, M.; Gostick, J. T.; Kientiz, B.; Weber, A. Z.; Kim, M. H., Role of water states on water uptake and proton transport in Nafion using molecular simulations and bimodal network. *Polymer* **2011,** *52* (12), 2584-2593.
144. Spohr, E.; Commer, P.; Kornyshev, A. A., Enhancing Proton Mobility in Polymer Electrolyte Membranes: Lessons from Molecular Dynamics Simulations. *J. Phys. Chem. B* **2002,** *106* (41), 10560-10569.
145. Bear, J., *Dynamics of fluids in porous media*. Dover: New York, 1988; p 1.
146. Eikerling, M.; Kulikovsky, A. A., *Polymer electrolyte fuel cells : physical principles of materials and operation*. Boca Raton : CRC Press, [2015]: 2015.
147. Pisani, L.; Valentini, M.; Hofmann, D. H.; Kuleshova, L. N.; D'Aguanno, B., An analytical model for the conductivity of polymeric sulfonated membranes. *Solid State Ionics* **2008,** *179* (13–14), 465-476.
148. Choi, P.; Jalani, N. H.; Datta, R., Thermodynamics and Proton Transport in Nafion II. Proton Diffusion Mechanisms and Conductivity. *J. Electrochem. Soc.* **2005,** *152* (3), E123-E130.
149. Eikerling, M.; Kornyshev, A. A.; Stimming, U., Electrophysical Properties of Polymer Electrolyte Membranes: A Random Network Model. *J. Phys. Chem. B* **1997,** *101* (50), 10807-10820.
150. Safiollah, M.; Melchy, P.-E. A.; Berg, P.; Eikerling, M., Model of Water Sorption and Swelling in Polymer Electrolyte Membranes: Diagnostic Applications. *J. Phys. Chem. B* **2015,** *119* (25), 8165-8175.
151. Tse, Y.-L. S.; Herring, A. M.; Kim, K.; Voth, G. A., Molecular Dynamics Simulations of Proton Transport in 3M and Nafion Perfluorosulfonic Acid Membranes. *J. Phys. Chem. C* **2013,** *117* (16), 8079-8091.
152. Savage, J.; Tse, Y.-L. S.; Voth, G. A., Proton Transport Mechanism of Perfluorosulfonic Acid Membranes. *J. Phys. Chem. C* **2014,** *118* (31), 17436-17445.
153. Clark Ii, J. K.; Paddison, S. J., Ab initio molecular dynamics simulations of water and an excess proton in water confined in carbon nanotubes. *Phys. Chem. Chem. Phys.* **2014,** *16* (33), 17756.
154. Clark Ii, J. K.; Paddison, S. J., Proton dissociation and transfer in proton exchange membrane ionomers with multiple and distinct pendant acid groups: An ab initio study. *Electrochim. Acta* **2013,** *101*, 279-292.
155. Choe, Y.-K.; Tsuchida, E.; Ikeshoji, T.; Yamakawa, S.; Hyodo, S.-a., Nature of proton dynamics in a polymer electrolyte membrane, nafion: a first-principles molecular dynamics study. *Phys. Chem. Chem. Phys.* **2009,** *11* (20), 3892.
156. Bontha, J. R.; Pintauro, P. N., Water Orientation and Ion Solvation Effects during Multicomponent Salt Partitioning in a Nafion Cation-Exchange Membrane. *Chem. Eng. Sci.* **1994,** *49* (23), 3835-3851.
157. Kumar, M.; Edwards, B. J.; Paddison, S. J., A macroscopic model of proton transport through the membrane-ionomer interface of a polymer electrolyte membrane fuel cell. *J. Chem. Phys.* **2013,** *138* (6), 064903.
158. Paul, R.; Paddison, S. J., Structure and Dielectric Saturation of Water in Hydrated Polymer Electrolyte Membranes: Inclusion of the Internal Field Energy. *J. Phys. Chem. B* **2004,** *108* (35), 13231-13241.

159. Eikerling, M.; Kornyshev, A. A., Proton transfer in a single pore of a polymer electrolyte membrane. *J. Electroanal. Chem.* **2001,** *502* (1–2), 1-14.
160. Commer, P.; Cherstvy, A. g.; Spohr, E.; Kornyshev, A. a., The effect of water content on proton transport in polymer electrolyte membranes. *Fuel Cells* **2002,** *2* (3-4), 127-136.
161. Kusoglu, A.; Shi, S.; Weber, A. Z., in preperation.
162. Crothers, A. R.; Radke, C. J.; Weber, A. Z., Multiscale Model of Proton Transport in Perfluorosulfonic-Acid Membrane. *ECS Transactions* **2015,** *69* (17), 731-742.
163. Brenner, H., The slow motion of a sphere through a viscous fluid towards a plane surface. *Chem. Eng. Sci.* **1961,** *16* (3), 242-251.
164. Goldman, A. J.; Cox, R. G.; Brenner, H., Slow viscous motion of a sphere parallel to a plane wall—I Motion through a quiescent fluid. *Chem. Eng. Sci.* **1967,** *22* (4), 637-651.
165. Faxén, H., Der Widerstand gegen die Bewegung einer starren Kugel in einer zähen Flüssigkeit, die zwischen zwei parallelen ebenen Wänden eingeschlossen ist. *Annalen der Physik* **1922,** *373* (10), 89-119.
166. Hubbard, J. B., Dielectric dispersion and dielectric friction in electrolyte solutions. II. *J. Chem. Phys.* **1978,** *68* (4), 1649-1664.
167. Zoski, C. G., *Handbook of Electrochemistry*. Elsevier: 2006; p 935.
168. Marcus, Y., Ions and Their Properties. In *Ions in Solution and their Solvation*, John Wiley & Sons, Inc: 2015; pp 10-62.
169. Bockris, J. O. M.; Conway, B. E.; White, R. E., *Modern aspects of electrochemistry*. Springer Science & Business Media: 2012; Vol. 22.
170. Noyes, R. M., Thermodynamics of Ion Hydration as a Measure of Effective Dielectric Properties of Water. *J. Am. Chem. Soc.* **1962,** *84* (4), 513-522.
171. Palascak, M. W.; Shields, G. C., Accurate Experimental Values for the Free Energies of Hydration of H+, OH-, and H3O+. *J. Phys. Chem. A* **2004,** *108* (16), 3692-3694.
172. Robinson, R. A.; Stokes, R. H., *Electrolyte solutions*. Courier Corporation: 2002.
173. *CRC handbook of chemistry and physics*. Cleveland, Ohio : CRC Press, ©1977-: 1978.
174. Vacha, R.; Buch, V.; Milet, A.; Devlin, J. P.; Jungwirth, P., Autoionization at the surface of neat water: is the top layer pH neutral, basic, or acidic? *Phys. Chem. Chem. Phys.* **2007,** *9* (34), 4736-4747.
175. Bikerman, J., XXXIX. Structure and capacity of electrical double layer. *Philos. Mag. (1798-1977)* **1942,** *33* (220), 384-397.
176. Ehrlich, P., Dielectric properties of teflon from room temperature to 314 C and from frequencies of 102 to 105 c/s. *J. Res. Nat. Bur. Stand* **1953,** *51*, 185-8.
177. Onsager, L.; Samaras, N. N. T., The Surface Tension of Debye-Hückel Electrolytes. *J. Chem. Phys.* **1934,** *2* (8), 528-536.
178. Booth, F., The Dielectric Constant of Water and the Saturation Effect. *J. Chem. Phys.* **1951,** *19* (4), 391-394.
179. Lamm, G.; Pack, G. R., Calculation of Dielectric Constants near Polyelectrolytes in Solution. *J. Phys. Chem. B* **1997,** *101* (6), 959-965.
180. Gur, Y.; Ravina, I.; Babchin, A. J., On the electrical double layer theory. II. The Poisson—Boltzmann equation including hydration forces. *J. Colloid Interface Sci.* **1978,** *64* (2), 333-341.
181. Haggis, G. H.; Hasted, J. B.; Buchanan, T. J., The Dielectric Properties of Water in Solutions. *J. Chem. Phys.* **1952,** *20* (9), 1452-1465.
182. Chang, Y.; Mohanty, A. D.; Smedley, S. B.; Abu-Hakmeh, K.; Lee, Y. H.; Morgan, J. E.; Hickner, M. A.; Jang, S. S.; Ryu, C. Y.; Bae, C., Effect of Superacidic Side Chain Structures on

High Conductivity Aromatic Polymer Fuel Cell Membranes. *Macromolecules* **2015,** *48* (19), 7117-7126.
183. Hristov, I. H.; Paddison, S. J.; Paul, R., Molecular Modeling of Proton Transport in the Short-Side-Chain Perfluorosulfonic Acid Ionomer. *J. Phys. Chem. B* **2008,** *112* (10), 2937-2949.
184. Currie, J. A., Gaseous diffusion in porous media. Part 2. - Dry granular materials. *Br. J. Appl. Phys.* **1960,** *11* (8), 318.
185. Takamatsu, T.; Eisenberg, A., Densities and expansion coefficients of nafion polymers. *J. Appl. Polym. Sci.* **1979,** *24* (11), 2221-2235.
186. Yasuda, H.; Lamaze, C. E.; Peterlin, A., Diffusive and hydraulic permeabilities of water in water-swollen polymer membranes. *J. Polym. Sci. A-2 Polym. Phys.* **1971,** *9* (6), 1117-1131.
187. Giffin, G. A.; Haugen, G. M.; Hamrock, S. J.; Di Noto, V., Interplay between Structure and Relaxations in Perfluorosulfonic Acid Proton Conducting Membranes. *J. Am. Chem. Soc.* **2013,** *135* (2), 822-834.
188. Roy, A.; Hickner, M. A.; Yu, X.; Li, Y.; Glass, T. E.; McGrath, J. E., Influence of chemical composition and sequence length on the transport properties of proton exchange membranes. *J. Polym. Sci., Part B: Polym. Phys.* **2006,** *44* (16), 2226-2239.
189. Bae, B.; Yoda, T.; Miyatake, K.; Uchida, H.; Watanabe, M., Proton-Conductive Aromatic Ionomers Containing Highly Sulfonated Blocks for High-Temperature-Operable Fuel Cells. *Angew. Chem. Int. Ed.* **2010,** *49* (2), 317-320.
190. Evans, D. F.; Tominaga, T.; Hubbard, J. B.; Wolynes, P. G., Ionic mobility. Theory meets experiment. *J. Phys. Chem.* **1979,** *83* (20), 2669-2677.
191. Collazo, N.; Shin, S.; Rice, S. A., Molecular-dynamics studies of the structure and properties of monolayers of perfluorinated amphiphiles. *J. Chem. Phys.* **1992,** *96* (6), 4735-4742.
192. Delacourt, C.; Ridgway, P. L.; Kerr, J. B.; Newman, J., Design of an Electrochemical Cell Making Syngas ($CO + H2$) from CO2 and H2O Reduction at Room Temperature. *J. Electrochem. Soc.* **2008,** *155* (1), B42-B49.
193. Luo, T.; Abdu, S.; Wessling, M., Selectivity of ion exchange membranes: A review. *Journal of Membrane Science* **2018,** *555*, 429-454.
194. Parasuraman, A.; Lim, T. M.; Menictas, C.; Skyllas-Kazacos, M., Review of material research and development for vanadium redox flow battery applications. *Electrochim. Acta* **2013,** *101*, 27-40.
195. Skyllas-Kazacos, M.; Goh, L., Modeling of vanadium ion diffusion across the ion exchange membrane in the vanadium redox battery. *Journal of Membrane Science* **2012,** *399-400*, 43-48.
196. Ashraf Gandomi, Y.; Zawodzinski, T. A.; Mench, M. M., Concentrated Solution Model of Transport in All Vanadium Redox Flow Battery Membrane Separator. *ECS Transactions* **2014,** *61* (13), 23-32.
197. Narębska, A.; Kujawski, W.; Koter, S., Irreversible thermodynamics of transport across charged membranes: Part II-ion-water interactions in permeation of alkali. *Journal of Membrane Science* **1987,** *30* (2), 125-140.
198. Kamcev, J.; Paul, D. R.; Freeman, B. D., Equilibrium ion partitioning between aqueous salt solutions and inhomogeneous ion exchange membranes. *Desalination* **2018,** *446*, 31-41.
199. Kamcev, J.; Paul, D. R.; Manning, G. S.; Freeman, B. D., Ion Diffusion Coefficients in Ion Exchange Membranes: Significance of Counterion Condensation. *Macromolecules* **2018**.
200. Tandon, R.; Pintauro, P. N., Divalent/monovalent cation uptake selectivity in a Nafion cation-exchange membrane: Experimental and modeling studies. *Journal of Membrane Science* **1997,** *136* (1-2), 207-219.

201. Saito, M.; Arimura, N.; Hayamizu, K.; Okada, T., Mechanisms of Ion and Water Transport in Perfluorosulfonated Ionomer Membranes for Fuel Cells. *J. Phys. Chem. B* **2004,** *108* (41), 16064-16070.
202. Flory, P. J., *Principles of Polymer Chemistry*. Cornell University Press: 1953.
203. Giddings, J. C.; Kucera, E.; Russell, C. P.; Myers, M. N., Statistical theory for the equilibrium distribution of rigid molecules in inert porous networks. Exclusion chromatography. *J. Phys. Chem.* **1968,** *72* (13), 4397-4408.
204. Kontogeorgis, G. M.; Maribo-Mogensen, B.; Thomsen, K., The Debye-Hückel theory and its importance in modeling electrolyte solutions. *Fluid Phase Equilibria* **2018,** *462*, 130-152.
205. Israelachvili, J. N., *Intermolecular and surface forces*. Academic press: 2011.
206. Stokes, R. H.; Robinson, R. A., Ionic Hydration and Activity in Electrolyte Solutions. *J. Am. Chem. Soc.* **1948,** *70* (5), 1870-1878.
207. Schönert, H., The Debye-Hückel Theory for Hydrated Ions. I. Osmotic and Activity Coefficients of Binary Aqueous Solutions of Some 1 : 1 Electrolytes at 25°C. *Berichte der Bunsengesellschaft für physikalische Chemie* **1990,** *94* (6), 658-664.
208. Schönert, H., The Debye-Hückel Theory for Hydrated Ions. II. Osmotic and Activity Coefficients of Ternary Aqueous Solutions of Hydrogen and Alkali Halogenides at 25°C. *Berichte der Bunsengesellschaft für physikalische Chemie* **1990,** *94* (6), 664-670.
209. Manning, G. S.; Zimm, B. H., Cluster Theory of Polyelectrolyte Solutions. I. Activity Coefficients of the Mobile Ions. *J. Chem. Phys.* **1965,** *43* (12), 4250-4259.
210. Scatchard, G., Concentrated Solutions of Strong Electrolytes. *Chem. Rev.* **1936,** *19* (3), 309-327.
211. Kusoglu, A.; Santare, M. H.; Karlsson, A. M., Mechanics-based model for non-affine swelling in perfluorosulfonic acid (PFSA) membranes. *Polymer* **2009,** *50* (11), 2481-2491.
212. Bai, Y.; Schaberg, M. S.; Hamrock, S. J.; Tang, Z.; Goenaga, G.; Papandrew, A. B.; Zawodzinski, T. A., Density Measurements and Partial Molar Volume Analysis of Different Membranes for Polymer Electrolyte Membrane Fuel Cells. *Electrochim. Acta* **2017,** *242*, 307-314.
213. Smyrl, W. H.; Newman, J., Potentials of cells with liquid junctions. *J. Phys. Chem.* **1968,** *72* (13), 4660-4671.
214. Overbeek, J. T., The donnan equilibrium. *Prog. Biophys. Biophys. Chem* **1956,** *6* (1), 57-84.
215. Moré, J. J., The Levenberg-Marquardt algorithm: implementation and theory. In *Numerical analysis*, Springer: 1978; pp 105-116.
216. Nocedal, J.; Wright, S. J., Numerical optimization 2nd. Springer: 2006.
217. Tang, Z.; Keith, R.; Aaron, D. S.; Lawton, J. S.; Papandrew, A. P.; Zawodzinski, T. A., Proton Exchange Membrane Performance Characterization in VRFB. *ECS Transactions* **2012,** *41* (23), 25-34.
218. Cui, S.; Paddison, S. J., A Molecular Dynamics Study of the Effects of V2+ and V3+ on the Local Structure of Hydrated Nafion. *J. Phys. Chem. C* **2015,** *119* (23), 12848-12855.
219. Bass, M.; Freger, V., Hydration of Nafion and Dowex in liquid and vapor environment: Schroeder's paradox and microstructure. *Polymer* **2008,** *49* (2), 497-506.
220. Kusoglu, A.; Santare, M. H.; Karlsson, A. M.; Cleghorn, S.; Johnson, W. B., Micromechanics model based on the nanostructure of PFSA membranes. *J. Polym. Sci., Part B: Polym. Phys.* **2008,** *46* (22), 2404-2417.
221. Bonner, O. D., Study of methanesulfonates and trifluoromethanesulfonates. Evidence for hydrogen bonding to the trifluoro group. *J. Am. Chem. Soc.* **1981,** *103* (12), 3262-3265.

222. Kusoglu, A. Mechanical characterization of perfluorosulfonic acid (PFSA) ionomer membranes. Ph.D., University of Delaware, Ann Arbor, 2009.
223. Skyllas-Kazacos, M.; Cao, L.; Kazacos, M.; Kausar, N.; Mousa, A., Vanadium Electrolyte Studies for the Vanadium Redox Battery—A Review. *ChemSusChem* **2016,** *9* (13), 1521-1543.
224. Bai, Y. Membrane and performance study in polymer electrolyte membrane fuel cells and hydrogen bromine redox flow batteries. University of Tennessee - Knoxville, 2013.
225. Yeo, R. S.; Chin, D. T., A Hydrogen-Bromine Cell for Energy Storage Applications. *J. Electrochem. Soc.* **1980,** *127* (3), 549-555.
226. Narębska, A.; Koter, S.; Kujawski, W., Irreversible thermodynamics of transport across charged membranes: Part I — Macroscopic resistance coefficients for a system with nafion 120 membrane. *Journal of Membrane Science* **1985,** *25* (2), 153-170.
227. Galizia, M.; Manning, G. S.; Paul, D. R.; Freeman, B. D., Ion partitioning between brines and ion exchange polymers. *Polymer* **2019,** *165*, 91-100.
228. Arges, C. G.; Li, K.; Zhang, L.; Kambe, Y.; Wu, G.-P.; Lwoya, B.; Albert, J. N. L.; Nealey, P. F.; Kumar, R., Ionic conductivity and counterion condensation in nanoconfined polycation and polyanion brushes prepared from block copolymer templates. *Molecular Systems Design & Engineering* **2019,** *4* (2), 365-378.
229. Freger, V., Hydration of Ionomers and Schroeder's Paradox in Nafion. *J. Phys. Chem. B* **2009,** *113* (1), 24-36.
230. Onishi, L. M.; Prausnitz, J. M.; Newman, J., Water−Nafion Equilibria. Absence of Schroeder's Paradox. *J. Phys. Chem. B* **2007,** *111* (34), 10166-10173.
231. Lyklema, J., Simple Hofmeister series. *Chemical Physics Letters* **2009,** *467* (4), 217-222.
232. Rahman, F.; Skyllas-Kazacos, M., Solubility of vanadyl sulfate in concentrated sulfuric acid solutions. *Journal of Power Sources* **1998,** *72* (2), 105-110.
233. Martell, A. E.; Hancock, R. D., *Metal complexes in aqueous solutions*. Springer Science & Business Media: 2013.
234. Dumont, J. H.; Baker, A. M.; Maurya, S.; Kim, Y. S.; Mukundan, R.; Myers, D. J.; Borup, R. L., Effect of Cerium, Cobalt and Nickel Contaminants on the Oxygen Reduction Reaction at Platinum Electrodes. *ECS Transactions* **2017,** *80* (8), 861-867.
235. Baker, A. M.; Mukundan, R.; Spernjak, D.; Judge, E. J.; Advani, S. G.; Prasad, A. K.; Borup, R. L., Cerium Migration during PEM Fuel Cell Accelerated Stress Testing. *J. Electrochem. Soc.* **2016,** *163* (9), F1023-F1031.
236. Stewart, S. M.; Spernjak, D.; Borup, R.; Datye, A.; Garzon, F., Cerium Migration through Hydrogen Fuel Cells during Accelerated Stress Testing. *ECS Electrochemistry Letters* **2014,** *3* (4), F19-F22.
237. Coms, F. D.; Liu, H.; Owejan, J. E., Mitigation of Perfluorosulfonic Acid Membrane Chemical Degradation Using Cerium and Manganese Ions. *ECS Transactions* **2008,** *16* (2), 1735-1747.
238. Weng, L.-C.; Bell, A. T.; Weber, A. Z., Towards membrane-electrode assembly systems for CO2 reduction: a modeling study. *Energy & Environmental Science* **2019,** *12* (6), 1950-1968.
239. Renner, J. N.; Greenlee, L. F.; Ayres, K. E.; Herring, A. M., Electrochemical Synthesis of Ammonia: A Low Pressure, Low Temperature Approach. *The Electrochemical Society Interface* **2015,** *24* (2), 51-57.
240. Oren, Y. S.; Biesheuvel, P. M., Theory of Ion and Water Transport in Reverse-Osmosis Membranes. *Physical Review Applied* **2018,** *9* (2), 024034.

241. Tedesco, M.; Hamelers, H. V. M.; Biesheuvel, P. M., Nernst-Planck transport theory for (reverse) electrodialysis: I. Effect of co-ion transport through the membranes. *Journal of Membrane Science* **2016,** *510*, 370-381.
242. Zawodzinski, T. A.; Davey, J.; Valerio, J.; Gottesfeld, S., The water content dependence of electro-osmotic drag in proton-conducting polymer electrolytes. *Electrochim. Acta* **1995,** *40* (3), 297-302.
243. Michael, P. H. A multicomponent membrane model for the vanadium redox flow battery. University of Texas at Austin, 2012.
244. Pintauro, P. N.; Bennion, D. N., Mass transport of electrolytes in membranes. 2. Determination of sodium chloride equilibrium and transport parameters for Nafion. *Ind. Eng. Chem. Fundam.* **1984,** *23* (2), 234-243.
245. Kontturi, K.; Murtomäki, L.; Manzanares, J. A., *Ionic transport processes: in electrochemistry and membrane science*. OUP Oxford: 2008.
246. Baker, A. M.; Komini Babu, S.; Chintam, K.; Kusoglu, A.; Mukundan, R.; Borup, R. L., Ce Cation Migration and Diffusivity in Perfluorosulfonic Acid Fuel Cell Membranes. *ECS Transactions* **2019,** *92* (8), 429-438.
247. Crothers, A. R.; darling, R. M.; Kusoglu, A.; Radke, C. J.; Weber, A. Z., Theory of Multicomponent Phenomena in Cation-Exchange Membranes: Part I. Thermodynamic Model and Validation. *J. Electrochem. Soc.* **2020,** *167* (1), 013547.
248. Benion, D. *Mass Transport of Binary Electrolyte Solutions in Membranes, Water Resources Center Desalination Report No. 4*; Tech. Rep. 66–17, Department of Engineering, University of California, Los …: 1966.
249. Meyers, J. P. Simulation and analysis of the direct methanol fuel cell. University of California, Berkeley, 1998.
250. Fornasiero, F.; Krull, F.; Prausnitz, J. M.; Radke, C. J., Steady-state diffusion of water through soft-contact-lens materials. *Biomaterials* **2005,** *26* (28), 5704-5716.
251. Barthel, J. M.; Krienke, H.; Kunz, W., *Physical chemistry of electrolyte solutions: modern aspects*. Springer Science & Business Media: 1998; Vol. 5.
252. Ghanbarian, B.; Hunt, A. G.; Ewing, R. P.; Sahimi, M., Tortuosity in Porous Media: A Critical Review. *Soil Science Society of America Journal* **2013,** *77* (5), 1461-1477.
253. Hiemenz, P. C., *Principles of colloid and surface chemistry*. M. Dekker New York: 1986; Vol. 9.
254. Kerkhof, P. J. A. M., A modified Maxwell-Stefan model for transport through inert membranes: the binary friction model. *The Chemical Engineering Journal and the Biochemical Engineering Journal* **1996,** *64* (3), 319-343.
255. Hunter, R. J., *Zeta Potential in Colloid Science*. Academic Press: 1981.
256. Friedman, S. P., Soil properties influencing apparent electrical conductivity: a review. *Computers and Electronics in Agriculture* **2005,** *46* (1), 45-70.
257. Koter, S., Transport of simple electrolyte solutions through ion-exchange membranes—the capillary model. *Journal of Membrane Science* **2002,** *206* (1–2), 201-215.
258. Sørensen, T. S.; Compañ, V., On the Gibbs-Duhem equation for thermodynamic systems of mixed Euler order with special reference to gravitational and nonelectroneutral systems. *Electrochim. Acta* **1997,** *42* (4), 639-649.
259. Hawkins Cwirko, E.; Carbonell, R. G., Transport of electrolytes in charged pores: Analysis using the method of spatial averaging. *J. Colloid Interface Sci.* **1989,** *129* (2), 513-531.

260. Afzal, M.; Saleem, M.; Mahmood, M. T., Temperature and concentration dependence of viscosity of aqueous electrolytes from 20.degree.C to 50.degree.C chlorides of (sodium(1+), potassium(1+), magnesium(2+), calcium(2+), barium(2+), strontium(2+), cobalt(2+), nickel(2+), copper(2+) and chromium(3+). *Journal of Chemical & Engineering Data* **1989,** *34* (3), 339-346.
261. Sum, E.; Skyllas-Kazacos, M., A study of the V(II)/V(III) redox couple for redox flow cell applications. *Journal of Power Sources* **1985,** *15* (2), 179-190.
262. Oriji, G.; Katayama, Y.; Miura, T., Investigation on V(IV)/V(V) species in a vanadium redox flow battery. *Electrochim. Acta* **2004,** *49* (19), 3091-3095.
263. Nightingale, E. R., Phenomenological Theory of Ion Solvation. Effective Radii of Hydrated Ions. *J. Phys. Chem.* **1959,** *63* (9), 1381-1387.
264. Sum, E.; Rychcik, M.; Skyllas-kazacos, M., Investigation of the V(V)/V(IV) system for use in the positive half-cell of a redox battery. *Journal of Power Sources* **1985,** *16* (2), 85-95.
265. Schwenzer, B.; Zhang, J.; Kim, S.; Li, L.; Liu, J.; Yang, Z., Membrane Development for Vanadium Redox Flow Batteries. *ChemSusChem* **2011,** *4* (10), 1388-1406.
266. Jiang, B.; Wu, L.; Yu, L.; Qiu, X.; Xi, J., A comparative study of Nafion series membranes for vanadium redox flow batteries. *Journal of Membrane Science* **2016,** *510*, 18-26.
267. Jiang, B.; Yu, L.; Wu, L.; Mu, D.; Liu, L.; Xi, J.; Qiu, X., Insights into the Impact of the Nafion Membrane Pretreatment Process on Vanadium Flow Battery Performance. *ACS Applied Materials & Interfaces* **2016,** *8* (19), 12228-12238.
268. Ashraf Gandomi, Y.; Aaron, D.; Mench, M., Influence of Membrane Equivalent Weight and Reinforcement on Ionic Species Crossover in All-Vanadium Redox Flow Batteries. *Membranes* **2017,** *7* (2), 29.
269. Lei, Y.; Zhang, B. W.; Bai, B. F.; Zhao, T. S., A transient electrochemical model incorporating the Donnan effect for all-vanadium redox flow batteries. *Journal of Power Sources* **2015,** *299*, 202-211.
270. Oh, K.; Won, S.; Ju, H., A comparative study of species migration and diffusion mechanisms in all-vanadium redox flow batteries. *Electrochim. Acta* **2015,** *181*, 238-247.
271. Gubler, L., Membranes and Separators for Redox Flow Batteries. *Current Opinion in Electrochemistry* **2019**.
272. Yang, X.-G.; Ye, Q.; Cheng, P.; Zhao, T. S., Effects of the electric field on ion crossover in vanadium redox flow batteries. *Applied Energy* **2015,** *145*, 306-319.
273. Oh, K.; Moazzam, M.; Gwak, G.; Ju, H., Water crossover phenomena in all-vanadium redox flow batteries. *Electrochim. Acta* **2019,** *297*, 101-111.
274. Hao, L.; Wang, Y.; He, Y., Modeling of Ion Crossover in an All-Vanadium Redox Flow Battery with the Interfacial Effect at Membrane/Electrode Interfaces. *J. Electrochem. Soc.* **2019,** *166* (8), A1310-A1322.
275. Darling, R. M.; Shiau, H.-S.; Weber, A. Z.; Perry, M. L., The Relationship between Shunt Currents and Edge Corrosion in Flow Batteries. *J. Electrochem. Soc.* **2017,** *164* (11), E3081-E3091.
276. Gerhardt, M. R.; Wong, A. A.; Aziz, M. J., The Effect of Interdigitated Channel and Land Dimensions on Flow Cell Performance. *J. Electrochem. Soc.* **2018,** *165* (11), A2625-A2643.
277. Won, S.; Oh, K.; Ju, H., Numerical analysis of vanadium crossover effects in all-vanadium redox flow batteries. *Electrochim. Acta* **2015,** *177*, 310-320.
278. Barton, J. L.; Brushett, F. R., A One-Dimensional Stack Model for Redox Flow Battery Analysis and Operation. *Batteries* **2019,** *5* (1), 25.

279. Milshtein, J. D.; Tenny, K. M.; Barton, J. L.; Drake, J.; Darling, R. M.; Brushett, F. R., Quantifying Mass Transfer Rates in Redox Flow Batteries. *J. Electrochem. Soc.* **2017,** *164* (11), E3265-E3275.
280. Boettcher, P. A.; Agar, E.; Dennison, C. R.; Kumbur, E. C., Modeling of Ion Crossover in Vanadium Redox Flow Batteries: A Computationally-Efficient Lumped Parameter Approach for Extended Cycling. *J. Electrochem. Soc.* **2016,** *163* (1), A5244-A5252.
281. Zheng, Q.; Li, X.; Cheng, Y.; Ning, G.; Xing, F.; Zhang, H., Development and perspective in vanadium flow battery modeling. *Applied Energy* **2014,** *132*, 254-266.
282. Darling, R. M.; Perry, M. L., The Influence of Electrode and Channel Configurations on Flow Battery Performance. *J. Electrochem. Soc.* **2014,** *161* (9), A1381-A1387.
283. Krishna, R., A generalized film model for mass transfer in non-ideal fluid mixtures. *Chem. Eng. Sci.* **1977,** *32* (6), 659-667.
284. Krishna, R.; Standart, G. L., A multicomponent film model incorporating a general matrix method of solution to the Maxwell-Stefan equations. *AIChE J.* **1976,** *22* (2), 383-389.
285. Integration and Optimization of Novel Ion Conducting Solids (IONICS). *Department of Energy ARPA-E* **2016**.
286. Kok, M. D. R.; Jervis, R.; Tranter, T. G.; Sadeghi, M. A.; Brett, D. J. L.; Shearing, P. R.; Gostick, J. T., Mass transfer in fibrous media with varying anisotropy for flow battery electrodes: Direct numerical simulations with 3D X-ray computed tomography. *Chem. Eng. Sci.* **2019,** *196*, 104-115.
287. Saltelli, A., Making best use of model evaluations to compute sensitivity indices. *Comput. Phys. Commun.* **2002,** *145* (2), 280-297.
288. Hickner, M. A.; Pivovar, B. S., The Chemical and Structural Nature of Proton Exchange Membrane Fuel Cell Properties. *Fuel Cells* **2005,** *5* (2), 213-229.
289. Cwirko, E. H.; Carbonell, R. G., Ionic equilibria in ion-exchange membranes: a comparison of pore model predictions with experimental results. *Journal of Membrane Science* **1992,** *67* (2), 211-226.
290. Thieu, L. M.; Zhu, L.; Korovich, A. G.; Hickner, M. A.; Madsen, L. A., Multiscale Tortuous Diffusion in Anion and Cation Exchange Membranes. *Macromolecules* **2019,** *52* (1), 24-35.
291. Koter, S.; Kujawski, W.; Koter, I., Transport of electrolytes through charged membranes—on the relations between the independent transport coefficients. *Desalination* **2009,** *241* (1-3), 75-80.
292. Cwirko, E. H.; Carbonell, R. G., Interpretation of transport coefficients in Nafion using a parallel pore model. *Journal of Membrane Science* **1992,** *67* (2), 227-247.
293. Mackie, J.; Meares, P. In *The diffusion of electrolytes in a cation-exchange resin membrane. I. Theoretical*, Proceedings of the Royal Society of London A: Mathematical, Physical and Engineering Sciences, The Royal Society: 1955; pp 498-509.
294. Amsden, B., Solute Diffusion within Hydrogels. Mechanisms and Models. *Macromolecules* **1998,** *31* (23), 8382-8395.
295. Schultz, S. G.; Schultz, S., *Basic principles of membrane transport*. CUP Archive: 1980; Vol. 2.
296. Galluzzo, M. D.; Loo, W. S.; Wang, A. A.; Walton, A.; Maslyn, J. A.; Balsara, N. P., Measurement of Three Transport Coefficients and the Thermodynamic Factor in Block Copolymer Electrolytes with Different Morphologies. *J. Phys. Chem. B* **2020,** *124* (5), 921-935.

297. de Groot, S. R.; Mazur, P., *Nonequilibrium thermodynamics*. Dover Publications, Inc., New York: 1984.
298. Curtis, R. A., Chapter 11 - Molecular Thermodynamics of Protein Systems. In *Thermodynamics of Phase Equilibria in Food Engineering*, Pereira, C. G., Ed. Academic Press: 2019; pp 443-506.
299. Obliger, A.; Jardat, M.; Coelho, D.; Bekri, S.; Rotenberg, B., Pore network model of electrokinetic transport through charged porous media. *Physical Review E* **2014,** *89* (4), 043013.
300. *Nafion NR211 and NR212 Ion Exchange Materials*; The Chemours Company, 2016.
301. DeGroot, M. H.; Schervish, M. J., *Probability and statistics*. 3rd ed. ed.; Addison-Wesley: 2002.
302. Brent, R. P., *Algorithms for minimization without derivatives*. Courier Corporation: 2013.
303. Su, G. M.; Cordova, I. A.; Yandrasits, M. A.; Lindell, M.; Feng, J.; Wang, C.; Kusoglu, A., Chemical and Morphological Origins of Improved Ion Conductivity in Perfluoro Ionene Chain Extended Ionomers. *J. Am. Chem. Soc.* **2019,** *141* (34), 13547-13561.
304. Loupe, N.; Abu-Hakmeh, K.; Gao, S.; Gonzalez, L.; Ingargiola, M.; Mathiowetz, K.; Cruse, R.; Doan, J.; Schide, A.; Salas, I.; Dimakis, N.; Jang, S. S.; Goddard, W. A.; Smotkin, E. S., Group Vibrational Mode Assignments as a Broadly Applicable Tool for Characterizing Ionomer Membrane Structure as a Function of Degree of Hydration. *Chemistry of Materials* **2020,** *32* (5), 1828-1843.
305. Moukheiber, E.; De Moor, G.; Flandin, L.; Bas, C., Investigation of ionomer structure through its dependence on ion exchange capacity (IEC). *Journal of Membrane Science* **2012,** *389*, 294-304.
306. Kreuer, K. D.; Schuster, M.; Obliers, B.; Diat, O.; Traub, U.; Fuchs, A.; Klock, U.; Paddison, S. J.; Maier, J., Short-side-chain proton conducting perfluorosulfonic acid ionomers: Why they perform better in PEM fuel cells. *Journal of Power Sources* **2008,** *178* (2), 499-509.
307. Ahmet, K.; J., D. T.; Z., W. A., Nanostructure/Swelling Relationships of Bulk and Thin-Film PFSA Ionomers. *Adv. Funct. Mater.* **2016,** *26* (27), 4961-4975.
308. Edmondson, C. A.; Fontanella, J. J., Free volume and percolation in S-SEBS and fluorocarbon proton conducting membranes. *Solid State Ionics* **2002,** *152-153*, 355-361.
309. Zawodzinski Jr, T. A.; Springer, T. E.; Uribe, F.; Gottesfeld, S., Characterization of polymer electrolytes for fuel cell applications. *Solid State Ionics* **1993,** *60* (1–3), 199-211.
310. Zawodzinski, T. A., Water Uptake by and Transport Through Nafion® 117 Membranes. *J. Electrochem. Soc.* **1993,** *140* (4), 1041.
311. Maldonado, L.; Perrin, J.-C.; Dillet, J.; Lottin, O., Characterization of polymer electrolyte Nafion membranes: Influence of temperature, heat treatment and drying protocol on sorption and transport properties. *Journal of Membrane Science* **2012,** *389*, 43-56.
312. Ochi, S.; Kamishima, O.; Mizusaki, J.; Kawamura, J., Investigation of proton diffusion in Nafion®117 membrane by electrical conductivity and NMR. *Solid State Ionics* **2009,** *180* (6–8), 580-584.
313. Sone, Y.; Ekdunge, P.; Simonsson, D., Proton Conductivity of Nafion 117 as Measured by a Four-Electrode AC Impedance Method. *J. Electrochem. Soc.* **1996,** *143* (4), 1254-1259.
314. Peron, J.; Mani, A.; Zhao, X.; Edwards, D.; Adachi, M.; Soboleva, T.; Shi, Z.; Xie, Z.; Navessin, T.; Holdcroft, S., Properties of Nafion® NR-211 membranes for PEMFCs. *Journal of Membrane Science* **2010,** *356* (1), 44-51.

315. Luo, Z.; Chang, Z.; Zhang, Y.; Liu, Z.; Li, J., Electro-osmotic drag coefficient and proton conductivity in Nafion® membrane for PEMFC. *International Journal of Hydrogen Energy* **2010,** *35* (7), 3120-3124.
316. Ise, M.; Kreuer, K. D.; Maier, J., Electroosmotic drag in polymer electrolyte membranes: an electrophoretic NMR study. *Solid State Ionics* **1999,** *125* (1), 213-223.
317. Fuller, T. F.; Newman, J., Experimental Determination of the Transport Number of Water in Nafion 117 Membrane. *J. Electrochem. Soc.* **1992,** *139* (5), 1332-1337.
318. Ge, S.; Yi, B.; Ming, P., Experimental Determination of Electro-Osmotic Drag Coefficient in Nafion Membrane for Fuel Cells. *J. Electrochem. Soc.* **2006,** *153* (8), A1443.
319. Xu, F.; Leclerc, S.; Stemmelen, D.; Perrin, J.-C.; Retournard, A.; Canet, D., Study of electro-osmotic drag coefficients in Nafion membrane in acid, sodium and potassium forms by electrophoresis NMR. *Journal of Membrane Science* **2017,** *536*, 116-122.
320. Edmondson, C. A.; Fontanella, J. J.; Chung, S. H.; Greenbaum, S. G.; Wnek, G. E., Complex impedance studies of S-SEBS block polymer proton-conducting membranes. *Electrochim. Acta* **2001,** *46* (10), 1623-1628.
321. Gong, X.; Bandis, A.; Tao, A.; Meresi, G.; Wang, Y.; Inglefield, P. T.; Jones, A. A.; Wen, W. Y., Self-diffusion of water, ethanol and decafluropentane in perfluorosulfonate ionomer by pulse field gradient NMR. *Polymer* **2001,** *42* (15), 6485-6492.
322. Ma, Z.; Jiang, R.; Myers, M. E.; Thompson, E. L.; Gittleman, C. S., NMR studies of proton transport in fuel cell membranes at sub-freezing conditions. *Journal of Materials Chemistry* **2011,** *21* (25), 9302-9311.
323. Tsushima, S.; Teranishi, K.; Hirai, S., Water diffusion measurement in fuel-cell SPE membrane by NMR. *Energy* **2005,** *30* (2), 235-245.
324. Zawodzinski, T. A.; Neeman, M.; Sillerud, L. O.; Gottesfeld, S., Determination of water diffusion coefficients in perfluorosulfonate ionomeric membranes. *J. Phys. Chem.* **1991,** *95* (15), 6040-6044.
325. Savage, J.; Voth, G. A., Persistent Subdiffusive Proton Transport in Perfluorosulfonic Acid Membranes. *J. Phys. Chem. Lett.* **2014,** *5* (17), 3037-3042.
326. Chapman, T. W.; Newman, J., A COMPILATION OF SELECTED THERMODYNAMIC AND TRANSPORT PROPERTIES OP BINARY ELECTROLYTES IN AQUEOUS SOLUTION. **1968**.
327. Rizzo, P.; Albright, J. G.; Miller, D. G., Measurements of Interdiffusion Coefficients and Densities for the System HCl + H2O at 25 °C. *Journal of Chemical & Engineering Data* **1997,** *42* (3), 623-630.
328. Dippel, T.; Kreuer, K. D., Proton transport mechanism in concentrated aqueous solutions and solid hydrates of acids. *Solid State Ionics* **1991,** *46* (1), 3-9.
329. Tyrrell, H. J. V.; Harris, K. R., Chapter 6 - Theoretical interpretations of diffusion coefficients. In *Diffusion in Liquids*, Tyrrell, H. J. V.; Harris, K. R., Eds. Butterworth-Heinemann: 1984; pp 258-310.
330. Kreuer, K.-D.; Dippel, T.; Meyer, W.; Maier, J. In *Nafion® Membranes: Molecular Diffusion, Proton Conductivity and Proton Conduction Mechanism*, 1992; 1992.
331. Gostick, J.; Aghighi, M.; Hinebaugh, J.; Tranter, T.; Hoeh, M. A.; Day, H.; Spellacy, B.; Sharqawy, M. H.; Bazylak, A.; Burns, A.; Lehnert, W.; Putz, A., OpenPNM: A Pore Network Modeling Package. *Computing in Science & Engineering* **2016,** *18* (4), 60-74.

332. Münchinger, A.; Kreuer, K.-D., Selective ion transport through hydrated cation and anion exchange membranes I. The effect of specific interactions. *Journal of Membrane Science* **2019,** *592*, 117372.
333. Lingwood, M. D.; Zhang, Z.; Kidd, B. E.; McCreary, K. B.; Hou, J.; Madsen, L. A., Unraveling the local energetics of transport in a polymer ion conductor. *Chem. Commun.* **2013,** *49* (39), 4283-4285.
334. Diederichsen, K. M.; McShane, E. J.; McCloskey, B. D., Promising Routes to a High Li+ Transference Number Electrolyte for Lithium Ion Batteries. *ACS Energy Letters* **2017,** *2* (11), 2563-2575.
335. Blanco, D. E.; Prasad, P. A.; Dunningan, K.; Modestino, M. A., Insights into membrane-separated organic electrosynthesis: the case of adiponitrile electrochemical production. *Reaction Chemistry & Engineering* **2020,** *5* (1), 136-144.
336. Schalenbach, M.; Hoeh, M. A.; Gostick, J. T.; Lueke, W.; Stolten, D., Gas Permeation through Nafion. Part 2: Resistor Network Model. *J. Phys. Chem. C* **2015,** *119* (45), 25156-25169.
337. Weber, A. Z.; Kusoglu, A., Unexplained transport resistances for low-loaded fuel-cell catalyst layers. *Journal of Materials Chemistry A* **2014,** *2* (41), 17207-17211.
338. Tesfaye, M.; Kushner, D. I.; Kusoglu, A., Interplay between Swelling Kinetics and Nanostructure in Perfluorosulfonic Acid Thin-Films: Role of Hygrothermal Aging. *ACS Applied Polymer Materials* **2019,** *1* (4), 631-635.
339. Kushner, D. I.; Kusoglu, A.; Podraza, N. J.; Hickner, M. A., Substrate-Dependent Molecular and Nanostructural Orientation of Nafion Thin Films. *Adv. Funct. Mater.* **2019,** *29* (37), 1902699.
340. Crothers, A. R.; Radke, C. J.; Prausnitz, J. M., 110th Anniversary: Theory of Activity Coefficients for Lithium Salts in Aqueous and Nonaqueous Solvents and in Solvent Mixtures. *Ind. Eng. Chem. Res* **2019,** *58* (39), 18367-18377.
341. Pinto, N. G.; Graham, E. E., Multicomponent diffusion in concentrated electrolyte solutions: Effect of solvation. *AIChE J.* **1987,** *33* (3), 436-443.